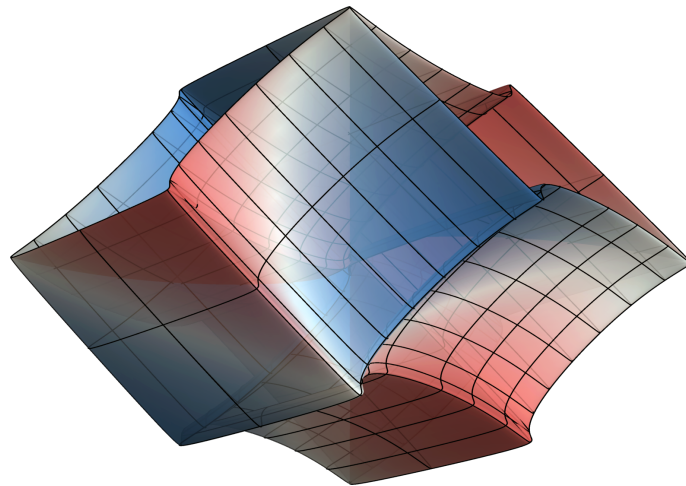

Topological Charge Pumping with Ultracold Bosonic Atoms in Optical Superlattices

Michael Carl Wilhelm Lohse



München 2018

Topological Charge Pumping with Ultracold Bosonic Atoms in Optical Superlattices



Dissertation an der Fakultät für Physik
Ludwig-Maximilians-Universität München

vorgelegt von

Michael Carl Wilhelm Lohse

aus Heidelberg

München, den 16. Januar 2018

Tag der mündlichen Prüfung: 27. Februar 2018

Erstgutachter: Prof. Immanuel Bloch

Zweitgutachter: Prof. Frank Pollmann

Weitere Prüfungskommissionsmitglieder: Prof. Thomas Weitz, Prof. Ralf Jungmann

Zusammenfassung

Elektrische Ströme werden üblicherweise durch eine externe Spannung hervorgerufen, die zu einem dissipativen Ladungstransport in Richtung des Gradienten führt. Schon in der Antike war jedoch bekannt, dass eine gerichtete Bewegung auch durch periodische Modulation eines Systems erzeugt werden kann wie etwa bei der Archimedes-Schraube. Ein quantenmechanisches Analogon wurde 1983 von David Thouless vorgeschlagen – die topologische Ladungspumpe. In einem solchen 1D System werden Teilchen durch eine adiabatische, zyklische Änderung des Hamilton-Operators gezielt in eine Richtung bewegt. Erstaunlicherweise können damit selbst in normalerweise isolierenden Medien Ströme erzeugt werden. Darüber hinaus ist die Bewegung für homogen besetzte Bänder in periodischen Potentialen quantisiert. Diese Quantisierung kann auf eine höherdimensionale topologische Invariante, die erste Chern-Zahl, zurückgeführt werden. Eine 1D topologische Ladungspumpe kann daher als eine dynamische Version des 2D Quanten-Hall-Effekts aufgefasst werden. Dies eröffnet die Möglichkeit, Quanten-Hall-Physik auch in höherdimensionalen Räumen experimentell zu untersuchen. Für 4D Systeme wurde ein neuartiger Quanten-Hall-Effekt vorhergesagt, bei dem ein quantisierter nichtlinearer Hall-Strom auftritt, der 4D topologische Eigenschaften aufweist. Dieser 4D Quanten-Hall-Effekt stellt das fundamentale Modell dar, auf dem die meisten niederdimensionalen topologischen Isolatoren basieren, und weist faszinierende Randeigenschaften wie isolierte Weyl-Punkte auf.

Diese Arbeit befasst sich mit der experimentellen Realisierung von 1D und 2D topologischen Ladungspumpen für ultrakalte bosonische Atome in optischen Übergittern. Durch die periodische Modulation eines 1D Übergitters wird eine Bewegung von Atomen in einem fraktionellen Mott-Isolator induziert. Diese wird mit Hilfe von in-situ Abbildungen und sogenanntem *site-resolved band mapping* quantitativ vermessen. Damit wird zum ersten Mal für eine topologische Ladungspumpe ein quantisierter Transport in einem ausgedehnten System beobachtet. Daneben werden die Transporteigenschaften des ersten angeregten Bandes untersucht, in dem die Bewegung in die entgegengesetzte Richtung erfolgt. Dieses anomale Verhalten belegt unzweifelhaft den quantenmechanischen Ursprung dieses Transports. Des Weiteren kann in diesem Band die Existenz eines topologischen Übergangs in Abhängigkeit der Gittertiefe nachgewiesen werden.

Mit Hilfe einer 2D topologischen Ladungspumpe wird eine dynamische Version des 4D Quanten-Hall-Effekts realisiert. Dessen Hauptmerkmal, der nichtlineare Hall-Strom, wird in einem zeitabhängigen, gewinkelten 2D Übergitter in-situ beobachtet – der erste Nachweis einer Bewegung mit intrinsischer 4D Symmetrie. Mit einer kleinen Atomwolke werden die geometrischen Eigenschaften dieser Bewegung lokal bestimmt und daraus das Verhalten eines unendlich großen Systems rekonstruiert. Die Quantisierung des Transports kann durch die Bestimmung der damit verknüpften 4D topologischen Invarianten, der zweiten Chern-Zahl, nachgewiesen werden. Die Nichtlinearität dieser Bewegung wird aufgezeigt, indem ihre Abhängigkeit von den verantwortlichen externen Störungen untersucht wird. Die hier zusammengefassten Ergebnisse stellen den ersten Schritt der Erforschung topologisch nichttrivialer Phasen in höherdimensionalen Systemen dar.

Abstract

Electric currents are usually generated by applying a voltage, leading to a dissipative transport of charge in the direction of the external bias. Yet, already in ancient times it was known that a motion can also be induced by a periodic modulation in absence of any bias as exemplified by the Archimedes screw. A quantum mechanical analogue of this was proposed by David Thouless in 1983 – the topological charge pump. In such a device, an adiabatic cyclic variation of the Hamiltonian of a one-dimensional (1D) system gives rise to a unidirectional motion of particles. Remarkably, this scheme enables the generation of currents even in otherwise insulating media. Moreover, the resulting transport is quantized for uniformly occupied bands in periodic potentials. This quantization can be related to a higher-dimensional topological invariant, the first Chern number. A 1D topological charge pump can thus be interpreted as a dynamical version of the 2D quantum Hall effect. As such, topological charge pumping provides a unique tool to study higher-dimensional quantum Hall physics, which is otherwise inaccessible to experiments. In 4D, a novel quantum Hall effect was predicted, whose characteristic feature is a quantized non-linear Hall response with 4D topology. Furthermore, 4D quantum Hall systems form the fundamental model for many lower-dimensional topological insulators and exhibit intriguing boundary effects such as isolated Weyl points.

This thesis reports on the experimental implementation of 1D and 2D topological charge pumps for ultracold bosonic atoms in dynamically controlled optical superlattices. By periodically modulating a 1D superlattice, atoms forming a fractional Mott insulator are displaced by a quantized distance per cycle. This motion is studied quantitatively using in-situ imaging and site-resolved band mapping. A quantized bulk transport by a topological charge pump is observed for the first time. In addition, the transport properties of the first excited band are probed. This reveals an anomalous pumping response in the direction opposite to the one for ground-state atoms, thereby unambiguously demonstrating the transport's quantum mechanical origin. Additionally, a topological transition is detected in the excited band as a function of the lattice depths.

The concept of topological charge pumping is extended to 2D systems to implement a dynamical version of the 4D integer quantum Hall effect. Its key signature, the non-linear Hall response, is observed in-situ in a time-dependent, angled 2D superlattice. This constitutes the first observation of a bulk response with intrinsic 4D symmetries in any physical system. By locally probing the geometric properties of the non-linear response with a small atom cloud, the response of an infinite system is reconstructed. Its quantization is demonstrated by determining the associated 4D topological invariant, the second Chern number. Furthermore, the non-linear character of the response is revealed by studying its dependence on the external perturbations that generate the response. The results presented here serve as the first step towards the exploration of topologically non-trivial phases in higher-dimensional systems.

Contents

1	Introduction	1
2	Topological Charge Pumping	9
2.1	Transport in Time-Dependent Systems	10
2.1.1	Adiabatic Evolution	10
2.1.2	Geometric Charge Pumping	11
2.1.3	Topological Charge Pumping	13
2.2	Properties of Topological Charge Pumps	17
2.2.1	Bulk-Edge Correspondence	17
2.2.2	Relation to the Zak Phase and the Theory of Polarization	18
2.2.3	Topological Protection	20
2.3	Relation to 2D Quantum Hall Physics	24
2.3.1	The Laughlin Charge Pump	24
2.3.2	Mapping in the Tight-Binding Regime	27
2.4	Applications and Implementations of Charge Pumps	31
2.4.1	Applications for Topological Charge Pumps	31
2.4.2	Previous Implementations of Charge Pumps	32
3	Ultracold Atoms in Optical Superlattices	35
3.1	Overview of the Experimental Setup	35
3.2	Optical Superlattices	37
3.2.1	Experimental Implementation	37
3.2.2	Superlattice Bose-Hubbard Model	40
4	Realization of a 1D Topological Charge Pump	45
4.1	Topological Charge Pumping in a Dimerized Superlattice	46
4.1.1	Pump Cycle in the Rice-Mele Model	46
4.1.2	Experimental Sequence	48
4.2	Experimental Results - Ground-State Band	50
4.2.1	Quantized Transport and Topological Protection	50
4.2.2	Efficiency of the Pumping Protocol	53
4.3	Experimental Results - First Excited Band	60
4.3.1	Reversed Transport	60
4.3.2	Topological Transition	61

5	Topological Charge Pumping in 2D	65
5.1	The 4D Quantum Hall Effect	66
5.1.1	Generalization of the Quantum Hall Effect to 4D	66
5.1.2	Relevance of the 4D Quantum Hall Effect	68
5.1.3	Hall Responses of a 4D Quantum Hall System	70
5.1.4	The 4D Harper-Hofstadter Model	77
5.2	Exploring 4D Quantum Hall Physics with a 2D Topological Charge Pump . .	78
5.2.1	Mapping a 4D Quantum Hall System to a Topological Charge Pump .	80
5.2.2	Transport Properties	83
5.2.3	Lorentz-Type Pumping Response	84
5.2.4	Density-Type Pumping Response	86
5.2.5	General Pumping Response	88
6	Implementation of a 2D Topological Charge Pump	91
6.1	Experimental Implementation in a 2D Optical Superlattice	92
6.1.1	Angled 2D Superlattice	92
6.1.2	Determination of the Tilt Angle	95
6.1.3	The Pump Cycle	97
6.1.4	Local Probing	100
6.2	Resolving the Non-Linear Response In-Situ	101
6.2.1	Initial State Preparation	101
6.2.2	Double-Differential In-Situ Imaging	106
6.2.3	In-Situ Measurement of the Non-Linear Response	107
6.3	Local Probing of the Non-Linear Response by Site-Resolved Band Mapping .	108
6.3.1	Measurement of the Double-Well Imbalance	109
6.3.2	Model for Double-Well Imbalance with Experimental Imperfections .	111
6.3.3	Non-Linear Response for Different Lattice Configurations	116
6.4	Measurement of the Second Chern Number	117
6.4.1	Reconstructing the Quantized Response of an Infinite System	118
6.4.2	Direct Determination of the Second Chern Number	118
6.4.3	Determination of the Second Chern Number with Corrections	121
6.4.4	Scaling of the Non-Linear Response with the Perturbing Angle	121
7	Conclusion and Outlook	125
	References	131
	Acknowledgements	153

Introduction

Controlling electronic transport may well be the single-most important application of physical phenomena, underlying everything from electric lighting and telecommunications to modern-day electronics. According to Ohm's law [1], an electric current is generated by applying an external bias to a conducting material. In 1900, this empirical conclusion was derived from a microscopic model by Paul Drude. The model assumes that the electrons in a metal can be considered as a classical gas of particles, which acquire a constant drift velocity in response to an external electric field due to scattering with the surrounding ions [2]. This theory was later extended by Arnold Sommerfeld to account for quantum mechanical effects and in particular the Fermi-Dirac statistics of electrons [3]. Combined with the band theory of crystalline solids [4], it constitutes a – in light of its simplicity – surprisingly successful description of the electronic transport properties of a wide range of materials, from metals and insulators to semiconductors and semimetals.

Its key assumption, however, that the band structure describing the electrons' energy-momentum dispersion fully captures their dynamics, later turned out to be invalid under certain circumstances, notably in the presence of magnetic fields. This is exemplified by the anomalous Hall effect in ferromagnetic materials, which can exhibit a Hall response that is orders of magnitudes larger than expected naively from their magnetization [5]. In a ground-breaking paper in 1954, Karplus and Luttinger demonstrated that the spin-orbit interaction between spin-polarized electrons can modify the Bloch wave functions in such a way that an additional off-diagonal contribution to the velocity of the particles appears – the so-called anomalous velocity [6]. It arises from an admixture of other eigenstates during the adiabatic evolution in response to an external electric field and – unlike the group velocity resulting solely from the band dispersion – depends on the intrinsic structure of the wave functions [7]. This illustrated that the eigenstates themselves also play a crucial role for the transport properties of a system. In the modern framework based on the concept of geometric phases, introduced by Michael Berry generalizing earlier work of Shivaramakrishnan Pancharatnam [8, 9], the anomalous velocity is determined by the Berry curvature. This geometric quantity describes the evolution of the eigenstates in the parameter space of the Hamiltonian and can be interpreted as the equivalent of a gauge field in this space.

In 1983, David Thouless realized that this provides an alternative way to create particle currents, namely by applying a periodic and adiabatic modulation to a system's Hamiltonian to induce a directional anomalous motion [10, 11]. This type of transport has since become known as charge pumping because it does not rely on an external bias and can even occur in the presence of a weak opposing gradient, similar to a quantum version of the Archimedes screw [12]. Furthermore, the contribution from the anomalous velocity depends only on geometric properties of the respective eigenstates, but it is independent of the modulation speed provided that adiabaticity still holds.

Most importantly, charge pumping allows for the generation of currents even in otherwise insulating states of matter. Moreover, the motion is quantized in this case and can be related to a higher-dimensional topological invariant [10]. For a non-interacting system with discrete translational invariance, this quantity is obtained by integrating the Berry curvature over a generalized Brillouin zone and can be interpreted as the magnetic charge of a monopole inside this closed manifold. This invariant is identical to the one characterizing the quantized linear Hall response of the 2D integer quantum Hall effect [13] and is equivalent to the first Chern number [14], which was introduced in mathematics in the study of vector bundles [15]. This implies that such a topological charge pump is extraordinarily robust against many perturbations since the value of a topological invariant can only change if the system becomes gapless [11]. Topological charge pumps could thus serve as extremely stable current sources [16] and a foundation for a new definition of the ampere [17], completing the quantum metrology triangle [18, 19]. On a more fundamental level, topological charge pumping in 1D systems is closely related to the Zak phase [20] and forms the basis of the modern theory of polarization in crystalline solids developed in the 1990s [21, 22].

The first experiments towards an implementation of a topological charge pump were conducted in solid state systems, demonstrating a quantized transport of charge with single electron pumps [23–26]. Yet, the motion in these devices is not a coherent quantum mechanical evolution, but rather a classical transport phenomenon with the quantization being enforced by a Coulomb blockade as opposed to the topology of the band structure. The way towards quantum mechanical pumping was paved in the late 1990s by extending Thouless' idea to open mesoscopic systems as they are typically realized in condensed matter experiments [27–29]. In these systems, a so-called parametric pump can be implemented by an out-of-phase modulation of at least two external parameters, e.g. gate voltages. It generates a quasi-adiabatic, non-quantized current that is proportional to the area enclosed in parameter space and can be described by a scattering matrix [28]. This was realized in an open quantum dot soon after [30], but the induced pump current could not be distinguished clearly from parasitic effects arising from a capacitive coupling [31, 32]. An explicit demonstration of coherent pumping was achieved in superconducting circuits via the measurement of the associated Berry phase [33]. However, the implementation of a real topological charge pump exhibiting quantized transport has not been accomplished in condensed matter experiments up to now. A big step towards this goal was made recently in an artificially engineered system formed by a 1D photonic waveguide array. The

Hamiltonian underlying a topological charge pump was realized in quasicrystalline structures as evidenced by the observation of the associated edge states and the non-quantized pumping of these modes [34, 35]. Building on this, the first part of this thesis reports on the implementation of a topological charge pump with ultracold bosonic atoms in a 1D optical superlattice and the first observation of the associated quantized bulk response.

Topological States of Matter

From a fundamental point of view, interest in topological charge pumping arises mainly due to its close relation to the 2D integer quantum Hall effect, whose discovery [36] and subsequent theoretical explanation [13] inspired Thouless' original proposal. This relation is already indicated by the connection to the same topological invariant, the first Chern number. Moreover, the pumping response of a 1D topological charge pump and the linear Hall response in a non-interacting 2D quantum Hall system can be shown to be mathematically equivalent via dimensional reduction [34, 37, 38]. The integer quantum Hall effect constitutes the first example of a topologically non-trivial state – a gapped phase that cannot be described in the Ginzburg-Landau framework of spontaneous symmetry breaking [39]. Instead of local order parameters, such phases are characterized by global topological invariants with two states being topologically equivalent if they can be connected by a smooth deformation without closing the gap. This explains the astonishing precision of the Hall response's quantization, which was first derived as a consequence of gauge invariance [37] and later related to the first Chern number [13, 14].

Subsequently, the observation of the fractional quantum Hall effect showed that similar phenomena can also occur in interacting 2D systems [40, 41]. Around the same time, seminal work by Duncan Haldane demonstrated that topological phases also appear in other systems, namely 1D spin chains [42, 43]. Here, the action contains a topological term such that quantum fluctuations generate an energy gap for integer values of the spin, while the ground state is gapless for half-integer spins. This was verified experimentally for antiferromagnetic spin-1 chains [44], which exhibit a Haldane phase – the paradigmatic example of a symmetry-protected topological state. In the context of quantum Hall physics, another key insight goes back to Haldane, who found that topologically non-trivial bands can also exist in 2D systems without a net magnetic field if the model intrinsically breaks time-reversal symmetry. An example for these so-called Chern insulators is the quantized version of the anomalous Hall effect discussed above, which was recently observed in magnetic topological insulators [45].

After it became clear that the quantum Hall effect cannot be generalized to 3D geometries [46], it was believed that this phenomenon is special to 2D systems with broken time-reversal symmetry. In 2000/2001, however, the existence of a quantum Hall state in 4D was postulated, which is characterized by the appearance of a novel quantized non-linear Hall response [47, 48]. Besides its higher-dimensional nature, the 4D quantum Hall effect can occur in systems both with and without time-reversal symmetry, thereby invalidating both of the aforementioned assumptions. This proposal marked the beginning

of the search for time-reversal symmetric topological states in experimentally accessible systems, resulting in the theoretical prediction of 2D topological insulators a few years later [49–52]. These materials are characterized by the appearance of counterpropagating edge states with opposite spins on top of an insulating bulk [53]. Experimental evidence for such a quantum spin Hall state was presented soon after in HgTe/CdTe quantum wells [54–56]. At the same time, it was proposed that a similar phase should exist in 3D systems [57–59], which was observed in experiments almost immediately [60, 61]. Interestingly, both 2D and 3D topological insulators can be derived from a time-reversal invariant 4D quantum Hall model by means of dimensional reduction [38]. Subsequently, an extensive classification of topological states of matter in terms of their dimensionality and symmetries has been developed [62–64]. In recent years, the theoretical and experimental study of topological phases has intensified, including e.g. topological superconductors [65], symmetry-protected phases with spatial symmetries [66, 67] as well as Dirac [68] and Weyl semimetals [69, 70].

Of the topological phases discussed above, the 4D quantum Hall effect is the most notable exception that has not yet been realized experimentally, for the obvious reason that there are only three spatial dimensions. Yet, the close connection between topological charge pumps and higher-dimensional quantum Hall systems provides the unique possibility to implement a dynamical version of the 4D quantum Hall effect in a 2D topological charge pump as proposed in [71]. The first realization of this using ultracold atoms in optical lattice potentials constitutes the second part of this thesis.

Ultracold Atoms

Experimental progress in the study of transport in general and topological phases in particular has been driven almost exclusively by condensed matter systems in the continuing pursuit to achieve an ever better understanding of the intricate quantum many-body phenomena that arise from the interplay of many, seemingly simple constituents, the electrons and atomic nuclei. The above-mentioned pumping of topological edge states in coupled optical waveguides [34, 35] and the observation of Weyl points in microwave photonic crystals [69] exemplify a new approach that has been developed in the past decades: the experimental simulation of quantum systems using artificially-engineered model systems that enable the accurate implementation of a desired Hamiltonian, while offering distinct advantages over solid state experiments in terms of controllability and accessibility [72, 73]. Besides photonic systems, these also include for example trapped ions or superconducting circuits.

Another prominent example for this are ultracold atoms in optical dipole potentials, which form almost perfectly isolated clean systems with flexible control of interactions, external potentials and internal states [74, 75]. This has allowed for the observation of many textbook examples of transport effects including Bloch oscillations [76], dissipationless superfluid flow [77] and localization phenomena [78–80]. Probing transport in closed systems like a cloud of ultracold atoms is often quite different from conventional solid state

experiments, in which measurements are usually conducted in a steady state in connection with external reservoirs. While familiar quantities like currents are therefore difficult to measure, ultracold atoms offer new observables such as the momentum distribution and the centre-of-mass position, which can facilitate the observation of novel effects [81, 82]. At the same time, remarkable progress has been made in implementing solid-state-like geometries with reservoirs [83]. In this way, transport measurements resembling those in mesoscopic systems can be performed including the observation of quantized conductance in ballistic channels [84].

Realizing topological states of matter in cold atom systems has become a very active field of research over the past few years. A major obstacle for this is the charge neutrality of atoms, preventing a direct application of an external magnetic field as in electronic quantum Hall systems. Starting with pioneering experiments in rotating systems exploiting the similarity between the Lorentz and the Coriolis force [85], a variety of techniques for realizing so-called artificial gauge fields have been proposed and implemented experimentally, for example using Raman transitions between internal states [86] as well as laser-assisted tunnelling [87] and shaking in optical lattices [88]. Based on this, both the 2D Hofstadter [89–91] and the Haldane model [92] were realized and the topologically non-trivial nature of their Bloch bands was demonstrated by measuring the resulting Hall response. In parallel, novel methods to directly probe geometric properties of band structures have been developed [93–96], which provide an unprecedented level of accessibility.

These experiments showcase the new possibilities offered by artificially engineered systems, which can go beyond what is deemed possible in condensed matter systems. This applies in particular to the 4D quantum Hall effect introduced in the previous section and very recently the first steps in this direction were taken. Using internal degrees of freedom like the atomic hyperfine states, synthetic dimensions can be realized [97]. Here, the internal state acts as an additional discrete spatial variable, enabling the realization of higher-dimensional tight-binding models, which can also include artificial gauge fields [98]. This idea has already been implemented experimentally to create thin 2D Hofstadter strips in 1D lattices [99, 100] and can potentially be extended to higher dimensions [101]. Furthermore, ultracold atoms can be used to realize mathematical toy models describing essential features of higher-dimensional quantum Hall systems. In particular, the creation of a non-Abelian gauge field corresponding to an $SU(2)$ Yang monopole was reported recently in an atomic four-level system [102]. Using an elaborate measurement scheme [103], the Berry phase in this artificially generated parameter space can be reconstructed, which was used to measure the second Chern number in this setting.

Outline

This thesis reports on the experimental implementation of 1D and 2D topological charge pumps using ultracold bosonic atoms in dynamically controlled optical superlattices. In Chapter 2, the concept of topological charge pumping in 1D systems is introduced. Starting with the derivation of the adiabatic evolution of a quantum mechanical wave function

under a time-dependent Hamiltonian, it is shown how a periodic and adiabatic modulation can give rise to a unidirectional quantized motion of particles, characterized by the first Chern number (Section 2.1). Key properties of this transport that result from the relation to a higher-dimensional topological invariant are discussed, e.g. the appearance of edge states and the topological robustness against perturbations (Section 2.2). This surprising behaviour of a 1D system originates from the fundamental connection to 2D quantum Hall models, onto whose Fourier components the Hamiltonian of a 1D charge pump can be mapped (Section 2.3). The chapter concludes with a brief discussion of potential applications and a review of preceding experiments in Section 2.4.

Chapter 3 contains a concise overview of the apparatus used for the experiments (Section 3.1), with special emphasis on the implementation of the dynamical superlattice potential (Section 3.2). For a more detailed description of the setup, the reader is referred to references [104–106]. Additionally, the tight-binding description of atoms in an optical superlattice in terms of the superlattice Bose-Hubbard model and the corresponding phase diagram are presented in Section 3.2.

As discussed above, ultracold atoms constitute a very flexible and powerful model system for the study of various physical problems. As shown in Chapter 4, this also applies to topological charge pumps, which are realized and probed with the techniques introduced in Chapter 3. In Section 4.1, the general framework developed in Chapter 2 is applied to the period-two superlattice configuration used in the experiment and a summary of the experimental sequence is given. Subsequently, the quantized motion of atoms in the lowest band of the superlattice is demonstrated, constituting the first observation of a quantized bulk transport by a topological charge pump, and the efficiency of the pumping protocol is quantified (Section 4.2). The first excited subband is of particular interest in a period-two superlattice as it can exhibit a negative first Chern number, which manifests in a reversed pumping response as compared to ground-state atoms. This classically counter-intuitive behaviour, which is associated with a topological transition, is studied in Section 4.3.

Topological charge pumping in 1D systems has mostly received attention as a textbook example of geometric and topological effects and due to its potential application as a current standard. By extending it to more dimensions, however, it can also serve as a probe for fundamental phenomena originating in higher-dimensional quantum Hall systems, which are otherwise out-of-reach for experiments. This holds in particular for the 4D quantum Hall effect, a dynamical version of which can be realized in the form of a 2D topological charge pump – the subject of Chapter 5. In Section 5.1, the generalization of the quantum Hall effect to four dimensions is reviewed, with a particular focus on its characteristic signature – a non-linear Hall response with 4D topology. Subsequently, following the original proposal in [71], the mapping onto a topological charge pump in a 2D superlattice and its pumping response are discussed in Section 5.2.

Chapter 6 is concerned with the experimental realization of such a 2D topological charge pump and the probing of the non-linear pumping response as the equivalent of the non-linear 4D Hall response. After discussing the experimental implementation in an angled 2D superlattice in Section 6.1, the direct observation of the resulting non-linear

transverse bulk displacement by in-situ imaging is presented (Section 6.2). This response can be quantified with a site-resolved band mapping technique, allowing for a local probing of its geometric properties using a small cloud of atoms (Section 6.3). From this, the response of an infinite system is reconstructed and its quantized nature is demonstrated by determining the associated 4D topological invariant – the second Chern number (Section 6.4).

The thesis concludes with a brief summary of the experimental findings, followed by a critical discussion of future perspectives (Chapter 7). In particular, this incorporates an outlook on interaction effects in topological pumps, both in connection to the fractional quantum Hall effect and as an interesting topic in itself.

List of Publications

The present thesis is based on the following two publications:

- M. Lohse, C. Schweizer, O. Zilberberg, M. Aidelsburger, and I. Bloch. *A Thouless quantum pump with ultracold bosonic atoms in an optical superlattice*. Nat. Phys. **12**, 350–354 (2016)
- M. Lohse, C. Schweizer, H. M. Price, O. Zilberberg, and I. Bloch. *Exploring 4D quantum Hall physics with a 2D topological charge pump*. Nature **553**, 55–58 (2018)

In addition, the below-listed papers were published during the course of this thesis:

- M. Aidelsburger, M. Atala, M. Lohse, J. T. Barreiro, B. Paredes, and I. Bloch. *Realization of the Hofstadter Hamiltonian with Ultracold Atoms in Optical Lattices*. Phys. Rev. Lett. **111**, 185301 (2013)
- M. Atala, M. Aidelsburger, M. Lohse, J. T. Barreiro, B. Paredes, and I. Bloch. *Observation of chiral currents with ultracold atoms in bosonic ladders*. Nat. Phys. **10**, 588–593 (2014)
- M. Aidelsburger, M. Lohse, C. Schweizer, M. Atala, J. T. Barreiro, S. Nascimbene, N. R. Cooper, I. Bloch, and N. Goldman. *Measuring the Chern number of Hofstadter bands with ultracold bosonic atoms*. Nat. Phys. **11**, 162–166 (2015)
- C. Schweizer, M. Lohse, R. Citro, and I. Bloch. *Spin Pumping and Measurement of Spin Currents in Optical Superlattices*. Phys. Rev. Lett. **117**, 170405 (2016)

Topological Charge Pumping

In quantum mechanics, the term "adiabatic" refers to changes in the Hamiltonian of a system that occur so slowly compared to the characteristic energy scales that the system can "adiabatically" follow the evolving eigenstates [107]. Naively, this implies that a periodically modulated system will always return to its initial state upon completion of a cycle. Whereas this is true for the occupation probabilities of the eigenstates, the wave function typically acquires an additional phase factor – the Berry phase [8, 9], which has important physical implications ranging from the molecular Aharonov-Bohm effect [108] to the quantum Hall effect [13]. While working on the latter, David Thouless came up with the ingenious idea that in this way the cyclic modulation of a periodic potential could give rise to a directed motion of particles by purely geometric means [10]. For insulating states, where usually no transport would be expected, the resulting motion should be quantized and determined by the topology of the pump cycle – a topological charge pump. In essence, it constitutes a dynamical analogue of the integer quantum Hall effect, thereby inheriting many of its remarkable properties like the appearance of edge states [34, 109, 110] and a topological protection of the quantized transport [11]. Topological charge pumps might thus be suitable for a variety of applications like precise current sources [16], adiabatic quantum motors [111] and quantum information [112].

In this chapter, the concept of a topological charge pump is introduced and important features of this type of transport are discussed. In Section 2.1, the adiabatic evolution of states in time-dependent systems is derived and applied to geometric charge pumping of individual eigenstates as well as topological charge pumping in homogeneously populated bands. Subsequently, key properties of topological charge pumps are covered like the robustness against external perturbations and the bulk-edge correspondence (Section 2.2). The relation between 1D topological charge pumps and 2D quantum Hall systems is illustrated in detail in Section 2.3, presenting a direct mapping in two limiting cases – the Landau levels of free particles and the Harper-Hofstadter model on a lattice. The chapter concludes with a brief summary of potential applications and an overview of previous implementations of various kinds of charge pumps. To a large extent, the content of this chapter has already been discussed elsewhere and, in addition to the original papers cited here, there are numerous review articles on this. For an excellent introduction to the topic see e.g. [7], on which parts of this chapter are based.

2.1 Transport in Time-Dependent Systems

2.1.1 Adiabatic Evolution

Let us consider a single particle that is initially prepared in a given eigenstate $|u_n(t=0)\rangle$ of a non-degenerate system which is slowly modulated in time. This modulation can be parametrized by a parameter $\varphi(t)$ such that the time-dependent Hamiltonian of the system is given by $\hat{H}(\varphi(t))$. At each point in time, the instantaneous eigenstates $|u_m(t)\rangle$ of \hat{H} form a complete basis, in which the particle's wave function can be expanded

$$|\psi(t)\rangle = \sum_m c_m(t) e^{-\frac{i}{\hbar} \int_0^t dt' E_m(t')} |u_m(t)\rangle \quad (2.1)$$

with $E_m(t)$ denoting the eigenenergy of $|u_m(t)\rangle$. By inserting this ansatz into the time-dependent Schrödinger equation, one obtains a system of coupled first-order differential equations for the coefficients c_m :

$$\dot{c}_m(t) = -c_m(t) \langle u_m(t) | \partial_t | u_m(t) \rangle - \sum_{l \neq m} c_l(t) e^{-\frac{i}{\hbar} \int_0^t dt' (E_l - E_m)} \langle u_m(t) | \partial_t | u_l(t) \rangle \quad (2.2)$$

If the variation of $\hat{H}(\varphi(t))$ is very slow relative to the energy gaps in the spectrum $E_l - E_m$, the second term can be neglected as the phase of the exponential will oscillate very fast compared to the slow variation of $\langle u_m(t) | \partial_t | u_l(t) \rangle$. A rigorous mathematical proof for this was first given by Max Born and Vladimir Fock [107] and later extended by Tosio Kato to also include degenerate systems [113]. For a sufficiently slow modulation, the set of equations in Eq. (2.2) thus decouples and its solution is given by

$$c_m(t) = e^{-\int_0^t dt' \langle u_m | \partial_{t'} | u_m \rangle} c_m(t=0) \quad (2.3)$$

Due to the normalization of the eigenstates, the exponent in Eq. (2.3) is purely imaginary and the modulus of the coefficients does not change to zero-th order in $\partial_t \varphi$. The particle will thus adiabatically follow the instantaneous eigenstate $|u_n(t)\rangle$ corresponding to its initial state and at most acquire a complex phase.

While this complex phase was already noted in the original proof, it was deemed irrelevant due to its lack of gauge invariance, i.e. its dependence on the specific choice of the eigenstates' phases. Its physical relevance was recognized only later, first by Shivarama-krishnan Pancharatnam when studying optical interference effects in crystals [8] and later in the seminal work by Michael Berry on adiabatically evolving systems [9]. For a modulation along a closed loop in parameter space, this phase – the so-called Berry phase – becomes gauge invariant. Moreover, it only depends on geometric properties of the eigenstates and the modulation, but not on the speed of the modulation $\partial_t \varphi$ as long as it remains adiabatic:

$$\gamma_B^{(n)} = i \int_0^t dt' \langle u_n | \partial_{t'} | u_n \rangle = \int_{\varphi(0)}^{\varphi(t)} d\varphi' \underbrace{i \langle u_n | \partial_{\varphi'} | u_n \rangle}_{A_n^{\varphi}(\varphi')} \quad (2.4)$$

with $A_n^\varphi(\varphi)$ being the Berry connection. The Berry phase manifests in a variety of physical phenomena like the Aharonov-Bohm effect [114] and even has a mechanical analogue in the Foucault pendulum [115].

When extending this analysis to include first order corrections, small modifications arise to the time evolution discussed above. As $c_{m \neq n} \ll c_n$, only contributions from the initial state $|u_n\rangle$ have to be taken into account in Eq. (2.2) and the coefficients can be obtained via integration by parts. For the initially unoccupied eigenstates, this yields

$$c_m(t) = i\hbar e^{i\gamma_B^{(n)}(t)} e^{i(\gamma_D^{(n)} - \gamma_D^{(m)})} \frac{\langle u_m(t) | \partial_t | u_n(t) \rangle}{E_m - E_n} \quad (2.5)$$

where $\gamma_D^{(m)} = -\frac{1}{\hbar} \int_0^t dt' E_m$ denotes the dynamical phase picked up by the eigenstate $|u_m\rangle$. The full wave function can thus be expressed as¹

$$|\psi(t)\rangle = e^{i(\gamma_D^{(n)} + \gamma_B^{(n)})} \left(|u_n(\varphi)\rangle + i\hbar \partial_t \varphi \sum_{m \neq n} \frac{\langle u_m(\varphi) | \partial_\varphi | u_n(\varphi) \rangle}{E_m - E_n} |u_m(\varphi)\rangle \right) \quad (2.6)$$

The variation of $\varphi(t)$ thus leads to a small admixture of other eigenstates to the wave function. This admixture is proportional to the rate of change $\partial_t \varphi$ and determined by geometric properties of the eigenstates, namely the off-diagonal elements of the Berry connection $A_{mn}^\varphi = i\langle u_m | \partial_\varphi | u_n \rangle$. While this may seem counter-intuitive for a supposedly adiabatic evolution, it is important to note that this admixture is purely virtual in the sense that – in contrast to non-adiabatic Landau-Zener transitions – it disappears completely when the modulation is stopped smoothly, $\partial_t \varphi \rightarrow 0$.

2.1.2 Geometric Charge Pumping

A Thouless charge pump consists of an extended spatial potential that is adiabatically varied in a cyclic way [10]. Despite its periodic nature, such a modulation can give rise to a directional motion of particles in this system as we will demonstrate in this section. A cyclic pumping scheme can for example be realized in a 1D superlattice potential, which consists of two periodic potentials with different periods d_1 (the long lattice) and $d_s = \alpha d_1$ with $\alpha < 1$ (the short lattice):

$$V_{\text{SL}}(x) = V_s \mathcal{V}_s(x) + V_l \mathcal{V}_l(x - \frac{d_1}{2\pi} \varphi_x) \quad (2.7)$$

Here, \mathcal{V}_s and \mathcal{V}_l are arbitrary smooth periodic functions, which are normalized to the range $[0, 1]$, and V_s and V_l denote the depth of the lattice potentials. The superlattice phase φ_x is an external parameter, which determines the relative position between the two potentials. In the following, we will often consider sinusoidal potentials of the form

$$V_{\text{SL}}(x) = V_s \sin^2(\pi x/d_s) + V_l \sin^2(\pi x/d_l - \varphi_x/2) \quad (2.8)$$

¹In this derivation, the eigenstates are assumed to be single-valued in parameter space, in contrast to the condition of parallel transport $\langle u_m | \partial_t | u_m \rangle = 0$, which is sometimes used as well. For the latter, the phases of the wave functions are chosen such that the eigenstates are uniquely defined as a function of t rather than φ , in which case the Berry phase is contained in the eigenstates themselves [7].

as they occur naturally in optical lattice potentials (see Section 3.2). While α can in principle take any arbitrary value between 0 and 1, we will restrict our analysis to commensurate lattice constants $\alpha = p/q$ with p and q being coprime integers. In this case, the combined potential is periodic as well with a unit cell of length $a_x = qd_s$ and its eigenstates are Bloch waves of the form $\psi_{n,k_x} = e^{ik_x x} u_{n,k_x}(x)$, where n is the band index, $\hbar k_x$ the quasi-momentum and u_{n,k_x} the cell-periodic part of the wave function. Using the Bloch waves as a basis, the system's single-particle Hamiltonian can be expressed in the momentum representation as $\hat{H}(k_x, \varphi_x) = e^{-ik_x x} \hat{H}(x, \varphi_x) e^{ik_x x}$ with eigenstates $|u_n(k_x, \varphi_x)\rangle$. Due to the translational invariance of \mathcal{V}_1 , $\hat{H}(k_x, \varphi_x)$ is periodic in both k_x and φ_x . The period as a function of k_x is given by the size of the Brillouin zone of the combined potential, $k_x \in]-\pi/(qd_s), +\pi/(qd_s)[$, whereas the one for φ_x corresponds to a shift by one period of the long lattice d_1 , i.e. $\varphi_x \in [0, 2\pi[$. Hence, the parameter space of the system has the same torus-like topology as the Brillouin zone of a periodic 2D system and can be considered as a 2D generalized Brillouin zone, which is spanned by k_x and φ_x as opposed to the two quasi-momenta k_x and k_y in a 2D system.

Accordingly, a Thouless pump can be implemented by slowly varying the pump parameter $\varphi_x(t)$ in time, i.e. moving one potential with respect to the other. This generates a periodic modulation of $\hat{H}(k_x, \varphi_x)$ with one pump cycle of duration T corresponding to $\varphi_x = 0 \rightarrow 2\pi$, at which point the potential becomes identical to the initial configuration. The time evolution of a particle that is initially prepared in an eigenstate $|u_n(k_x, \varphi_x = 0)\rangle$ of a given non-degenerate band n can be calculated with the formalism developed in Section 2.1.1 and, at a given point in the pump cycle, its wave function is determined to first order by Eq. (2.6). Because the lattice potential remains translationally invariant at all times, only states with the same quasi-momentum, but from different bands contribute. The expectation value for the velocity of the particle can be obtained from the instantaneous Hamiltonian using the Ehrenfest theorem

$$v(k_x, \varphi_x) = d\langle \hat{x} \rangle / dt = \frac{i}{\hbar} \langle [\hat{H}, \hat{x}] \rangle = \frac{1}{\hbar} \left\langle \frac{\partial \hat{H}(k_x, \varphi_x)}{\partial k_x} \right\rangle \quad (2.9)$$

When inserting Eq. (2.6), this yields in first order²:

$$v(k_x, \varphi_x) = \underbrace{\frac{1}{\hbar} \frac{\partial E_n(k_x, \varphi_x)}{\partial k_x}}_{v_{\text{gr}}(k_x, \varphi_x)} + \underbrace{i \partial_t \varphi_x \sum_{m \neq n} \left(\frac{\langle u_m | \partial_{\varphi_x} | u_n \rangle \langle u_n | \partial_{k_x} \hat{H} | u_m \rangle}{E_m - E_n} - \text{c.c.} \right)}_{v_a(k_x, \varphi_x)} \quad (2.10)$$

with $|u_m\rangle = |u_m(k_x, \varphi_x)\rangle$. The first term is the group velocity of the instantaneous eigenstate $|u_n(k_x, \varphi_x)\rangle$ resulting from the dispersion of the band $E_n(k_x, \varphi_x)$ in the current configuration. In addition to this, the admixture of eigenstates from other bands gives rise to an extra term, the anomalous velocity $v_a(k_x, \varphi_x)$. Using the fact that the $|u_m\rangle$ form a complete set of orthonormal eigenstates of $\hat{H}(k_x, \varphi_x)$, the anomalous velocity can be rewritten in the following way:

$$v_a(k_x, \varphi_x) = \Omega_n(k_x, \varphi_x) \partial_t \varphi_x \quad (2.11)$$

²For a discussion on higher-order corrections to the pumping-induced transport see Section 2.2.3

introducing the gauge-invariant Berry curvature

$$\Omega_n(k_x, \varphi_x) = \partial_{\varphi_x} A_n^{k_x} - \partial_{k_x} A_n^{\varphi_x} = i (\langle \partial_{\varphi_x} u_n | \partial_{k_x} u_n \rangle - \langle \partial_{k_x} u_n | \partial_{\varphi_x} u_n \rangle) \quad (2.12)$$

Interestingly, the anomalous velocity is thus purely determined by geometric properties of the eigenstate corresponding to the initial state, even though it is induced by the virtual occupation of other eigenstates. The comparison of Eq. (2.10) and Eq. (2.11) reveals the origin of a non-trivial Berry curvature, that is the residual coupling to other eigenstates resulting from an adiabatic change of the Hamiltonian. In this sense, the Berry curvature can be interpreted as a consequence of the continuous projection onto the instantaneous eigenstate $|u_n(k_x, \varphi_x)\rangle$ enforced by the condition of adiabaticity [7]. Loosely speaking, it is the admixture of other eigenstates to the wave function, which allows the state $|u_n\rangle$ to change as a function of φ_x .

The total displacement of the particle during one pump cycle can be obtained by integrating the velocity over time, $t \in [0, T]$. Depending on the exact shape of the potentials, the contribution from the group velocity can take an arbitrary value and, in particular, also depends on the pumping speed $\partial_t \varphi_x$. On the other hand, the anomalous velocity term, as it is proportional to $\partial_t \varphi_x$, upon integration over t leads to a displacement that is independent of the pumping speed and only determined by the geometry of the pump path in parameter space. For this reason, this type of transport is referred to as geometrical charge pumping. The distribution of $\Omega_n(k_x, \varphi_x)$ depends on the structure of the eigenstates, which in turn is determined by the lattice potential. It can be either positive or negative, such that – unlike in a classical system – the motion of the particle is not necessarily in the same direction as the one of the moving lattice, which induces the pumping. Moreover, the displacement per cycle for a given eigenstate can take any value and is not quantized in general.

2.1.3 Topological Charge Pumping

For a homogeneously populated band, where all k_x -states have the same mean occupation, the centre-of-mass displacement is obtained by additionally averaging over k_x . Due to the periodicity of the band structure in momentum space, $E_n(k_x = -\pi/a_x, \varphi_x) = E_n(k_x = +\pi/a_x, \varphi_x)$, the contribution from the group velocity to the mean displacement vanishes for a uniformly occupied band. The centre-of-mass drift after one pump cycle is thus given by the integral of the Berry curvature over the entire 2D generalized Brillouin zone:

$$\delta x_{\text{COM}} = \frac{a_x}{2\pi} \oint dk_x d\varphi_x \Omega_n(k_x, \varphi_x) \quad (2.13)$$

The fact that the Berry curvature corresponds to the curl of the Berry connection in the generalized momentum space [Eq. (2.12)] implies that the above integral can be rewritten using Stokes' theorem. However, due to its periodicity in k_x and φ_x , the generalized Brillouin zone does not constitute a simply connected manifold and in particular does not have a boundary. This problem can be overcome by artificially dividing the Brillouin zone

into two parts, separated by a boundary ∂S (Fig. 2.1) [14, 116, 117]. The displacement can then be expressed as the sum of the integrals over both surfaces, each of which can be converted to an integral over the Berry connection along the boundary by applying Stokes' theorem:

$$\delta x_{\text{COM}} = \frac{a_x}{2\pi} \left(\oint_{\partial S} d\mathbf{k} \cdot \mathbf{A}_n^{(1)}(k_x, \varphi_x) - \oint_{\partial S} d\mathbf{k} \cdot \mathbf{A}_n^{(2)}(k_x, \varphi_x) \right) \quad (2.14)$$

with $\mathbf{k} = (k_x, \varphi_x)$ and $\mathbf{A}_n = (A_n^{k_x}, A_n^{\varphi_x})$. The superscript of \mathbf{A}_n indicates the surface that the Berry connection is defined on. Note that the minus sign results from the opposite orientation of the boundaries.

The Bloch waves possess a gauge freedom as at any point (k_x, φ_x) their global phase can be chosen at will, $|u_n(k_x, \varphi_x)\rangle \rightarrow e^{-i\lambda(k_x, \varphi_x)}|u_n(k_x, \varphi_x)\rangle$. While this transformation leaves all physically observable quantities including the Berry curvature invariant, this does not hold for the Berry connection, which transforms as

$$\mathbf{A}_n(k_x, \varphi_x) \rightarrow \mathbf{A}_n(k_x, \varphi_x) + \nabla_{\mathbf{k}}\lambda(k_x, \varphi_x) \quad (2.15)$$

where $\nabla_{\mathbf{k}} = (\partial_{k_x}, \partial_{\varphi_x})$. As both terms in Eq. (2.14) are gauge invariant, a different gauge can be chosen in the two parts of the Brillouin zone. Both parts are then connected by a gauge transformation λ_{12} at the boundary. This implies

$$\delta x_{\text{COM}} = \nu_1 a_x \quad (2.16)$$

with the first Chern number

$$\nu_1 = \frac{1}{2\pi} \oint dk_x d\varphi_x \Omega_n(k_x, \varphi_x) = \frac{1}{2\pi} \oint_{\partial S} \nabla_{\mathbf{k}}\lambda_{12}(k_x, \varphi_x) \quad (2.17)$$

As the gauge transformation must be uniquely defined at each point, ν_1 has to be an integer. Note that this result can also be derived by mapping the Brillouin zone to a rectangle with special boundary conditions, which result from the single-valued definition of the Bloch waves, and calculating the Berry phase around a closed loop along the edges of the rectangularized Brillouin zone [7, 13]. The quantization of the first Chern number is a general property of closed 2D manifolds independent of the specific realization and thus occurs in all systems whose Hamiltonian is periodic in two parameters. This is a consequence of the Gauss-Bonnet theorem known from differential geometry since the Berry curvature is analogous to a Gaussian curvature [15]. The Chern number therefore also manifests in quantized phenomena in other physical systems, most prominently the integer quantum Hall effect [13], which is closely related to topological charge pumping as detailed in Section 2.3.

Eq. (2.16) and Eq. (2.17) have a number of far-reaching consequences for the particle transport in homogeneously populated bands. First of all, since the Chern number is an integer quantity, the average displacement per cycle is quantized in units of a_x , i.e. the size of the unit cell of the superlattice [10]. Furthermore, as ν_1 can take any integer value, it can be negative, corresponding to a particle transport in the opposite direction as the motion of the underlying lattice, or larger than one, implying a faster motion than the

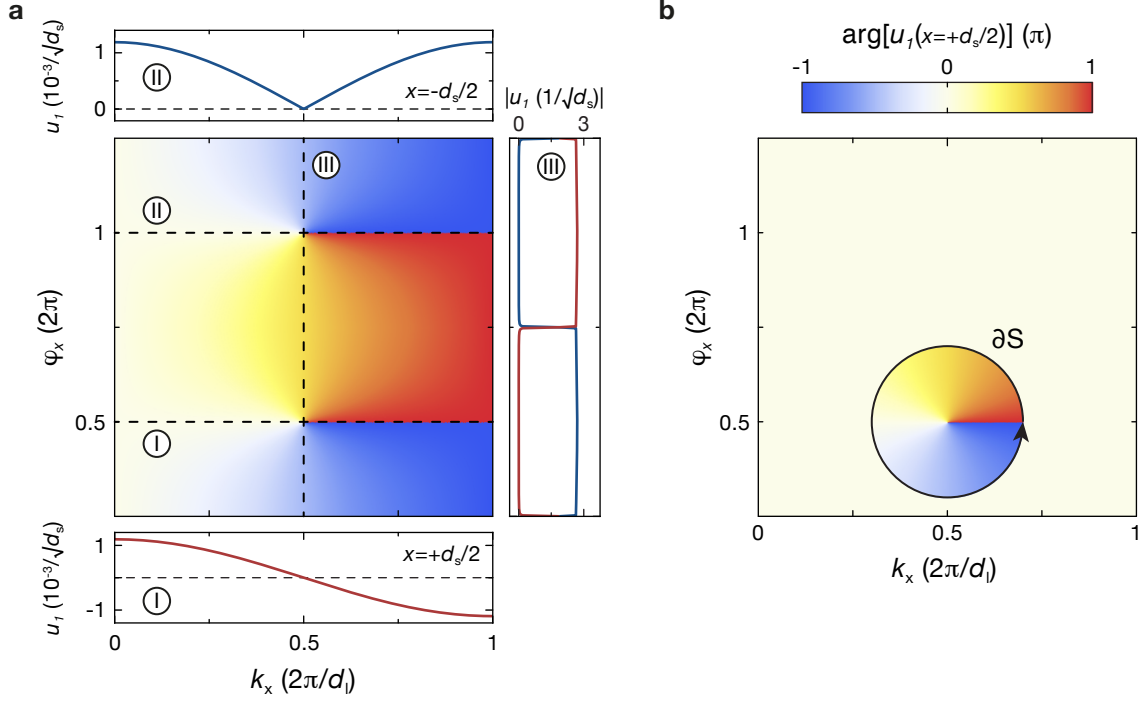


Figure 2.1 – First Chern number of the pump cycle in a dynamical superlattice. (a) The main plot shows the phase of the ground-state Bloch wave function $\arg(u_1(k_x, \varphi_x))$ in the 2D generalized Brillouin zone evaluated at $x = +d_s/2$ for a sinusoidal superlattice as in Eq. (2.8) with $d_l = 2d_s$. For each (k_x, φ_x) , the phase of u_1 is chosen such that u_1 is real and positive at $x = -d_s/2$. Due to the topologically non-trivial nature of the pump cycle, two singularities occur. At $(k_x = \pi/d_l, \varphi_x = \pi)$, $u_1(x = +d_s/2)$ vanishes (see cut at $\varphi_x = \pi$ in lower panel) and its phase exhibits a vortex-like pattern around this singularity. A similar feature, but with opposite orientation appears at $(k_x = \pi/d_l, \varphi_x = 2\pi)$. This vortex, however, has a different origin as it results from a singularity of the phase reference $u_1(x = -d_s/2)$ (upper panel), which prohibits an unambiguous definition for the phase of u_1 over the entire Brillouin zone – a characteristic property of systems with non-zero Chern number. On the other hand, $u_1(x = +d_s/2)$ is non-zero everywhere in this region (right panel). (b) The Brillouin zone can therefore be partitioned in two areas, separated by the boundary ∂S , throughout each of which the phase of $u_1(x = +d_s/2)$ is well defined. This is shown here using the phase choice from (a) in the vicinity of $(k_x = \pi/d_l, \varphi_x = \pi)$, whereas $u_1(x = +d_s/2)$ is chosen to be real and positive outside of it. At the boundary ∂S , the two wave functions can be related to each other via a gauge transformation $\lambda_{12}(k_x, \varphi_x)$. This transformation defines the pump cycle's Chern number, which is determined by the vorticity of the singularity of $u_1(x = +d_s/2)$. Thus, it is an integer, in this case $\nu_1 = +1$ [Eq. (2.17)].

lattice – both of which is impossible in a classical system. However, a displacement does not necessarily occur as a response to the pumping since $\nu_1 = 0$ is also possible. This can easily be seen from Eq. (2.17): Whenever it is possible to choose the same gauge for all Bloch functions within the Brillouin zone, $\lambda_{12} = 0$ and thus ν_1 vanishes as well. This is indeed the case in most generic systems such that in general an adiabatic modulation of a lattice potential does not induce a particle transport. Only in special cases this is not possible and $\nu_1 \neq 0$. Such a situation occurs whenever the cell-periodic part of the Bloch wave function at a given position, which is used to define the phase reference, vanishes

at some point in the Brillouin zone [117]. To obtain an unambiguous choice for the phase of the Bloch wave functions in this case, the Brillouin zone has to be divided into two different regions as discussed above using a different gauge in the vicinity of such a singularity³. The gauge transformation connecting the different phase choices at the boundary between the regions is defined by the phase distribution around the singularity. In particular, it inherits its vorticity, i.e. the number of phase windings, which in turn defines the Chern number of the pump cycle following Eq. (2.17). This is exemplified for a pump cycle in a dynamical superlattice with $d_1 = 2d_s$ in Fig. 2.1.

While this derivation provides a criterion when a directional transport of particles can occur, it does not give much insight under which circumstances the Chern number can be non-trivial. To this end, it is helpful to rewrite the Berry curvature in the following way:

$$\Omega_n(k_x, \varphi_x) = i \sum_{m \neq n} \left(\frac{\langle u_n | \partial_{k_x} \hat{H} | u_m \rangle \langle u_m | \partial_{\varphi_x} \hat{H} | u_n \rangle}{(E_m - E_n)^2} - \text{c.c.} \right) \quad (2.18)$$

This expression can be obtained analogously to the derivation of Eq. (2.11) from Eq. (2.10). From Eq. (2.18), it becomes clear that a singularity appears in Ω_n whenever there is a degeneracy in the energy spectrum, $E_n = E_m$. Under the assumption that only two states become degenerate, the behaviour of these states in the vicinity of the degeneracy point can be described by a generic two-level Hamiltonian of the form $\mathbf{R} \cdot \boldsymbol{\sigma}$ with three independent parameters R_i and the Pauli matrices σ_i , $i \in \{x, y, z\}$ [9]. In this parameter space, the Berry curvature $\boldsymbol{\Omega}_n(\mathbf{R})$ takes the form of the magnetic field of a Dirac monopole [118] and the Chern number defined on a surface enclosing the degeneracy is equal to the charge of the monopole [9, 116]. In this sense, a degeneracy in parameter space can be interpreted as the source of a non-zero Berry curvature. This implies an important condition, namely that the parameter space has to be at least three dimensional, since in the absence of special symmetries more than two parameters are required for a degeneracy to occur [119]. While the pump cycle is parametrized by a single parameter φ_x in addition to the 1D quasi-momentum $\hbar k_x$, a change in φ_x will in general affect multiple microscopic parameters $\mathcal{R}(\varphi_x)$ of the superlattice Hamiltonian (e.g. the tight-binding parameters, c.f. Section 4.1.1). For the pumping process to be non-trivial, the pump cycle in the k_x - $\mathcal{R}(\varphi_x)$ parameter space has to enclose a degeneracy point, otherwise $\nu_1 = 0$.

The relation between the Chern number and the degeneracies enclosed by the pump path has an important consequence: In order for the Chern number of the pump to change, a band crossing has to occur somewhere along the cycle such that a degeneracy point can enter or leave the volume surrounded by the pump path. In particular, this means that as long as the band gaps remain open, ν_1 remains the same irrespective of the microscopic details like the exact shape and depth of the lattice potentials, i.e. it constitutes a topological invariant [10]. Furthermore, if two bands touch, their Chern numbers can

³Depending on the number and distribution of singularities of the wave functions, more than two regions might be required. The procedure introduced above then has to be extended accordingly, which leads to the theory of fibre bundles [14, 117].

change, but their sum has to remain the same, provided that no additional degeneracies with other bands occur during the pump cycle [120]. Because of this, the particle transport of a charge pump in homogeneously populated bands is extraordinarily robust against perturbations like the presence of disorder or inter-particle interactions [11] (see Section 2.2.3). Due to this topological protection, such systems are referred to as topological charge pumps and hold promise for a variety of technological applications, e.g. as extremely stable current sources [16] (see Section 2.4.1).

2.2 Properties of Topological Charge Pumps

2.2.1 Bulk-Edge Correspondence

As discussed in Section 2.1.3, topological invariants like the first Chern number can only change whenever a gap closes in the energy spectrum. This implies that such a degeneracy has to occur at the boundary between a topologically non-trivial system and its surroundings, leading to the appearance of localized edge states crossing the bulk energy gaps. The properties of these boundary modes are intimately connected to the topological characteristics of the bulk. This phenomenon is known as the bulk-edge correspondence and was first studied in the context of 2D quantum Hall physics, where the Hall conductance of the bulk quantified by the first Chern number of the energy bands is connected to the winding number of the accompanying edge states [110, 121]. Similar effects are thus expected at the edge of a 1D topological charge pump in a finite-sized system. Such boundary modes were observed experimentally in 1D quasicrystalline waveguide arrays [34] and have recently been studied theoretically in [122, 123].

To illustrate this, let us consider a dynamical superlattice with $d_s/d_l = p/q$ in a system with size L_x and open boundary conditions, whose low-energy spectrum consists of q subbands with $L_x/(qd_s)$ states each (see Fig. 2.2). After a full pump cycle, the lattice configuration becomes identical to the initial one, which in particular means that the number of states per band is the same. Therefore, if there is a localized boundary mode that emerges from one band and traverses the gap to a neighbouring band as the pump parameter φ_x is varied, there must be another state that exhibits the opposite behaviour, i.e. edge states always appear in pairs that counter-propagate in the energy spectrum. We will now evaluate the system's pumping response starting from a configuration where all states belonging to the lowest band are uniformly populated. If the pumping is adiabatic, the first $L_x/(qd_s)$ states in the spectrum will maintain their homogeneous occupation during the cycle and an edge state forming from the bulk of the lowest band will be occupied as well. Assuming perfect global adiabaticity, if two edge states cross at some point, particles in the state with increasing energy will be transferred to the other one such that the system always remains in the state that is adiabatically connected to the initial state⁴. For edge

⁴Note that the condition of global adiabaticity is typically not fulfilled in experiments as the coupling between the edges is exponentially small in the system size. This allows for a quantized particle transport even in finite systems.

states that are localized on opposite ends of the system, this gives rise to a discontinuity in the particles' centre-of-mass position (Fig. 2.2c). In the limit where the edge states' localization length is negligible compared to the system size, the centre-of-mass position changes by $\delta x_e = \pm q d_s$, i.e. the size of a unit cell a_x . At all other points in the cycle, the motion of the particles is continuous, resulting in an additional displacement δx_b , which can be calculated from the states' Berry curvature as discussed in Sections 2.1.2 and 2.1.3. The total displacement for one cycle can then be expressed as

$$\delta x = \delta x_b - \nu_{1,e} \delta x_e \quad (2.19)$$

with $\nu_{1,e}$ counting the net contribution from the edge state crossings between the first two bands⁵. Since the system returns exactly to its initial state at the end of the cycle, δx has to be zero in a finite system if adiabaticity holds. Moreover, the continuous part δx_b , which contains contributions from the bulk as well as the edge states away from the crossing points, becomes equal to the centre-of-mass displacement in an infinite system $\delta x_{\text{COM}} = \nu_1 a_x$ [Eq. (2.16)] for large systems $L_x \gg q d_s$ [122]. In this limit, we thus obtain

$$\nu_1 = \nu_{1,e} \quad (2.20)$$

i.e. the Chern number characterizing the bulk response in an infinite system is equal to $\nu_{1,e}$, which can be identified as the winding number of the edge states [121, 122]. Therefore, a non-zero particle transport in the bulk requires the presence of topological edge states at the boundary of a finite system, which in turn guarantees the quantization of the bulk response as it causes quantized discontinuities in the centre-of-mass motion.

2.2.2 Relation to the Zak Phase and the Theory of Polarization

The Berry curvature, which determines the anomalous velocity, can be expressed as the curl of the Berry connection, $\Omega_n(k_x, \varphi_x) = \partial_{\varphi_x} A_n^{k_x} - \partial_{k_x} A_n^{\varphi_x}$ [Eq. (2.12)]. If a gauge is chosen, in which the Bloch waves are single valued as a function of φ_x as in Section 2.1.1, the term $\partial_{\varphi_x} A_n^{k_x}$ vanishes when integrating over a full cycle. The geometric contribution to the displacement per cycle for a given quasi-momentum then simplifies to

$$\delta x_{k_x} = - \oint d\varphi_x \partial_{k_x} A_n^{\varphi_x} = -\partial_{k_x} \gamma_B \quad (2.21)$$

i.e. it is determined by the derivative of the Berry phase with respect to k_x . Note that apart from the contribution from the group velocity, this is precisely the result that one obtains when calculating the position of the adiabatically evolved state, $|\psi(t=T)\rangle = e^{i(\gamma_D + \gamma_B)} |u_n(k_x, \varphi_x = 0)\rangle$. Using the position operator in momentum representation, $\hat{x}(k_x) = i\partial_{k_x}$, this gives

$$\langle \psi(T) | \hat{x} | \psi(T) \rangle = \langle \psi(0) | \hat{x} | \psi(0) \rangle - \partial_{k_x} (\gamma_D + \gamma_B) \quad (2.22)$$

⁵The derivation presented here assumes that pairs of edge states always cross within the band gap. Otherwise, a similar argument can be made using a constant chemical potential in a fermionic system such that the edge states become occupied/unoccupied whenever their energy crosses the Fermi surface. See [122] for details.

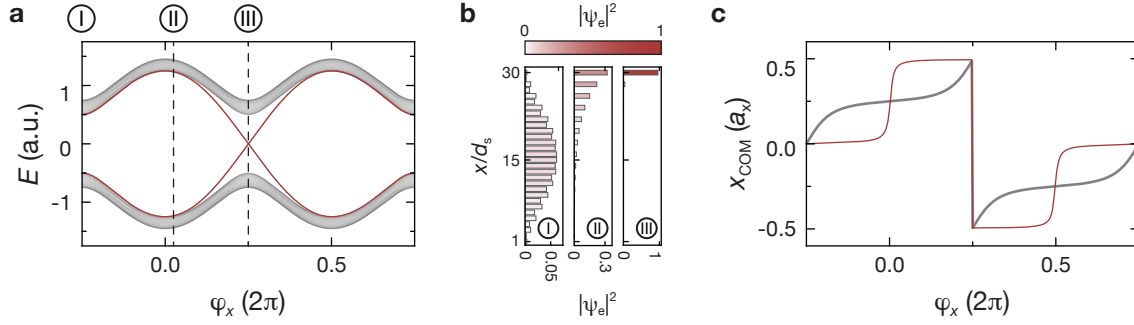


Figure 2.2 – Bulk-edge correspondence for a topological charge pump. (a) Evolution of the energy spectrum during a pump cycle for a dynamical 1D superlattice with $d_l = 2d_s$. The superlattice is described by a generalized Harper model (see Section 2.3.2) in the tight-binding limit with $\delta J_x = 2J_x/3 = 0.1\Delta_x$ comprising 100 sites. The spectrum consists of two bulk bands (grey), which are connected by two gap-traversing edge states (red) appearing out of the bulk in the vicinity of $\varphi_x = \pi/2$. (b) Spatial distribution of the eigenstates. The occupation probability of each lattice site is plotted for the lower-lying edge state ψ_e in a system with $L_x = 30d_s$ at $\varphi_x = -\pi/2$ (left), 0.05π (centre) and $\varphi_x = \pi/2$ (right). At $\varphi_x = -\pi/2$, ψ_e is part of the lower bulk band and thus delocalized over the entire system, but with increasing φ_x it separates from the bulk and becomes localized on the system's right boundary with an exponentially decaying occupation probability away from the edge. The state becomes maximally localized at $\varphi_x = \pi/2$, where its energy crosses the one of the edge state originating from the excited band, which is localized on the opposing end. Subsequently, the right-localized edge state approaches the higher band and disappears into the bulk again, while the left-localized one becomes lower in energy and merges into the lowest band. (c) Centre-of-mass position of a system in which the lowest $L_x/(2d_s)$ eigenstates are occupied homogeneously, calculated for $L_x = 100d_s$. The grey curve shows the position averaged over all particles and the red line illustrates the contribution of the edge states. The occupation transfer between the edge states localized on the right and left boundary leads to a quantized discontinuity at $\varphi_x = +\pi/2$, which enforces the quantization of the bulk response.

For a uniformly populated band, the centre-of-mass displacement can thus be written as

$$\delta x_{\text{COM}} = -\frac{a_x}{2\pi} \oint dk_x \partial_{k_x} \gamma_B \quad (2.23)$$

On the other hand, one can also choose a different gauge where the eigenstates are single-valued as a function of k_x , sometimes referred to as the periodic gauge [124]. In that case, if we consider a uniformly occupied band, the contribution from $\partial_{k_x} A_n^{\varphi_x}$ is identically zero and the average velocity is given by

$$v_{\text{COM}}(\varphi_x) = \frac{a_x}{2\pi} \partial_t \varphi_x \oint dk_x \partial_{\varphi_x} A_n^{k_x} = \frac{a_x}{2\pi} \partial_t \varphi_x \partial_{\varphi_x} \gamma_Z \quad (2.24)$$

introducing the Zak phase [20]

$$\gamma_Z(\varphi_x) = i \oint dk_x \langle u_n | \partial_{k_x} | u_n \rangle \quad (2.25)$$

The Zak phase corresponds to the Berry phase that is acquired when adiabatically traversing the 1D Brillouin zone at a fixed superlattice phase. After one cycle, the displacement can then be expressed in an analogous form as Eq. (2.23):

$$\delta x_{\text{COM}} = \frac{a_x}{2\pi} \oint d\varphi_x \partial_{\varphi_x} \gamma_Z \quad (2.26)$$

This highlights the symmetric roles of k_x and φ_x in the generalized Brillouin zone.

The Zak phase plays an important role in the modern understanding of the macroscopic polarization in crystalline dielectrics [7, 21, 22, 124]. The polarization is given by the electric dipole moment per volume. In crystals, it cannot be defined uniquely due to the periodicity of the charge density, but its value depends on the choice of origin [125]. In spite of its very basic character and great relevance, a complete theory of polarization was developed only in the 1990s [21, 22]. This theory focuses on the change in polarization between two configurations as opposed to its absolute value because the latter has no physical significance. This approach is closely related to charge pumping since the polarization difference is given by the charge transport during an adiabatic evolution connecting the two states in question. Accordingly, the rate of change in the polarization is proportional to the anomalous velocity. Following the derivation above, the polarization difference between two configurations for dielectric media can be expressed as the difference of the Zak phases similar to Eq. (2.26) [21]. This allows for an efficient computation because only the initial and final states are required. However, due to the periodicity of the potential, the polarization change can only be defined up to a displacement by an integer multiple of unit cells since an arbitrary number of closed cycles can be added to the path. While the Zak phase can in principle take any value, it can be shown that in inversion symmetric systems it is restricted to multiples of π [20]. Furthermore, while the Zak phase is gauge invariant with respect to the phase choice for the Bloch wave functions, it does depend on the choice of origin – just like the absolute value of the polarization. This position dependence is important in the context of Wannier-Stark ladders, where the Zak phase was first introduced, as it leads to a correction in the energy spectrum that ensures translational invariance [20, 126]. The Zak phase is also of importance for the existence of edge states in 1D systems [127] as well as excitations with fractional charges [128–130] and has recently been measured with ultracold atoms in a dimerized optical lattice [93].

2.2.3 Topological Protection

Interactions and Disorder

The connection between the centre-of-mass displacement per cycle and a topological invariant [Eq. (2.16)] implies that the induced transport is robust against any changes in the lattice potentials provided that the system remains gapped. However, the discussion in Section 2.1.3 relies on two important conditions: the absence of interactions as well as the periodicity of the superlattice potentials. Only in that case the problem can be treated in terms of the single-particle Bloch waves, which are periodic in both k_x and φ_x – a key requirement for the motion’s quantization. While this applies to a wide range of ideal systems, these conditions are in general not fulfilled in possible experimental implementations. In the latter, particles might be interacting with each other and the presence of disorder can easily destroy the perfect periodicity of the system. This naturally raises the

question whether a quantized transport of particles is still possible under these circumstances.

This issue was addressed by Niu and Thouless, who demonstrated that the current in response to adiabatic pumping is quantized even in disordered and interacting systems if the following two conditions are met: the many-body state that the system is initially prepared in possesses a finite gap to all other states throughout the pump cycle (i.e. in particular is not degenerate) and it does not exhibit any long-range correlations [11]. This can be shown by introducing generalized periodic boundary conditions of the form

$$\Psi(x_1, \dots, x_n + L_x, \dots, x_N) = e^{i\kappa_x L_x} \Psi(x_1, \dots, x_n, \dots, x_N) \quad (2.27)$$

for the N -particle wave function Ψ , where x_n denotes the position of the n -th particle and L_x the system size. In this case, the quantity κ_x characterizing the boundary condition plays a similar role as the Bloch wave vector k_x in non-interacting, periodic systems. The evolution of the system during the pumping can be obtained as in Section 2.1.1. The resulting velocity can thus be expressed in terms of a Berry curvature $\Omega(\kappa_x, \varphi_x)$ in the same way as in Eq. (2.10)-(2.12) [7]. Since κ_x is a periodic variable with period $2\pi/L_x$, the parameter space spanned by κ_x and φ_x has the same form as the generalized Brillouin zone. Hence, the displacement per cycle averaged over κ_x is necessarily quantized. However, κ_x is not an intrinsic physical parameter like the Bloch wave vector, which is naturally averaged over by homogeneously populating a band. Therefore, this quantization does not have direct physical consequences. But if the above conditions are fulfilled, the average velocity is a local operator, whose dependence on the specific choice for the boundary condition decays exponentially with the system size [11]. In the thermodynamic limit $L_x \rightarrow \infty$, the motion of the particles is thus independent of κ_x . In this case, the centre-of-mass displacement per cycle in a system with periodic boundary conditions $\kappa_x = 0$ can be rewritten as an integral over the entire parameter space and hence is proportional to an integer topological invariant. Therefore, the particle transport in a topological charge pump is robust against many perturbations and remains quantized even in the presence of interactions and disordered potentials. The same approach was later used to derive a topological invariant for interacting quantum Hall systems [131].

Non-Adiabatic Transitions

Other mechanisms that can potentially lead to deviations from exact quantization are higher-order corrections to the first-order adiabatic evolution discussed in Section 2.1.1 and non-adiabatic Landau-Zener transitions [132, 133] that occur during the pumping for finite pumping speeds. As the other bands generally exhibit different transport properties, these effects will modify the adiabatic evolution and induce corrections compared to the ideal quantized motion. An elegant way to study this problem is based on the Floquet theory and was first put forward in [134], which is briefly summarized in the following.

In time-periodic systems like a topological charge pump, the eigenstates will naturally exhibit the same periodicity in time, with the exception of very specific cases, in which

time-translational symmetry is broken [135, 136]. In analogy to the Bloch theorem for space-periodic systems, the Floquet theorem states that the eigenstates can then be expressed as [137]

$$|\psi_{n,k_x}(t)\rangle = e^{-i\epsilon_n(k_x)t/\hbar} |\tilde{\psi}_{n,k_x}(t)\rangle \quad (2.28)$$

Here, $|\tilde{\psi}_{n,k_x}\rangle$ is the time-periodic part of the wave function and $\epsilon_n(k_x)$ is the quasi-energy, which determines the phase that the eigenstate acquires during each cycle. Accordingly, the latter is only defined up to an integer multiple of h/T with T denoting the duration of one cycle. In addition, it is assumed that the system is spatially periodic at each point in time as in a dynamical superlattice such that the states can be labelled by their quasi-momentum k_x and band index n . Comparing this to the adiabatic evolution of a state discussed in Section 2.1.1 immediately implies that in the adiabatic limit $|\tilde{\psi}_{n,k_x}\rangle$ is given by the instantaneous eigenstates and the quasi-energy for each quasi-momentum k_x is determined by the corresponding dynamical and geometrical phase:

$$\epsilon_n(k_x) = -\frac{\hbar}{T} [\gamma_D(k_x) + \gamma_B(k_x)] \quad (2.29)$$

As shown in the previous section, the centre-of-mass displacement per cycle for a homogeneously occupied band can be related to the difference of the Berry phase between the left and right edge of the 1D Brillouin zone [Eq. (2.23)]. Combining this with Eq. (2.29), we find

$$\delta x_{\text{COM}} = \frac{a_x}{2\pi} \oint dk_x \underbrace{\frac{1}{\hbar} \frac{\partial \epsilon_n}{\partial k_x}}_{\tilde{v}_{\text{gr}}(k_x)} T \quad (2.30)$$

In analogy to the regular group velocity arising from the dispersion of a Bloch band, \tilde{v}_{gr} can be interpreted as the effective group velocity of the Floquet eigenstate. The latter, however, includes both the group velocity of the instantaneous eigenstates as well as their anomalous velocity⁶. The transport's quantization in this case is ensured by the periodicity of the Brillouin zone as the phase acquired by the states on the left and right edge can at most differ by a multiple of 2π . Since \tilde{v}_{gr} is a smooth function of k_x , the integral over it in Eq. (2.30) has to give an integer multiple of $2\pi/T$. For topologically non-trivial configurations, the Floquet modes are chiral as their quasi-energy winds around the Floquet-Brillouin zone [138].

This approach can easily be generalized beyond the adiabatic limit [134]. As the quasi-energy is restricted to the range of $[0, h/T[$, a large number of crossings occur between the Floquet states associated with different subbands in the limit of $T \rightarrow \infty$. For finite T , a small gap opens at crossings that are not protected by symmetries of the Hamiltonian due to a coupling between different Floquet states, which is associated with a degeneracy of their time-averaged energies [139]. This leads to a discontinuity of the quasi-energy for the Floquet state corresponding to a given band. In this case, the centre-of-mass motion is given by a piecewise integration of \tilde{v}_{gr} excluding the singularities. As the boundary

⁶ δx_{COM} in principle also contains the contribution from the dynamical phase [c.f. Eq. (2.22)], which, however, is not stated explicitly in Eq. (2.23) as it vanishes for a uniformly populated band

condition remains unchanged, the transport is no longer quantized due to the missing contribution at the discontinuities. This deviation can be quantified by explicitly calculating the Floquet eigenstates and numerical simulations show it is exponentially small in $1/T$ over a wide range of pumping speeds [134, 140]. Intuitively, this can be understood from the fact that the Schrödinger equation for the Floquet states is equivalent to a Wannier-Stark ladder in frequency space, where the coupling between states belonging to different bands results from the overlap of their exponentially decaying wings [141]. These findings are further supported by related analyses for quantum Hall systems, showing that non-adiabatic corrections are exponentially suppressed for infinitely differentiable Hamiltonians [142] and a rigorous proof demonstrating that the quantized Hall response is exact up to infinite order in the electric perturbation [143]. So while there are corrections to the quantized adiabatic transport for finite pumping speeds, these are exponentially small due to the pump's topological nature.

As the pumping speed is increased, additional modifications appear in the time-averaged energy spectrum of the Floquet states: extended degeneracies that - unlike the ones discussed above - are not accompanied by avoided crossings in the quasi-energy spectrum [134]. These degeneracies signal the breakdown of the adiabatic approximation due to non-adiabatic Landau-Zener transitions, causing a mixing of different bands such that it is no longer possible to disentangle the individual contributions to the particle transport.

The discussion so far was only concerned with the evolution of the Floquet states, which describe the transport properties of a given energy subband of the superlattice Hamiltonian for finite pumping speeds. In experiments, however, it is often highly non-trivial to prepare such a configuration since the system is usually initialized in a static Hamiltonian before starting the pumping process. Away from the adiabatic limit $T \rightarrow \infty$, the instantaneous eigenstates are in general not identical to the Floquet states, which can lead to additional corrections. These effects were recently studied for a tight-binding superlattice model in [140]. For an eigenstate of the initial Hamiltonian, it could be shown that the deviation resulting from a sudden start of the pumping is indeed not exponentially suppressed, but rather scales quadratically in $1/T$ in the long-time limit. This matches with the intuitive expectation as the overlap between an eigenstate of the initial Hamiltonian and the corresponding adiabatically evolved wave function scales with $(\partial_t \varphi_x)^2$ [Eq. (2.6)]. The resulting admixture of other Floquet states can in principle be minimized by choosing a smooth ramp-up function for $\varphi_x(t)$ as well as an appropriate starting point, at which the energy gaps are large and the off-diagonal elements of the Berry curvature are small. When performing a large number of pump cycles, the dominant contribution is rather expected to arise from Landau-Zener transitions. These transitions predominantly take place at the point in the cycle, at which the energy gap to the neighbouring bands is minimal, and create an incoherent occupation of states from other bands in addition to the adiabatic admixture. While the transition probability also scales exponentially with the ratio of the pumping speed to the respective band gap [132, 133], the effect is magnified as these transitions potentially occur during each cycle and thus lead to a population in

other bands that successively increases over time. This is particularly relevant if the band's Chern numbers have opposite signs, in which case even a small fraction of excited particles can have a pronounced effect on the centre-of-mass motion.

2.3 Relation to 2D Quantum Hall Physics

The centre-of-mass displacement generated by a 1D topological charge pump can be expressed by the first Chern number ν_1 [Eq. (2.16)], the 2D topological invariant that also describes the quantized Hall response in 2D quantum Hall systems [13]. This indicates that this transport phenomenon is related to the physics of the integer quantum Hall effect – a connection that was already emphasized by Thouless in his first proposal [10]. In the following, we will show that a topological charge pump can indeed be mapped directly onto the Fourier components of a 2D quantum Hall model in two important limiting cases: (i) the quantum sliding lattice (Landau limit), where the short lattice potential vanishes $V_s \rightarrow 0$ (Section 2.3.1). This corresponds to the Landau levels of a free particle in a homogeneous external magnetic field [144]. (ii) the tight-binding limit in a sinusoidal superlattice with a very deep short lattice (Section 2.3.2), which maps onto a lattice quantum Hall model - the Harper-Hofstadter model [145–147]. In addition, many other superlattice configurations are either topologically equivalent to the aforementioned cases or can be related to other 2D quantum Hall models. A 1D topological charge pump can thus be interpreted as a dynamical version of the integer quantum Hall effect where the adiabatic variation of the pump parameter corresponds to the insertion of magnetic flux through a cylindrical quantum Hall system [37]. The induced particle transport is therefore equivalent to the Hall response.

2.3.1 The Laughlin Charge Pump

The connection between a topological charge pump and a 2D quantum Hall system can be understood following the gedankenexperiment of Robert Laughlin (Fig. 2.3a), which demonstrates how gauge invariance enforces the quantization of the Hall response in 2D systems [37, 148]. In the underlying cylindrical geometry, the quantum Hall effect can be interpreted as a topological charge pump, relating the Hall current to the quantized particle transport in a periodically modulated 1D system.

Free particles with charge q moving in an external magnetic field are described by a Hamiltonian of the form

$$\hat{H}_{LL} = \frac{1}{2m_a} \left(\hat{\mathbf{p}} - q\hat{\mathbf{A}} \right)^2 \quad (2.31)$$

where m_a is the particle mass and $\hat{\mathbf{A}}$ the electromagnetic vector potential. In the following, we will consider a system where the particles are confined to the xz -plane, which is pierced by a perpendicular magnetic field $\mathbf{B} = -B_{xz}\mathbf{e}_y$ with \mathbf{e}_y being the unit vector in the y -direction. When using the Landau gauge, $\hat{\mathbf{A}} = B_{xz}\hat{x}\mathbf{e}_z$, the above Hamiltonian commutes with the momentum operator along z , \hat{p}_z , and the common eigenstates with

a given momentum $\hbar k_z$ can be expressed as $\psi(\mathbf{r}) = e^{ik_z z} \psi_{k_z}(x)$. By inserting this ansatz into Eq. (2.31), \hat{H}_{LL} reduces to a series of 1D harmonic oscillators, whose eigenvalues are the well-known Landau levels [144, 149]:

$$\hat{H}_{LL} = \frac{\hat{p}_x^2}{2m_a} + \frac{1}{2}m_a\omega_c^2 \left(\hat{x} - \frac{\hbar k_z}{m_a\omega_c} \right)^2 \quad (2.32)$$

with $\omega_c = qB_{xz}/m_a$ denoting the cyclotron frequency. The states within a given Landau level are thus the corresponding harmonic oscillator states, centred at a position $x_m = \hbar k_z/(m_a\omega_c)$, which is determined by the transverse momentum (Fig. 2.3b).

The Hall response arises when an electric field is applied, which without loss of generality we assume to point along z , $\mathbf{E} = E_z \mathbf{e}_z$. The resulting force on the particles changes the transverse momentum, which following Eq. (2.32) leads to a motion of the oscillator centres along x with velocity E_z/B_{xz} – the Hall current. In a system of length L_z along z , k_z can only be an integer multiple of $2\pi/L_z$ and correspondingly the distance between neighbouring states is $d_x = h/(m_a\omega_c L_z)$. After a time $T = h/(qE_z L_z)$, the system thus returns to its initial configuration, but each harmonic oscillator has moved by one site $\delta x = d_x$. For a single completely filled Landau level, i.e. the n -th state in all harmonic oscillators is occupied, this motion corresponds to a current along x

$$I_H = \frac{q}{T} = \frac{q^2}{h} U_H \quad (2.33)$$

with the transverse voltage $U_H = E_z L_z$. This is precisely the quantized Hall conductivity of a single Landau level, corresponding to a Chern number of $\nu_1 = +1$ [13, 37]. Importantly, the current is independent of the magnetic field strength as the density of states increases linearly with B_{xz} and is thus inversely proportional to the drift velocity $v_x = E_z/B_{xz}$.

A very elegant way to study this phenomenon, introduced by Laughlin [37], is to consider a cylindrical geometry, in which the edges of a 2D quantum Hall system in the z -direction are attached to one another (Fig. 2.3a). In this geometry, the electric field can be induced by adding a magnetic flux ϕ_x along the axis of the cylinder and varying it in time. Assuming that this flux is contained in the interior of the cylinder, i.e. there is no additional magnetic field on the cylinder's surface, this leads to a time-dependent vector potential along z , $\hat{A}_z = B_{xz}\hat{x} + \phi_x(t)/L_z$ and hence an electric field $\mathbf{E} = -\partial_t \hat{\mathbf{A}} = -(\partial_t \phi_x/L_z)\mathbf{e}_z$. The displacement of the Landau level eigenstates can then be related to the amount of flux $\Delta\phi_x$ threaded through the cylinder

$$\delta x = -\frac{\Delta\phi_x}{B_{xz}L_z} = -\frac{\Delta\phi_x}{\Phi_0} d_x \quad (2.34)$$

where $\Phi_0 = h/q$ is the magnetic flux quantum. For each inserted flux quantum, the oscillator centres shift by one period and one particle is thus transported between the edges of the cylinder.

The importance of this gedankenexperiment lies in the fact that it allows us to relate the quantization of the Hall response to the general principle of gauge invariance,

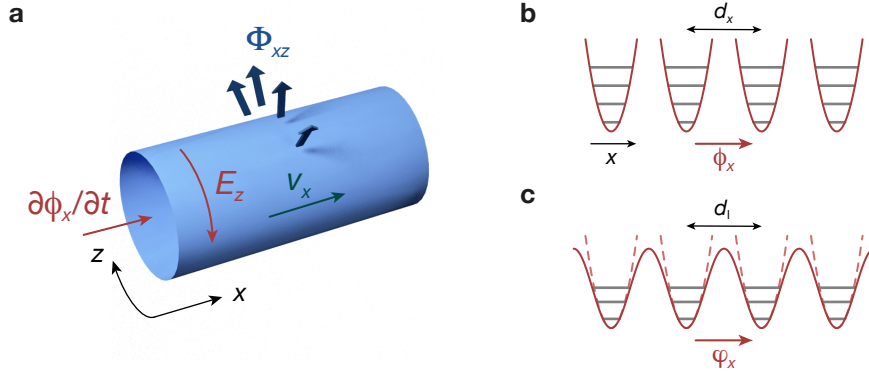


Figure 2.3 – The 2D integer quantum Hall effect as a 1D topological charge pump. (a) 2D quantum Hall system in the Laughlin geometry. The surface of the cylinder is pierced by a uniform magnetic flux Φ_{xz} , leading to the formation of Landau levels. When an additional magnetic flux $\phi_x(t)$ along the axis of the cylinder is changed in time, an electric field E_z is induced along z . This gives rise to the Hall response with a drift velocity v_x in the x -direction. Figure adapted from [150]. (b) The states in each Landau level can be expressed as eigenstates of localized harmonic oscillators along x with a spacing d_x determined by the circumference of the cylinder in the transverse z -direction. The threading of the flux ϕ_x through the cylinder causes a quantized sliding motion of the harmonic oscillator potentials along x – the Hall response. (c) This situation is equivalent to the trivial limit of a 1D Thouless pump where only the moving lattice with period d_l is present, i.e. $V_s = 0$. In this case, the superlattice phase φ_x acts as the pump parameter in the same way as the threaded flux ϕ_x for the 2D Landau levels.

thereby explaining its robustness against disorder and independence from material properties [148]. Furthermore, it provides a natural setting to study the role of edge states in quantum Hall systems [109]. When comparing two static configurations with different ϕ_x , these are related by a gauge transformation, which by definition leaves all physical observables invariant. However, in the cylindrical geometry, the boundary condition for extended states along z permit only certain gauge transformations, namely those that differ by an integer multiple of flux quanta [37]. As the flux is threaded, a particle transport can thus occur, but after each flux quantum all eigenstates have to be identical to the starting point and the motion of the oscillator states localized along x must be quantized – even in the presence of a random potential.

The sliding motion of the Landau levels along x is equivalent to a topological charge pump in the limit where the short lattice vanishes $V_s \rightarrow 0$ (Fig. 2.3). In this case, the quantization of the resulting particle transport becomes trivial as a change in the pump parameter φ_x corresponds to a global translation of the system. The particles will naturally follow this motion as long as it remains adiabatic and thus move by a lattice constant d_l per pump cycle, i.e. $\nu_1 = +1$ for each band as for the Landau levels [Eq. (2.16)]. Note that while in this limit a motion would also occur in classical systems, the quantization is robust only in quantum mechanical systems, where it is protected by the band gap. For a classical particle, the motion of the lattice would excite oscillations around the minima for any finite pumping speed, which destroy the exact quantization in the generic case.

The deviation can be shown to scale inversely with the cycle time T as opposed to an exponential suppression of excitations in quantum systems [151] (see also Section 2.2.3).

This analogy can be formalized for a deep sinusoidal lattice potential $V_1 \sin^2(\pi\alpha x/d_s - \varphi_x/2)$, which up to second order can be approximated by a sum of harmonic oscillators located at the lattice sites $x_{m_x} = \frac{d_s}{\alpha}(m_x - \frac{\varphi_x}{2\pi})$:

$$\hat{H}_1 = \frac{\hat{p}_x^2}{2m_a} + V_1 \frac{\pi^2 \alpha^2}{d_s^2} \sum_{m_x} (\hat{x} - x_{m_x})^2 \quad (2.35)$$

This approximation is valid for $V_1 \gg E_{r,1}$ with the recoil energy $E_{r,1} = \hbar^2/(8m_a d_1^2)$. In this limit, the tunnel coupling between neighbouring lattice sites is negligible, such that Eq. (2.35) becomes a series of decoupled harmonic oscillators analogous to Eq. (2.32). The quantum Hall effect in the Laughlin geometry can therefore be mapped onto a 1D topological charge pump consisting of a sliding long lattice. In this case, the flux through the cylinder ϕ_x plays the role of the pump parameter, i.e. the superlattice phase φ_x .

2.3.2 Mapping in the Tight-Binding Regime

A similar mapping can be performed for a sinusoidal superlattice in the opposite limit of a very deep short lattice $V_s \gg V_1^2/(4E_{r,s})$. To this end, we rely on the procedure of dimensional extension, where the Hamiltonian of a lower-dimensional system with an external parameter φ_x is interpreted as a Fourier component of a higher-dimensional model labelled by its transverse momentum $\hbar k_z$ [152]. This approach constitutes the opposite of the dimensional reduction method introduced in [38], which generalizes the Laughlin interpretation to relate topological models in different dimensions by the compactification of a cylindrical geometry (see Section 5.1.2).

Tight-Binding Hamiltonian and Generalized Harper Model

For a sufficiently deep short lattice, for which the tunnel coupling between neighbouring sites is small compared to the energy gap to higher Bloch bands for all φ_x , the tight-binding approximation can be used for the superlattice potential [153, 154]. In this approximation, the Hilbert space is restricted to the ground state on each lattice site, which is described by the corresponding maximally localized Wannier function [155–157]. The superlattice Hamiltonian in this basis is given by (see Section 3.2.2 for details)

$$\begin{aligned} \hat{H}_{\text{SL}}(\varphi_x) = & - \sum_{m_x} [J_x(\varphi_x) + \delta J_x^{m_x}(\varphi_x)] \hat{a}_{m_x+1}^\dagger \hat{a}_{m_x} + \text{h.c.} \\ & + \sum_{m_x} \Delta_x^{m_x}(\varphi_x) \hat{a}_{m_x}^\dagger \hat{a}_{m_x} \end{aligned} \quad (2.36)$$

with $\hat{a}_{m_x}^\dagger$ (\hat{a}_{m_x}) denoting the creation (annihilation) operator on the m_x -th site of the short lattice. The first term describes the tunnel coupling between neighbouring sites and the last term contains the on-site energy $\Delta_x^{m_x}$ of each site. In the presence of the long

lattice, both quantities are modulated periodically in space by $\delta J_x^{m_x}(\varphi_x)$ and $\Delta_x^{m_x}(\varphi_x)$, respectively, and depend on the superlattice phase.

If the long lattice is very weak compared to the short lattice, its dominant contribution is the modulation of the on-site energies [154, 158]. To first order in V_1/V_s , it is simply given by the local potential created by the long lattice [159, 160]:

$$\Delta_x^{m_x}(\varphi_x) = -\frac{\Delta_x^{(0)}}{2} \cos \left[2\pi \frac{d_s}{d_1} m_x - \varphi_x \right] \quad (2.37)$$

with $\Delta_x^{(0)} \approx V_1$. The modification of the tunnelling rates is substantially smaller and is caused mostly by a slight change in the position of the short lattice sites [160]. In the first-order approximation, the shift can be obtained by expanding the long lattice potential in the vicinity of each lattice site and is of order $V_1 d_s^2 / (V_s d_1) \ll d_s$. The tunnel coupling, which decreases exponentially with the site separation, can then be approximated as

$$J_x(\varphi_x) + \delta J_x^{m_x}(\varphi_x) = J_x + \frac{\delta J_x^{(0)}}{2} \cos \left[2\pi \frac{d_s}{d_1} (m_x + 1/2) - \varphi_x \right] \quad (2.38)$$

with J_x being the bare tunnelling rate in the short lattice. As $\delta J_x^{(0)}/J_x \propto V_1/\sqrt{V_s E_{r,s}} \ll 1$, the modulation of the tunnelling rates is typically much smaller than the one of the on-site energies. For interacting particles, the modified lattice potential also leads to a small change of the on-site interaction energy, but this modification is negligible in most cases [160].

In this limit and for $\delta J_x^{m_x} = 0$, the superlattice Hamiltonian of Eq. (2.36) reduces to the 1D Harper model, which was introduced by P. G. Harper when studying particles in a 2D square lattice pierced by a uniform magnetic field – the Harper-Hofstadter model (see below) [145–147]. The 1D Harper model describes the corresponding eigenvalue problem for states with a well-defined transverse quasi-momentum $\hbar k_z$ (see also Section 5.1.4). In the context of localization phenomena, this Hamiltonian for incommensurate lattice periods is also known as the Aubry-André model [161]. If the tunnelling rates are modulated as well $\delta J_x^{m_x} \neq 0$, which is typically the case in optical superlattice potentials, we refer to this model as the generalized Harper model [162].

Dimensional Extension

In analogy to the connection between the sliding long lattice and the free-particle Landau levels discussed in Section 2.3.1, we would now like to relate the particle transport of a topological charge pump in the deep tight-binding limit $V_s \gg V_1^2/(4E_{r,s})$ to the Hall response of a 2D quantum Hall system. The key insight for this is the fact that for $\delta J_x^{m_x} = 0$ the Hamiltonian of the 1D superlattice is identical to the Harper model, which constitutes a 1D Fourier component of the 2D Harper-Hofstadter model with $k_z = \varphi_x/d_s$ (see below). When the pump parameter φ_x is varied, the eigenstate $|u_n(k_x, \varphi_x)\rangle$ in the superlattice (see Section 2.1.2) will thus evolve in exactly the same way as the wave function along x of a particle that is prepared in the eigenstate $|u_n(k_x, k_z)\rangle$ in the Harper-Hofstadter model,

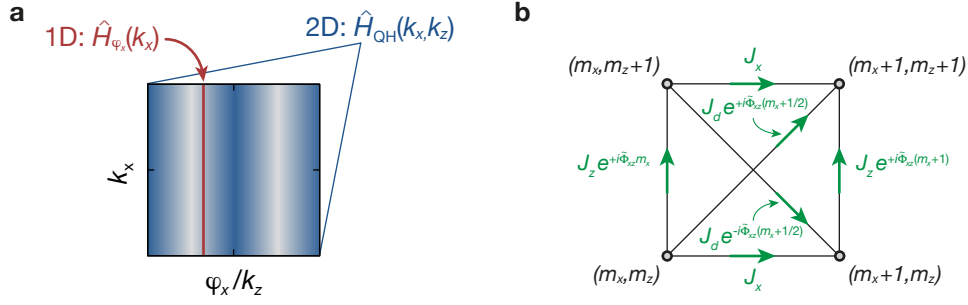


Figure 2.4 – Dimensional extension in the tight-binding limit. (a) At each point in the cycle, the Hamiltonian of a 1D charge pump in the momentum representation, $\hat{H}_{\varphi_x}(k_x)$, is equal to a single Fourier component of the Hamiltonian of a 2D quantum Hall system, $\hat{H}_{QH}(k_x, k_z)$. During a full cycle, all Fourier components are sampled sequentially, covering the entire Brillouin zone. For the 1D system, k_x and φ_x thus span a 2D generalized Brillouin zone. (b) The Harper-Hofstadter-Hatsugai model describes a square lattice in the tight-binding regime with nearest-neighbour (J_x, J_z) and next-nearest-neighbour tunnel couplings (J_d) in the presence of a uniform magnetic flux $\Phi_{xz} = \Phi_0 \tilde{\Phi}_{xz}/(2\pi)$ per unit cell. Figure adapted from [163].

when an external electric field is applied along z , which induces Bloch oscillations with $\hbar\dot{k}_z = qE_z$. A detailed discussion of the corresponding equations of motion can be found in Section 5.1.3 and Section 5.2.2. The generalized Brillouin zone of the topological charge pump is identical to the Brillouin zone of the 2D quantum Hall model since all Fourier components of the Harper-Hofstadter Hamiltonian are realized sequentially during a pump cycle (see Fig. 2.4a). In this sense, the external parameter φ_x of the 1D model can be regarded as an additional dimension. Therefore, the pumping response of the dynamical 1D superlattice is equivalent to the Hall response of the 2D Harper-Hofstadter model.

For the generalized Harper model, the corresponding quantum Hall system can be found in a similar way via a dimensional extension. The 2D Hamiltonian in real space is obtained by integrating over all Fourier components

$$\hat{H}_{QH} = \frac{1}{2\pi} \int_0^{2\pi} \hat{H}_{SL}(\varphi_x) d\varphi_x \quad (2.39)$$

and subsequently performing an inverse Fourier transform by expressing the 1D creation and annihilation operators for a given φ_x as

$$\hat{a}_{m_x, \varphi_x}^\dagger = \sum_{m_z} e^{i\varphi_x m_z} \hat{a}_{m_x, m_z}^\dagger \quad \text{and} \quad \hat{a}_{m_x, \varphi_x} = \sum_{m_z} e^{-i\varphi_x m_z} \hat{a}_{m_x, m_z} \quad (2.40)$$

Here, $\hat{a}_{m_x, m_z}^\dagger$ and \hat{a}_{m_x, m_z} denote the creation and annihilation operator in a 2D tight-binding lattice with sites labelled by m_x and m_z . This yields

$$\hat{H}_{QH} = \hat{H}_{HH} + \hat{H}_{\delta J} \quad (2.41)$$

The first term is the Harper-Hofstadter model, which is a tight-binding model governing the motion of non-interacting particles in a square periodic potential that is subject to a uniform magnetic field [145–147]:

$$\hat{H}_{\text{HH}} = - \sum_{m_x, m_z} \left(J_x \hat{a}_{m_x+1, m_z}^\dagger \hat{a}_{m_x, m_z} + \frac{\Delta_x^{(0)}}{4} e^{i\tilde{\Phi}_{xz} m_x} \hat{a}_{m_x, m_z+1}^\dagger \hat{a}_{m_x, m_z} \right) + \text{h.c.} \quad (2.42)$$

The magnetic flux per unit cell of the lattice is $\Phi_{xz} = (d_s/d_l)\Phi_0$ and $\tilde{\Phi}_{xz} = 2\pi\Phi_{xz}/\Phi_0$. The tunnelling in the z -direction is a consequence of the φ_x -dependence of the on-site energies $\Delta_x^{m_x}$ and the complex phases of the tunnelling matrix elements result from the spatial periodicity of $\Delta_x^{m_x}$. Therefore, the strength of the magnetic field in the 2D model is determined by the ratio between the short and long lattice constants in the 1D superlattice. The Harper-Hofstadter Hamiltonian is one of the paradigmatic models for quantum Hall systems. The competition between the lattice periodicity and the magnetic length scale gives rise to a fractal band structure, the Hofstadter butterfly [147]. In the same way that the presence of the long lattice leads to a separation into subbands in a 1D superlattice, the Bloch bands of the 2D lattice split into a number of subbands determined by the strength of the magnetic field. Due to the breaking of time-reversal symmetry by the magnetic flux, these subbands are topologically non-trivial and characterized by non-zero first Chern numbers. Recently, the long sought goal of realizing this model, which requires strong magnetic fields, has been accomplished using moiré superlattice structures in condensed matter systems [164, 165, 165] as well as with cold atoms in optical lattices [89–91]. Similar models have also been studied in photonic materials [166, 167].

The second term in Eq. (2.41) arises from the periodic modulation of the tunnelling rates and is given by

$$\begin{aligned} \hat{H}_{\delta J} = & - \frac{\delta J_x^{(0)}}{4} \sum_{m_x, m_z} e^{i\tilde{\Phi}_{xz}(m_x+1/2)} \hat{a}_{m_x+1, m_z+1}^\dagger \hat{a}_{m_x, m_z} + \text{h.c.} \\ & - \frac{\delta J_x^{(0)}}{4} \sum_{m_x, m_z} e^{-i\tilde{\Phi}_{xz}(m_x+1/2)} \hat{a}_{m_x+1, m_z-1}^\dagger \hat{a}_{m_x, m_z} + \text{h.c.} \end{aligned} \quad (2.43)$$

This Hamiltonian adds diagonal tunnelling matrix elements coupling next-nearest neighbours, while maintaining the same uniform flux per square unit cell Φ_{xz} . The combined Hamiltonian \hat{H}_{QH} is known as the Harper-Hofstadter-Hatsugai model (Fig. 2.4b) and was first studied in [162]. Its energy spectrum is similar to the Harper-Hofstadter model as the lattice band structure also fractalizes into topologically non-trivial subbands due to the magnetic field (Fig. 2.5). The appearance of the diagonal coupling, however, can give rise to spectral changes, in particular the opening of additional gaps between subbands that touch for $\delta J_x^{(0)} = 0$. This occurs for example at $\Phi_{xz} = \Phi_0/(2l)$, $l \in \mathbb{N}$, where the magnetic unit cell contains an even number of lattice sites. At $\Phi_{xz} = \Phi_0/2$, the Harper-Hofstadter-Hatsugai model for fermionic particles becomes identical to a mean-field model for chiral spin states that violate space-time reflection (PT) symmetry, when the lowest subband is

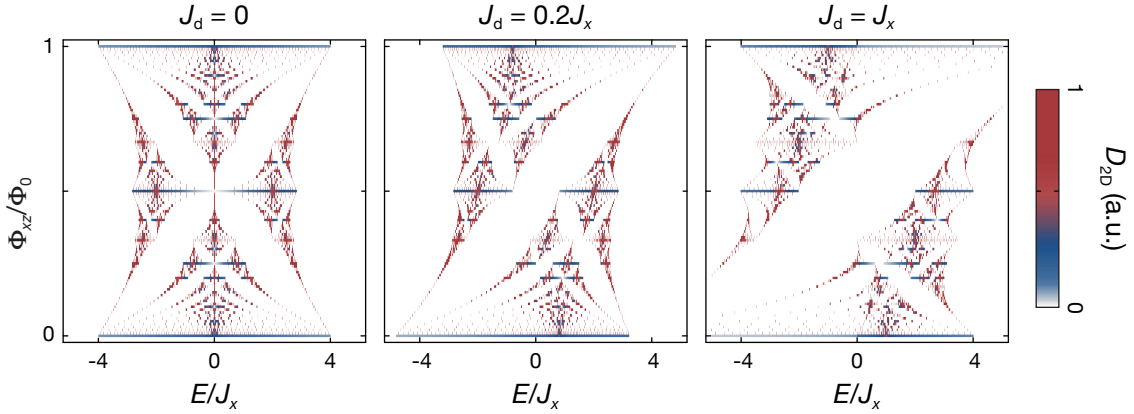


Figure 2.5 – Energy spectrum of the Harper-Hofstadter-Hatsugai model. Density of states in the 2D Harper-Hofstadter-Hatsugai model versus energy E and magnetic flux per unit cell Φ_{xz} for $J_x = J_z = \Delta_x^{(0)}/4$ and various diagonal coupling strengths $J_d = \delta J_x^{(0)}/4$. Without next-nearest neighbour tunnelling ($J_d = 0$), the Hamiltonian reduces to the Harper-Hofstadter model, where the interplay between the two length scales set by the lattice spacing and the strength of the magnetic field leads to a fractalization of the energy spectrum - the Hofstadter butterfly [147]. A finite $J_d \neq 0$ breaks the symmetry of the band structure with respect to $\Phi_{xz} = \Phi_0/2$ as the smallest possible closed path is now given by a triangle with half the size of the square lattice unit cell (see Fig. 2.4b). The spectrum thus becomes $(2\Phi_0)$ -periodic in Φ_{xz} . The energy spectrum was obtained by numerically calculating the eigenstates of the generalized Harper model for $k_z \in]-\pi/d_s, \pi/d_s]$ in a system consisting of 500 sites and with flux $\Phi_{xz}/\Phi_0 = p/100$, $p \in [0, 100]$. The band structure of the Harper-Hofstadter-Hatsugai model was first computed in [162].

completely filled [162]. These states were predicted for frustrated 2D Heisenberg anti-ferromagnets and discussed in the context of high-temperature superconductivity [168]. The underlying single-particle Harper-Hofstadter-Hatsugai Hamiltonian is precisely the higher-dimensional analogue of the topological charge pump realized in the experiment for $d_l = 2d_s$ (see Section 4). Furthermore, if the tunnelling rates on the two diagonals can be tuned independently (which is not the case for the dimensional extension of the generalized Harper model), the Harper-Hofstadter-Hatsugai model can be continuously transformed to a triangular lattice geometry by removing one of the two couplings [162].

2.4 Applications and Implementations of Charge Pumps

2.4.1 Applications for Topological Charge Pumps

The extraordinary robustness of the particle transport by a topological charge pump allows for the realization of very precise current sources [16, 169], which were proposed as suitable candidates for the definition of a new standard for the electric current based on the elementary charge [17]. This would enable the completion of the "triangle of quantum metrology", the long-standing goal in metrology to obtain reliable standards based on quantum mechanical effects for the three quantities related by Ohm's law – voltage, resis-

tance and current [18, 19, 170]. For the two former ones, this has already been accomplished. A voltage standard was defined based on the ac Josephson effect [171], where an oscillating current applied to two weakly coupled superconductors leads to a voltage difference that is proportional to an integer multiple of the driving frequency [172, 173]. For resistance, a definition using the von Klitzing constant was introduced, relying on the topological protection of the quantized Hall response [174]. In a similar manner, implementing a topological charge pump – sharing the same topological origin as the quantum Hall effect – would make it possible to relate the generated quantized current to the pump cycle frequency, which can easily be controlled and measured very precisely. Moreover, the transport’s quantization is protected by a quantum mechanical energy gap, e.g. the band gap for a filled band of non-interacting fermions, which exponentially suppresses any deviation that could for example arise from a finite temperature or non-adiabatic transitions [134, 143] (see Section 2.2.3). Similarly, the attachment of external contacts that is necessarily required to generate electric currents would only lead to corrections that are exponentially small in the device size due to the localization of the emerging edge states. Besides the generation of very precise currents, the ability to transport a well-defined number of electrons can also be used to build an accurate standard for capacitance [175].

Another possible application for topological charge pumps are adiabatic quantum motors [111, 176]. These could be realized by operating a charge pump in reverse, i.e. by driving a current through a pump to induce an oscillation of its control parameters, e.g. gate voltages in mesoscopic systems (see Section 2.4.2). By appropriately coupling a mechanical system like for example a wheel with an alternating charge distribution, this oscillation could be converted into mechanical motion. As the transport in a topological charge pump occurs without an external bias and is thus dissipationless, such motors could in principle achieve an ideal efficiency of 100% [111]. Another way to implement a quantum motor would be via coupling to the motion of particles in a forward-operated charge pump, e.g. by interaction between different atomic species [177, 178].

Topological charge pumps have also been discussed in the context of quantum information processing as they offer a way for a topologically protected transport of qubits [112]. To this end, the qubit could be encoded in the internal state of an atom that is part of a Mott-insulating many-body state and thus localized in one unit cell. By applying a sequence of multiple pump cycles, this particle could be moved through the lattice by a well-defined distance without affecting its internal state. Such a scheme could also be extended to generate entanglement between distant particles by initially preparing two entangled particles localized in the same unit cell, but in different subbands with opposite Chern numbers and subsequently separating the particles by a series of pump cycles [179].

2.4.2 Previous Implementations of Charge Pumps

While topological charge pumping was initially mostly of interest in fundamental condensed matter physics in the context of the quantum Hall effect, a first concrete proposal for the implementation of such a device focussing on real-world applications was put for-

ward in 1990 [16, 169]. It suggested to use a quantum wire with voltage leads to realize a "digitized" sliding lattice with a time-dependent global offset voltage to control the Fermi energy. In condensed matter systems, however, it is extremely challenging to obtain the required degree of control as well as to maintain adiabaticity since mesoscopic systems often exhibit a continuum of states. Therefore, the first implementations of solid-state-based quantized charge pumps instead relied on the Coulomb blockade to ensure quantization [180]. In mesoscopic devices, the interaction energy is typically the dominant energy scale at low temperatures and thus allows for the precise control of the electron number and single-electron dynamics. Based on this principle, single-electron transport was first demonstrated with metallic tunnel junctions [23] and soon after using quantum dots [24] in turnstile-like devices, where the transport occurs in the direction of an external bias voltage. The first realization of a real charge pump, demonstrating quantized transport in absence of a bias, was reported in [25, 26]. For these experiments, a sample was fabricated that consists of a linear array of three metallic tunnel junctions, formed by thin insulating barriers and separated by conducting islands with variable gate voltages. Via an out-of-phase modulation of the two gate voltages around a threefold degeneracy point in the stability diagram of charge states, a single electron is transported between two reservoirs with the direction of motion entirely determined by the orientation of the pump cycle. While these first realizations only achieved a relative accuracy on the percent level, mostly limited by simultaneous cotunnelling of multiple electrons [181], this could be drastically improved by increasing the number of tunnel junctions, reaching a deviation from quantization on the order of 10^{-8} in a device with seven junctions [182]. Even though this would be suitable for metrological applications, the resulting current is too low for most purposes. For overcoming this limitation, quantum-dot pumps seem to be promising candidates as tunnel barriers can also be controlled by external voltages [183]. In addition, other pumping techniques have also been implemented, e.g. using surface-acoustic waves in semiconducting quantum point contacts [184]. An extensive overview of recent developments in single-electron pumps can be found in [17].

Even though charge pumping based on the Coulomb blockade can achieve exceptional precision, the resulting motion in general rather resembles classical transport and does not constitute coherent quantum dynamics. As mentioned above, the situation in solid states systems is often very different from the isolated, gapped systems that topological charge pumping was first proposed for. To account for this, Thouless' idea was extended to open mesoscopic systems, leading to the concept of parametric pumping, where a non-quantized particle transport is induced by a periodic and adiabatic variation of at least two external parameters [28, 29]. Contrary to a topological charge pump, the motion in this case depends strongly on the microscopic details of the specific implementation and is proportional to the area enclosed by the pump path in parameter space. Subsequently, such a parametric charge pump was realized in an open quantum dot by locally manipulating the electron wave function through a small cyclic variation of the confining potential in the contact leads of the quantum dot [30]. There are, however, doubts as to whether this experiment actually realized an adiabatic quantum pump as capacitive

coupling of the modulated gate voltages also creates an oscillating bias voltage between the reservoirs, which generates an additional current with similar characteristics [31, 32]. Additionally, the condition of adiabaticity in these devices is only fulfilled in the sense that the modulation is slow compared to the relaxation time scales such that at each point in the cycle the system has time to relax to the instantaneous ground state [185].

Another approach to achieve adiabatic quantum transport is to replace the metallic tunnel junctions in the early experiments by superconducting quantum interference devices (SQUIDs), which are connected through a superconducting gate [186]. A coherent directional motion can then be generated by modulating the critical current of the SQUIDs via the enclosed magnetic flux in combination with the gate voltage. In this case, the transported charge can be related to the Berry phase, which in the absence of any additional supercurrent is simply given by the phase difference of the macroscopic wave function between the two ends [187, 188]. When placing the pump in a closed loop, the phase difference and thus the particle transport can be controlled by the magnetic flux penetrating the loop. The realization of such a device was reported in [33], demonstrating coherent transport as well as a measurement of the associated Berry phase.

In condensed matter systems, the main focus of charge pumping experiments are practical applications like current sources and experimental realizations are limited to rather small systems of up to a couple of junctions. In artificially engineered photonic systems, on the other hand, arrays of coupled waveguides provide a platform to realize extended lattice models exhibiting topological band structures and thus allow for the study of more fundamental questions [189]. Each single-mode waveguide forms a lattice site, whose on-site energy is determined by the refractive index as this controls the phase that is acquired by the propagating light. If the waveguides are sufficiently close, the modes overlap, giving rise to a tunnel coupling between the sites. The direction of propagation along the waveguides defines the time axis in these systems and a time-dependent modulation can be realized by changing the parameters as a function of the position. An advantage of these systems is the possibility to locally inject and detect light on individual sites, making them particularly suited to observe edge state phenomena. This flexibility allowed for the first realization of the Hamiltonian of a topological charge pump as envisioned by Thouless, both in an incommensurate Aubry-André lattice [34] and a Fibonacci quasicrystal [35]. While these experiments could nicely demonstrate the existence and the pumping of edge states, indicating the non-trivial topology of the underlying bulk bands, a quantized bulk transport could not be observed.

Even though the use of optical lattices to implement a topological charge pump for ultracold atoms was suggested already in 1998 [190], only a limited number of experiments have been performed in this direction prior to the work presented here. These include for example the realization of a Brownian motor [191] and a quantum ratchet [192]. For a more detailed overview see Section 4.

Ultracold Atoms in Optical Superlattices

In this thesis, the implementation of 1D and 2D topological charge pumps with ultracold bosonic atoms in dynamically controlled optical superlattices is presented. Due to the unprecedented levels of control and access provided by these artificially engineered systems, they provide an ideal model system to study such phenomena. The main experimental setup used for the experiments in Section 4 and Section 6 has already been described in great detail elsewhere, see e.g. [104, 105] for the vacuum system and [106] for a summary of recent modifications. Therefore, only a brief overview of the experimental setup and techniques is given here (Section 3.1), focussing on the relevant parts for the implementation of a topological charge pump and in particular the dynamical optical superlattices (Section 3.2).

3.1 Overview of the Experimental Setup

The core of the experiment is a vacuum system comprising two main chambers, which are connected by an L-shaped differential pumping section to allow for a pressure difference between the chambers. In this setup, bosonic ^{87}Rb atoms are cooled to quantum degeneracy before loading them into the optical lattice potential, in which the actual experiments are performed. Afterwards, the distribution of atoms is determined either in-situ or after a time-of-flight expansion using a standard absorption imaging technique.

Trapping and Cooling

Each experimental sequence starts with the loading of a three-dimensional magneto-optical trap (MOT) [193] in the first chamber from the background gas of Rb atoms, which are evaporated from an attached oven with a Rb reservoir. The MOT is formed by three pairs of counterpropagating laser beams and a quadrupole magnetic field generated by a pair of coils in anti-Helmholtz configuration. The laser beams contain light with two different frequencies resonant with the D_2 line of ^{87}Rb (780 nm): the cooling light, which is slightly detuned from the $|5^2S_{1/2}, F = 2\rangle \rightarrow |5^2P_{3/2}, F = 3\rangle$ transition, as well as a repumper on the $|5^2S_{1/2}, F = 1\rangle \rightarrow |5^2P_{3/2}, F = 2\rangle$ transition. After the loading of the MOT, the atom cloud consisting of approximately 10^9 particles is compressed by increasing the

magnetic field gradient and cooled to about $20\mu\text{K}$ in an optical molasses after switching off the gradient. Subsequently, the atoms are spin polarized by optical pumping to the low-field seeking $|5^2S_{1/2}, F = 1, m_F = -1\rangle$ hyperfine ground state

The atom cloud is then transferred by magnetic transport through the differential pumping section to the second chamber, a rectangular glass cell. To this end, the atoms are confined in a magnetic quadrupole trap, whose minimum is continuously shifted by sequential ramping of the currents through nine pairs of partially overlapping coils along the connecting tube [104]. Following the transport, two stages of evaporative cooling are conducted to prepare a Bose-Einstein condensate (BEC) [194, 195] as the starting point of each experiment. The first step is radio-frequency (rf) induced evaporation in a magnetic quadrupole trap, where the hottest atoms are selectively transferred to a non-trapped state by a frequency ramp of an rf field. To prevent Majorana spin flips in the vicinity of the zero crossing of the magnetic field, a blue-detuned laser beam at 767 nm is focussed onto the trap's centre. At the end of the frequency ramp, the atoms are captured in a crossed optical dipole trap formed by two orthogonal, tightly focussed laser beams at 1064 nm. Finally, the atoms undergo a forced evaporation by lowering the trap depth in the presence of an external potential gradient, creating a BEC with negligible thermal fraction. The end point of this evaporation ramp is adjusted to obtain the desired atom number for the specific experiment, which is typically on the order of 5000-10000 atoms.

Optical Lattices

After the BEC is prepared in the crossed dipole trap, the three-dimensional optical lattice potential, in which the experiment takes place, is ramped up adiabatically. This potential is formed by mutually orthogonal, retro-reflected laser beams along all three spatial directions. The interaction between the light field and the dipole moment that it induces in the atoms creates an optical dipole potential $V_{\text{dip}}(\mathbf{r}) = -\text{Re}[\alpha(\omega)] |\mathbf{E}(\mathbf{r})|^2/4$. Here, \mathbf{E} is the position-dependent amplitude of the oscillating electric field, ω the frequency of the light and α the frequency-dependent atomic polarizability [196]. If the atom can be approximated as a two-level system and ω is sufficiently close to its resonance ω_0 for the rotating wave approximation to be valid, the polarizability is inversely proportional to the detuning such that $V_{\text{dip}}(\mathbf{r}) \propto |\mathbf{E}(\mathbf{r})|^2/(\omega - \omega_0)$. The detuning, which determines the sign of the potential, is chosen large enough to suppress heating due to photon scattering, which scales as $|\mathbf{E}(\mathbf{r})|^2/(\omega - \omega_0)^2$. The standing wave pattern of a retro-reflected beam with wavelength λ thus creates a perfectly sinusoidal potential with period $d = \lambda/2$ – the optical lattice. Due to their almost perfect uniformity, comparatively large length scales and correspondingly slow time scales, ultracold atoms in optical lattices are an ideally suited system for the quantum simulation of many condensed matter problems. For this, the atoms mimic the electrons in a crystalline material, whose periodic structure is replicated by the optical lattice. An excellent in-depth introduction to the physics of atoms in optical lattices can be found in [197] and recent developments in the field have been reviewed in [74, 75, 198].

In the horizontal plane, superlattice potentials can be created along both the x - and y -axis by overlapping two beams with different wavelengths λ_s and $\lambda_l > \lambda_s$, in this case with $\lambda_s = 767$ nm and $\lambda_l = 2\lambda_s$. The superlattice setup and experimental techniques are covered in detail in Section 3.2. Along the vertical z -direction, there is a single-period lattice with $\lambda_z = 844$ nm, which is mostly used for isolating different horizontal planes. The depth of each lattice is controlled by an acousto-optic modulator via an active feedback loop stabilizing the intensity on a monitor photodiode. All frequencies and polarizations are chosen such that there is no mutual interference between different lattice beams.

Detection

At the end of the experimental sequence in the optical lattice, the atoms are imaged to obtain either the in-situ density directly or their momentum distribution following a ballistic time-of-flight expansion. In both cases, absorption imaging [194] is employed, where the atoms are illuminated with a large resonant imaging beam in conjunction with a transverse re-pumper beam. The imaging laser is locked onto the $|5^2S_{1/2}, F = 2\rangle \rightarrow |5^2P_{3/2}, F = 3\rangle$ transition by Doppler-free frequency-modulation spectroscopy [199, 200] and also serves as a reference for the MOT cooling laser. When passing through the atom cloud, the imaging light is partially absorbed depending on the integrated atomic density along the imaging axis. The latter can be extracted by imaging the light onto a CCD camera and comparing it with a reference image of the same beam with no atoms present.

To determine the momentum distribution, all trapping potentials are switched off such that the atoms can expand freely. In the far-field limit after a sufficiently long expansion time, the initial cloud size becomes negligible and the spatial density corresponds to the final momentum distribution in the trap. The release from the lattice can be performed in two ways, either instantaneously or adiabatically. For the former, the Bloch waves in the lattice are projected onto the momentum eigenstates of free particles. The momentum distribution is given by the Fourier transform of the one-particle density matrix $\langle \hat{a}_m^\dagger \hat{a}_n \rangle$, multiplied by an envelope proportional to the Fourier transform of the on-site Wannier function [201]. If the lattices are switched off adiabatically compared to the band gaps, often referred to as band mapping, the Bloch waves are adiabatically connected to the corresponding plane waves and states from different bands end up in different Brillouin zones as in an extended Brillouin zone scheme. The band mapping sequence can be extended to a site-resolved band mapping technique as discussed in Section 3.2.1, which provides a powerful tool to obtain additional information about the in-situ density distribution.

3.2 Optical Superlattices

3.2.1 Experimental Implementation

Along both the x - and the y -axis, there are two independent optical lattices with different lattice spacings, a short lattice with period $d_s \equiv d_{s,x} = d_{s,y}$ and a long lattice with $d_l \equiv$

$d_{1,x} = d_{1,y} = 2d_s$. In each direction, this creates a superlattice potential consisting of double wells when both lattices are switched on at the same time (Fig. 3.1a). The two setups are almost identical and to simplify the notation we will thus focus on the x -axis in the following description unless mentioned otherwise. The light for both short lattices is generated by a single Ti:Sa laser (M Squared SolsTiS) set to 767 nm, while for the long lattices at 1534 nm either a RIO ORION 3135, amplified by a 5 W Nufern NuAMP amplifier, or a 5 W NP Photonics Rock fibre laser are used. The short and long lattice beams are overlapped on a dichroic mirror, before being focussed on the atom cloud by a lens (see also Section 6.1 and Fig. 6.1). After passing a collimation lens behind the vacuum glass cell, both beams are retro-reflected by the same mirror to create the standing wave pattern. The superposition of the two potentials gives rise to a superlattice potential of the form

$$V_{\text{SL}}(x) = V_{s,x} \sin^2(\pi x/d_{s,x}) + V_{l,x} \sin^2(\pi x/d_{l,x} - \varphi_x/2) \quad (3.1)$$

with the superlattice phase φ_x indicating the position of the long lattice relative to the short one (Fig. 3.1a). The wave vectors of the lattice beams are $k_{s,x} = \pi/d_{s,x}$ and $k_{l,x} = \pi/d_{l,x}$, respectively, and the lattice depths $V_{s,x}$ and $V_{l,x}$ are typically given in units of the corresponding recoil energy $E_{r,i} = \hbar^2 k_{i,x}^2 / (2m_a)$, $i \in \{s, l\}$ with m_a denoting the mass of the atoms. To obtain a homogeneous potential, the two incoming lattice beams have to be overlapped very accurately. To this end, a thick glass block is placed in one of the beams and for each beam a mirror is positioned at the front focus point of the first lens prior to the overlapping. In this way, the relative angle and the transverse position at the location of the atom cloud can be controlled independently (see Section 6.1).

Control of the Superlattice Phase

The relative position along x between the short and long lattice at the location of the atoms is determined by the distance L_M between the atom cloud and the retro mirror as well as the lattice wavelengths. The latter in turn depend on the frequency of the respective light and the frequency-dependent refractive index of the surrounding air. Therefore, the superlattice phase φ_x can be controlled by tuning the frequency of the long lattice laser as illustrated in Fig. 3.1a. Shifting the frequency by $\Delta\nu$ changes the phase by

$$\Delta\varphi_x = 4\pi \frac{L_M}{c} \Delta\nu \quad (3.2)$$

neglecting any deviation of the refractive index from unity. While this necessarily leads to a situation where $d_l \neq 2d_s$, the difference is negligible over the extent of the cloud if the cloud size L_x is much smaller than L_M . In the experiment, L_M is about 0.2 m and a shift of φ_x by 2π corresponds to a frequency difference of $\Delta\nu = c/(2L_M) \approx 750$ MHz, i.e. a relative change of $\Delta d_l/d_l = -\Delta\nu/\nu \approx -4 \times 10^{-6}$. For $L_x = 30d_s$, this causes a phase shift between the two edges of the cloud of $2\pi L_x/L_M \approx 10^{-4}\pi$, which is much smaller than the experimental uncertainty in the phase.

The frequency of the long lattice lasers is actively stabilized using the short lattice as a reference via the offset lock shown in Fig. 3.1b. For this, part of the long lattice light is

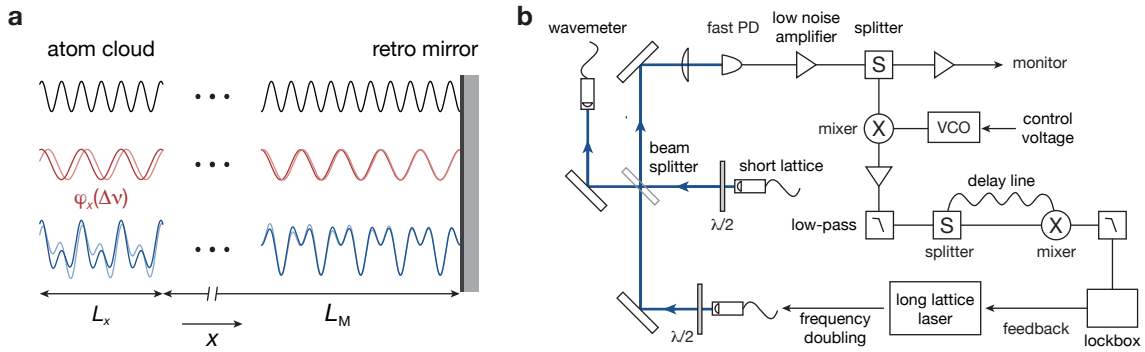


Figure 3.1 – Controlling the phase of the dynamical superlattice. (a) The superlattice is created by retro-reflecting the short and long lattice beams from the same retro mirror, which serves as a common reference position. The superlattice phase φ_x at the position of the atom cloud is controlled by changing the frequency of the laser used for generating the long lattice. This slightly modifies the period of the standing wave, leading to a shift of the position of the long lattice relative to the short one at the atom position. As the distance between the atom cloud and the retro mirror (L_M) is very large compared to the extent of the cloud (L_x), the change in the superlattice phase over the size of the cloud is negligible. (b) Frequency offset lock for the superlattice phase. The frequency of the long lattice laser is doubled and then stabilized relative to the one of the short lattice by comparing the beat frequency measured on a fast photodiode (PD) to a tunable reference frequency generated by a voltage-controlled oscillator (VCO). Figure adapted from [106].

frequency-doubled in a periodically poled lithium niobate crystal and overlapped on a fast photodiode with a beam from the short lattice laser. The beat signal is then compared with the output of a voltage-controlled oscillator, whose input voltage is used to control the superlattice phase. To do this, the mixed signals are low-pass filtered, split and subsequently sent through a delay line. When combining the signals again, the DC component of the output is proportional to $\cos [2\pi(\nu_{\text{beat}} - \nu_{\text{VCO}})\tau_{\text{delay}}]$ [202]. The signal passes through another low-pass filter to generate an error signal, which is used to stabilize the frequency difference to a fixed value by modulating the piezo element of the long lattice laser. A detailed description of the locking scheme is given in [203]. With this, dynamical control of the superlattice phase is achieved allowing for continuous phase ramps with a speed that is limited by the maximum tuning speed of the lasers. Furthermore, the fluctuations of the beat frequency can be reduced to approximately 2 MHz, corresponding to a superlattice phase stability on the order of $3 \times 10^{-3} \pi$. Alternatively, a commercially available offset phase lock (Vescent Photonics, D2-135) is used for one of the superlattice lasers.

There are, however, additional effects that can change φ_x which are not compensated for by the offset lock. This applies in particular to the pressure and temperature dependence of the refractive index, which can cause substantially larger long-term drifts of φ_x on the order of 0.05π . As these typically take place over the course of hours, the superlattice phase can easily be adjusted accordingly using a phase centring sequence. In this sequence, a Mott-insulating state with unit filling is prepared in a 3D optical lattice with only the long lattice in the direction of the respective superlattice. The long lattice sites are then split into double wells by adiabatically ramping up the short lattice. The superlattice phase is set to a symmetric double-well configuration, $\varphi_x = (l + 1/2)\pi$, $l \in \mathbb{Z}$, such

that no population imbalance is expected between the left and right site of each double well (see also Section 3.2.2). By measuring the double-well imbalance using site-resolved band mapping (see below), drifts of φ_x can be detected and corrected for. By performing such a phase centring in regular intervals, a long-term phase stability of $5 \times 10^{-3} \pi$ can be achieved. Additionally, this technique enables a precise calibration of the superlattice phase by measuring the frequency difference between symmetric double-well configurations shifted by $\Delta\varphi_x = \pi$.

Site-Resolved Band Mapping

The ability to create a superlattice with a dynamically controlled phase enables a variety of techniques for the preparation, manipulation and detection of states. These include, for example, the preparation of charge-density waves with an alternating density pattern [204], of particles in excited bands (see Section 4.3) and of multiply occupied lattice sites [205]. Furthermore, dynamical superlattices allow for the detection of occupation fractions and band excitations (see Section 6.3.2) and the measurement of particle [206] and spin currents [178]. For the study of topological charge pumps, a powerful tool is the capability to detect the fraction of atoms on the two distinct sublattice sites forming the double-well structure of a period-two superlattice (see Section 3.2.2). This is possible with a site-resolved band mapping technique first introduced in [205, 207]. In order to do this, the atom distribution is frozen at the end of the sequence by quickly ramping up the short lattice to fully suppress tunnelling. Afterwards, a non-adiabatic superlattice phase ramp is performed such that the ground state on the even lattice sites becomes the third-lowest double-well eigenstate. Depending on the initial configuration, this may involve one or more rapid crossings with excited states localized on the other site. Then the short lattice is slowly switched off to adiabatically bring atoms on the even sites into the third Bloch band of the long lattice, while atoms on the odd sites remain in the lowest band. A subsequent band mapping will thus transfer atoms from odd (even) site to the first (third) Brillouin zone, allowing for an overlap-free counting of the atoms after time-of-flight.

3.2.2 Superlattice Bose-Hubbard Model

As the beams forming the three-dimensional lattice are mutually orthogonal in the experiment, the single-particle eigenstates factorize into three independent wave functions along x , y and z , each of which is governed by a one-dimensional Schrödinger equation. Due to the periodicity of the superlattice potential, here assumed to be along x , its eigenstates are Bloch waves $\psi_{n,k_x} = e^{ik_x x} u_{n,k_x}(x)$ as discussed in Section 2.1.2. Similar to a single-period lattice, they can be obtained by a Fourier expansion of the Schrödinger equation, see e.g. [208] for an explicit derivation. With $d_1 = 2d_s$, the combined potential exhibits the same period as the long lattice with a unit cell comprising two non-equivalent sites, $a_x = 2d_s$. The doubling of the unit cell leads to a splitting of each Bloch band of the short lattice into two subbands as the Brillouin zone is restricted to $k_x \in]-\pi/a_x, \pi/a_x]$.

Wannier Functions

From the delocalized Bloch waves of a given band, Wannier functions with a well-defined position can be constructed by an equal-weight superposition of all quasi-momenta in the Brillouin zone:

$$w_{n,j_x}(x) = \frac{1}{\sqrt{L_x/a_x}} \sum_{k_x} e^{-ik_x j_x a_x} \psi_{n,k_x} \quad (3.3)$$

with j_x denoting the j_x -th unit cell and L_x the system size in the superlattice direction. The Wannier functions constitute a convenient basis for topological charge pumps as w_{n,j_x} contains information about the topological properties of the entire band. Indeed, the centre-of-mass motion of a uniformly populated band can be understood entirely from the evolution of w_{n,j_x} in response to a change of φ_x [16] (see also Section 4.1.1). Due to the gauge freedom in choosing the Bloch waves' phases, the Wannier functions are not defined uniquely. In particular, they exhibit different spatial variances for different phase gauges. While the maximally localized Wannier functions [209] in a simple lattice can easily be obtained due to the well-defined parity of the wave functions, this approach fails in a superlattice potential. An elegant way to overcome this is based on the insight that the eigenstates of the position operator projected onto a certain band, $\hat{x}_n = \hat{P}_n \hat{x} \hat{P}_n$, are identical to the maximally localized Wannier functions of that band [155, 156]. This provides an efficient method to calculate these functions in superlattices as detailed in [157, 210].

For a single band, the Wannier functions extend over the two-site unit cell. In many cases, however, it is more appropriate to consider the two lowest subbands for the description of the superlattice due to the rather small band gap in between. This corresponds to using the ground-state Wannier functions that are localized on the left and right site of a double well, respectively (see below). One of the main advantages of the aforementioned approach relying on the band-projected position operator is the fact that it can easily be extended to include multiple bands by simply choosing the appropriate projection operator. When taking into account the two lowest bands, the resulting eigenstates are the Wannier functions that are maximally localized on individual lattice sites, $w_{m_x} \equiv w_{12,m_x}$ with m_x indicating the m_x -th lattice site. Similar to Eq. (3.3), w_{12,m_x} consists of a superposition of Bloch waves of all quasi-momenta, but in this case from both bands $n = 1$ and $n = 2$, which typically will have different weights. Note that depending on the specific lattice configuration, special care has to be taken when choosing the appropriate subband manifold, e.g. if the gap between the second and third band becomes smaller than the one between the first and second [210].

Tight-Binding Hamiltonian

In the generic case, the Hamiltonian of interacting bosons in an optical lattice is written in terms of the bosonic field operators in second quantization form. Using the Wannier functions as a basis, the field operators can be expressed as creation and annihilation operators acting on individual lattice sites [153]. While in general the complete set of Wannier functions comprising all bands is required, it is often sufficient to only consider the lowest

state w_{m_x} on each site as mentioned above. In a superlattice, this tight-binding approximation is valid if the depth of the short lattice is large enough such that the hopping between neighbouring sites, the on-site interaction as well as the energy offsets between the lattice sites are small relative to the energy difference to the first excited states on the lattice sites [154]. Within this limit, the Hamiltonian for an optical superlattice with $d_l = 2d_s$ is given by an extension of the archetype bosonic tight-binding Hamiltonian, the Bose-Hubbard model [153, 211, 212]:

$$\begin{aligned} \hat{H}_{\text{SLBH}}(\varphi_x) = & - \sum_{m_x} \left[J_x(\varphi_x) + \frac{1}{2}(-1)^{m_x} \delta J_x(\varphi_x) \right] \hat{a}_{m_x+1}^\dagger \hat{a}_{m_x} + \text{h.c.} \quad (3.4) \\ & + \sum_{m_x} \frac{1}{2}(-1)^{m_x} \Delta_x(\varphi_x) \hat{n}_{m_x} \\ & + \sum_{m_x} \frac{U}{2} \hat{n}_{m_x} (\hat{n}_{m_x} - 1) + \sum_{m_x} (V_{m_x} - \mu_0) \hat{n}_{m_x} \end{aligned}$$

with $\hat{n}_{m_x} = \hat{a}_{m_x}^\dagger \hat{a}_{m_x}$.

The first two lines are equivalent to the single-particle superlattice Hamiltonian introduced in Eq. (2.36) for the specific superlattice configuration $d_l = 2d_s$. The strength of the tunnel coupling can be calculated by evaluating the transition matrix element between neighbouring Wannier functions of the single-particle Hamiltonian $-\hbar^2 \partial_x^2 / (2m_a) + V_{\text{SL}}(x)$. The energy offset, on the other hand, is the corresponding energy expectation value of the respective Wannier function. The resulting tight-binding Hamiltonian is known as the Rice-Mele model. It is characterized by alternating tunnelling rates and energy offsets, both of which depend on φ_x . This model was first introduced to study elementary excitations in linearly conjugated diatomic polymers [130] and has since become an exemplary two-band model, used e.g. to study fractionally charged excitations [128] and ferroelectric phenomena in 1D [213]. In the symmetric double-well configuration $\Delta_x = 0$, the Rice-Mele model reduces to the Su-Schrieffer-Heeger (SSH) model [129], a paradigmatic 1D model with two topologically distinct phases $\delta J_x > 0$ and $\delta J_x < 0$ (see also Section 4.1.1).

The first term in the last line describes the on-site interaction U between atoms located on the same site, arising from their two-body van-der-Waals interaction. At low temperatures, it is dominated by s -wave scattering and U becomes proportional to the s -wave scattering length quantifying the strength of the corresponding δ -shaped pseudo-potential [149]. Here, it is assumed that U is not site-dependent. This condition is approximately fulfilled in most cases, but in particular for a shallow short lattice with $\Delta_x \neq 0$ it no longer holds. Finally, μ_0 denotes the chemical potential, which controls the particle number, and V_{m_x} accounts for additional external potentials, e.g. a trapping potential resulting from the finite waist of the Gaussian lattice beams.

Phase Diagram

As an extension to the Bose-Hubbard model, the superlattice Hamiltonian in Eq. (3.4) exhibits three different types of phases arising from the competition of the different energy

scales and temperature: an incompressible Mott-insulating phase with localized particles dominated by the interaction, a superfluid phase with long-range phase coherence favoured by the kinetic energy term and a normal fluid at large temperatures [212]. The corresponding phase diagram was first studied qualitatively within the mean-field approximation [214] and later using quantum Monte-Carlo and exact diagonalization [215] as well as techniques based on matrix product states [216]. This analysis was also extended to quasi-periodic configurations, in which gapless localized phases are predicted [154, 160]. Experimental results for $\delta J_x = 0$ together with a pedagogical overview of the phase diagram can be found in [203].

Here, we focus on the two relevant cases for the preparation of the initial state with uniform occupation of a single band for the topological charge pumping experiments presented in Chapter 4 and 6. These are the symmetric double-well configuration $\Delta_x = 0$ and the staggered configuration $\delta J_x = 0$ at zero temperature. If both $\Delta_x = 0$ and $\delta J_x = 0$, Eq. (3.4) reduces to the standard Bose-Hubbard Hamiltonian. Its phase diagram as a function of J_x and μ exhibits characteristic Mott lobes with a fixed integer occupation number $\langle \hat{n}_{m_x} \rangle = l$, $l \in \mathbb{N}$. The lobes are centred around $\mu_0 = (l - 1/2)U$ and are surrounded by the superfluid phase. For $|\delta J_x| > 0$, additional Mott-insulating phases appear between these lobes in the vicinity of $\mu_0 = lU$. These, however, do not possess integer filling as usual, but rather are characterized by a half-integer number of particles localized in each unit cell and are thus termed fractional Mott insulators (MI) [214]. Similar phases with other fractional fillings occur for superlattices with a different ratio of lattice constants. For $d_l = 2d_s$, the fractional phase can be understood as a unit filled MI with a double well constituting the fundamental unit. This allows for a partial localization to minimize the interaction energy, while at the same time reducing the kinetic energy by delocalizing over the double well. Accordingly, these phases show increased correlations between neighbouring sites. Enhanced nearest-neighbour correlations also develop in the integer-filled Mott phases for $|\delta J_x| > 0$. When the short lattice vanishes, $V_s \rightarrow 0$, the fractional MI is continuously connected to an integer MI in the long lattice. In this limit, the energy gap becomes comparable to half the on-site interaction energy provided that the tight-binding approximation is still applicable. In general, however, the fractional MIs are more fragile as the effective interaction energy on a double well is given by

$$U_{\text{DW}} = 2J_x^{\text{DW}} + \frac{U}{2} \left[1 - \sqrt{1 + (4J_x^{\text{DW}}/U)^2} \right] < 2J_x^{\text{DW}} \quad (3.5)$$

The intra-double-well tunnelling $J_x^{\text{DW}} = J_x + |\delta J_x/2|$ decreases rapidly with increasing V_s .

In the staggered configuration $\delta J_x = 0$, the Bose-Hubbard phase diagram is modified in a similar way. As $|\Delta_x|$ is increased from zero, insulating phases with half-integer filling develop between the integer Mott lobes. Whereas the integer MIs have a homogeneous density, the fractional phases exhibit a modulated density pattern following the alternating energy offset. With increasing $|\Delta_x|$, the fractional MIs become more and more robust, while the regions of the integer phases shrink. The latter cease to exist at $|\Delta_x| = U$ and are superseded by a superfluid with filling one half on top of a background of localized atoms, which effectively compensate Δ_x by an additional atom on each lower-lying site.

Realization of a 1D Topological Charge Pump

An optical superlattice realizes precisely the type of two-period potential discussed by Thouless in his original proposal for a topological charge pump [10]. Combined with the ability to dynamically control the superlattice phase, ultracold atoms in a superlattice thus provide an excellent platform for the implementation of a topological charge pump. Ultracold atoms have previously been used to study a wide range of transport phenomena [81], including the quantized conductance in quantum point contacts between biased reservoirs [83, 84] and Hall response measurements in topologically non-trivial lattice models [91, 92]. In the context of charge pumping, notable experiments demonstrating directed transport without an external bias are the realization of a Brownian motor inducing a stochastically driven motion [191] as well as the implementation of a non-dissipative quantum ratchet [192]. In the former experiment, an oscillating driving force with two harmonic frequencies is applied to a near-resonant, spin-dependent optical lattice. Due to the breaking of time-reversal symmetry by the driving, a motion is generated through optical pumping processes between different spin states. In a quantum ratchet, on the other hand, an effective unidirectional motion is created by a periodic modulation of the amplitude of a sawtooth-like optical potential.

The use of time-dependent superlattice potentials for topological charge pumping was already proposed early on in 1998 [190]. Yet, this work was largely overlooked, possibly due to the lack of the required experimental techniques. Following the first experimental implementations of optical superlattices [205, 207], particle transport through periodic modulation of a superlattice potential was studied theoretically as a tool for quantum computation [112] and the formation of non-local entangled pairs of atoms [179]. While these works focused on fine-tuned non-adiabatic dynamics for the implementation of successive swap gates, the possibility of realizing a topological charge pump was addressed again in subsequent years [151, 217, 218]. These coincided with related experiments in photonic systems demonstrating the non-quantized transport of edge states with a topological charge pump [34].

In this chapter, we discuss the implementation of a 1D topological charge pump with ultracold bosonic atoms using the optical superlattice setup presented in Section 3.2. In

Section 4.1, the theory of topological charge pumping developed in Section 2 is applied to the dimerized superlattice used in the experiment and the experimental sequence is illustrated. Afterwards, in Section 4.2, the quantized transport of atoms forming a half-filled Mott insulator in the lowest band is demonstrated using in-situ imaging and site-resolved band mapping. In the following Section 4.3, results for localized atoms prepared in the first excited band are presented, which exhibit a reversed motion compared to the one of the underlying long lattice inducing the pumping. Finally, a topological transition in the excited band is studied that takes place when tuning the depth of the short lattice. The work presented here is based on the publication in [163], constituting the first realization of a topological charge pump with ultracold atoms as well as the first observation of the associated quantized bulk transport. Simultaneously, similar results have been obtained with a fermionic quantum gas [219] and the implementation of a non-quantized geometric charge pump for an atomic Bose-Einstein condensate was reported in [220].

4.1 Topological Charge Pumping in a Dimerized Superlattice

4.1.1 Pump Cycle in the Rice-Mele Model

The superlattice implemented in the experiment constitutes a special form of the general case discussed in Section 2.1, namely a sinusoidal period-two superlattice with $d_1 = 2d_s$ [Eq. (3.1)]. For non-interacting particles in the tight-binding limit with no additional external trapping potential, this system is described by the 1D Rice-Mele Hamiltonian [Eq. (3.4)] introduced in Section 3.2.2. It is characterized by an alternating, phase-dependent modulation of both the on-site energies, $\pm\Delta_x(\varphi_x)/2$, and the nearest-neighbour tunnelling matrix elements, $J_x(\varphi_x) \pm \delta J_x(\varphi_x)/2$ (see Fig. 4.1a). Its unit cell comprises two lattice sites and accordingly the lowest Bloch band of the short lattice fragments into two subbands separated by an energy gap. The corresponding 2D quantum Hall system when applying the mapping from Section 2.3.2 is a Harper-Hofstadter-Hatsugai model with one half of a flux quantum per unit cell of the square lattice, $\Phi_{xz} = (d_s/d_1)\Phi_0$. In this configuration, the modulation of the hopping δJ_x profoundly modifies the energy spectrum as it ensures that the gap between the two subbands remains open at the points where $\Delta_x = 0$. Therefore, the Harper-Hofstadter-Hatsugai model exhibits a gapped spectrum unlike the Harper-Hofstadter model for $\Phi_{xz} = \Phi_0/2$. The Chern numbers, which can be calculated numerically following [221], are $\nu_1^{\text{gs}} = +1$ for the lowest band and $\nu_1^{\text{exc}} = -1$ for the excited one. Thus, a centre-of-mass displacement by $\pm d_1$ is expected per cycle. The negative Chern number of the upper band causes a counter-intuitive reversed particle transport, which points in the opposite direction as the motion of the underlying long lattice (see Section 4.3).

During a pump cycle, as φ_x is varied by 2π , the tight-binding parameters are modulated periodically, outlining a closed loop in the δJ_x - Δ_x parameter space (Fig. 4.1b). This pump path encloses the origin $\delta J_x = \Delta_x = 0$, where a singularity occurs. At this point, the

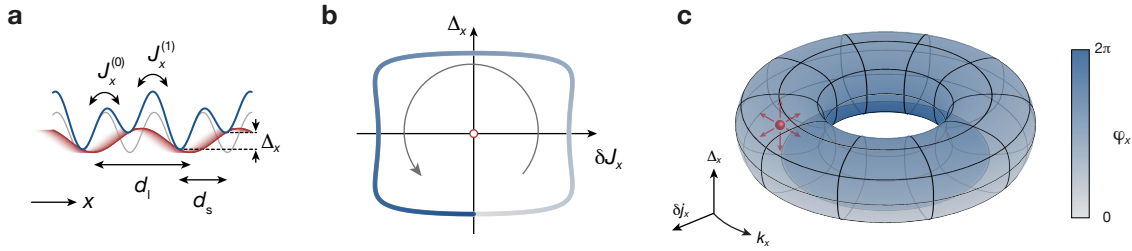


Figure 4.1 – Pump cycle in the Rice-Mele model. (a) Tight-binding parameters in the period-two superlattice with $d_l = 2d_s$: the dimerized tunnel couplings $J_x^{(0)} = J_x + \delta J_x/2$ and $J_x^{(1)} = J_x - \delta J_x/2$ and the alternating energy offset $\pm \Delta_x/2$ (b) When moving the long lattice along x by varying φ_x , both δJ_x and Δ_x are modulated periodically, tracing out a closed path in the δJ_x - Δ_x parameter space. This pump path surrounds a singularity at the origin, where the two lowest subbands of the Rice-Mele model touch. (c) Illustration of the pump cycle in the 3D parameter space spanned by the two tight-binding parameters $\delta j_x = (1 + J_x^{(0)}/J_x)/2$ and Δ_x and the quasi-momentum $\hbar k_x$ using cylindrical coordinates. The cyclic modulation of δJ_x and Δ_x combined with the periodic Brillouin zone traces out a torus-like surface, enclosing the degeneracy point at $\delta J_x = \Delta_x = 0$ and $k_x = \pm \pi/d_l$, at which the band gap closes. This singularity is the source of the topologically non-trivial character of the surrounding pump cycle. Figure adapted from [163].

Hamiltonian reduces to the one of the short lattice only and the two subbands merge to a single one, touching at the edge of the 1D Brillouin zone $k_x = \pm \pi/d_l$ (Fig. 4.1c). This degeneracy point prohibits a unique phase choice for the Bloch wave functions throughout the 2D generalized Brillouin zone and thereby gives rise to the pump cycle's non-trivial topology (see Section 2.1.3). Therefore, whenever the pump path encloses the origin, a quantized transport takes place, whereas otherwise the particles always return to their initial positions. From this, the robustness of the transport against disorder can be seen immediately. If a disorder potential is present that locally changes the on-site energies, this will lead to a modification of Δ_x on each double well and will thus shift the pump cycle shown in Fig. 4.1b. But as long as the disorder is small compared to the maximum double-well tilt $\Delta_x^{\max} = |\Delta_x(\varphi_x = 0)|$ in the staggered configuration, the path for a given double well is still encircling the degeneracy point and a quantized transport will occur. The same argument can be applied for disordered tunnelling rates. Note, however, that in an extended system the criterion for adiabatic quantized transport is stricter and the disorder has to be smaller than the minimum band gap during the cycle.

The pump cycle smoothly connects the two topologically distinct phases of the SSH model with $\delta J_x > 0$ and $\delta J_x < 0$ for $\Delta_x = 0$, to which the superlattice corresponds in the two symmetric double-well configurations at $\varphi_x = \pi/2$ and $\varphi_x = 3\pi/2$. The difference of the Zak phases of the two configurations is π due to the opposite winding of the eigenstates when traversing the Brillouin zone and their respective polarizations thus differ by one lattice site [21]. Hence, the centre-of-mass motion induced by the pumping is not only quantized to $\pm d_l$ for a full cycle, but also displays a fractional quantization $\pm d_s$ after each half of a cycle [222] (see also Section 6.4.1). The Zak phase difference in the SSH model has previously been measured in this experimental setup [93, 206]. In systems with sharp boundaries, the topologically non-trivial nature of the pump cycle is necessarily accompa-

nied by the appearance of edge states in one of the symmetric double-well configurations – depending on the position of the boundaries (see Fig. 2.2 and Section 2.2.1). In the experiment, however, such phenomena are not expected since only a weak harmonic confinement is present. Moreover, the system size is determined by the interaction energy and the chemical potential rather than the extent of the single-particle states (see Section 4.2.2).

In the experiment, the pumping is performed with bosonic atoms forming a fractional Mott-insulating state with half filling, where one atom is localized in the ground state of each double well. In this limit, the quantized transport can be understood intuitively by looking at the evolution of the Wannier functions associated with the lowest band (Fig. 4.2). As each Wannier function is a homogeneous superposition of all quasi-momenta in the first Brillouin zone, its anomalous velocity is identical to the average anomalous velocity of a uniformly populated band, where each delocalized Bloch wave is occupied with the same probability [16]. The individual Wannier functions thus exhibit the same topological transport properties as the entire band. The particle transport is driven by tunnelling between neighbouring lattice sites, following the instantaneous double-well ground state (Fig. 4.2). Accordingly, the Berry curvature $\Omega_1^x = \Omega_1(k_x, \varphi_x)$ is distributed inhomogeneously over the generalized Brillouin zone, exhibiting pronounced peaks centred at the phase values corresponding to the symmetric double-well configurations (Fig. 4.2). After a full cycle, the lattice configuration becomes the same as the initial one again. The respective Wannier functions are thus identical, but during the cycle each Wannier function is continuously connected to the one localized in the neighbouring unit cell.

4.1.2 Experimental Sequence

The experiments presented in the following sections are conducted in a 3D optical lattice with the superlattice oriented in the x -direction. In the transverse directions, the short lattice along y and the z -lattice at a depth of $30E_{r,s}$ and $30E_{r,z}$, respectively, are used to create a 2D array of effectively decoupled 1D systems with large repulsive on-site interaction. As an initial state for the pumping, starting from the BEC in the crossed dipole trap, a half-filled Mott insulator (MI) is prepared in a given subband in the symmetric double-well configuration at $\varphi_x = \varphi_x^{(0)} = 0.50(1)\pi$ to obtain a homogeneous occupation of all k_x -states. To this end, the long x -lattice and the transverse lattices are first ramped up to $30E_{r,i}$, $i \in \{l, s, z\}$ during 150 ms, creating a unit-filled MI in the long lattice. When studying the lowest subband, each lattice site is split to a double well by increasing the short lattice along x and lowering the long lattice to their final values ($10.0(3)E_{r,s}$ and $20(1)E_{r,l}$, respectively, unless mentioned otherwise) within 10 ms. For a description of the loading sequence for the first excited subband see Section 4.3. Compared to the direct preparation of the fractional MI, this sequence creates much less excitations due to the substantially larger energy gap of the unit-filled MI (see Section 4.2). It was confirmed by a direct band mapping measurement that the atoms are uniformly delocalized over the entire first Brillouin zone and no residual phase coherence is present.

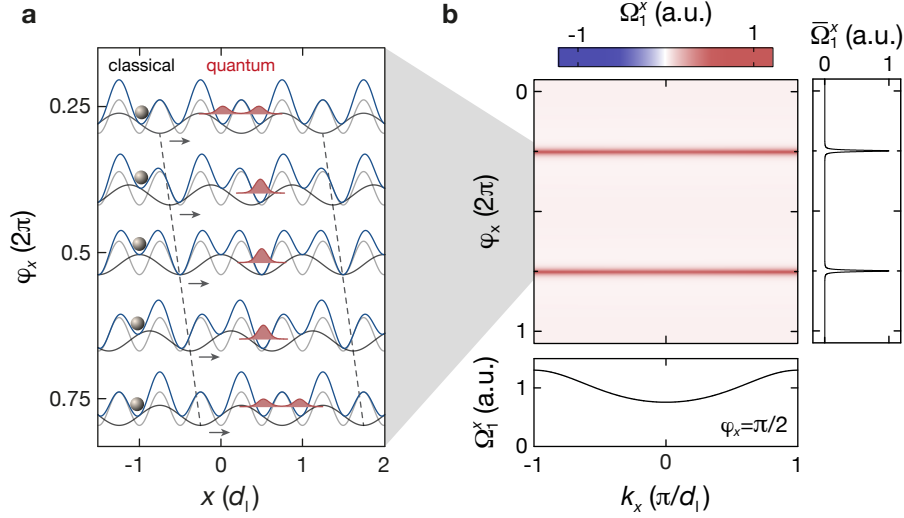


Figure 4.2 – Quantized particle transport by topological charge pumping in a period-two superlattice. (a) Adiabatic evolution of a Wannier function of the lowest subband (red) during one half of the pump cycle. At $\varphi_x = \pi/2$, a particle localized in the ground state of the centre double well is in a symmetric superposition between the left and right site. As φ_x is increased, the double well is tilted to the right and the atom tunnels to the lower-lying site. It stays there until the superlattice approaches the other symmetric double-well configuration at $\varphi_x = 3\pi/2$. At this point, the atom delocalizes again over the double well, which is now shifted by one lattice site compared to the starting point. In this way, the atom adiabatically follows the motion of the sliding long lattice, giving rise to a quantized particle transport. A classical particle (grey ball), on the other hand, would remain at its initial position as the individual lattice sites do not shift in space and the motion purely arises from quantum mechanical tunnelling. (b) Distribution of the Berry curvature Ω_1^x of the lowest subband in the Rice-Mele model over the generalized Brillouin zone, plotted for $V_{s,x} = 10E_{r,s}$ and $V_{l,x} = 20E_{r,l}$ as in the measurements presented in Section 4.2. The largest Ω_1^x occurs in the vicinity of the symmetric double-well configurations, $\varphi_x = (l + 1/2)\pi$, $l \in \mathbb{Z}$, where the atoms tunnel between neighbouring sites. In the panel on the right, the Berry curvature averaged over all quasi-momenta k_x is shown as a function of φ_x . The lower panel shows $\Omega_1^x(k_x)$ at $\varphi_x = \pi/2$. Figure adapted from [163].

To perform the pumping, two separate lasers are used to create the long x -lattice due to the limited frequency tuning range of a single laser, which cannot achieve more than a single pump cycle. Both lasers are coupled into the same single-mode fibre to generate identical potentials and the respective lattice depths are controlled by individual acousto-optic modulators, stabilizing the intensity on the same photodiode after the fibre. This allows for a rapid switching between the two lasers in about $10 \mu\text{s}$, which is much faster than all relevant energy scales in the system. The first laser covers the range $\varphi \in [0.00(1)\pi, 1.12(1)\pi]$ and the second one $[1.12(1)\pi, 2.00(1)\pi]$. By a successive handover, an unlimited number of cycles can be performed. The phase ranges are chosen such that the switching occurs in the vicinity of the staggered configuration, where the atoms are well localized on the lower-lying lattice sites. By measuring the band occupations before and after a switch, it was verified experimentally that the handover does not create any measurable band excitations. Each cycle is split into four s-shaped ramps $[0.00(1)\pi, 0.50(1)\pi]$, $[0.50(1)\pi, 1.12(1)\pi]$, $[1.12(1)\pi, 1.50(1)\pi]$ and $[1.50(1)\pi, 2.00(1)\pi]$ in or-

der to minimize the probability of non-adiabatic Landau-Zener transitions in the vicinity of the symmetric double-well configurations, at which the band gap is smallest and the atoms tunnel from one site to the other. For $V_{s,x} = 10.0(3)E_{r,s}$ and $V_{l,x} = 20(1)E_{r,l}$, the duration of each phase ramp is 50 ms, while for all other lattice configurations it is scaled accordingly with the minimum band gap.

The motion of the atom cloud in response to the pumping is tracked by taking in-situ images of the density distribution immediately after switching off all confining potentials. From this, the centre-of-mass position of the atoms x_{COM} can be determined. To minimize the influence of slow drifts of the atom cloud's centre, this position is measured differentially by comparing it either to the centre-of-mass position at the end of a reference sequence or the one for pumping in the opposite direction with the images being taken in alternating order. The reference sequence has the same length as the respective pumping sequence and uses identical lattice parameters, but the superlattice phase is kept constant at its initial value $\varphi_x^{(0)}$.

4.2 Experimental Results - Ground-State Band

4.2.1 Quantized Transport and Topological Protection

To study the transport properties of the lowest subband in the tight-binding regime, the pumping is performed by adiabatically increasing φ_x starting from $\varphi_x^{(0)} = 0.50(1)\pi$ with a half-filled Mott insulator uniformly occupying the ground-state band as described in Section 4.1.2. Subsequently, the centre-of-mass position of the atom cloud is determined as a function of $\Delta\varphi_x = \varphi_x - \varphi_x^{(0)}$. The resulting evolution during the first pump cycle is shown in Fig. 4.3 for the lattice configuration $V_{s,x} = 10.0(3)E_{r,s}$ and $V_{l,x} = 20(1)E_{r,l}$. As expected for the strongly peaked Berry curvature in the Rice-Mele model (see Fig. 4.2), the measurement clearly demonstrates the step-like character of the displacement – in contrast to the smooth linear motion of the long lattice along x giving rise to the pumping. This highlights the role of quantum mechanical tunnelling between neighbouring sites as the mechanism underlying the transport in the tight-binding limit. The cloud predominantly moves in the vicinity of the symmetric double-well configurations $\varphi_x = (l + 1/2)\pi$ with $l \in \mathbb{Z}$, where the localized atoms tunnel from the left to the right site in each double well. Additionally, there is a slow movement of the centre-of-mass position in between, where the atoms are well localized on the lower-lying sites. This arises from a slight shift of the position of the lattice sites induced by the long lattice, which manifests in a non-zero value of the Berry curvature throughout the generalized Brillouin zone. This contribution vanishes in the limit $V_{s,x} \gg V_{l,x}$. Note that while this shift would also occur for a classical particle localized on one lattice site, it would reverse in the second half of the pump cycle unless the particle tunnels since the site necessarily has to return to its initial position at $\Delta\varphi_x = 2\pi$. Therefore, there is no classical transport by a topological charge pump in the tight-binding regime (Fig. 4.2a).

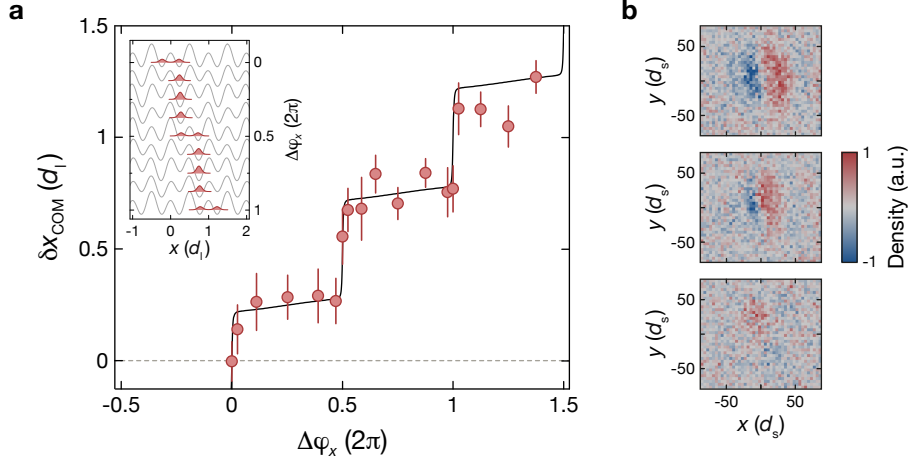


Figure 4.3 – Measurement of the quantized centre-of-mass displacement for ground-state atoms during a single pump cycle. (a) The differential centre-of-mass position of the atom cloud δx_{COM} is shown as a function of the pump parameter $\Delta\varphi_x = \varphi_x - \varphi_x^{(0)}$ starting from $\varphi_x^{(0)} = 0.50(1)\pi$ for $V_{s,x} = 10.0(3)E_{r,s}$ and $V_{l,x} = 20(1)E_{r,l}$. The black line depicts the evolution of the expected centre-of-mass position for a localized ground-state Wannier function, which is also illustrated in the inset. δx_{COM} is obtained by comparing the measured position after pumping by $\Delta\varphi_x$ to a reference sequence of identical length, but constant phase $\varphi_x = \varphi_x^{(0)}$. The points are the average of ten data sets with the error bars indicating the error of the mean. Each data set consists of ten images for each sequence, taken in alternating order and averaged to determine the two centre-of-mass positions, which are then subtracted. For the points with $\Delta\varphi_x \leq 1.3\pi$, a single laser was used for the long x -lattice and the pumping was performed with only two s -shaped ramps of 100 ms duration each, $\varphi_x \in [0.50(1)\pi, 1.50(1)\pi]$ and $\varphi_x \in [1.50(1)\pi, 1.80(1)\pi]$. (b) The panels show examples of the differential atom density for single data sets at $\Delta\varphi_x = 0.00(1)\pi$, $0.50(1)\pi$ and $2.00(1)\pi$ from bottom to top. Note that the extent of the atomic density does not correspond to the cloud size as the imaging is performed after switching off all lattices and trapping potentials and the cloud is thus already expanding. Figure adapted from [163].

The cloud's displacement agrees very well with the one expected for a homogeneously occupied lowest subband (Fig. 4.3a). The latter is determined by the evolution of the corresponding localized Wannier function and with $\nu_1^{\text{gs}} = +1$ predicts a quantized motion by $+d_l$ per pump cycle (see Section 4.1.1). This can be confirmed with a fit of the calculated centre-of-mass position to the data by scaling it with a constant prefactor, which gives an experimental estimate of the pump's Chern number. Taking into account only the first cycle, $0 \leq \Delta\varphi_x \leq 2\pi$, this yields

$$\nu_1^{\text{gs}} = 0.96(5) \quad (4.1)$$

in agreement with the assumption of quantized transport. Here, the error indicates the fit error. When continuing the pumping beyond the first cycle, the measured displacement starts to deviate from the theory curve, indicating a finite pumping efficiency due to experimental imperfections (see Section 4.2.2).

Owing to its topological character, the transport induced by the pumping is extraordinarily robust against changes in the system since the associated topological invariant can only change discontinuously to other integer values if the gap to another band closes at

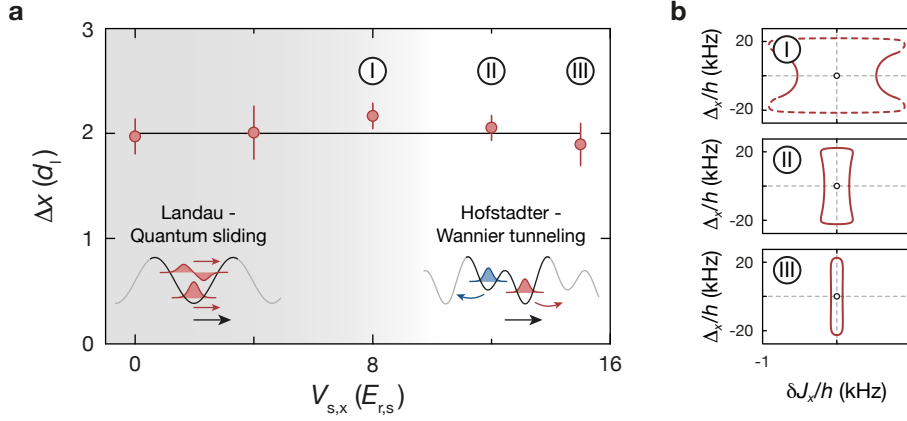


Figure 4.4 – Topological protection of the quantized transport in the lowest band. (a) Differential centre-of-mass displacement $\Delta x = x_{\text{COM}}(\Delta\varphi_x = 2\pi) - x_{\text{COM}}(\Delta\varphi_x = -2\pi)$ after one pump cycle versus short lattice depth $V_{s,x}$ with $V_{l,x} = 25(1)E_{r,l}$. The depth of the short lattice is varied from the quantum sliding lattice at $V_{s,x} = 0$ to the Wannier tunnelling regime for $V_{s,x} > V_{l,x}^2/(4E_{r,s}) \approx 9.8 E_{r,s}$. The deflection of the atom cloud is measured differentially between positive and negative pumping direction with each data point comprising ten data sets of ten averaged images for each direction (see Fig. 4.3). The error bars show the error of the mean. The insets at the bottom illustrate the origin of the particle transport in the Landau limit and Hofstadter regime, namely a continuous translation and tunnelling between Wannier states on neighbouring sites, respectively. (b) Pump cycles in the δJ_x - Δ_x parameter space for the data points in the tight-binding regime indicated in the main plot. At $V_{s,x} = 8E_{r,s}$ (upper panel), the two-band tight-binding approximation is not valid any more for large double-well tilts as the second band approaches the third band. The dashed line illustrates the region, in which the corresponding band gap is smaller than ten times the maximum intra-double-well tunnelling rate $J_x^{\text{DW}}(\varphi_x = \pi/2)$ and the tight-binding parameters are thus not well-defined. Figure adapted from [163].

some point in the cycle as a result of this modification (see Section 2.1.3). In particular for the lowest band studied in this section, this not only implies that all pump paths in the δJ_x - Δ_x parameter space enclosing the band touching point at the origin lead to the same quantized displacement per cycle, but moreover the transport is completely independent of the depth of the short lattice along x , $V_{s,x}$. This special property of the lowest band is preserved even outside of the tight-binding regime, in spite of the fact that the microscopic origin of the transport is quite different in the two limiting cases, the quantum sliding lattice at $V_{s,x} = 0$ and the Wannier tunnelling limit for $V_{s,x} > V_{l,x}^2/(4E_{r,s})$ (see also Section 4.3.2). In the latter, the motion is driven by tunnelling between neighbouring sites as discussed above, whereas in the former it results from a smooth global translation of the potential, which the atoms follow continuously¹ (see insets in Fig. 4.4a). That both configurations exhibit the same quantized transport is a consequence of the fact that the lowest bands in the associated 2D quantum Hall models, the lowest Landau level for $V_{s,x} \rightarrow 0$ and the lowest subband in the Harper-Hofstadter-Hatsugai model for $V_{s,x} \gg V_{l,x}^2/(4E_{r,s})$ (see Section 2.3), are topologically equivalent, i.e. they can be connected by a continuous crossover without closing the gap to the first excited band.

¹In this limit, classical particles would be transported as well, however, the resulting motion is not exactly quantized due to the lack of a quantum mechanical energy gap, which prevents excitations (see Section 2.3.1)

To confirm this, the centre-of-mass displacement is measured as a function of $V_{s,x}$ for $V_{1,x} = 25(1)E_{r,1}$, probing the crossover between the two regimes (Fig. 4.4). The measurement is conducted differentially by comparing two sequences with a full pump cycle in positive ($\Delta\varphi_x > 0$) and negative pumping direction ($\Delta\varphi_x < 0$), respectively, which generate a transport in opposite directions (see Section 4.2.2). Within the experimental uncertainties, all data points are consistent with $\nu_1^{\text{gs}} = +1$.

4.2.2 Efficiency of the Pumping Protocol

The pumping can be continued beyond a single cycle by successively repeating the phase ramps from $\varphi_x = 0 \rightarrow 2\pi$ in combination with the handover between the two lasers used for generating the long x -lattice as described in Section 4.1.2. As shown in Fig. 4.5 for the same parameters as in Fig. 4.3, the centre-of-mass displacement increases continuously with the phase shift $\Delta\varphi_x$. Moreover, the direction of motion can be reversed by changing the pumping direction ($\Delta\varphi_x < 0$). After a few pump cycles, a noticeable discrepancy builds up between the measured position and the one expected for ideal quantized transport as already indicated by the measurement in Fig. 4.3. In the following, we will show that the largest contribution reducing the displacement in the experiment arises from non-adiabatic Landau-Zener transitions to the first excited subband. In the tight-binding regime, atoms in the second subband have a particularly large effect on the transport, since the Chern number of the pump cycle has the opposite sign compared to the lowest band, $\nu_1^{\text{exc}} = -1$. An additional reduction can be attributed to non-adiabatic transitions between neighbouring double wells, which are induced by the external trapping potential present in the experiment (see below).

Band Excitations

The band excitations created during the pumping can be observed by studying the evolution of the population imbalance between odd and even sites in the pumping direction. Using the site-resolved band mapping technique introduced in Section 3.2.1, the total number of atoms on even (N_e^x) and odd sites (N_o^x) can be determined at each point in the pump cycle. From this, one can define the double-well (odd-even) imbalance

$$\mathcal{I}_x = \frac{N_o^x - N_e^x}{N_o^x + N_e^x} \quad (4.2)$$

The directional transport generated by the pumping correspondingly translates into an alternating pattern in \mathcal{I}_x . In the Wannier tunnelling limit, the double-well imbalance exhibits a similar step-like behaviour as the centre-of-mass position, indicating the tunnelling of the atoms between neighbouring sites (Fig. 4.6). If the double-well tilt $|\Delta_x|$ is much larger than intra-well coupling J_x^{DW} , the Wannier function belonging to the lowest subband is fully localized on the lower-lying site ($\mathcal{I}_x = \pm 1$), while the one of the excited subband resides on the other site ($\mathcal{I}_x = \mp 1$). By measuring \mathcal{I}_x , one can thus immediately infer the fraction of atoms in each band, n_{gs}^x and n_{exc}^x . For the measurements in

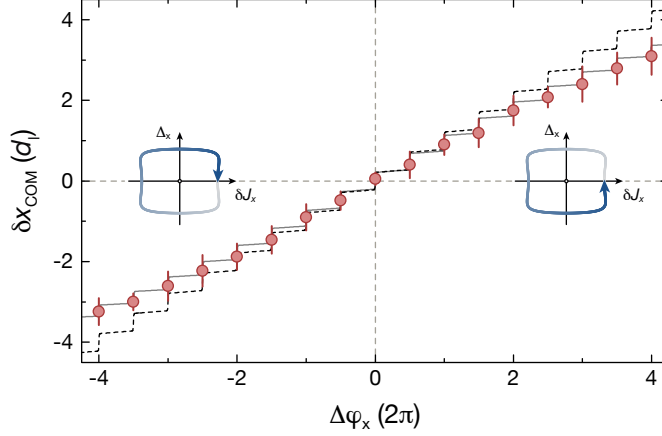


Figure 4.5 – Evolution of the centre-of-mass position in the lowest band over multiple cycles. (a) Differential centre-of-mass position δx_{COM} for multiple pump cycles in positive ($\Delta\varphi_x > 0$) and negative pumping direction ($\Delta\varphi_x < 0$) measured as in Fig. 4.3 with identical lattice parameters. The dashed black line depicts the ideally expected motion for a uniformly populated lowest band. The grey line accounts for a finite pumping efficiency of $\beta_{\text{gs}} = 97.9(2)\%$ per one half of a pump cycle using the model explained in the main text. The value for β_{gs} is obtained from a fit of Eq. (4.7) to the data assuming a perfect state preparation $\beta_0 = 1$. Figure adapted from [163].

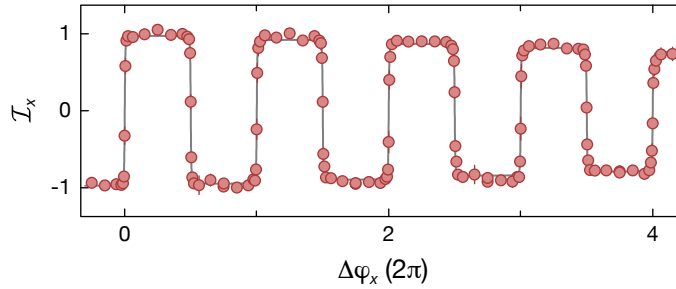


Figure 4.6 – Double-well imbalance during the pumping. Average occupation imbalance \mathcal{I}_x between odd and even sites along x versus $\Delta\varphi_x = \varphi_x - \varphi_x^{(0)}$ with $\varphi_x^{(0)} = 0.50(1)\pi$ using the same lattice configuration as in Fig. 4.3 and 4.5. The data points are averaged over five independent measurements and the error bars show the resulting standard deviation. The solid grey line depicts a fit to the data according to Eq. (4.5) using the double-well imbalances calculated from the ground and excited state Wannier functions. This gives $\beta_{\text{gs}} = 98.7(1)\%$ for $\beta_0 = 1$. Figure adapted from [163].

Fig. 4.3 and Fig. 4.5 with $V_{s,x} = 10.0(3)E_{r,s}$ and $V_{l,x} = 20(1)E_{r,s}$, this condition is very well fulfilled close to the staggered superlattice configurations, in which $\Delta_x^{\text{max}} = 17.6$ kHz and $J_x^{\text{DW}} = 0.2$ kHz. With increasing number of pump cycles, the step height at the symmetric double-well configurations does indeed decrease from its initial value close to two, signalling a growing number of atoms in the excited subband.

To quantify this, the double-well imbalance data in Fig. 4.6 is fitted with a simple two-band model. The underlying assumption of this model is that the band excitations are predominantly created when crossing the symmetric double-well configurations at

$\varphi_x = (l + 1/2)\pi$, $l \in \mathbb{Z}$. The reason for this is that these points correspond to an avoided crossing in the double-well energy spectrum, where the band gap is minimal and the atoms are transferred between the two sites. Accordingly, the pumping efficiency β_j , $j \in \{\text{gs}, \text{exc}\}$, is defined as the fraction of atoms that remain in the respective band when ramping over a symmetric double-well configuration and thus move by one lattice site like the corresponding Wannier function. The remaining fraction $1 - \beta_j$, on the other hand, stays on the initial lattice site and is thereby transferred to the other band during this process. Note that the symmetric double-well configuration occurs twice per pump cycle. After the i -th crossing of a symmetric double-well configuration, the band occupation fractions can thus be expressed as

$$\mathbf{n}(i) = \boldsymbol{\beta}^i \cdot \mathbf{n}(0) \quad (4.3)$$

with

$$\mathbf{n}(i) = \begin{pmatrix} n_{\text{gs}}^x(i) \\ n_{\text{exc}}^x(i) \end{pmatrix} \quad \text{and} \quad \boldsymbol{\beta} = \begin{pmatrix} \beta_{\text{gs}} & 1 - \beta_{\text{exc}} \\ 1 - \beta_{\text{gs}} & \beta_{\text{exc}} \end{pmatrix}$$

For ideal Landau-Zener transitions, the two pumping efficiencies should be identical. In the experiment, however, atoms in the excited band exhibit a finite lifetime before decaying into the lowest band and thus β_{exc} is typically larger than β_{gs} . The initial state can be written as $\mathbf{n}(0) = (\beta_0, 1 - \beta_0)$ with β_0 denoting the fraction of atoms initially in the lowest band. It is determined by the loading procedure and preparation fidelity.

Here, we will focus on the measurements for the lowest band, where $1 - \beta_0 \ll 1$, but the derivation can easily be extended to the preparation of the atoms in the excited band discussed in Section 4.3, for which $\beta_0 \ll 1$. If the pumping efficiencies are very high, $1 - \beta_j \ll 1$, such that the population in the excited band remains small throughout the sequence, Eq. (4.3) can be expanded in orders of $(1 - \beta_j)$. To first order, this yields

$$\mathbf{n}(i) = \begin{pmatrix} \beta_0 \beta_{\text{gs}}^i \\ 1 - \beta_0 \beta_{\text{gs}}^i \end{pmatrix} \quad (4.4)$$

If the evolution of the average double-well imbalance for the two bands can be calculated as in the experimental superlattice configuration, a fit function can be constructed for the measured imbalance:

$$\mathcal{I}_x(\Delta\varphi_x) = \beta_0 \beta_{\text{gs}}^i \mathcal{I}_x^{\text{gs}}(\varphi_x) + (1 - \beta_0 \beta_{\text{gs}}^i) \mathcal{I}_x^{\text{exc}}(\varphi_x) \quad (4.5)$$

with $i = \lceil |\Delta\varphi_x|/\pi \rceil$ for a pumping sequence that starts in the symmetric double-well configuration² as in the experiments presented here with $\varphi_x^{(0)} = \pi/2$. Should $\mathcal{I}_x^{\text{gs}}$ and $\mathcal{I}_x^{\text{exc}}$

²This implicitly assumes that the number of band excitations that are created when starting the phase ramp at $\varphi_x^{(0)}$ is the same as for a complete crossing of a symmetric double-well configuration. While this is probably a slight overestimation, its effect is negligible when considering multiple pump cycles, in particular when assuming $\beta_0 = 1$ as in the following, which neglects the (very small) number of excitations created during the state preparation.

not be known, one can still obtain information about band excitations if the system can adiabatically be brought to a state, for which it is known that particles in different bands localize on different sites as discussed above (see also Section 6.3.2).

In the experiment, the number of band excitations in the initial state is negligible compared to the ones created during the pumping, $\beta_0 \approx 1$ (see below). Eq. (4.5) can then be reduced to an expression with a single fit parameter β_{gs} . By fitting this to the measured imbalance, the pumping efficiency β_{gs} can be determined, which quantifies the adiabaticity of the pumping scheme. For the data presented in Fig. 4.6, this results in

$$\beta_{\text{gs}} = 98.7(1)\% \quad (4.6)$$

with the error giving the uncertainty of the fit. The experimental efficiency is reduced not only by non-adiabatic transitions generated through the pumping itself, but also due to technical heating caused by phase and intensity fluctuations of the superlattice potential. This imposes a limit for β_{gs} , which could otherwise be increased to unity by decreasing the pumping speed.

This approach can also be used to model the centre-of-mass motion by weighting the expected displacement for each band with the respective occupation fraction. The displacement between the i -th and $(i + 1)$ -th symmetric double-well configuration, where the band occupations are assumed to remain constant, is given by $\pm \mathbf{n}(i) \cdot \boldsymbol{\nu}_1 d_s$ with $\boldsymbol{\nu}_1 = (\nu_1^{\text{gs}}, \nu_1^{\text{exc}})$ and the sign depending on the pumping direction. The centre-of-mass position at $\varphi_x = (l + 1/2)\pi$, $l \in \mathbb{Z}$ can thus be expressed as

$$\delta x_{\text{COM}}(\Delta\varphi_x) = \text{sgn}(\Delta\varphi_x) \sum_{i=1}^{|\Delta\varphi_x|/\pi} (2\beta_0\beta^i - 1) d_s \quad (4.7)$$

assuming that the pumping starts from a symmetric double-well configuration as in the experiment, i.e. $\Delta\varphi_x/\pi \in \mathbb{Z}$. When performing a fit to the experimentally determined centre-of-mass position shown in Fig. 4.5 with $\beta_0 = 1$, one obtains a pumping efficiency of

$$\beta_{\text{gs}} = 97.9(2)\% \quad (4.8)$$

where the error indicates the fit error as above. This value is smaller than the one from the imbalance measurement in Eq. (4.6) of $\beta_{\text{gs}} = 98.7(1)\%$, suggesting that there are other processes in addition to band excitations that reduce the centre-of-mass drift. Possible mechanisms for this are discussed in the following paragraphs.

Trapping Potential

A potential source reducing the centre-of-mass pumping efficiency is the presence of a weak harmonic confining potential, the dominant contributions to which arise from the crossed dipole trap and the red-detuned vertical lattice. For the parameters used in the experiment, the trapping frequency in the pumping direction is $\omega_x = 2\pi \times 83(2)$ Hz. Locally, this can be approximated as a small position-dependent gradient $\delta_x x/d_s$.

On the scale of a single double well, the gradient predominantly modifies the energy offset Δ_x . Only for very strong gradients, the tunnel coupling is also affected significantly. As discussed in Section 4.1.1, the particle transport is robust against such local perturbations of the on-site potential as long as the pump path still encircles the gap closing point of the Rice-Mele model, i.e. $\delta_x < \Delta_x^{\max}$. With $\Delta_x^{\max} = 17.6$ kHz for $V_{s,x} = 10E_{r,s}$ and $V_{l,x} = 20E_{r,s}$, this condition is very well fulfilled even at the edges of the cloud, which extends over about 20 lattice sites along x . While the modification of the intra-double-well tunnelling rate slightly reduces the minimum band gap in the symmetric double-well configuration, the corresponding increase in the rate for non-adiabatic transitions is completely negligible for the experimental lattice parameters.

When considering an extended system, the trapping potential can additionally induce non-adiabatic transitions between neighbouring double wells during the pumping. The external gradient leads to an energy offset between the double wells, which partially compensates the effective interaction energy U_{DW} for placing a second particle in an occupied double well. In Fig. 4.7, this is illustrated for a system consisting of two adjacent double wells. Like the single-particle band gap, the energy gap preventing doubly-occupied double wells in the half-filled Mott insulator is smallest in the symmetric double-well configuration. In this case, U_{DW} is given by Eq. (3.5), which is about $h \times 371$ Hz for the aforementioned lattice depths. In the presence of a gradient δ_x , the gap decreases approximately as $U_{\text{DW}} - 2\delta_x$ for small δ_x . This facilitates non-adiabatic inter-double-well transitions, for which the centre-of-mass displacement is zero when pumping against the gradient as shown in Fig. 4.7. Subsequently, the created doublon can potentially delocalize over the cloud, leading to a sizeable reduction of the centre-of-mass displacement.

To estimate the influence of these processes, the time evolution during a ramp over the symmetric double-well configuration can be calculated numerically in this model system. The inter-double-well transition rate is substantially smaller than the observed band excitation rate for $\delta_x < h \times 100$ Hz and only becomes comparable for $\delta_x \sim h \times 125$ -150 Hz. For the trapping frequency observed in the experiment, the gradient at the edge of the cloud in the initial state is about $\delta_x = h \times 88$ Hz when assuming a radius of $10d_s$ in the pumping direction. This increases to $h \times 150$ Hz approximately 17 sites away from the centre. It is thus expected that trap-induced transitions start to play a role after multiple pump cycles. However, given that the atom number close to the outer edge is rather small compared to the bulk, the effect on the pumping efficiency is estimated to be below 1%, despite the large centre-of-mass shift caused by the delocalization of a doublon. Nevertheless, this constitutes a possible origin for the observed discrepancy between the centre-of-mass pumping efficiency and the band excitation rate.

The fact that the pumping is performed in a finite trapped system raises two other issues: the role of edge effects as well as whether the relation between the centre-of-mass displacement of the confined atom cloud and the first Chern number as the topological invariant classifying an infinite bulk system remains valid. Topological edge states as they are expected for a system with open boundaries (see Section 2.2.1) are not present for a harmonic confinement. The rather smooth potential renders a clear distinction from

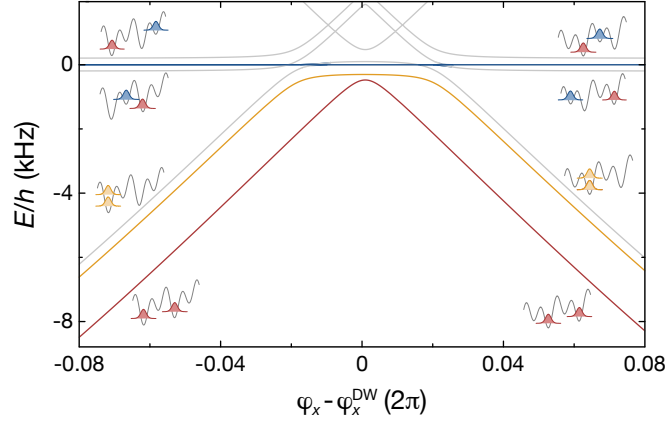


Figure 4.7 – Trap-induced inter-double-well transitions. Energy spectrum for two particles on two neighbouring double wells as a function of the superlattice phase in the presence of an external gradient $\delta_{x,x}/d_s$. The spectrum is calculated numerically for $V_{s,x} = 10E_{r,s}$, $V_{l,x} = 20E_{r,l}$ and $\delta_x = h \times 100$ Hz in the vicinity of the symmetric double-well configuration at $\varphi_x^{\text{DW}} = (l + 1/2)\pi$, $l \in \mathbb{Z}$. The two-particle ground (first excited) state is coloured in red (orange). The blue lines depict the states with single-particle band excitations, but no double occupancy as illustrated by the little schematics. All other states are shown as grey lines. The gradient creates an energy offset between the double wells, which reduces the energy gap between the ground and first excited state. While this effect is negligible away from φ_x^{DW} , where the gap is mostly determined by the large on-site interaction U , it facilitates pumping-induced transitions close to φ_x^{DW} , at which point the effective double-well interaction energy U_{DW} is substantially smaller. If such a transition occurs, the particle that is initially localized in the ground state of the right double well for $\varphi_x < \varphi_x^{\text{DW}}$ tunnels to the double well on the left. This creates a doublon and no centre-of-mass transport takes place. Figure adapted from [163].

the bulk states impossible, for which a much sharper boundary would be required [93]. Furthermore, the system size in the Mott-insulating regime is not determined by the kinetic energy scale, but by the chemical potential and the effective double-well interaction energy, which leads to the localization of particles on separate double wells. Nonetheless, if global adiabaticity is preserved, no centre-of-mass transport should occur in a finite system during a full pump cycle because the initial and final Hamiltonian are identical and the same applies to their ground states [122] (see Section 2.2.1). Yet, the time scale required for the equilibration between the system's edges increases drastically with the system size and by far exceeds the duration of the experiment, in particular given that the state remains insulating throughout the pumping [122].

As for the fundamental relation between the Chern number and the centre-of-mass displacement, the derivation implicitly assumes an infinite system or periodic boundary conditions such that the eigenstates have well-defined momenta. However, it can be shown that boundary effects are exponentially suppressed with the energy gap in finite insulating systems [223]. Therefore, the Chern number can be regarded as a property that is local on a length scale determined by a correlation length $l_c \propto 1/E_{\text{gap}}^2$ with only exponentially small corrections arising from other parts of the system. Intuitively, this can be understood from the fact that the Wannier function on a single unit cell already contains information

about the entire band and is itself exponentially localized in space [157, 209]. This was confirmed by numerical simulations of the centre-of-mass drift for a topological charge pump in the presence of a harmonic trapping potential using realistic parameters for a cold atom implementation [151].

Finite Temperature

Additionally, the pumping efficiency can be reduced by excitations in the fractional Mott insulator prepared at the beginning of the sequence, which are caused by the finite temperature of the initial state. The most important effect of a finite entropy is the creation of holes in the uniform density distribution of localized particles. But unless the fraction of holes becomes large enough that the remaining atoms start to delocalize, the quantized centre-of-mass motion should not be affected since holes do not contribute to the centre-of-mass. It was confirmed experimentally that the initial state exhibits a uniform occupation in momentum space as expected.

The low-energy excitations of the half-filled Mott insulator in the superlattice are band excitations as well as the appearance of doubly-occupied double wells. If two atoms are localized on the same double well, the repulsive interaction between them will modify the transport properties as it hinders the localization on the lower-lying site that the pumping relies on. However, since the maximum double-well tilt Δ_x^{\max} exceeds the on-site interaction energy by far, the two-particle ground state on a double well exhibits the same quantized displacement after a full cycle as a single localized atom. In equilibrium, the doublons are expected to be delocalized over the cloud with the additional atoms forming a superfluid on top of the Mott-insulating background. Their motion should thus be determined by the geometric properties of the corresponding momentum eigenstate, resulting in a non-quantized displacement. But the variation of the Berry curvature averaged over one pump cycle is rather small throughout the Brillouin zone for the lattice depths used in the experiment (Fig. 4.2b). Furthermore, the generation of doublons during the preparation of the initial state is strongly suppressed by the large energy gap of the unit-filled Mott insulator in the long lattice with $U = h \times 1.45$ kHz at $V_{1,x} = 30E_{r,1}$ (see Section 4.1.2). Even though this gap decreases to the effective double-well interaction energy U_{DW} for the half-filled Mott insulator in the superlattice, the doublon fraction in the initial state is estimated to be only on the order of 1%. Therefore, a sizeable effect on the pumping efficiency is not expected.

Similar arguments apply to the band excitations since the lowest band is initially separated from the first excited band by a huge gap of $h \times 9.5$ kHz in the long lattice with $V_{1,x} = 30E_{r,1}$. This is substantially larger than all other relevant energy scales. The subsequent splitting of each site into the final superlattice configuration, during which the band gap decreases to about $h \times 474$ Hz for the symmetric double wells at $V_{s,x} = 10E_{r,s}$ and $V_{1,x} = 20E_{r,s}$, is almost perfectly adiabatic. This can be verified experimentally by determining the band occupations after a quarter pump cycle from the double-well imbalance measurement of Fig. 4.6. Including all data with $0.1\pi < |\Delta\varphi_x| \leq 0.5\pi$, where the

two bands are fully localized on different sites, the fraction of atoms in the second band is $n_{\text{exc}}^x = 0.011(6)$. These excitations can be attributed almost exclusively to the pumping efficiency of 98.7(1)%. The initial fraction of band excitations is thus irrelevant in relation to the excitations created during the pumping and does not have a significant effect on the particle transport.

4.3 Experimental Results - First Excited Band

4.3.1 Reversed Transport

The excited subband in the Rice-Mele model is predicted to exhibit remarkable transport properties as the corresponding pump cycle is characterized by a negative Chern number $\nu_1^{\text{exc}} = -1$ in the Wannier tunnelling regime. As a result of the pumping, particles prepared in this band are thus expected to move in the direction opposite to the sliding long lattice. This unambiguously demonstrates the quantum mechanical character of a topological charge pump as there is no analogue for this in classical systems – in contrast to the unidirectional transport of the ground-state band, which, even though not quantized, could occur in the sliding long lattice and even the Wannier tunnelling limit in the form of a fluctuation-driven Brownian motor [191].

While the preparation of particles in an excited band is typically a non-trivial task, the flexibility offered by the dynamically controlled superlattice allows for the implementation of an efficient loading scheme for such a state. To this end, a unit-filled Mott insulator is prepared in the long lattice as for the loading into the lowest band (see Section 4.1.2). For the subsequent splitting procedure, the superlattice phase is initially set to $\varphi_x = 0.61(1)\pi$ before ramping up the short lattice along x to $30E_{\text{T,S}}$. In this configuration, the particles localize on the lower-lying site corresponding to the lowest band. Then a non-adiabatic phase ramp to a configuration with opposite tilt at $\varphi_x = 0.42(1)\pi$ is performed, during which the atoms remain on their initial site as tunnelling is fully suppressed by the deep short lattice. Thereby, they are transferred to the first excited subband. Afterwards, the lattice depths are lowered to their final values within 2 ms and the superlattice phase is shifted adiabatically to its starting value for the pumping sequence $\varphi_x^{(0)} = 0.50(1)\pi$ during 10 ms. In this way, a half-filled Mott insulator is prepared in the excited state with almost no occupation of the ground-state band.

The pumping is conducted in the same way as for the lowest band (see Section 4.1.2). The resulting evolution of the measured centre-of-mass position and double-well imbalance can be found in Fig. 4.8, using identical lattice parameters as in the corresponding measurements for the lowest band in Fig. 4.5 and Fig. 4.6. Indeed, the behaviour is exactly reversed to the one of atoms in the ground state: when the long lattice is shifted in the positive x -direction, the cloud starts moving in the opposite direction (Fig. 4.8a). In the same way, the double-well imbalance is precisely mirrored compared to the lowest band since atoms in the excited state on a double well localize on the higher-lying site when

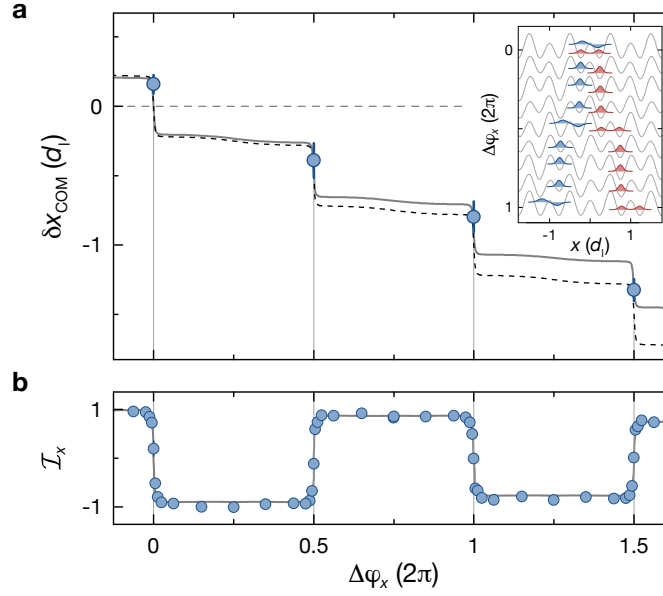


Figure 4.8 – Pumping in the first excited subband. (a) Differential centre-of-mass displacement as a function of $\Delta\varphi_x$ for a half-filled Mott insulator prepared in the first excited subband with $V_{s,x} = 10.0(3)E_{r,s}$ and $V_{l,x} = 20(1)E_{r,l}$. The black dashed line shows the expected evolution for a uniformly populated band and the solid grey line is a fit as in Eq. (4.7) with a pumping efficiency $\beta_{\text{exc}} = 97(2)\%$ for $\beta_0 = 0$. The data is obtained as described in Fig. 4.3. Each point is the average of ten data sets and the error bars show the error of the mean. In the inset, the motion of the Wannier functions initially localized at $x = 0$ is illustrated for the lowest (red) and first excited subband (blue), which have opposite Chern numbers. (b) Corresponding evolution of the odd-even imbalance along x versus $\Delta\varphi_x$. The data is averaged over 3-6 repetitions for each point and the error bar indicates the respective standard deviation. A fit to the data analogous to Eq. (4.5) using the ideally expected double-well imbalance for the Wannier functions of the first and second band yields a pumping efficiency $\beta_{\text{exc}} = 96.7(3)\%$ with β_0 fixed to 0 (grey line). Figure adapted from [163].

the double well is tilted to one side (Fig. 4.8b). The pumping efficiency obtained from the double-well imbalance data by a fit analogous to Eq. (4.5) assuming $\beta_0 = 0$ is considerably smaller than for the pumping in the lowest band, namely $\beta_{\text{exc}} = 96.7(3)\%$ as opposed to $\beta_{\text{gs}} = 98.7(1)\%$ (c.f. Section 4.2.2). The reason for this is the finite lifetime of the atoms in the excited subband. Even without pumping, the atoms tend to relax to the lowest band at a faster rate than the reversed heating process observed for ground-state atoms. This mechanism appears to be the dominating factor limiting the transport of particles in the excited subband. The pumping efficiency obtained by fitting the centre-of-mass drift yields a similar result with $\beta_{\text{exc}} = 97(2)\%$. The comparatively large error for this value results from the small number of data points in Fig. 4.8a.

4.3.2 Topological Transition

As demonstrated in Section 4.2.1, the pump cycles of the quantum sliding lattice at $V_{s,x} = 0$ and in the Wannier tunnelling regime for $V_{s,x} > V_{l,x}^2/(4E_{r,s})$ are topologically equivalent for the lowest band. This does not apply to the higher bands as can be seen

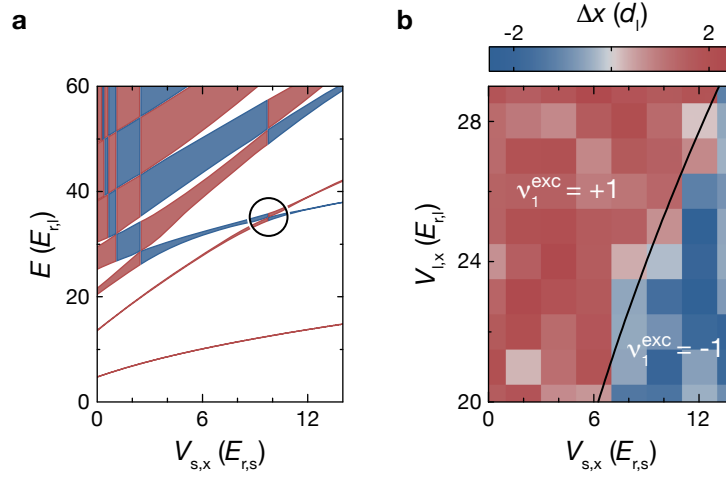


Figure 4.9 – Topological transition between the Landau limit and the Hofstadter regime. (a) Superlattice band structure in the staggered configuration $\varphi_x = 0$ and distribution of the Chern numbers as a function of $V_{s,x}$ for $V_{l,x} = 25E_{r,l}$. The energy spectrum is calculated by numerically diagonalizing the single-particle superlattice Hamiltonian in momentum representation $\hat{H}_{SL}(k_x, \varphi_x)$. The shaded regions correspond to the band widths of the subbands and are coloured according to the Chern number of the associated pump cycle with red denoting $\nu_1 = +1$ and blue $\nu_1 = -1$. The topological transition in the second subband that is investigated in (b) is marked by the black circle. (b) Transition between the Landau limit and the Hofstadter regime in the first excited band. The differential deflection between positive and negative pumping direction after one pump cycle, $\Delta x = x_{\text{COM}}(\Delta\varphi_x = 2\pi) - x_{\text{COM}}(\Delta\varphi_x = -2\pi)$, is measured as a function of $V_{s,x}$ and $V_{l,x}$ for a homogeneously occupied second band. The topological transition at $V_{s,x} = V_{l,x}^2 / (4E_{r,s})$, where the second and third subband touch during the cycle, is drawn as a solid black line. At this point, the Chern number of the second band changes from $\nu_1^{\text{exc}} = +1$ for $V_{s,x} < V_{l,x}^2 / (4E_{r,s})$ to $\nu_1^{\text{exc}} = -1$ for $V_{s,x} > V_{l,x}^2 / (4E_{r,s})$. Every square is a single data set consisting of 10-12 pairs of images for the two directions. Figure adapted from [163].

immediately from the distribution of Chern numbers over the bands in these two limiting cases (Fig. 4.9a). At $V_{s,x} = 0$, where the pump cycle maps onto the Landau levels in a homogeneous 2D quantum Hall system (see Section 2.3.1), all Chern numbers are equal to +1. In the opposite limit $V_{s,x} \gg V_{l,x}^2 / (4E_{r,s})$, the Chern numbers of the pump cycle alternate between the bands, being +1 for bands with odd band index n and -1 for n even. This result can correspondingly be inferred from the respective Harper-Hofstadter-Hatsugai model by extending the dimensional extension technique introduced in Section 2.3.2 to higher bands. Therefore, when connecting these two regimes by changing the depth of the short lattice along x , an infinite series of topological transitions has to take place. At these points, the gap between two bands vanishes during the pump cycle in the staggered superlattice configurations at $\varphi_x = l\pi$, $l \in \mathbb{Z}$. When $V_{s,x}$ is changed through such a transition, the bands involved exchange their Chern numbers. In this way, as $V_{s,x}$ is decreased starting from the Hofstadter limit, the negative Chern numbers sequentially move upwards in the band structure and the Chern numbers of the lower-lying bands become positive – similar to the topological transitions that occur in a 2D quantum Hall lattice model when the periodic potential is removed.

For the first excited band, in particular, a single transition takes place, where it touches the third band and its Chern number changes from $\nu_1^{\text{exc}} = -1$ in the Hofstadter limit to $\nu_1^{\text{exc}} = +1$ in the Landau regime. The microscopic origin of this transition can be understood on the double-well scale as a degeneracy, which occurs in the staggered configuration between the first excited Wannier function localized on the lower-lying site (belonging to the third band for large $V_{s,x}$) and the lowest Wannier function on the upper site (second band). If the depth of the short lattice is large, the Wannier functions on a single lattice site approximately correspond to harmonic oscillator states with an energy $E_n = (n + 1/2)\hbar\omega$, which is determined by the on-site trapping frequency

$$\omega = \sqrt{\frac{2\pi^2 V_{s,x}}{m_a d_s^2}} = \frac{2}{\hbar} \sqrt{V_{s,x} E_{r,s}} \quad (4.9)$$

In the same limit, the maximum double-well tilt is equal to the depth of the long lattice, $\Delta_x^{\text{max}} = V_{l,x}$. The two states thus become degenerate for

$$V_{l,x} = 2\sqrt{V_{s,x} E_{r,s}} \quad (4.10)$$

at which point the two-band tight-binding model breaks down completely. This defines the transition to the Wannier tunnelling limit $V_{s,x} > V_{l,x}^2/(4E_{r,s})$, in which the Chern number distribution is identical to the Harper-Hofstadter-Hatsugai model. This argument can be extended to other ratios of lattice constants. Whenever the long lattice constant is an integer multiple of $2d_s$, the transition point into the Wannier tunnelling limit for the lowest manifold of subbands is the same as in Eq. (4.10). Otherwise, it provides an upper bound for the lattice depth $V_{s,x}$, at which the transition takes place.

This transition is studied in the experiment by measuring the centre-of-mass displacement versus the two superlattice depths, $V_{s,x}$ and $V_{l,x}$, for a half-filled Mott insulator prepared in the first excited band (Fig. 4.9b). The results confirm the expected behaviour. The atoms move in the opposite direction as the long lattice for $V_{s,x} > V_{l,x}^2/(4E_{r,s})$, consistent with a Chern number of $\nu_1^{\text{exc}} = -1$. For $V_{s,x} < V_{l,x}^2/(4E_{r,s})$, on the other hand, the transport is suddenly reversed and the excited state atoms are pumped in the direction of the moving lattice in the same way as in the lowest band, corresponding to $\nu_1^{\text{exc}} = +1$.

Topological Charge Pumping in 2D

As demonstrated by the example of the 1D Thouless pump, topological charge pumps generate quantized currents in response to a periodic and adiabatic modulation, which have similar topological properties as the Hall response of a higher-dimensional quantum Hall system. This allows for the realization of dynamical analogues of topological phases in dimensions exceeding the three spatial dimensions of our universe. Dimensionality is of great importance for topological states of matter [38, 62–64] and only in recent years have topologically non-trivial phenomena been observed that go beyond the 2D geometry of the quantum Hall effect. This includes many intriguing examples like the Zak phase of the Su-Schrieffer-Heeger model [93] and Majorana bound states [224] in 1D as well as Weyl semimetals [69, 70] and strong topological insulators [61] in 3D. In seminal works [47, 48], it was shown that a generalization of the integer and fractional quantum Hall effect exists in four-dimensional systems. These systems have a number of remarkable properties, for example the appearance of a novel quantized non-linear Hall response and the fact that – in contrast to its 2D equivalent – the 4D quantum Hall effect can occur in both time-reversal invariant and time-reversal broken systems. While all of this might be regarded as a mathematical curiosity, 4D quantum Hall physics is related to a variety of phenomena in 2D and 3D systems, namely lower-dimensional topological insulators [38, 53] and Weyl semimetals [225], but also seemingly far-fetched topics like the generation of cosmic magnetic fields [47, 226] and even quantum gravity [48, 227, 228]. Extending the concept of topological charge pumping to 2D systems enables the implementation of a dynamical version of the integer quantum Hall effect in 4D [71]. Its key feature is a non-linear pumping response in the bulk, which is equivalent to the non-linear Hall response of 4D quantum Hall systems and thus inherits the corresponding topological properties and intrinsic 4D symmetries.

In this chapter, the generalization of the quantum Hall effect to 4D systems is introduced at first (Section 5.1), starting with a general overview (Section 5.1.1) and a discussion on the importance of 4D quantum Hall physics for real-world physical systems (Section 5.1.2). Subsequently, the different types of non-linear Hall responses that occur in a 4D quantum Hall system, i.e. Lorentz- and density-type responses, are derived in detail (Section 5.1.3) and a minimal tight-binding implementation, the 4D Harper-Hofstadter model, is presented (Section 5.1.4). In Section 5.2, we discuss how a dynamical ana-

logue can be realized with a 2D topological charge pump (Section 5.2.1) and show how the 4D Hall response translates into a quantized non-linear pumping response in the bulk (Section 5.2.2 and 5.2.5), focussing in particular on how the Lorentz- and density-type responses arise (Section 5.2.3 and 5.2.4).

5.1 The 4D Quantum Hall Effect

5.1.1 Generalization of the Quantum Hall Effect to 4D

Whether a given system can host topologically non-trivial phases is determined by two very general properties: the dimensionality and the symmetries of its Hamiltonian [38, 62–64]. Following the discovery of the quantum Hall effect [36, 40], its key ingredients were soon found to be the sample’s two-dimensional geometry as well as the breaking of time-reversal symmetry [13, 37, 229]. This naturally raised the question whether similar effects could also occur in three-dimensional systems. In 1986, the observation of a quantized Hall conductance in a stacked GaAs/(AlGa)As superlattice structure with a 3D dispersion was reported [230]. Based on this, generalizations of the quantum Hall effect to three dimensions were proposed for electrons in periodic lattice potentials [231, 232]. Subsequently, however, with the development of a topological field theory for quantum Hall systems in the low-energy limit [233, 234], it became clear that in general a quantum Hall state does not exist in 3D systems. The main feature of this field theory is the appearance of a topological Chern-Simons term in the effective action, obtained by a mapping of the quantum Hall model to a system of interacting bosons. It can be shown that such a Chern-Simons field theory can be formulated in all even spatial dimensions, whereas the topological term cannot appear in odd dimensions [46]. Therefore, the above-mentioned phenomena, which are sometimes referred to as the 3D quantum Hall effect, constitute weak topological states that can only occur in translationally invariant lattice systems and can be thought of as multiple copies of 2D quantum Hall systems¹ [57, 63]. In particular, their properties are not topologically protected against disorder. Intuitively, the reason why the quantum Hall effect cannot be generalized to 3D can be understood from the fact that the Hall response has to be transverse to the perturbing electric field generating it. Contrary to 2D systems, this direction is not uniquely defined for three spatial directions since there is no natural antisymmetric tensor with rank two in 3D [237].

Four-dimensional systems, on the other hand, could exhibit a quantum Hall effect and corresponding generalizations were proposed independently in very different contexts, namely cosmology [47, 238] and condensed matter physics [48]. These proposals constituted an important step in the study of topological states of matter, as they not only demonstrated the existence of topologically non-trivial phases in higher-dimensional

¹This can nonetheless give rise to interesting effects, e.g. a 3D version of the Hofstadter butterfly in a 3D lattice subject to a tilted magnetic field, which exhibits a Hall response whose orientation changes depending on the filling [235, 236]

systems, but also that they can occur in systems, in which time-reversal symmetry is not broken [48, 53]. Thereby, they nicely illustrated the importance of both dimensionality and symmetries for topological effects. While the Chern-Simons term in 2D breaks time-reversal symmetry, its four-dimensional counterpart is time-reversal invariant [38, 47, 238, 239]. In this sense, the 4D quantum Hall effect is much richer than the 2D one, as it can occur in both time-reversal invariant systems as well as in systems, which explicitly violate time-reversal symmetry. This can be related to very general properties of level crossings [38], which were already studied by von Neumann and Wigner in 1929 [119]. In absence of time-reversal symmetry, such a singularity can already occur in a three-dimensional parameter space (see also Section 2.1.3), whereas at least five parameters are required in a symplectic time-reversal invariant system. In quantum Hall systems, this applies to the degeneracies that generate the non-commutative geometry (i.e. non-trivial Berry curvature) in momentum space, which can be represented as a d -dimensional closed surface in a $(d + 1)$ -dimensional parameter space (see Section 2.1.3).

Similar to the 2D quantum Hall effect, its 4D generalization also manifests in a Hall response to a perturbing external gauge field. Specifically, its hallmark feature is the appearance of a novel type of response – a non-linear Hall current that arises when applying a weak magnetic field in addition to the electric field inducing the well-known linear Hall response in a 2D quantum Hall system [38, 47, 238] (see Section 5.1.3 for a detailed discussion). The non-linear response is quantized as well, but it is characterized by a different topological invariant. This invariant is given by the prefactor of the 4D Chern-Simons term in the effective action [38]. For non-interacting systems, it corresponds to the second Chern number ν_2 , which is a higher-dimensional analogue of the first Chern number defined over the 4D Brillouin zone of the system [15, 240, 241]. Besides quantum Hall physics, the second Chern number also appears in other contexts, e.g. topological contributions to the electric polarization in inhomogeneous crystals [242] and the characterization of Yang monopoles [102, 243]. Furthermore, via the dimensional reduction discussed below, it can also be related to the \mathbb{Z}_2 invariant characterizing 3D topological insulators, which manifests in the topological magneto-electric effect [38, 244, 245].

In addition, 4D quantum Hall systems exhibit higher-dimensional analogues of characteristic phenomena known from its 2D counterpart, e.g. a single-particle ground state with large degeneracy and an energy gap in the bulk, giving rise to incompressible phases at both integer and certain fractional fillings [48]. Due to its topologically non-trivial nature, continuous boundary states appear in these gaps, which have excited considerable interest in very diverse contexts due to their 3D nature (see Section 5.1.2). An explicit wave function for both non-interacting and interacting fermionic systems can be constructed by extending the mapping of a 2D quantum Hall system onto a compact spherical geometry introduced by Haldane [246]. For a time-reversal invariant 4D quantum Hall system, the corresponding model is a 4-sphere surrounding a $SU(2)$ Yang monopole [48, 243]. It can be shown that at fractional fillings of $1/(2l + 1)^3$ for $l \in \mathbb{N}$ excitations with fractional charge $1/(2l + 1)^3$ appear. Additionally, there are topologically protected excitations with fractional statistics, which unlike in 2D are not point-like, but extended objects similar to

those studied in string theory [239, 247]. The above-mentioned mapping also reveals a connection between the geometry of quantum Hall systems and algebraic properties of their boundaries, namely that the hyperedges of both 2D and 4D spaces are isomorphic to mathematical groups, $U(1)$ and $SU(2)$, respectively [237].

5.1.2 Relevance of the 4D Quantum Hall Effect

In particular the fact that time-reversal symmetric topologically non-trivial states can exist in 4D quantum Hall systems attracted a lot of attention. This initiated an intense study of these types of models, leading to the theoretical proposal [49–52] and subsequent experimental realization of 2D topological insulators [54, 55]. In this context, the 4D quantum Hall effect plays an important role as it constitutes the fundamental model from which the 2D topological insulator and its 3D generalization [57–59], which was discovered soon after [60, 61], can be derived [38]. These lower-dimensional models can be obtained from a time-reversal invariant 4D quantum Hall system by dimensional reduction [38, 53], similar to the procedure used for drawing the analogy between a 1D topological charge pump and the 2D quantum Hall effect in Section 2.3. The dimensional reduction is performed by introducing periodic boundary conditions along one direction, which is then integrated out, yielding the lower-dimensional model – analogous to the Kaluza-Klein compactification used in string theory [248, 249]. This relation between topological insulators in 2D and 3D and the 4D quantum Hall effect is of particular importance as it facilitated the development of a topological field theory for time-reversal symmetric topological insulators [38] based on the corresponding theory for 4D quantum Hall systems developed previously [239]. In fact, all \mathbb{Z}_2 topological insulators were shown to belong to groups of three closely related topological states, formed by a d -dimensional \mathbb{Z} -type topological insulator that serves as a parent model for two topological insulators in $d - 1$ and $d - 2$ dimensions, characterized by a \mathbb{Z}_2 invariant [63]. This led to the development of a "periodic table" classifying topological phases by their dimensionality and symmetries [38, 62–64].

In cosmology, the 4D generalization of the quantum Hall effect was first proposed in the context of the chiral anomaly and its role in the generation of cosmic magnetic fields. The origin of such fields, which occur for example in spiral galaxies, remains unknown up to now [47, 226, 238]. A potential mechanism for the creation of magnetic fields in the early universe is a difference between the chemical potential of charged fermions with left- and right-handed chirality, which could give rise to an instability of the electromagnetic fields [250]. Such massless chiral fermions appear as boundary phenomena on the 3D surfaces of a finite fermionic 4D quantum Hall system due to its topologically non-trivial nature in a similar way as the 1D chiral edge states of a 2D quantum Hall sample [47]. A difference in chemical potential can be induced by applying an electric field transverse to the surface. In combination with a perturbing magnetic field, it induces a non-linear Hall response as discussed above. Via Maxwell's equations, this response leads to a back action onto the electromagnetic fields and thereby creates modes with exponentially diverging field strengths [47].

In a very similar context, 4D quantum Hall physics is currently being discussed in the physics of Weyl semimetals. Inspired by particle physics, these three-dimensional materials have been the focus of numerous theoretical studies in condensed matter physics [225, 251] and were discovered recently in photonic crystals [69] and solid state systems [70]. Their characteristic feature is the appearance of Weyl points in the band structure, which are topologically protected band touching points with a defined chirality and a linear dispersion in all three directions. These Weyl nodes also exhibit a chiral anomaly that manifests in a violation of charge conservation in the presence of both electric and magnetic fields. In analogy to the chiral elementary fermions mentioned above, Weyl points can be interpreted as boundary states of a 4D quantum Hall system with broken time-reversal symmetry, i.e. the 3D edge states traversing the energy gap between two bands, which have opposite chirality on opposite sides of the 4D sample [225]. Extending a similar interpretation of the 2D quantum Hall effect [252], the chiral anomaly in this case arises as a result of the 4D non-linear Hall response, which transfers particles between the boundaries and thereby changes the chiral charge. In a 3D Weyl semimetal, the Weyl points always appear in pairs with opposite chirality, which are localized in momentum space but overlap in real space. Contrary to this, the surface states of a 4D quantum Hall system are spatially separated and could thus be addressed individually.

Another, seemingly completely unrelated area that 4D quantum Hall physics has been discussed in very intensively is quantum gravity, i.e. a quantum mechanical framework for general relativity [48, 227, 228, 237]. It has been proposed that general relativity might arise as an emergent phenomenon in the effective low-energy description of a non-relativistic quantum many-body system [253, 254]. In this case, the relativistic elementary particles would correspond to the system's quasiparticle excitations. This would constitute an example for the seminal idea of emergence introduced by P. W. Anderson, namely that the lower-energy degrees of freedom of a many-body system can behave drastically different compared to its microscopic constituents and, in particular, can exhibit symmetries that do not occur in the full Hamiltonian [255]. In a fermionic 4D quantum Hall system with finite size, bosonic collective excitations with a relativistic dispersion and well-defined helicity are predicted to occur at the 3D boundary, which might provide a toy model for an emergent relativistic quantum theory [48, 227].

This approach is inspired by the relativistic edge physics that already occurs in 2D quantum Hall systems, in which bound particle-hole pairs can appear at the boundary, whose motion is governed by a linear dispersion relation [256, 257]. Surprisingly, these excitations are also present in non-interacting systems, where one would naively expect that bound states should not be possible due to the uncertainty principle and dispersion. As a consequence of the non-commutative geometry in the presence of the magnetic field, however, the single-particle wave functions are modified in such a way that particle-hole excitations in the vicinity of the edge become relativistic and thus can form bound states due to their 1D nature even in the absence of interactions. This can easily be seen for example for the lowest Landau level in a cylindrical geometry, as discussed in Section 2.3.1, in the presence of a confining potential $V(x)$ along the axis of the cylinder, which defines

the boundaries $\pm x_e$ of the system. For a given eigenstate in the Landau gauge, the linear momentum $\hbar k_z$ parallel to the boundary is proportional to the position x_m in the transverse direction. A particle-hole pair can be created by exciting a particle from an occupied state at $|x_m| < x_e$ close to the edge to an unoccupied one at $|x_n| > x_e$ just outside of the boundary. In the vicinity of the boundary, $V(x)$ can be linearized. This correspondingly results in a linear dispersion relation for the pair with a velocity along the edge such that the Lorentz force exactly compensates the gradient resulting from the confinement. Therefore, states with different momenta can be combined to form a well-localized bound state. In a 2D geometry, however, these 1D edge states are always chiral and due to the decoupling of the spin degree of freedom do not possess a well-defined helicity.

Time-reversal symmetric quantum Hall systems in 4D display related boundary phenomena, which are even richer due to the interplay of the internal spin degree of freedom and the external $SU(2)$ gauge field [48, 227, 228]. Similar to the 2D case, bound particle-hole pairs are predicted with a linear relation between the momentum parallel to the boundary and the size in the perpendicular direction, giving rise to a relativistic dispersion. Moreover, unlike in 2D, these excitations have a well-defined helicity resulting from a spin-orbit coupling induced by the $SU(2)$ gauge field and it can be shown that they are described by local bosonic operators, whose Heisenberg equations of motion are identical to massless relativistic wave equations [227]. In particular, there are graviton-like collective excitations with a spin and helicity of two, for which the equation of motion is the (linearized) Einstein equation. There are, however, a number of obstacles for obtaining a toy model for the emergence of gravity from this [228]. In addition to the graviton-like states, there also exist particle-hole excitations with different helicities as well as a continuum of unbound states with a non-relativistic spectrum. While it has been proposed that adding suitable interactions might create a gap for these additional modes [48, 227], it is not clear whether the particle-hole pairs remain bound in the presence of interactions [258]. Additionally, the Weinberg-Witten theorem implies that under these conditions the states with helicity two should disappear as well [228, 259]. From an experimental point of view, another problem is the fact that the spin of the system's bare fermionic constituents has to become infinitely large to obtain a flat boundary corresponding to the three-dimensional space [48, 228].

5.1.3 Hall Responses of a 4D Quantum Hall System

The topological properties of a 4D quantum Hall system manifest in quantized transport phenomena in response to a perturbation by an external electromagnetic vector potential \mathbf{A} . As mentioned in Section 5.1.1, the key feature of the 4D quantum Hall effect is the appearance of an additional quantized non-linear Hall response that occurs when a perturbing magnetic field is applied together with the electric perturbation, which induces the 2D linear Hall response. This non-linear response was already noted in the first proposals in cosmology [47, 238] and later discussed for time-reversal invariant 4D quantum Hall systems in a field-theoretical frame work [38]. In the following, the Hall responses

of a 4D quantum Hall system on a lattice are derived from the semiclassical equations of motion based on a more detailed derivation in Refs. [82, 101].

Current Density in a 4D Quantum Hall System

Let us consider a 4D system with periodic potentials along all directions and a non-commutative geometry e.g. due to the presence of strong magnetic fluxes. This system is perturbed by two weak external fields, an electric field $\mathbf{E} = -\partial\mathbf{A}/\partial t$ and a magnetic field $B_{\mu\nu} = \partial_\mu A_\nu - \partial_\nu A_\mu$ with $\mu, \nu \in \{w, x, y, z\}$. Both perturbations are assumed to be static and uniform. The unperturbed system is described by a Hamiltonian \hat{H}_{4D} , whose eigenstates in a given non-degenerate band n are denoted as $|u_n(\mathbf{k})\rangle$. In a semiclassical approximation assuming perfect adiabaticity, the response of the system can be evaluated by solving the semiclassical equations of motion for a wave packet that is centred at a position \mathbf{r} and a quasi-momentum \mathbf{k} [7, 260, 261]. Since the non-linear Hall response is a second-order effect, this requires a more rigorous treatment than the corresponding derivation for the 2D Hall effect. In particular, first-order modifications of the eigenstates due to the perturbing fields have to be taken into account, which lead to an admixture of states from other bands and thereby slightly modify the energy spectrum and Berry curvature [262] (see also Section 2.1.1). For a filled or uniformly populated band, however, the contribution from these corrections to the overall response vanishes [101]. For simplicity, we will therefore neglect these effects in the following. A detailed discussion on this can be found in Ref. [101].

For a particle with charge q , the semiclassical equations of motion are [7, 260, 261]

$$\dot{r}^\mu(\mathbf{k}) = \frac{1}{\hbar} \frac{\partial \mathcal{E}(\mathbf{k})}{\partial k_\mu} + \dot{k}_\nu \Omega^{\nu\mu}(\mathbf{k}) \quad (5.1)$$

$$\hbar \dot{k}_\mu = qE_\mu + q\dot{r}^\nu B_{\mu\nu} \quad (5.2)$$

Here, the band index n is omitted to simplify the notation, $\mathcal{E}(\mathbf{k})$ denotes the energy of the corresponding eigenstate² and the Einstein notation is applied to the spatial indices $\mu, \nu \in \{w, x, y, z\}$. The Berry curvature is defined for each 2D plane in the same way as in a 2D quantum Hall system with $\Omega^{\nu\mu}(\mathbf{k}) = i (\langle \partial_{k_\nu} u | \partial_{k_\mu} u \rangle - \langle \partial_{k_\mu} u | \partial_{k_\nu} u \rangle)$. The velocity in Eq. (5.1) has a similar form as the one in a 1D geometric charge pump derived in Section 2.1.2. It contains contributions from the group velocity, arising from the dispersion of the band $\mathcal{E}(\mathbf{k})$, and from the anomalous velocity. The latter results from the non-trivial intrinsic structure of the eigenstates for $\Omega^{\nu\mu} \neq 0$ and in response to a change of the quasi-momentum. This change is determined by the force acting on the particle as a result of the external fields [Eq. (5.2)]. Compared to the usual semiclassical dynamics in the 2D quantum Hall effect, the magnetic perturbation leads to an additional Lorentz force term for moving particles.

²This notation deviates from the one used in the previous chapters, in which the energy was denoted as $E(\mathbf{k})$, in order to avoid confusion with the electric field E_μ .

The average velocity of the wave packet can be obtained by expressing \dot{k}_ν in Eq. (5.1) by Eq. (5.2) and then iteratively inserting Eq. (5.1) into itself. To second order in the perturbing fields, the velocity is given by

$$\dot{r}^\mu(\mathbf{k}) = \frac{1}{\hbar} \frac{\partial \mathcal{E}}{\partial k_\mu} + \frac{q}{\hbar} E_\nu \Omega^{\nu\mu} + \frac{q^2}{\hbar^2} E_\delta B_{\nu\gamma} \Omega^{\delta\gamma} \Omega^{\nu\mu} + v_{\mathbf{k}}^\mu \quad (5.3)$$

Besides the group velocity in the first term, the external perturbations in combination with the eigenstates' non-commutative nature excite two types of responses. The second term describes the linear Hall response as in a 2D quantum Hall system, i.e. a transverse anomalous velocity induced by the electric field. This motion in turn is accompanied by a Lorentz force generated by the magnetic field. This gives rise to an additional non-linear contribution, which depends on both perturbing fields and scales quadratically with the Berry curvature. The last part $v_{\mathbf{k}}^\mu$ contains additional terms resulting from the magnetic perturbation, including the Lorentz force due to the group velocity, which vanish for a uniformly populated band and are therefore neglected below [101].

The resulting particle current density for the entire band can be calculated from Eq. (5.3) by averaging over all \mathbf{k} :

$$\mathbf{j} = \frac{1}{L^4} \sum_{\mathbf{k}} n_{\mathbf{k}} \dot{\mathbf{r}}(\mathbf{k}) \quad (5.4)$$

assuming a homogeneous occupation of all \mathbf{k} -states $n_{\mathbf{k}} = n_0$ and with L being the size of the system in each direction. The sum in Eq. (5.4) can be expressed as a continuous integral using the density of states in momentum space, $D(\mathbf{k})$. For a system with both non-zero Berry curvature and a magnetic perturbation, $D(\mathbf{k})$ is modified compared to the standard form $D(\mathbf{k}) = L^4/(2\pi)^4$ because the physical and canonical position as well as momentum are not identical any more [263–266]. Including these corrections, the density of states in a 4D system is [101]:

$$D(\mathbf{k}) = \frac{L^4}{(2\pi)^4} \left(1 + \frac{1}{2} \frac{q}{\hbar} B_{\gamma\delta} \Omega^{\delta\gamma} + D_2(\mathbf{k}) \right) \quad (5.5)$$

where the last term $D_2(\mathbf{k})$ is an additional second-order correction, which does not contribute to the Hall response for symmetry reasons.

Combining Eqs. (5.3)–(5.5), the current density can be expressed as

$$\begin{aligned} \mathbf{j} &= \frac{n_0}{L^4} \oint_{\text{BZ}} d^4k D(\mathbf{k}) \dot{\mathbf{r}}(\mathbf{k}) \\ &= \frac{n_0}{(2\pi)^4} \oint_{\text{BZ}} d^4k \left[\frac{q}{\hbar} E_\nu \Omega^{\nu\mu} + \frac{q^2}{\hbar^2} \left(E_\delta B_{\nu\gamma} \Omega^{\delta\gamma} \Omega^{\nu\mu} + \frac{1}{2} E_\nu B_{\gamma\delta} \Omega^{\delta\gamma} \Omega^{\nu\mu} \right) \right] \mathbf{e}_\mu \end{aligned} \quad (5.6)$$

with all other terms, including the group velocity, averaging to zero for a uniformly populated band. Here, \mathbf{e}_μ denotes the unit vector in the μ -direction. The first term in Eq. (5.6) corresponds to the linear Hall response and the second term describes the non-linear Hall response, which contains contributions from the Lorentz force in Eq. (5.3) as well as from

the modified density of states in Eq. (5.5). Depending on the relative orientation of the perturbing fields, this gives rise to different types of non-linear responses, which can in general be classified as Lorentz-type or density-type as discussed below. By using the antisymmetry of the magnetic field and the Berry curvature with respect to an exchange of the spatial indices, Eq. (5.6) can be simplified to

$$\mathbf{j} = \frac{n_0}{(2\pi)^3} \frac{q}{\hbar} E_\nu \oint_{\text{BZ}} d^4k \Omega^{\nu\mu} \mathbf{e}_\mu + \frac{n_0}{2} \frac{q^2}{\hbar^2} \epsilon^{\mu\gamma\delta\nu} E_\nu B_{\gamma\delta} \nu_2 \mathbf{e}_\mu \quad (5.7)$$

with the 4D Levi-Civita symbol $\epsilon^{wxyz} = +1$ and

$$\nu_2 = \frac{1}{4\pi^2} \oint_{\text{BZ}} \Omega^{xw} \Omega^{zy} + \Omega^{xy} \Omega^{wz} + \Omega^{zx} \Omega^{wy} d^4k \quad (5.8)$$

being the second Chern number of the band under consideration.

From Eq. (5.7), one can immediately identify two important properties of the non-linear response: (i) It is a genuinely four-dimensional effect, which cannot occur in systems with less than four dimensions since the two perturbations have to be in orthogonal subspaces and the response in turn is transverse to both of them. Mathematically, this is ensured by the Levi-Civita symbol. (ii) The non-linear response can be related to an integer topological invariant, the second Chern number ν_2 . The latter is a 4D quantity that is obtained by integrating the second Chern form $\Omega \wedge \Omega$ over the 4D Brillouin zone, which corresponds to an integral of all possible permutations of the product of two Berry curvatures in orthogonal 2D subspaces as in Eq. (5.8). Therefore, the non-linear response is quantized in a similar way as the linear response.

Centre-of-Mass Response

Contrary to condensed matter systems as in [36], the current density \mathbf{j} is in general not directly accessible in cold atom experiments [81]. An alternative way to study transport properties is the measurement of centre-of-mass quantities like the average velocity of the atom cloud [267–269]. This can easily be implemented with ultracold atoms [91, 92], but on the other hand is very difficult to obtain in intrinsically open systems as in solid-state experiments.

The centre-of-mass velocity of an atom cloud prepared in a given band is defined as

$$\mathbf{v}_{\text{COM}} = \frac{1}{N} \sum_{\mathbf{k}} n_{\mathbf{k}} \dot{\mathbf{r}}(\mathbf{k}) \quad (5.9)$$

where N is the total number of particles and $n_{\mathbf{k}} = n_0$ for a uniformly populated band. It is thus related to the current density [Eq. (5.4)] via the particle density $n = N/L^4$:

$$\mathbf{v}_{\text{COM}} = \frac{\mathbf{j}}{n} \quad (5.10)$$

In absence of a perturbing magnetic field, the particle density is simply a constant proportionality factor $n = n_0/A_M$, where A_M is the size of the 4D magnetic unit cell. The

Hall response thus manifests in the same way in the current density and centre-of-mass velocity. For $B_{\mu\nu} \neq 0$, however, the particle density depends on the system's geometric properties due to the modified density of states [Eq. (5.5)] with

$$n = \frac{1}{L^4} \sum_{\mathbf{k}} n_{\mathbf{k}} = \frac{n_0}{A_M} + \frac{1}{2} \frac{n_0}{(2\pi)^3} \frac{q}{h} B_{\mu\nu} \oint_{\text{BZ}} d^4k \Omega^{\nu\mu} \quad (5.11)$$

As detailed in the next section, the centre-of-mass response can exhibit a profoundly different behaviour than the current density in this case [82].

Lorentz-Type and Density-Type Responses

As already mentioned above, the non-linear Hall response can be generated by the perturbing fields in two different ways: either through a Lorentz force acting on the particles, which move as a result of the linear Hall response, or through a modification of the density-of-states, which in turn also affects the current density. To further illustrate these two types of responses and how they manifest in different physical observables for probing the transport, we will now consider the simplest possible 4D quantum Hall system that exhibits a non-linear response, i.e. a non-trivial second Chern number. From Eq. (5.8), one can see that for $\nu_2 \neq 0$ the Berry curvatures in at least two orthogonal subspaces have to be non-trivial. This can be achieved by combining two 2D quantum Hall systems in orthogonal subspaces, e.g. one in the xz -plane and one in the yw -plane as illustrated in Fig. 5.1. Such a minimal model has previously been discussed in [71, 101] and an extensive study of the different types of Hall responses in the presence of a magnetic perturbation can be found in [82], on which the following discussion is based.

In a 4D space, the orientation of the magnetic perturbation transverse to a given electric field, e.g. $\mathbf{E} = E_z \mathbf{e}_z$, is not unique. For the geometry introduced above, one can distinguish two different types of configurations, namely a magnetic field in a plane connecting the 2D quantum Hall systems, e.g. $B_{xw} \neq 0$ (Fig. 5.1), or in the same plane as the other 2D system, i.e. $B_{yw} \neq 0$ (Fig. 5.2). As detailed below, the former gives rise to a purely Lorentz-type non-linear response, which is visible in both the current density and the centre-of-mass velocity. The latter, on the other hand, induces only a density-type response, which appears in the current density, but does not affect centre-of-mass quantities. Despite their different origin, both types of non-linear responses are characterized by the same 4D topological invariant, the second Chern number [Eq. (5.7)]. Note that while $B_{\mu\nu}$ has to be in an orthogonal subspace to \mathbf{E} for a non-linear response in the current density, another kind of non-linear Hall response in the centre-of-mass velocity can be observed already in a 2D quantum Hall system for $B_{xz} \neq 0$ [82].

In the configuration with $B_{xw} \neq 0$ depicted in Fig. 5.1, the magnetic perturbation is applied in a plane with trivial Berry curvature, $\Omega^{xw} = 0$. From Eq. (5.5) it follows that the density of states is not altered in this case and therefore the only contribution to the current density arises from the Lorentz force term in Eq. (5.6). Furthermore, the resulting

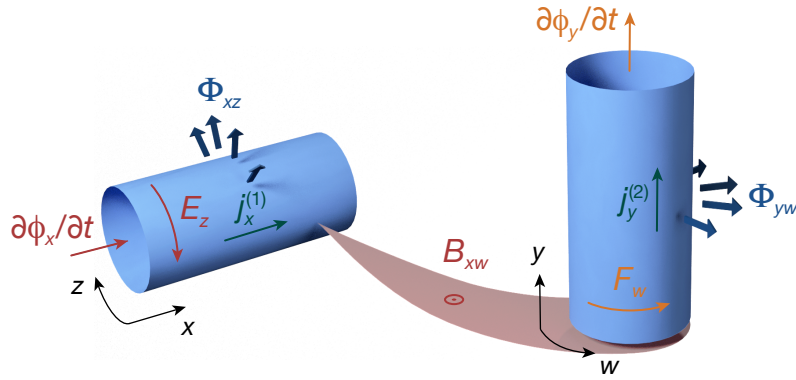


Figure 5.1 – Lorentz-type non-linear Hall response. A minimal model of a non-trivial 4D quantum Hall system can be formed by combining two 2D quantum Hall systems in orthogonal subspaces, e.g. in the xz - and yw -plane. The 2D systems, which are shown here in a cylindrical geometry, are pierced by uniform magnetic fluxes Φ_{xz} and Φ_{yw} , respectively. The threading of a time-dependent magnetic flux $\phi_x(t)$ along the axis of the cylinder containing the xz -plane generates an electric field E_z along the z -direction on the cylinder's surface and thereby induces a linear Hall response in the current density $j_x^{(1)}$ along x [37]. Adding a weak magnetic field in a plane connecting the 2D quantum Hall systems, e.g. B_{xw} , leads to a Lorentz-type non-linear Hall response. The magnetic perturbation creates a Lorentz force, F_w in this case, that acts on the particles moving in the x -direction. This force – which can also be interpreted as a Hall voltage generated by the current $j_x^{(1)}$ in the presence of the magnetic perturbation – corresponds to an *effective* threading of a flux $\phi_y(t)$ along the axis of the second cylinder. Thereby, it couples the motion in the two 2D quantum Hall systems and gives rise to a non-linear Hall response along y with a current density $j_y^{(2)}$. Figure adapted from [150].

current density and centre-of-mass velocity are directly proportional as $n = n_0/A_M$ and we obtain

$$\mathbf{j} = \frac{n_0}{A_M} \mathbf{v}_{\text{COM}} = \frac{n_0}{A_M^{yw}} \frac{q}{h} E_z \nu_1^{zx} \mathbf{e}_x - n_0 \left(\frac{q}{h}\right)^2 E_z B_{xw} \nu_2 \mathbf{e}_y \quad (5.12)$$

Here, A_M^{yw} denotes the size of the magnetic unit cell in the quantum Hall system in the yw -plane. The first term describes the linear Hall response, which in this case points in the x -direction and is quantified by the first Chern number ν_1^{zx} of the corresponding 2D quantum Hall system in the xz -plane. The second term is the non-linear Hall response along y , which is orthogonal to the linear response. In the semiclassical picture, it can be interpreted as being induced by a Lorentz force generated by B_{xw} for the particles moving along x due to the linear Hall response (Fig. 5.1).

For the other type of perturbation, the magnetic field $B_{yw} \neq 0$ is applied in the same subspace as the second 2D quantum Hall system, in which the Berry curvature Ω^{yw} is non-trivial (Fig. 5.2). Therefore, the magnetic perturbation modifies the density of states in Eq. (5.5), which in turn leads to an additional non-linear contribution to the current density. The term originating from the Lorentz force, on the other hand, vanishes in this configuration as the Berry curvature is zero in all 2D subspaces containing the electric field with the exception of the xz -plane, i.e. $\Omega^{z\gamma} = 0 \forall \gamma \neq x$. The current density is thus given by

$$\mathbf{j} = \frac{n_0}{A_M^{yw}} \frac{q}{h} E_z \nu_1^{zx} \mathbf{e}_x + n_0 \left(\frac{q}{h}\right)^2 E_z B_{yw} \nu_2 \mathbf{e}_x \quad (5.13)$$

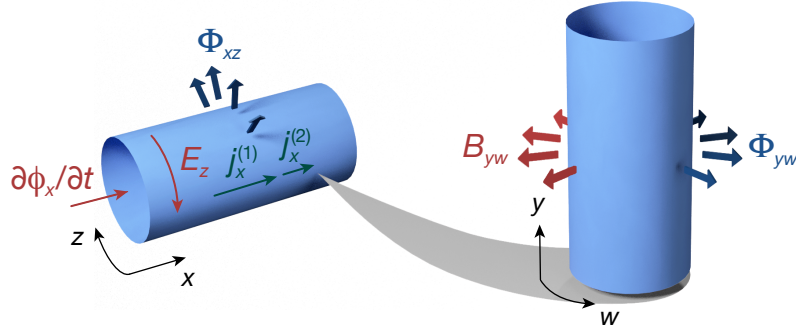


Figure 5.2 – Density-type non-linear Hall response. A density-type non-linear Hall response in the minimal 4D quantum Hall model introduced in Fig. 5.1 is induced by applying a magnetic perturbation through the plane of one of the 2D quantum Hall systems, while the perturbing electric field is in the orthogonal subspace of the other 2D system, e.g. $B_{yw} \neq 0$ and $E_z \neq 0$ as shown here. The magnetic field modifies the density of states in the yw -plane and thereby leads to an additional Hall current $j_x^{(2)}$ in the same direction as the linear response $j_x^{(1)}$. The centre-of-mass motion, however, is not affected by the magnetic perturbation and therefore only exhibits the linear response generated by E_z .

Unlike the Lorentz-type response in Eq. (5.12), this density-type non-linear response is parallel to the linear Hall response as it results from a change in the number of particles that are contained in a given band for a fixed filling factor n_0 and thus contribute to the linear Hall response. This also implies that the magnetic perturbation does not affect the centre-of-mass response of the system. Due to the modified density of states, the particle density in Eq. (5.11) becomes

$$n = \frac{n_0}{A_M} + \frac{n_0}{A_M^{xz}} \frac{q}{h} B_{yw} \nu_1^{wy} \quad (5.14)$$

As the unperturbed 4D system is fully separable into the xz - and yw -planes, its eigenstates can be written as product states of the two 2D quantum Hall systems. In this case, the Berry curvature $\Omega^{\mu\nu}$ only depends on the respective quasi-momenta k_μ and k_ν and the second Chern number corresponds to a product of the two first Chern numbers, $\nu_2 = \nu_1^{zx} \nu_1^{wy}$. With $A_M = A_M^{xz} A_M^{yw}$, we obtain for the centre-of-mass velocity:

$$\mathbf{v}_{\text{COM}} = \frac{q}{h} A_M^{xz} E_z \nu_1^{zx} \mathbf{e}_x \quad (5.15)$$

which is identical to the linear Hall response without any magnetic perturbation.

In addition to the configurations discussed here, where the non-linear response is solely of Lorentz- or density-type, there are also more complex geometries, in which both the Lorentz force and the modified density of states contribute to the current density. This applies in particular to systems with more than two non-trivial Berry curvature components. It is important to note, however, that in all cases the non-linear Hall response is proportional to the second Chern number of the respective band.

5.1.4 The 4D Harper-Hofstadter Model

In the presence of sufficiently deep periodic potentials in all four dimensions, the 4D quantum Hall system introduced in Section 5.1.3 is described by a 4D tight-binding lattice model composed of two Harper-Hofstadter models [145–147] in the xz - and yw -plane [101]. Using the Landau gauge, the Hamiltonian of this system for non-interacting particles can be expressed as

$$\begin{aligned} \hat{H}_{4D} = & - \sum_{\mathbf{m}} \left(J_x \hat{a}_{\mathbf{m}+\mathbf{e}_x}^\dagger \hat{a}_{\mathbf{m}} + J_z e^{i\tilde{\Phi}_{xz}m_x} \hat{a}_{\mathbf{m}+\mathbf{e}_z}^\dagger \hat{a}_{\mathbf{m}} + \text{h.c.} \right) \\ & - \sum_{\mathbf{m}} \left(J_y \hat{a}_{\mathbf{m}+\mathbf{e}_y}^\dagger \hat{a}_{\mathbf{m}} + J_w e^{i\tilde{\Phi}_{yw}m_y} \hat{a}_{\mathbf{m}+\mathbf{e}_w}^\dagger \hat{a}_{\mathbf{m}} + \text{h.c.} \right) \end{aligned} \quad (5.16)$$

where the positions of the sites in the 4D lattice are labelled by $\mathbf{m} = \{m_x, m_y, m_z, m_w\}$. The first line corresponds to the Harper-Hofstadter Hamiltonian \hat{H}_{xz} for a square lattice in the xz -plane that is penetrated by a uniform magnetic flux $\Phi_{xz} = \Phi_0 \tilde{\Phi}_{xz} / (2\pi)$ per unit cell (see Section 2.3.2). Accordingly, the second line describes a Harper-Hofstadter model \hat{H}_{yw} in the yw -plane with a flux of $\Phi_{yw} = \Phi_0 \tilde{\Phi}_{yw} / (2\pi)$.

The eigenstates of \hat{H}_{4D} are products of the eigenstates of \hat{H}_{xz} and \hat{H}_{yw} since the two Harper-Hofstadter models are in orthogonal subspaces and $\hat{H}_{4D} = \hat{H}_{xz} + \hat{H}_{yw}$. In the Landau gauge, the eigenstates of the 2D models are simple Bloch waves in the directions of the complex tunnelling phases, which are labelled by their quasi-momenta k_z and k_w [145]. The 4D eigenstates are thus of the form

$$\psi_{\mathbf{m}}(k_z, k_w) = e^{ik_z z} e^{ik_w w} \psi_{m_x, m_y} \quad (5.17)$$

with $z = d_{s,z} m_z$ and $w = d_{s,w} m_w$, where $d_{s,z}$ and $d_{s,w}$ indicate the lattice periods in the respective direction. Consequently, \hat{H}_{4D} can be rewritten by performing a partial Fourier transform of the creation and annihilation operators,

$$\hat{a}_{\mathbf{m}} = \frac{1}{\sqrt{l_z l_w}} \sum_{k_z, k_w} e^{i(k_z z + k_w w)} \hat{a}_{m_x, m_y}(k_z, k_w) \quad (5.18)$$

with $l_z = L_z / d_{s,z}$ and $l_w = L_w / d_{s,w}$ being the number of lattice sites along z and w , respectively. This dimensional reduction [38, 71] yields a sum over the Fourier components $\hat{H}_{xy}(k_z, k_w)$, each of which corresponds to the Hamiltonian governing the Bloch wave function at a given quasi-momentum $\{k_z, k_w\}$:

$$\hat{H}_{4D} = \sum_{k_z, k_w} \hat{H}_{xy}(k_z, k_w) \quad (5.19)$$

Here, $\hat{H}_{xy}(k_z, k_w)$ is the 2D version of the Harper model [145] introduced in Section 2.3.2:

$$\begin{aligned} \hat{H}_{xy}(k_z, k_w) = & \\ & - \sum_{m_x, m_y} \left[\left(J_x \hat{a}_{m_x+1, m_y}^\dagger \hat{a}_{m_x, m_y} + \text{h.c.} \right) + 2J_z \cos \left(\tilde{\Phi}_{xz} m_x - k_z d_{s,z} \right) \hat{n}_{m_x, m_y} \right] \\ & - \sum_{m_x, m_y} \left[\left(J_y \hat{a}_{m_x, m_y+1}^\dagger \hat{a}_{m_x, m_y} + \text{h.c.} \right) + 2J_w \cos \left(\tilde{\Phi}_{yw} m_y - k_w d_{s,w} \right) \hat{n}_{m_x, m_y} \right] \end{aligned} \quad (5.20)$$

with the occupation number operator $\hat{n}_{m_x, m_y} = \hat{a}_{m_x, m_y}^\dagger \hat{a}_{m_x, m_y}$. For simplicity, the momentum dependence of the creation/annihilation operators [Eq. (5.18)] is neglected here.

The energy spectrum of the 4D Harper-Hofstadter model is given by the Minkowski sum of the eigenenergies of the two 2D models. Due to the fractal structure of the 2D density of states as a function of the respective magnetic flux, this gives rise to a complex band structure. In general, it consists of a large number of different bands, each of which is formed by combining two bands of the 2D systems (Fig. 5.3). Correspondingly, the topological invariants characterizing the transport properties of a given non-degenerate 4D band are determined by the topology of the underlying 2D bands. In particular, its second Chern number is given by the product of the first Chern numbers of the two orthogonal 2D Hofstadter bands, $\nu_2 = \nu_1^{zx} \nu_1^{wy}$, as already discussed in Section 5.1.3.

5.2 Exploring 4D Quantum Hall Physics with a 2D Topological Charge Pump

Despite the great interest in 4D quantum Hall physics from disciplines as diverse as condensed matter physics and cosmology, a 4D quantum Hall system has so far never been realized experimentally in any physical setting. One obvious reason for this is the fact that there are only three spatial dimensions, which precludes a direct implementation for example in solid state devices. Artificially engineered systems like ultracold atoms and photonics, on the other hand, offer unparalleled possibilities for designing physical systems, including ones that at first appear to be impossible to realize. In particular, with respect to a system's dimensionality, a range of new options are provided by techniques for implementing so-called synthetic dimensions, where an additional degree of freedom serves as the equivalent of an extra spatial dimensions [97, 98]. This has recently been demonstrated with nuclear spin states of fermionic ^{173}Yb [99] and hyperfine states of bosonic ^{87}Rb [100] as well as in photonic systems using the orbital angular momentum of photons [270]. Based on these results, experimental schemes for realizing 4D quantum Hall systems have been proposed [101, 271], which up to now have remained out of reach for state-of-the-art experiments – even though they are feasible in principle.

Topological charge pumps provide another way to study higher-dimensional quantum Hall physics in lower-dimensional time-dependent systems, in which external parameters can play the role of additional dimensions as illustrated by the relation between a 1D topological charge pump and 2D quantum Hall systems. Extending this concept to two dimensions allows for the realization of a dynamical version of the 4D integer quantum Hall effect in an experimentally accessible system as first proposed in [71]. Similar to a 1D charge pump, the underlying idea is to engineer a 2D system with a Hamiltonian $\hat{H}_{2\text{D}}(\varphi_x, \varphi_y)$ that depends periodically on two external pump parameters φ_x and φ_y and for each set of parameters $\{\varphi_x, \varphi_y\}$ resembles a Fourier component $\{k_z, k_w\}$ of the higher-dimensional quantum Hall system. As a function of φ_x and φ_y , all Fourier components of the 4D model are sampled sequentially and the 2D topological charge pump therefore exhibits a particle

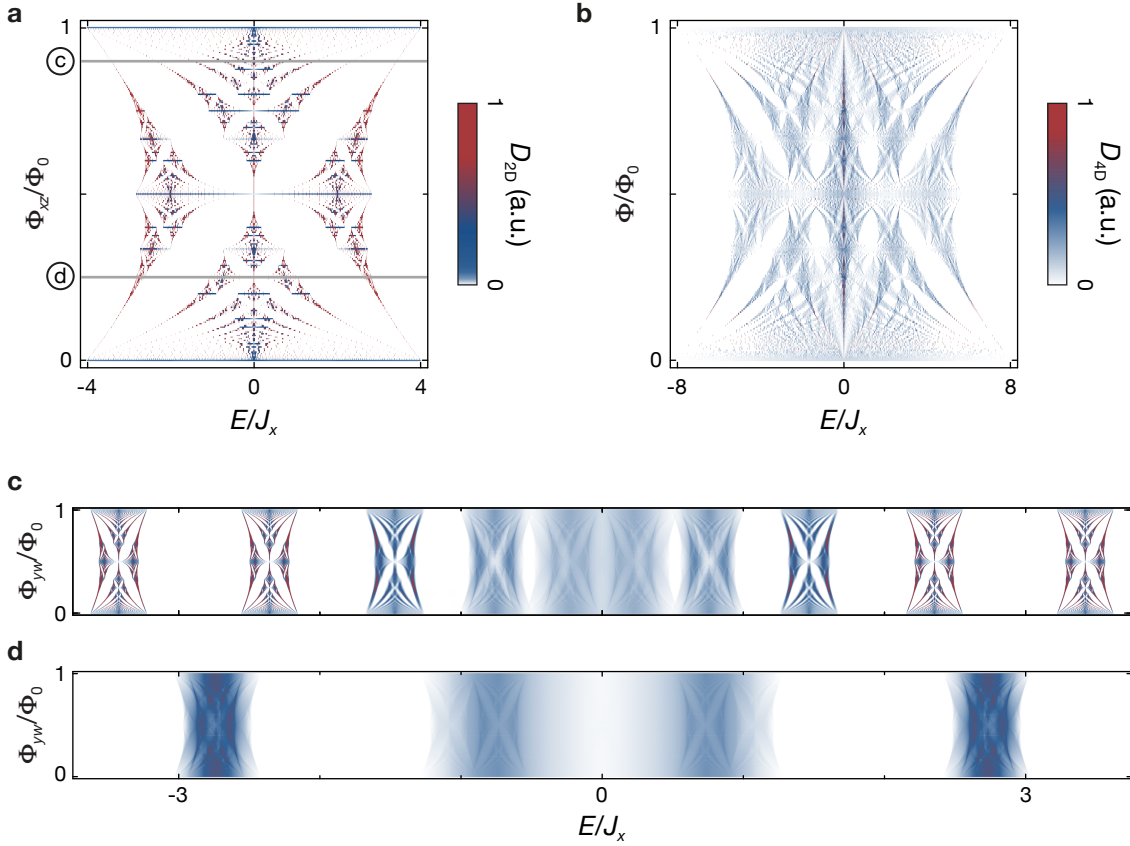


Figure 5.3 – Energy spectrum of the 4D Harper-Hofstadter model. (a) Density of states of the 2D Harper-Hofstadter model in the xz -plane, D_{2D} , as a function of the energy E and the magnetic flux per unit cell Φ_{xz} for $J_z = J_x$. The competition between the lattice period and the length scale associated with the magnetic flux causes a splitting of the lowest Bloch band into subbands, leading to a fractal energy spectrum – the well-known Hofstadter butterfly [147]. (b) Density of states in the 4D Harper-Hofstadter model, D_{4D} , versus energy E and magnetic flux, assuming the same flux per unit cell in the xz - and yw -plane, $\Phi = \Phi_{xz} = \Phi_{yw}$, and with equal tunnelling rates in all four directions. The presence of the additional magnetic flux Φ_{yw} leads to a further fractionalization of the band structure, where each subbands separates into even more subbands. (c) Density of states in the 4D Harper-Hofstadter model, D_{4D} , as a function of the energy E and the magnetic flux in the yw -plane, Φ_{yw} , for $\Phi_{xz} = 9/10$ with $J_y = J_w = 0.05J_x$ and $J_z = J_x$. (d) As (c), but with $\Phi_{xz} = 1/4$.

transport in response to a change of the pump parameters, which has the same geometrical and topological properties as the Hall response of the 4D system. Note that already in 1986 higher-dimensional generalizations of the 1D Thouless pump and the relation between the resulting quantized transport and the Chern numbers were studied in [272].

In this section, we first demonstrate how the minimal model of a 4D quantum Hall system with broken time-reversal symmetry introduced in Section 5.1.3 can be mapped onto a dynamical 2D lattice model (Section 5.2.1), following the procedure for the time-reversal invariant case introduced in [71]. Afterwards, the transport properties of such a 2D topological charge pump (Section 5.2.2) are studied and the different types of non-linear Hall responses in this setting are discussed (Section 5.2.3-5.2.5).

5.2.1 Mapping a 4D Quantum Hall System to a Topological Charge Pump

Dimensional Reduction of the 4D Harper-Hofstadter Model to a Dynamical 2D Superlattice

The Fourier components of the 4D Harper-Hofstadter model obtained by dimensional reduction along the z - and w -axes are described by the two-dimensional extension of the Harper model [Eq. (5.20)]. The latter is identical to the Hamiltonian of a two-dimensional square lattice in the xy -plane with tunnel coupling in both directions between neighbouring sites, whose on-site energy is modulated periodically. In analogy to the discussion for a 1D topological charge pump in Section 2.3.2, this is precisely the situation realized by a 2D superlattice potential in the extreme tight-binding limit, which is created by combining two orthogonal 1D superlattices along x and y with lattice constants $d_{1,\mu} > d_{s,\mu}$ and lattice depths $V_{s,\mu} \gg V_{1,\mu}$ for $\mu \in \{x, y\}$:

$$V(x, y) = \sum_{\mu \in \{x, y\}} [V_{s,\mu} \sin^2(\pi\mu/d_{s,\mu}) + V_{1,\mu} \sin^2(\pi\mu/d_{1,\mu} - \varphi_\mu/2)] \quad (5.21)$$

with φ_μ denoting the superlattice phases. In the tight binding regime, non-interacting particles in such a superlattice are described by the following Hamiltonian (see also Section 3.2.2):

$$\begin{aligned} \hat{H}_{2D}(\varphi_x, \varphi_y) = & - \sum_{m_x, m_y} [J_x(\varphi_x) + \delta J_x^{m_x}(\varphi_x)] \hat{a}_{m_x+1, m_y}^\dagger \hat{a}_{m_x, m_y} + \text{h.c.} \\ & - \sum_{m_x, m_y} [J_y(\varphi_y) + \delta J_y^{m_y}(\varphi_y)] \hat{a}_{m_x, m_y+1}^\dagger \hat{a}_{m_x, m_y} + \text{h.c.} \\ & + \sum_{m_x, m_y} [\Delta_x^{m_x}(\varphi_x) + \Delta_y^{m_y}(\varphi_y)] \hat{a}_{m_x, m_y}^\dagger \hat{a}_{m_x, m_y} \end{aligned} \quad (5.22)$$

In general, unlike in the 2D Harper model, both the tunnelling matrix elements in the first two rows as well as the potential energies of the lattices sites in the last row are modulated periodically in space due to the presence of the long lattices and thus depend on the superlattice phases. For $V_{s,\mu} \gg V_{1,\mu}$, the tight-binding parameters can be approximated as [160] (see Section 2.3.2 for details):

$$J_\mu(\varphi_\mu) = J_\mu \quad (5.23)$$

$$\delta J_\mu^{m_\mu}(\varphi_\mu) = \frac{\delta J_\mu^{(0)}}{2} \cos \left[2\pi \frac{d_{s,\mu}}{d_{1,\mu}} (m_\mu + 1/2) - \varphi_\mu \right] \quad (5.24)$$

$$\Delta_\mu^{m_\mu}(\varphi_\mu) = -\frac{\Delta_\mu^{(0)}}{2} \cos \left[2\pi \frac{d_{s,\mu}}{d_{1,\mu}} m_\mu - \varphi_\mu \right] \quad (5.25)$$

In the extreme tight-binding limit for $V_{s,\mu} \gg V_{1,\mu}$, the modulation of the tunnelling rates becomes negligible and Eq. (5.22) reduces to the 2D Harper model of Eq. (5.20), i.e. $\hat{H}_{2D}(\varphi_x, \varphi_y)$ becomes identical to a Fourier component $\hat{H}_{xy}(k_z, k_w)$ of the 4D Harper-Hofstadter model. As the 4D quantum Hall system is fully separable into the orthogonal 2D subspaces, the relation between the quantities in the 4D model and the 2D topological

charge pump is analogous to the mapping between a 2D quantum Hall system and a 1D charge pump (see Section 2.3.2). The position of a long lattice giving rise to the modulation of the on-site energies is determined by the respective superlattice phase φ_μ , similar to the transverse quasi-momentum k_ν , $\nu \in \{z, w\}$ in the 2D Harper model. By changing φ_x and φ_y , all Fourier components can be realized individually as a change by 2π covers the entire Brillouin zone in the respective direction. The ratio of the short and long lattice constants, i.e. the period of the modulation, plays the same role as the magnetic flux per unit cell with $d_{s,\mu}/d_{l,\mu} = \Phi_{\mu\nu}/\Phi_0$.

Dynamical 4D Integer Quantum Hall Effect

A 2D topological charge pump that corresponds to a dynamical version of the 4D Harper-Hofstadter model can therefore be implemented in a 2D superlattice potential with controllable superlattice phases (Fig. 5.4). In analogy to the 1D charge pump, φ_x and φ_y are the pump parameters and pumping is performed by changing them adiabatically. This is equivalent to a threading of magnetic flux along the axes of the quantum Hall cylinders, which generates the electric perturbation in the 4D model (Fig. 5.1, see also Section 2.3). To induce a non-linear Hall response, a magnetic perturbation is required in addition. Its equivalent for the 2D charge pump can be found by applying the partial Fourier transform of Eq. (5.18) to the corresponding term in the Hamiltonian of the 4D system.

The vector potential creating the magnetic field B_{xw} in the Lorentz-type configuration can for example be chosen in such a way that the tunnelling matrix elements in the w -direction in the 4D Harper-Hofstadter model of Eq. (5.16) contain an additional phase factor that depends on the position along x :

$$J_w e^{i(\tilde{\Phi}_{yw}m_y + \tilde{B}_{xw}m_x)} \hat{a}_{\mathbf{m}+\mathbf{e}_w}^\dagger \hat{a}_{\mathbf{m}} + \text{h.c.} \quad (5.26)$$

with $\tilde{B}_{xw} = 2\pi d_{s,x}d_{s,w}B_{xw}/\Phi_0$. This translates to a linear shift of the respective modulating potential as a function of m_x in the Fourier components $\hat{H}_{xy}(k_z, k_w)$. For the 2D superlattice, the magnetic perturbation B_{xw} therefore corresponds to a phase along y that changes linearly with x :

$$\varphi_y = \varphi_y^{(0)} - 2\pi b_{xw}x \quad (5.27)$$

with $b_{xw} = \tilde{B}_{xw}/(2\pi d_{s,x})$ and $\varphi_y^{(0)}$ being the global superlattice phase of the unperturbed superlattice. When adiabatically varying φ_x , this position dependence of φ_y induces a non-linear pumping response that is equivalent to a Lorentz-type non-linear Hall response as detailed in Section 5.2.3.

Similarly, a density-type magnetic perturbation $B_{yw} \neq 0$ can be added by modifying the phase factor $\tilde{\Phi}_{yw}$ that creates the magnetic flux in the yw -plane:

$$\tilde{\Phi}_{yw} \rightarrow \tilde{\Phi}_{yw} + \tilde{B}_{yw} \quad (5.28)$$

where $\tilde{B}_{yw} = 2\pi d_{s,y}d_{s,w}B_{yw}/\Phi_0$. This in turn leads to a linear dependence of φ_y on the position along y :

$$\varphi_y = \varphi_y^{(0)} - 2\pi b_{yw}y \quad (5.29)$$

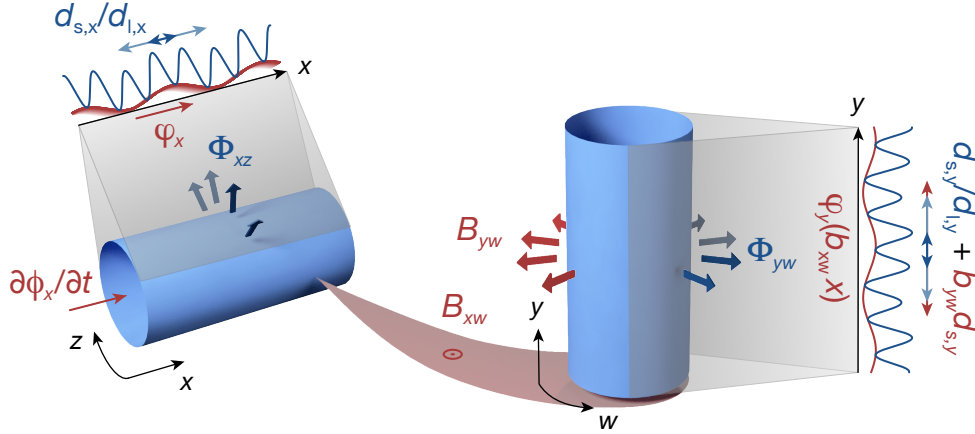


Figure 5.4 – Mapping of the 4D Harper-Hofstadter model to a 2D topological charge pump. In analogy to the relation between a 2D quantum Hall system and a 1D charge pump, the 2D Harper-Hofstadter models in the xz -plane and yw -plane each map onto a dynamical 1D superlattice along x and y , respectively. The ratio of the lattice constants $d_{s,\mu}/d_{l,\mu}$ with $\mu \in \{x, y\}$ corresponds to the flux per unit cell $\Phi_{\mu\nu}$ and a shift of the superlattice phase φ_x is equivalent to the threading of a magnetic flux ϕ_x along the axis of the quantum Hall cylinder in the xz -plane. The magnetic perturbation B_{xw} maps onto a transverse superlattice phase φ_y that depends linearly on x with $b_{xw} = d_{s,w}B_{xw}/\Phi_0$ [Eq. (5.27)]. The magnetic field B_{yw} , on the other hand, changes the period of the long lattice along y with $b_{yw} = d_{s,w}B_{yw}/\Phi_0$ [Eq. (5.29)].

for $b_{yw} = \tilde{B}_{yw}/(2\pi d_{s,y})$. Such a situation can be realized by slightly modifying the lattice constant of the long y -lattice compared to its value in the unperturbed system $d_{1,y}^{(0)} = (\Phi_0/\Phi_{yw})d_{s,y}$:

$$d_{1,y} = \frac{\Phi_0}{\Phi_{yw} + d_{s,y}d_{s,w}B_{yw}} d_{s,y} = \frac{d_{1,y}^{(0)}}{1 + d_{1,y}^{(0)}b_{yw}} \quad (5.30)$$

Upon a change of φ_x , this generates a non-linear pumping response corresponding to a density-type non-linear Hall response (see Section 5.2.4).

Off-Diagonal Harper Model

As discussed above, the Hamiltonian of a 2D superlattice $\hat{H}_{2D}(\varphi_x, \varphi_y)$ in Eq. (5.22) realizes the 2D Harper model of Eq. (5.20) only for very deep short lattices $V_{s,\mu} \gg V_{l,\mu}$, for which the on-site energies $\Delta_{\mu}^{m_{\mu}}$ are modulated sinusoidally [Eq. (5.25)] and the modulation of the tunnelling rates is negligible, $\delta J_{\mu}^{m_{\mu}} \approx 0$. For shallower lattices, the off-diagonal terms $\delta J_{\mu}^{m_{\mu}}$ become relevant, which leads to modifications of the 4D model that the 2D topological charge pump corresponds to analogous to the case of the 1D pump. Following the dimensional extension procedure introduced in Section 2.3.2, these can be determined by the inverse Fourier transform

$$\hat{a}_{m_x, m_y} = \sum_{m_z, m_w} e^{-i(\varphi_x m_z + \varphi_y^{(0)} m_w)} \hat{a}_{\mathbf{m}} \quad (5.31)$$

A subsequent integration over all Fourier components yields the 4D parent Hamiltonian [71]

$$\hat{H}_{4D} = \frac{1}{4\pi^2} \int_0^{2\pi} \hat{H}_{2D}(\varphi_x, \varphi_y) d\varphi_x d\varphi_y^{(0)} \quad (5.32)$$

Compared to the 4D Harper-Hofstadter model [Eq. (5.16)], this leads to the appearance of two additional terms $\hat{H}_{\delta J}^{xz} + \hat{H}_{\delta J}^{yw}$ with

$$\begin{aligned} \hat{H}_{\delta J}^{\mu\nu} = & \quad (5.33) \\ & - \frac{\delta J_\mu^{(0)}}{4} \sum_{\mathbf{m}} \left(e^{i\tilde{\Phi}_{\mu\nu}(m_\mu+1/2)} \hat{a}_{\mathbf{m}+\mathbf{e}_\mu+\mathbf{e}_\nu}^\dagger \hat{a}_{\mathbf{m}} + e^{-i\tilde{\Phi}_{\mu\nu}(m_\mu+1/2)} \hat{a}_{\mathbf{m}+\mathbf{e}_\mu-\mathbf{e}_\nu}^\dagger \hat{a}_{\mathbf{m}} \right) + \text{h.c.} \end{aligned}$$

One readily verifies that these terms describe diagonal tunnel couplings between next-nearest neighbour sites in each 2D quantum Hall system, thereby changing the Harper-Hofstadter models to Harper-Hofstadter-Hatsugai model [162] with the same uniform flux $\Phi_{\mu\nu}$ per unit cell of the square lattice.

As in the 1D case (Section 2.3.2), the modulation of the tunnelling rates can cause spectral changes to the model. In the configuration realized in the experiment (Section 6.1) with $d_{l,\mu} = 2d_{s,\mu}$, for example, the diagonal hopping creates an additional band gap that separates the lowest band into two distinct subbands and is proportional to $\delta J_\mu^{(0)}$. Additionally, when the depth of the short lattice is decreased further, Eq. (5.23)-(5.25) do not hold any more and the direct mapping to the 4D tight-binding model breaks down. Nonetheless, the modulations are still periodic in both space and the superlattice phase. As long as the corresponding pump cycles can be transformed into each without closing a gap in the band structure, the topology of the cycle and thus the response of a homogeneously filled band remains invariant. In particular, as for the 1D pump, the gap between the ground state and first excited band does not close even for $V_{s,\mu} \rightarrow 0$ and all configurations of the lowest band are thus topologically equivalent.

5.2.2 Transport Properties

A 2D topological charge pump can be described in a 4D generalized Brillouin zone that is formed by the two quasi-momenta along the lattice directions, k_x and k_y , and the two superlattice phases, φ_x and φ_y (see also Section 2.1.2). Due to the periodicity of the long lattices, the single particle Hamiltonian Eq. (5.22) is periodic in space as well as the superlattice phases, provided that the lattice constants in each direction are commensurate. The generalized Brillouin zone thus has the same geometry as the Brillouin zone in the 4D Harper-Hofstadter model because it is spanned by four cyclic variables with the external parameters φ_x and φ_y replacing the additional quasi-momenta k_z and k_w .

The system's transport properties can therefore be obtained analogous to a 4D quantum Hall system from the semiclassical equations of motion (see Section 5.1.3). For the sake of simplicity, we will focus on a single band and omit the band index in the following.

Assuming that no additional forces are applied ($\hbar\dot{k}_\mu = 0$), the equations of motion for a wave packet localized at position \mathbf{r} in a 2D superlattice are

$$\dot{r}^\mu(\mathbf{k}, \varphi) = \frac{1}{\hbar} \frac{\partial \mathcal{E}(\mathbf{k}, \varphi)}{\partial k_\mu} + \dot{\varphi}_\mu \Omega^\mu(\mathbf{k}, \varphi) \quad (5.34)$$

$$\dot{\varphi}_\mu = \dot{\varphi}_\mu^{(0)} + \frac{\partial \delta\varphi_\mu(\mathbf{r})}{\partial r_\nu} \dot{r}^\nu \quad (5.35)$$

with dynamical phases $\varphi = \{\varphi_x(t), \varphi_y(t)\}$ that can depend linearly on \mathbf{r} , $\varphi_\mu = \varphi_\mu^{(0)} + \delta\varphi_\mu(\mathbf{r})$, as derived in Section 5.2.1. In this case, the Berry curvatures Ω^μ are defined in the generalized Brillouin zone in the same way as for a 1D charge pump:

$$\Omega^\mu(\mathbf{k}, \varphi) = i (\langle \partial_{\varphi_\mu} u | \partial_{k_\mu} u \rangle - \langle \partial_{k_\mu} u | \partial_{\varphi_\mu} u \rangle) \quad (5.36)$$

with $|u(\mathbf{k}, \varphi)\rangle$ denoting the eigenstate of $\hat{H}_{2D}(\varphi_x, \varphi_y)$ with quasi-momentum \mathbf{k} . Note that even for a tiny magnetic perturbation, the perturbed system is in general not translationally invariant any more due to the position dependence of φ_μ . Moreover, the local superlattice potential can change quite drastically as φ_μ eventually covers the full range $[0, 2\pi[$. In the following, however, it is assumed that the perturbation is sufficiently small such that locally the system can be considered as homogeneous and the $|u(\mathbf{k}, \varphi)\rangle$ are well-defined as a function of the local superlattice phase $\varphi(\mathbf{r})$.

Comparing the equations above to the equations of motion in a 4D quantum Hall system, Eq. (5.1) and Eq. (5.2), one can see that the position dependence of $\delta\varphi_\mu(\mathbf{r})$ plays the same role as the magnetic perturbation, which generates the Lorentz force in the 4D model. It induces a velocity-dependent change of the superlattice phase, which in turn leads to an anomalous velocity $\dot{\varphi}_\mu \Omega^\mu(\mathbf{k}, \varphi)$. A change of $\varphi_\mu^{(0)}$, on the other hand, is equivalent to an electric perturbation as for a 1D charge pump. By solving the equations of motion, the pumping response of the system can be determined and the resulting centre-of-mass velocity and current density can be calculated by summing over all occupied \mathbf{k} -states. In the following, this is first discussed for a Lorentz-type and then a density-type superlattice configuration, before presenting the general result.

5.2.3 Lorentz-Type Pumping Response

We now consider a 2D topological charge pump with a Lorentz-type perturbation and study its response upon pumping in the x -direction by an adiabatic change of the pump parameter φ_x . As derived in Section 5.2.1, such a perturbation is created by a transverse superlattice phase φ_y that depends linearly on the position along x with $\delta\varphi_y(\mathbf{r}) = -2\pi b_{xw}x$ [Eq. (5.27)], while $\delta\varphi_x(\mathbf{r}) = 0$. The pumping along x , $d\varphi_x/dt$, gives rise to an anomalous velocity $\dot{\varphi}_x \Omega^x \mathbf{e}_x$ in the x -direction – the linear pumping response. For a uniformly occupied band, as in the 1D case, the resulting centre-of-mass displacement during one pump cycle $\varphi_x = 0 \rightarrow 2\pi$ is given by an integral of the anomalous velocity over a 2D generalized Brillouin zone spanned by k_x and φ_x and can thus be expressed in terms of the first Chern number of the 1D pump along x (see Section 2.1.3).

For $b_{xw} \neq 0$, this motion leads to a change of φ_y due to its dependence on the position along x . This *effective* threading of φ_y causes an additional anomalous velocity in the y -direction – the non-linear pumping response. For a given wave packet, the resulting velocity along y is equal to

$$v_y(\mathbf{k}, \varphi) = \dot{\varphi}_y \Omega^y \mathbf{e}_y = -2\pi b_{xw} \Omega^x \Omega^y \dot{\varphi}_x \mathbf{e}_y \quad (5.37)$$

Here, the group velocity is neglected since it does not contribute to the total velocity v_y for a uniformly filled band. Note that the Berry curvature Ω^y depends on x via the transverse phase $\varphi_y(x)$ and the above expression therefore not only depends on the momentum of the wave packet, but also its position in real space.

In this configuration, the perturbation b_{xw} does not change the density of states $D(\mathbf{k}) = L^2/(4\pi^2)$ in the superlattice with length L in both directions. The centre-of-mass velocity for a homogeneously populated band [Eq. (5.9)] at a given position can be obtained by integrating Eq. (5.37) over both quasi-momenta k_x and k_y :

$$v_{y,\text{COM}} = \frac{n_0}{N} \oint d^2k D(\mathbf{k}) v_y(\mathbf{k}, \varphi) = -b_{xw} \frac{A_{xy}}{2\pi} \oint d^2k \Omega^x \Omega^y \dot{\varphi}_x \quad (5.38)$$

Here, n_0 is the occupation of each \mathbf{k} -state, N the total particle number and $A_{xy} = a_x a_y$ denotes the size of the unit cell in the 2D superlattice. From this, the average displacement after one pump cycle δy_{COM} can be calculated by integrating over $\varphi_x \in [0, 2\pi[$, yielding

$$\delta y_{\text{COM}} = -b_{xw} A_{xy} \underbrace{\frac{1}{2\pi} \oint d^2k d\varphi_x \Omega^x \Omega^y}_{\bar{\Omega}(\varphi_y)} \quad (5.39)$$

This describes the centre-of-mass motion per cycle for a uniformly populated band, which is assumed to be confined to a small region along x , within which the change of $\varphi_y(x)$ and thus $\Omega^y(\mathbf{k}, \varphi)$ is negligible.

In an infinite system, on the other hand, the entire range of $\varphi_y \in [0, 2\pi[$ is sampled simultaneously and the average displacement along y is thus proportional to the integral of the anomalous velocity in Eq. (5.37) over the entire 4D generalized Brillouin zone. Therefore, it can be expressed in terms of the pump's second Chern number defined as

$$\nu_2 = 1/(4\pi^2) \oint_{\text{BZ}} dk_x dk_y d\varphi_x d\varphi_y \Omega^x \Omega^y \quad (5.40)$$

The mean displacement per pump cycle in an infinite system including the contribution from the linear response $\delta x_{\text{COM}} = \nu_1^x a_x$ is then given by

$$\delta \bar{\mathbf{r}}_{\text{COM}} = \frac{1}{2\pi} \oint d\varphi_y (\delta x_{\text{COM}} \mathbf{e}_x + \delta y_{\text{COM}} \mathbf{e}_y) = \nu_1^x a_x \mathbf{e}_x - b_{xw} A_{xy} \nu_2 \mathbf{e}_y \quad (5.41)$$

Here, $\nu_1^x = \oint dk_x d\varphi_x \Omega^x / (2\pi)$ denotes the first Chern number of the superlattice along x . The corresponding current density integrated over one pump cycle can be calculated from

the centre-of-mass shift by multiplying it with the particle density of the homogeneously populated band n_0/A_{xy} :

$$\bar{\mathbf{j}} = \frac{n_0}{A_{xy}} \delta \bar{\mathbf{r}}_{\text{COM}} = \frac{n_0}{a_y} \nu_1^x \mathbf{e}_x - n_0 b_{xw} \nu_2 \mathbf{e}_y \quad (5.42)$$

Analogous to the quantum Hall effect in 4D, the magnetic field-like perturbation b_{xw} thus indeed induces a non-linear response in addition to the linear pumping response. As expected, the linear and non-linear responses point in orthogonal directions in this configuration. Similar to a 4D quantum Hall system, both responses are characterized by a topological invariant, the pump's first Chern number along x and its second Chern number, respectively and are therefore quantized.

This pumping response is equivalent to the Lorentz-type non-linear Hall response in the minimal model for a 4D quantum Hall system introduced in Section 5.1.3. For the latter, the current density of a uniformly populated band is given by Eq. (5.12). Integrating this current density over one period of the Bloch oscillations induced by the perturbing electric field $\tau_B = h/(qE_z d_{s,z})$, which is the equivalent of a pump cycle, one obtains

$$\bar{\mathbf{j}}_{QH} = \mathbf{j}_{QH} \tau_B = \frac{n_0}{d_{s,z} A_M^{yw}} \nu_1^{zx} \mathbf{e}_x - \frac{n_0}{d_{s,w} d_{s,z}} b_{xw} \nu_2 \mathbf{e}_y \quad (5.43)$$

Following the mapping derived in Section 5.2.1, the size of the 2D magnetic unit cell in the Landau gauge corresponds to $A_M^{yw} = d_{s,w} a_y$. The two current densities are thus related by the size of the lattice unit cell in the wz -plane $d_{s,w} d_{s,z}$:

$$\bar{\mathbf{j}} = d_{s,w} d_{s,z} \bar{\mathbf{j}}_{QH} \quad (5.44)$$

5.2.4 Density-Type Pumping Response

The equivalent of a density-type response can be realized with a 2D charge pump by adding a y -dependent perturbation of the form $\delta\varphi_y(\mathbf{r}) = -2\pi b_{yw} y$ to the superlattice phase along y [Eq. (5.29)]. When pumping in the x -direction, the motion of the particles as a result of the linear response does not give rise to a Lorentz-like term in Eq. (5.35) in this case because – unlike for the Lorentz-type perturbation – φ_y is now independent of x . Therefore, the centre-of-mass motion is not affected by b_{yw} and it only exhibits the linear response along x ,

$$\delta \bar{\mathbf{r}}_{\text{COM}} = \nu_1^x a_x \mathbf{e}_x \quad (5.45)$$

However, similar to the corresponding situation in a 4D quantum Hall system, this perturbation modifies the density of states in the superlattice along y . Thereby, it changes the number of particles that are transported in the x -direction (Fig. 5.5) and gives rise to a non-linear pumping response in the current density.

For a given eigenstate at \mathbf{k} , the particle density in real space can be determined by calculating the distance between the cell-periodic parts of the Bloch wave function in neighbouring unit cells. In the unperturbed lattice, all unit cells are identical and this distance is thus equal to the size of unit cell in the y -direction, a_y . For $b_{yw} \neq 0$, however,

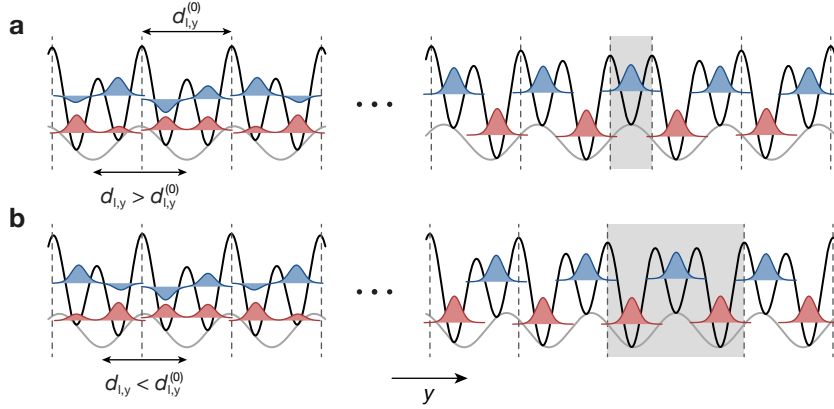


Figure 5.5 – Density-type perturbation in a 2D superlattice. (a) A change of the long lattice constant in the y -direction $d_{l,y}$ from its unperturbed value $d_{l,y}^{(0)}$ makes the superlattice phase φ_y dependent on the position along y , creating a density-type perturbation $b_{yw} \neq 0$ as in Eq. (5.29). This perturbation changes the particle density in the y -superlattice as illustrated here for $b_{yw} < 0$ ($d_{l,y} > d_{l,y}^{(0)}$) with $d_{l,y}^{(0)} = 2d_{s,y}$. The change of φ_y between neighbouring double wells, which are indicated by the dashed lines, shifts the centre-of-mass position of the cell-periodic part of a given eigenstate in the unperturbed lattice, shown here for the lowest (red) and first excited subband (blue). This shift is determined by the Berry curvature Ω^y and thus has opposite signs for two bands, reducing the density of ground state atoms while increasing the one of excited atoms. In the staggered configurations for $\varphi_y = l\pi$, $l \in \mathbb{Z}$ this leads to the appearance of an "unpaired" state in the excited band as shown on the right. (b) As in (a) but with $b_{yw} > 0$ ($d_{l,y} < d_{l,y}^{(0)}$). In this case, the density in the lowest band is increased and lowered in the excited band such that the "unpaired" states in the staggered configurations belong to the ground state band.

the superlattice phase in neighbouring unit cells is slightly different, leading to a small shift of the wave function's centre of mass. This shift can be evaluated in analogy to the linear pumping response:

$$\delta a_y = \int_{\varphi_y(y_m)}^{\varphi_y(y_m+a_y)} d\varphi_y \Omega^y(\mathbf{k}, \varphi) \approx -2\pi b_{yw} a_y \Omega^y(\varphi_y(y_m)) \quad (5.46)$$

assuming that the phase shift between neighbouring sites is sufficiently small such that the variation of Ω^y is negligible. To first order in b_{yw} , the local particle density of this state is then given by

$$n(\mathbf{k}, \varphi) = \frac{n_{\mathbf{k}} a_y}{L^2 a_y + \delta a_y} \approx \frac{n_{\mathbf{k}}}{L^2} [1 + 2\pi b_{yw} \Omega^y(\mathbf{k}, \varphi)] \quad (5.47)$$

This expression has exactly the same form like the density of states in a 4D quantum Hall system in Eq. (5.5). As φ_y changes with y , this density depends on the position in the lattice. In an infinite system, the mean density can be obtained by averaging Eq. (5.47) over φ_y . For a uniformly occupied band, $n_{\mathbf{k}} = n_0$, the total particle density can be calculated by additionally summing over all k_x and k_y :

$$n = \frac{1}{2\pi} \oint d^2 k d\varphi_y \frac{L^2}{4\pi^2} n(\mathbf{k}, \varphi) = \frac{n_0}{A_{xy}} + \frac{n_0 b_{yw}}{a_x} \nu_1^y \quad (5.48)$$

with $\nu_1^y = \oint dk_y d\varphi_y \Omega^y / (2\pi)$ denoting the first Chern number of the superlattice in the y -direction.

The current density is given by the product of the centre-of-mass velocity and the particle density [Eq. (5.10)]. When integrating this over one pump cycle, the current density is thus proportional to the centre-of-mass displacement and we obtain

$$\bar{\mathbf{j}} = \oint d\varphi_x n \mathbf{v}_{\text{COM}}(\varphi_x) = \frac{n_0}{a_y} \nu_1^x \mathbf{e}_x + n_0 b_{yw} \nu_2 \mathbf{e}_x \quad (5.49)$$

using the fact that $\nu_2 = \nu_1^x \nu_1^y$ since the unperturbed superlattice is separable into the x - and y -direction. Therefore, also a density-type magnetic field-like perturbation b_{yw} leads to the appearance of a non-linear quantized pumping response. Unlike for a Lorentz-type perturbation, the linear and the non-linear response are aligned in this case with the non-linear one only affecting the current density. Even though the two types of perturbations appear unrelated from a 2D point of view, the respective responses are quantified by the same 4D topological invariant ν_2 . This highlights the intrinsic 4D symmetries of a 2D topological charge pump, which it inherits from its "parent" model, a 4D quantum Hall system.

In the corresponding configuration in the minimal 4D quantum Hall model (Section 5.1.3), the current density integrated over one Bloch period is

$$\bar{\mathbf{j}}_{QH} = \mathbf{j}_{QH} \tau_B = \frac{n_0}{d_{s,z} A_M^{yw}} \nu_1^{zx} \mathbf{e}_x + \frac{n_0}{d_{s,w} d_{s,z}} b_{yw} \nu_2 \mathbf{e}_x \quad (5.50)$$

As for the Lorentz-type response, the two current densities only differ by the size of the unit cell in the wz -plane, $\bar{\mathbf{j}} = d_{s,w} d_{s,z} \bar{\mathbf{j}}_{QH}$.

5.2.5 General Pumping Response

The response of a 2D topological charge pump can be generalized by combining the two types of pumping responses discussed above. To highlight the analogy to the 4D quantum Hall effect, we use the following notation for this: the pumping direction is indicated by its electric field equivalent, $\varepsilon_z = 1$ for pumping along x and $\varepsilon_w = 1$ for the y -direction, and the pump's first Chern numbers are indexed by the corresponding plane in the quantum Hall system, i.e. $\nu_1^x \rightarrow \nu_1^{zx}$ and $\nu_1^y \rightarrow \nu_1^{wy}$. With this, the total integrated current density can be expressed as

$$\bar{\mathbf{j}} = \frac{n_0}{A_{xy}} a_\mu \varepsilon_\nu \nu_1^{\nu\mu} \mathbf{e}_\mu + \frac{n_0}{2} \varepsilon^{\mu\gamma\delta\nu} \varepsilon_\nu b_{\gamma\delta} \nu_2 \mathbf{e}_\mu \quad (5.51)$$

Up to the proportionality factor $d_{s,w} d_{s,z}$, this is identical to the general expression for the current density in a 4D quantum Hall system in Eq. (5.7) upon integration over a Bloch period and assuming the geometry of the minimal model introduced in Section 5.1.3, i.e. only the two Berry curvatures Ω^{zx} and Ω^{wy} are non-zero and the system is separable into the two orthogonal 2D subspaces.

The expression above again shows the equivalence of the non-linear pumping response of a 2D topological charge pump and the non-linear Hall response in a 4D quantum Hall system. Both responses are induced by two independent perturbations applied in orthogonal subspaces, i.e. the perturbing electric and magnetic fields E_ν and $B_{\gamma\delta}$ or the pumping

$d\varphi_\mu/dt$ and the magnetic field-like perturbation $b_{\gamma\delta}$ in the superlattice phases, respectively. Furthermore, Eq. (5.51) illustrates the 4D character of the non-linear response, resulting from the higher-dimensional non-commutative geometry of the 4D quantum Hall model that the 2D topological charge pump can be derived from. This explicitly manifests in the 4D Levi-Civita symbol in Eq. (5.51) as well as the second Chern number, which is a 4D topological invariant defined in the 4D generalized Brillouin zone of the charge pump. An equivalent non-linear response can therefore not be observed in any time-independent lower-dimensional system.

Implementation of a 2D Topological Charge Pump

In this chapter, the experimental realization of a dynamical 4D quantum Hall system and the observation of its quantized non-linear bulk response with 4D topology is presented. Based on the proposal in [71], a 2D topological charge pump is implemented with bosonic ^{87}Rb atoms forming a quarter-filled fractional Mott insulator in the lowest subband of an angled 2D superlattice. The response to the pumping, an adiabatic periodic modulation of the superlattice potential along one axis, is probed locally with a small atom cloud. Using in-situ imaging, signatures of the non-linear centre-of-mass response in the direction orthogonal to the pumping are observed – the key feature of the 4D Hall effect. This response is quantified by measuring the double-well imbalance transverse to the pumping with site-resolved band mapping. From the local geometric properties, the quantized bulk response of an infinite system can be reconstructed and its quantization is demonstrated by extracting the associated topological invariant, the second Chern number. The integrated response amounts to 80% of the expected quantized value, which shows that the experiment is very close to the quantum Hall regime. By identifying and independently quantifying the predominant experimental imperfections, the response of the lowest subband can be isolated. Its quantization is verified with high precision, thereby revealing the quantum nature of the 4D quantum Hall effect.

In Section 6.1, the experimental setup as well as the properties and the characterization of the angled 2D superlattice are discussed. Furthermore, we introduce the implementation of the pumping scheme and the local probing of the resulting non-linear response. The initial state preparation and the double-differential imaging technique for resolving the pumping response in-situ are described in Section 6.2 and the experimental observation of the non-linear centre-of-mass drift is presented. Section 6.3 focuses on the measurement of the non-linear response by site-resolved band mapping and the modelling of the system's transport properties including the experimental imperfections caused by heating. In Section 6.4, the reconstruction of the quantized response of an infinite system from the local measurements is discussed. With this method, the second Chern number of the lowest subband is determined. In addition, the non-linear character of the transverse response is demonstrated by studying its scaling with the perturbing superlattice angle.

6.1 Experimental Implementation in a 2D Optical Superlattice

A 2D topological charge pump, which can be interpreted as a dynamical version of the 4D integer quantum Hall effect as discussed in Section 5.2, can be implemented with ultracold atoms in a 2D optical superlattice. Analogous to a 4D quantum Hall system, a non-linear bulk response is induced by two perturbations in orthogonal subspaces: the pumping in one direction, which is performed by adiabatically shifting the corresponding superlattice phase $\varphi_x(t)$, as well as a position-dependent superlattice phase in the transverse direction $\varphi_y(\mathbf{r})$. Here, we focus on a Lorentz-type configuration (see Section 5.2.3), in which the transverse phase couples the motion between the two orthogonal directions similar to the Lorentz force generated by a magnetic perturbation in a 4D quantum Hall model (see Section 5.1.3). In this section, we show how such a situation can be created in an angled 2D superlattice for the specific case of $d_l = 2d_s$ used in the experiment. The properties of the resulting 2D Rice-Mele model [130] and a method for determining the tilt angle via Bloch oscillations are discussed. The pump cycle in the 4D tight-binding parameters space and its experimental implementation are introduced. Furthermore, we delineate how a small atom cloud can serve as a local probe of the geometric transport properties of this system.

6.1.1 Angled 2D Superlattice

A position-dependent transverse superlattice phase mimicking a Lorentz-type magnetic perturbation in a 4D quantum Hall system can be realized in an angled 2D superlattice, in which the long lattice along y is tilted by a small angle $\theta \ll 1$ with respect to the short lattice. In this case, the wave vector of the long lattice acquires a small component along x , $\mathbf{k}_{l,y} = k_{l,y} (\cos \theta \mathbf{e}_y + \sin \theta \mathbf{e}_x)$. To first order in θ , the resulting lattice potential is described by a superlattice phase that depends linearly on the position along x :

$$\varphi_y(x) = \varphi_y^{(0)} + 2\pi\theta x/d_{l,y} \quad (6.1)$$

The lattice spacing in the y -direction, on the other hand, remains approximately unchanged. It thus realizes precisely the situation described in Section 5.2 with the strength of the magnetic perturbation given by

$$B_{xw} = -\frac{\Phi_0}{d_{s,w}d_{l,y}} \theta \quad (6.2)$$

A tilt of the long lattice can be implemented experimentally with a glass block in the path of the incoming long lattice beam. Rotating this block introduces a parallel displacement from the optical axis, which is translated into an angle relative to the short lattice by the lens in front of the atom cloud (Fig. 6.1).

In the experiment, a 2D superlattice with $d_s \equiv d_{s,x} = d_{s,y}$ and $d_l \equiv d_{l,x} = d_{l,y} = 2d_s$ is used (Fig. 6.2a, see also Section 3.2.1). Each superlattice is created by superimposing two retro-reflected lattices, a short lattice with $\lambda_s = 767$ nm and a long lattice with $\lambda_l = 2\lambda_s$. In this case, the superlattice potential consists of double wells in the x - and y -direction

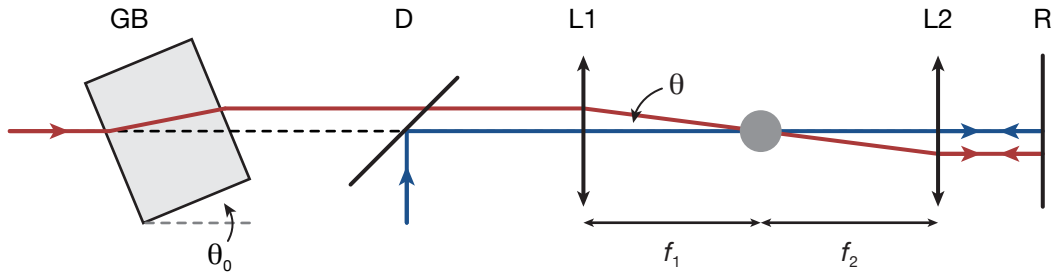


Figure 6.1 – Setup for the angled superlattice. To introduce a tilt angle θ of the long y -lattice relative to the short one, a glass block (GB) with thickness 25 mm is placed in the beam path of the incoming long lattice beam (red) in front of the dichroic mirror (D), where the beam is overlapped with the one for the short lattice (blue). If the glass block is rotated by an angle θ_0 with respect to the optical axes (black dashed line), the incoming beam is displaced parallel to the optical axis. This displacement is translated to an angle θ relative to the short lattice beam by the first lens (L1). The two beams intersect at the focus point of L1, which corresponds to the position of the atom cloud (grey circle). They are retroreflected by the mirror R after passing through the second lens L2, thereby creating the lattice potentials with the same relative angle θ . Note that this schematic is not to scale and that the additional mirrors in the incoming short and long lattice beams for controlling their positions at the location of the atom cloud are not shown (see Section 3.2.1).

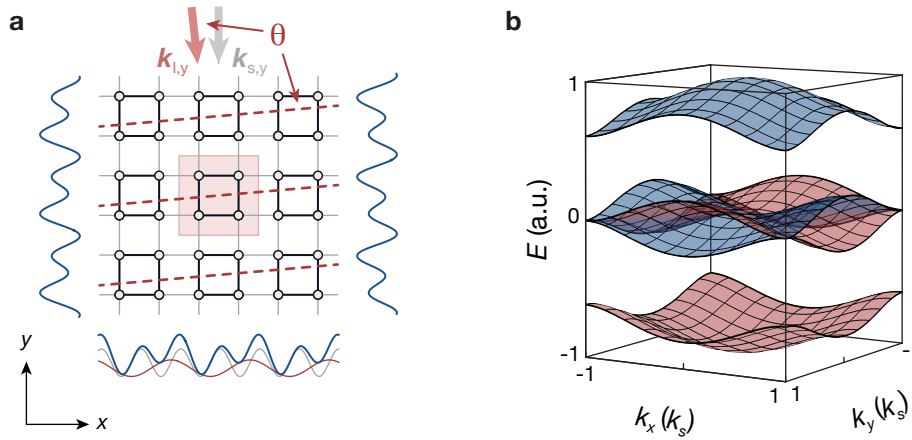


Figure 6.2 – Angled 2D superlattice and its band structure. (a) 2D superlattice potential (blue) with $d_l = 2d_s$ as used in the experiment. The wave vector $\mathbf{k}_{l,y}$ of the long lattice along y (red arrow) is tilted by an angle θ compared to the short lattice $\mathbf{k}_{s,y}$ (grey arrow). This leads to a transverse superlattice phase φ_y that depends linearly on the position along x as indicated by the potential minima of the long y -lattice (red dashed lines). Therefore, the form of the double wells along y changes with x . The presence of the long lattices gives rise to dimerized tunnel couplings between neighbouring lattice sites (black circles) with black (grey) lines indicating strong (weak) coupling. The unit cell (light red square) thus contains four non-equivalent sites. Figure adapted from [150]. (b) Band structure of the unperturbed 2D superlattice ($\theta = 0$) for $V_{s,x} = V_{s,y} = 13E_{r,s}$ and $V_{l,x} = V_{l,y} = 13E_{r,l}$ with $d_l = 2d_s$. Due to the enlarged unit cell, the lowest Bloch band of the short lattices splits into four subbands.

and its unit cell is thus a four-site plaquette with $a_x = a_y = 2d_s$. Correspondingly, the lowest Bloch band in the two short lattices splits into four subbands, two of which are degenerate if the lattice configuration is symmetric along x and y (Fig. 6.2b). In the tight-binding limit, in which these subbands are well separated from all other bands, non-interacting atoms in this lattice configuration are described by a 2D extension of the Rice-Mele Hamiltonian [130] (see also Section 3.2.2):

$$\begin{aligned} \hat{H}_{2D}(\varphi_x, \varphi_y) = & - \sum_{m_x, m_y} [J_x(\varphi_x) + (-1)^{m_x} \delta J_x(\varphi_x)/2] \hat{a}_{m_x+1, m_y}^\dagger \hat{a}_{m_x, m_y} + \text{h.c.} \quad (6.3) \\ & - \sum_{m_x, m_y} [J_y(\varphi_y) + (-1)^{m_y} \delta J_y(\varphi_y)/2] \hat{a}_{m_x, m_y+1}^\dagger \hat{a}_{m_x, m_y} + \text{h.c.} \\ & + \sum_{m_x, m_y} \frac{1}{2} [(-1)^{m_x} \Delta_x(\varphi_x) + (-1)^{m_y} \Delta_y(\varphi_y)] \hat{a}_{m_x, m_y}^\dagger \hat{a}_{m_x, m_y} \end{aligned}$$

For $d_l = 2d_s$, the long lattices generate an alternating modulation of the on-site energies with amplitudes Δ_x and Δ_y as well as a dimerization of the tunnelling matrix elements between neighbouring sites, which differ by δJ_x and δJ_y , respectively. Both modifications depend on the corresponding superlattice phase φ_μ with $\mu \in \{x, y\}$. The unperturbed system ($\theta = 0$) can be expressed as a direct sum of two 1D Rice-Mele models along x and y . Its eigenstates are products of the 1D eigenstates and their eigenenergy is given by the sum of the respective 1D eigenenergies. The structure of the energy spectrum of $\hat{H}_{2D}(\varphi_x, \varphi_y)$ can thus be inferred from the one of 1D Rice-Mele Hamiltonian (see Section 3.2.2 and 4.1.1). In particular, the second Chern number of the lowest subband is equal to the product of the corresponding first Chern numbers along x and y , $\nu_2 = \nu_1^x \nu_1^y = +1$.

Edge and Corner States

In a system with open boundary conditions in both directions, there are three distinct types of eigenstates (Fig. 6.3). The majority of eigenstates extend over the entire 2D system, which are the bulk states corresponding to the four subbands in an infinite system. The number of these states scales quadratically with the length of the system, $N_{\text{bulk}} \sim l_x l_y$, where $l_\mu = L_\mu/d_{s,\mu}$ is the number of lattice sites along μ . Furthermore, there are $N_{\text{edge}} = 2(l_x + l_y - 4)$ edge states, which are confined to one of the 1D boundaries of the system. The third kind of eigenstates are the four corner states, which are fully localized in one of the corners. The latter are very peculiar as they constitute topologically protected boundary states with a dimensionality that is not – as usual – one, but two lower than that of the full system [273, 274]. Similar modes, which have potential applications in photonic crystal materials like fibres and cavities, have recently been observed in 2D time-reversal invariant photonic waveguide arrays with chiral symmetry [275].

The appearance of edge and corner states is a consequence of the non-trivial topology of the underlying 4D model. These states only occur in certain lattice configurations and are localized in the band gaps of the energy spectrum (Fig. 6.3a). When the superlattice phases are varied, they cross the gaps before disappearing into the bulk of the system.

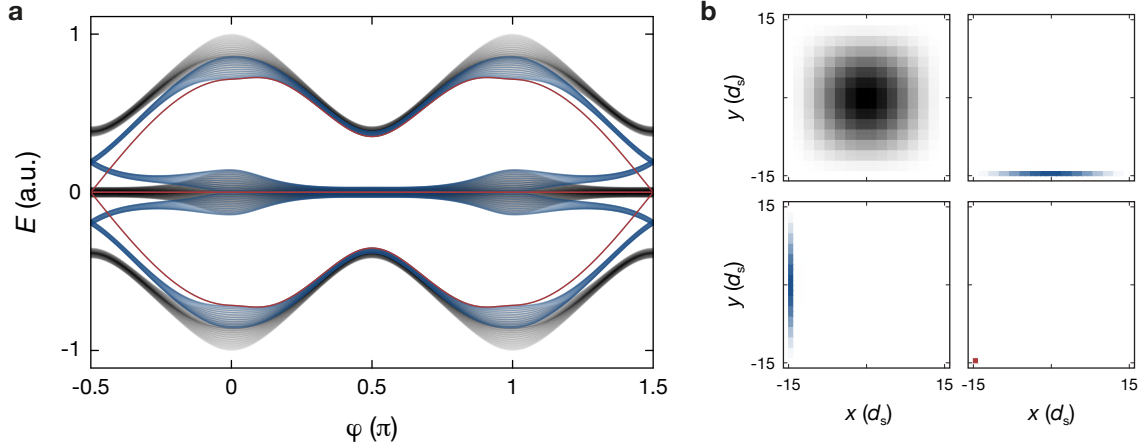


Figure 6.3 – Edge states in a 2D superlattice with open boundary conditions and $\theta = 0$. (a) Energy spectrum versus superlattice phase $\varphi \equiv \varphi_x = \varphi_y$ for a system with size $L_x = L_y = 30d_s$, $V_{s,x} = V_{s,y} = 10E_{r,s}$ and $V_{l,x} = V_{l,y} = 20E_{r,l}$. The eigenenergies are calculated by diagonalizing the tight-binding Hamiltonian of the system numerically, for which the double-well tilts Δ_μ , $\mu \in \{x, y\}$, are rescaled by a factor of 0.05 for better illustration. The spectrum contains three different kinds of eigenstates: bulk states (black), edge states (blue) and corner states (red). (b) Four examples of eigenstates at $\varphi = -\pi/2$ showing the density $|\psi_{m_x, m_y}|^2$ on each lattice site. Most eigenstates are bulk states (upper left), which are delocalized over the entire system and form the four subbands of the band structure. In the vicinity of $\varphi = -\pi/2$, edge states (upper right and lower left) appear in the band gaps. These states are localized on one edge of the system, but delocalized along the perpendicular direction. In addition, there are corner states (lower right), which are confined to one of the system's corners.

In analogy to the 1D topological charge pump (see Section 2.2.1), these states can be interpreted as ensuring the quantization of the bulk pumping response [122]. Simultaneously with the work presented here, the existence and topological pumping of such localized states has been demonstrated in a 2D photonic system [276]. Similar to the 1D case, the evolution of the edge and corner states during the pumping is directly related to the boundary modes occurring in 4D quantum Hall systems, namely chiral states that are confined to 3D hypersurfaces and 2D hyperedges, respectively. Therefore, the intrinsic 4D symmetries of a 2D topological charge pump also become apparent in these boundary phenomena. In particular, the non-linear transport associated with the edge states is equivalent to a density-type response in the 4D model: a magnetic perturbation in the direction of the respective edge, which changes the corresponding density of states, immediately affects the charge that is transported by these modes. The pumping of corner states in the presence of a perturbing tilt, on the other hand, is the analogue of a 4D Lorentz-type response, coupling the motion in two orthogonal directions.

6.1.2 Determination of the Tilt Angle

To study the non-linear pumping response, which scales linearly with the perturbing angle, a precise knowledge of the size of θ is required. It can be determined by taking advan-

tage of the modified on-site energies due to the position-dependent superlattice phase (Fig. 6.4a). For small angles $\theta \ll d_{1,y}/L_x$, the change of φ_y over the size of the cloud is very small and the double-well tilt in the y -direction can be approximated as:

$$\Delta_y^{m_y}(\varphi_y) \approx \Delta_y^{m_y}(\varphi_y^{(0)}) + (-1)^{m_y} \left. \frac{\partial \Delta_y}{\partial \varphi_y} \right|_{x=0} \pi \theta x/d_{1,y} \quad (6.4)$$

assuming that the atom cloud is centred around $x = 0$. This corresponds to a linear gradient, which has opposite signs on even and odd sites along y and a strength of $\delta = \partial \Delta_y / \partial \varphi_y \big|_{x=0} \pi \theta d_{s,x} / d_{1,y}$ per lattice constant $d_{s,x}$ for a given superlattice phase $\varphi_y^{(0)}$. By measuring the strength of the gradient, one can thus determine the superlattice angle θ .

This can for example be done by observing the Bloch oscillations that are induced by this additional gradient for particles which are localized on either even or odd sites. For a given Bloch wave that is an eigenstate of the superlattice Hamiltonian for $\theta = 0$, the gradient leads to a linear increase of the quasi-momentum in the x -direction. For $V_{1,x} = 0$, the time evolution of a 1D Bloch wave in the short lattice along x with quasi-momentum k_x can be expressed as

$$\begin{aligned} \psi_{k_x}^{\pm}(x, t) &= \frac{1}{\sqrt{l_x}} \sum_{m_x} e^{ik_x d_{s,x} m_x} e^{-i \Delta_y^{\pm}(\varphi_y) t / \hbar} w_{m_x}(x) \\ &= \frac{1}{\sqrt{l_x}} \sum_{m_x} e^{i \left(k_x \mp \frac{2\pi}{d_{s,x}} \frac{\delta}{\hbar} t \right) d_{s,x} m_x} w_{m_x}(x) \end{aligned} \quad (6.5)$$

neglecting the global phase resulting from $\Delta_y^{\pm}(\varphi_y^{(0)})$. Here, $\psi_{k_x}^+$ ($\psi_{k_x}^-$) denotes the wave function for particles on even (odd) sites in the y -direction and w_{m_x} the Wannier function on the m_x -th site along x . Depending on which sites the atoms are localized on, the quasi-momentum thus either increases or decreases with a rate of $2k_{s,x}/\tau_B$, where $k_{s,x} = \pi/d_{s,x}$ is the wave vector of the short x -lattice and $\tau_B = \hbar/\delta$ the period of the Bloch oscillations.

To determine δ experimentally, the Bloch oscillation period is measured independently in two different lattice configurations, in which all of the atoms are on even or odd sites along y , respectively. For this, a superfluid atom cloud is prepared at $\mathbf{k} = 0$ in a 2D lattice formed by the short x -lattice with $V_{s,x} = 13.0(4)E_{r,s}$ and the long y -lattice at $V_{1,y} = 10.0(3)E_{r,1}$. The lattice sites are then split along the y -direction by first increasing $V_{1,y}$ to $70(2)E_{r,1}$ in 0.2 ms and subsequently ramping up the short y -lattice to $V_{s,x} = 20.0(6)E_{r,s}$ in 0.4 ms. The superlattice phase $\varphi_y^{(0)}$ is set to either $0.344(5)\pi$ or $0.656(5)\pi$ to completely localize the atoms on even or odd sites along y , respectively. After a variable hold time, the momentum distribution is measured by switching off all lattice potentials instantaneously and imaging the atoms after 10 ms time-of-flight. The gradient δ is determined from the average of the Bloch oscillation periods for both phases, which minimizes the effect of any residual gradients that might be present in addition to the lattice potential. Two examples for such a measurement are shown in Fig. 6.4b and c. From this, one can then extract a value for θ by calculating $\partial \Delta_y / \partial \varphi_y \big|_{x=0}$ for the experimental lattice parameters.

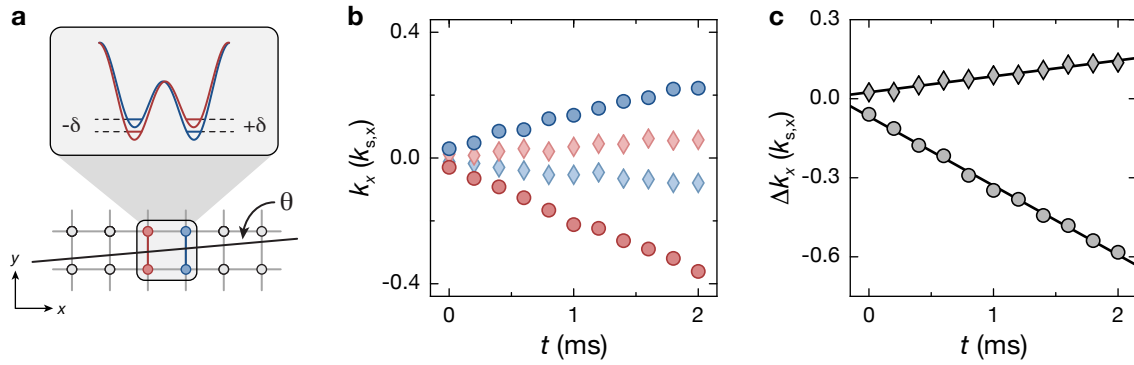


Figure 6.4 – Measurement of the superlattice tilt angle. (a) The perturbing superlattice angle θ leads to a position-dependent superlattice phase along y . Therefore, the corresponding double-well tilt depends on the position in the x -direction as illustrated for the two neighbouring double wells marked in red and blue (magnified frame). This leads to an energy difference $\pm\delta$ between neighbouring sites in the x -direction, which has opposite signs for even and odd sites along y . If θ is sufficiently small, δ is approximately constant over the size of the system and the additional potential is a linear gradient along x . (b) This gradient can be probed by studying the Bloch oscillations that it induces for a cloud which is initially prepared at $\mathbf{k} = 0$ in a 2D lattice with $V_{s,x} = 13.0(4)E_{r,s}$, $V_{s,y} = 20.0(6)E_{r,s}$ and $V_{l,y} = 70(2)E_{r,l}$. For this, the quasi-momentum along x , k_x , is measured as a function of the hold time t . The transverse superlattice phase $\varphi_y^{(0)}$ is either $0.344(5)\pi$ (blue points) or $0.656(5)\pi$ (red points) such that the atoms occupy only even or odd sites along y , respectively, and thus experience a gradient in opposite directions. The plot shows two examples of such a measurement for a smaller positive (diamonds) and larger negative tilt angle (circles). k_x is determined by a Gaussian fit to the central superfluid peak after 10 ms time-of-flight. Each data point is the average of 12 measurements and the statistical error is smaller than the size of the data points. (c) The effect of residual gradients can be removed by calculating the differential displacement between the two phases as shown here for the measurements from (b). The gradient δ is determined by a linear fit to the data points yielding $\delta = 15.1(8)$ Hz and $\delta = -65.7(1.2)$ Hz with the error indicating the fit error. This corresponds to a tilt angle of $\theta = 0.196(10)$ mrad and $\theta = -0.852(16)$ mrad, respectively. Note that the small offset at $t = 0$ is due to the finite ramp-up time of the short y -lattice for the preparation of the initial state (see text).

6.1.3 The Pump Cycle

To probe the non-linear pumping response of the lattice geometry shown in Fig. 6.2, the pump parameter φ_x is varied adiabatically, leading to a periodic modulation of the system's Hamiltonian. As for the 1D topological charge pump (see Section 4.1.1), a change by 2π constitutes one pump cycle, after which the Hamiltonian becomes identical to the initial state again. During this cycle, both δJ_x and Δ_x are modulated in such a way that the system evolves along a closed trajectory in the δJ_x - Δ_x parameter space (Fig. 6.5a). This pump path encloses the degeneracy point at $(\delta J_x = 0, \Delta_x = 0)$, where the two lowest subbands of the Rice-Mele Hamiltonian touch at $k_x = \pm\pi/d_1$. As detailed in Section 2.1.3 for the 1D case, this singularity can be thought of as the origin of the non-trivial distribution of the Berry curvature Ω^x . All paths enclosing the origin are therefore topologically equivalent in terms of the linear pumping response, i.e. are characterized by the same first Chern number.

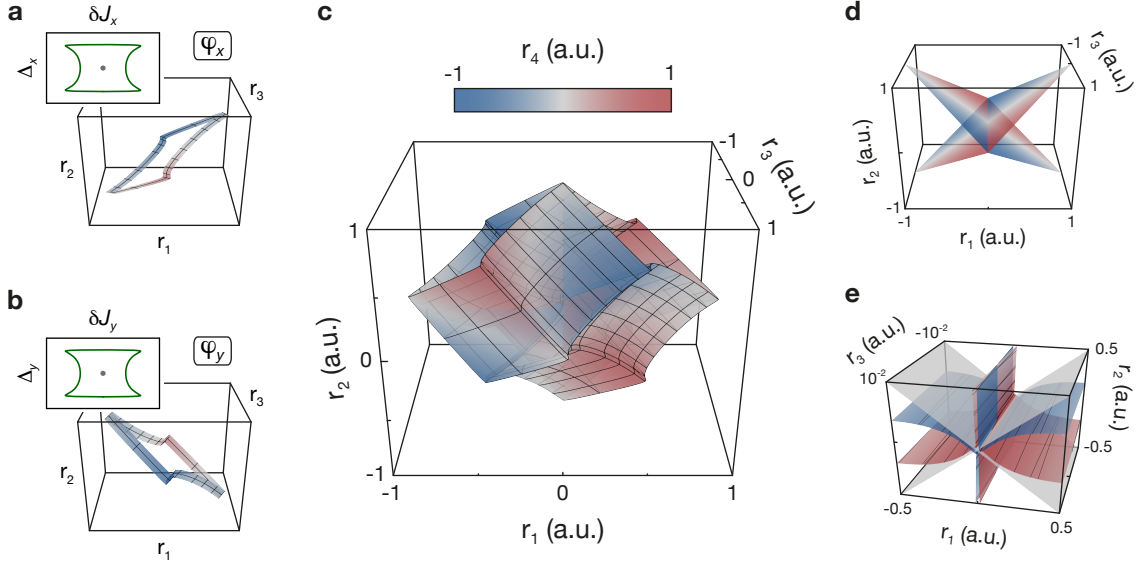


Figure 6.5 – Pump cycle of the 2D topological charge pump in the 4D tight-binding parameter space.

The tight-binding parameters δJ_x , Δ_x , δJ_y and Δ_y of the 2D superlattice Hamiltonian are calculated for $V_{s,x} = V_{s,y} = 7E_{r,s}$ and $V_{l,x} = V_{l,y} = 20E_{r,l}$ and transformed using Eq. (6.6) for visualization. **(a)** The inset shows the pump path (green) in the δJ_x - Δ_x parameter space when varying the pump parameter $\varphi_x = 0 \rightarrow 2\pi$. This modulates δJ_x and Δ_x periodically, corresponding to a closed loop surrounding the singularity at the origin (grey). For a given value of φ_y , the transformed pump path in the 4D parameter space is a closed line as well, depicted in the main plot for $\varphi_y \in [0.46\pi, 0.54\pi]$. The mesh grid indicates φ_x with a spacing of $\pi/10$ between the lines. **(b)** In the same way, a variation of φ_y changes δJ_y and Δ_y along a closed path as shown in the inset. In this parameter space, another band closing point exists at the origin. The transformed trajectory is depicted in the main plot for $\varphi_x \in [0.46\pi, 0.54\pi]$ with the mesh grid illustrating φ_y in steps of $\pi/10$. **(c)** 4D pump path mapped out by a large system of length $L_x \gg d_{l,y}/\theta$ during one pump cycle. In this case, φ_y extends over the full range $[0, 2\pi[$, realizing all combinations of δJ_y and Δ_y on the path shown in (b) at the same time. When performing the pumping by changing φ_x , this trajectory is translated along the pump path shown in (a) and the system maps out a closed surface in the 4D parameter space. **(d)** Degeneracy planes at $(\delta J_x = 0, \Delta_x = 0)$ and $(\delta J_y = 0, \Delta_y = 0)$ in the transformed 4D parameter space, in which they correspond to perpendicular planes in the (r_1, r_2, r_3) -space and intersect at the origin. **(e)** The 4D pump path from (c) (red/blue) and the degeneracy planes from (d) (grey) in the vicinity of $r_3 = 0$. In 4D, the pump path can completely surround the extended singularities. Even though they intersect in the 3D (r_1, r_2, r_3) -space, the value of r_4 is different for the pump path as compared to the degeneracy planes. Figure taken from on [150].

The lattice configuration in the y -direction in a given unit cell is described by a set of parameters $\delta J_y(\varphi_y)$, $\Delta_y(\varphi_y)$, which are determined by the local superlattice phase along y , $\varphi_y(x)$. As a result of the motion along x induced by the pumping, a particle that is initially localized in one unit cell sequentially samples different values of φ_y , eventually covering the entire range $[0, 2\pi[$ after $1/(\nu_1^x \theta)$ pump cycles. During this evolution, analogous to the x -direction, δJ_y and Δ_y trace out a closed loop in the corresponding parameter space (Fig. 6.5b), in which another degeneracy point exists at $(\delta J_y = 0, \Delta_y = 0)$.

In the full 4D parameter space spanned by δJ_x , Δ_x , δJ_y and Δ_y , the particle thus covers the closed surface that is obtained by translating the 1D pump path $(\delta J_x(\varphi_x), \Delta_x(\varphi_x))$

along the trajectory $(\delta J_y(\varphi_y), \Delta_y(\varphi_y))$. Note that in a large system of length $L_x \gg d_{1,y}/\theta$, all possible configurations $(\delta J_y(\varphi_y), \Delta_y(\varphi_y))$ are realized simultaneously and therefore the entire surface is sampled in a single pump cycle $\varphi_x = 0 \rightarrow 2\pi$. To illustrate this 4D pump path in Fig. 6.5c, the tight-binding parameters are normalized by their respective maximum values and transformed as

$$\begin{pmatrix} r_1 \\ r_2 \\ r_3 \\ r_4 \end{pmatrix} = \frac{1}{4} \begin{pmatrix} 1 & 1 & -1 & -1 \\ 1 & 1 & 1 & 1 \\ 1 & -1 & -1 & 1 \\ 1 & -1 & 1 & -1 \end{pmatrix} \cdot \begin{pmatrix} \delta J_x / \delta J_x^{(0)} \\ \Delta_x / \Delta_x^{(0)} \\ \delta J_y / \delta J_y^{(0)} \\ \Delta_y / \Delta_y^{(0)} \end{pmatrix} \quad (6.6)$$

The singularities at $(\delta J_x = 0, \Delta_x = 0)$ and $(\delta J_y = 0, \Delta_y = 0)$ correspond to two perpendicular planes in the 4D tight-binding parameter space that intersect at a single point – the origin. The transformation is chosen such that the two degeneracy planes are transformed to orthogonal planes in the (r_1, r_2, r_3) -space, which are the three spatial dimensions in Fig. 6.5. The singularities can then be expressed as $r_1 = -r_2$, $r_3 = -r_4$ and $r_1 = r_2$, $r_3 = r_4$ (Fig. 6.5d).

If the trajectories in the δJ_x - Δ_x and δJ_y - Δ_y parameter spaces each enclose the respective singularity, the 4D pump path encompasses the degeneracy planes (Fig. 6.5e). This is possible only due to the 4D nature of the parameter space. In analogy to the linear pumping response, these singularities can be interpreted as the source of the non-vanishing product of Berry curvatures $\Omega^x \Omega^y$ in the 4D generalized Brillouin zone, which induces the non-linear response along y . All pump paths that surround the singularities can be connected by a smooth transformation during which the gap between the ground-state band and the excited bands remains open. Even though the local distribution of $\Omega^x \Omega^y$ might change, these paths are thus characterized by the same value of the second Chern number and exhibit the same quantized non-linear pumping response. The latter is therefore topologically protected against all kinds of local and global perturbations as long as they do not cause a closing of the band gap, i.e. move the pump path across the singularities (see also Sections 2.1.3 and 2.2.3).

In the experiment, the pump parameter φ_x is changed by varying the frequency of the laser for the long x -lattice, which determines its position relative to the short lattice as detailed in Section 3.2. The cycle starts at $\varphi_x = \varphi_x^{(0)} = 0.000(5)$ in the staggered configuration with equal tunnel couplings $\delta J_x = 0$ and the maximum energy difference between neighbouring sites $|\Delta_x|$. One pump cycle $\varphi_x = 0 \rightarrow 2\pi$, i.e. a shift by one long lattice constant, is equivalent to a frequency difference of 1229 MHz. As the laser used for the long x -lattice (RIO ORION 3135) has a limited tuning range of about 1.8 GHz, an additional laser is required for performing multiple cycles similar to the experiments in Chapter 4. This second laser operates at a fixed frequency corresponding to a constant phase of $\varphi_x = 0.000(5)$. It is used to hold the atoms in a static lattice configuration while the frequency of the primary laser is ramped back to its initial value. With this, one can connect multiple cycles by performing an instantaneous switch from the primary laser to the secondary one at the end of each cycle, which leaves the lattice configuration invariant.

It was confirmed experimentally that the switching between the lasers does not cause any measurable band excitations. With the primary laser off, its frequency is changed to the starting point ($\varphi_x = 0$) within 5 ms and – after switching back from the secondary laser to the primary one – the next cycle begins.

To reduce non-adiabatic transitions to higher bands, which can be induced by the pumping, each cycle is split into three segments $\varphi_x \in [0, 0.5\pi]$, $[0.5\pi, 1.5\pi]$ and $[1.5\pi, 2\pi]$ with s-shaped phase ramps. This minimizes the speed around the symmetric double-well configurations at $\varphi_x = (l + 1/2)\pi$, $l \in \mathbb{Z}$, where the spatial overlap between the Wannier functions of the ground and first excited band along x is largest and the respective band gap is smallest. The duration is 7 ms for the $\pi/2$ -ramps and 14 ms for the π -ramp. For the lattice parameters used for the measurements in Sections 6.3 and 6.4 ($V_{s,x} = 7.0(2)E_{r,s}$, $V_{l,x} = 20.0(6)E_{r,l}$), this ramp speed minimizes the band excitations that are created during one cycle by pumping-induced transitions and technical heating in the superlattice.

6.1.4 Local Probing

For a given eigenstate at k_x and k_y in a lattice configuration defined by the local superlattice phases φ_x and $\varphi_y(x)$, the anomalous velocity along y is $v_y(k_x, \varphi_x, k_y, \varphi_y) = \frac{2\pi}{d_{l,y}}\theta \Omega^x \Omega^y \dot{\varphi}_x$ as derived in Section 5.2.2. This geometric property can be probed locally by studying the non-linear pumping response with a small atom cloud that is localized in momentum space. If the extent of the system in the x -direction is very small compared to $d_{l,y}/\theta$, the change of $\Omega^x \Omega^y$ over the cloud size is negligible and its response is characterized by $\Omega^x \Omega^y(\varphi_y^{(0)})$. An example for the distribution of $\Omega^x \Omega^y$ in the 4D generalized Brillouin zone is shown in Fig. 6.6a for $V_{s,x} = V_{s,y} = 7E_{r,s}$ and $V_{l,x} = V_{l,y} = 20E_{r,l}$. In the tight-binding regime, $\Omega^x \Omega^y$ varies quite strongly throughout the Brillouin zone and, in particular, exhibits two pronounced peaks along both φ_x and φ_y for $d_l = 2d_s$. They occur at $\varphi_\mu = (l + 1/2)\pi$ with $l \in \mathbb{Z}$ and $\mu \in \{x, y\}$. These are the symmetric double-well configurations, in the vicinity of which the particles tunnel from one site to the neighbouring one during the pumping.

In the same way, one can observe the local transport properties of an entire band. This can either be done with fermionic atoms that completely fill the respective band or – as in the present work – with bosonic ones that populate the band homogeneously. In analogy to the 1D case, the latter can for example be achieved by localizing the particles in individual unit cells of the lattice. For each atom, the localization in real space then leads to a uniform occupation of the entire subband corresponding to the state that the atom is prepared in. Its anomalous velocity is thus determined by the integrated quantity $\overline{\Omega^x \Omega^y}(\varphi_x, \varphi_y) = \int \Omega^x \Omega^y d^2k$, which is depicted in Fig. 6.6b. The peaks of the Berry curvature in the 4D generalized Brillouin zone also manifest in the motion of a localized particle as the non-linear drift per pump cycle shows a clear maximum at $\varphi_y = (l + 1/2)\pi$. In its vicinity, the response can be substantially larger than the quantized response of an infinite system. The latter can be obtained from the local transport measurements by repeating them for different values of $\varphi_y^{(0)}$ as detailed in Section 6.4.1.

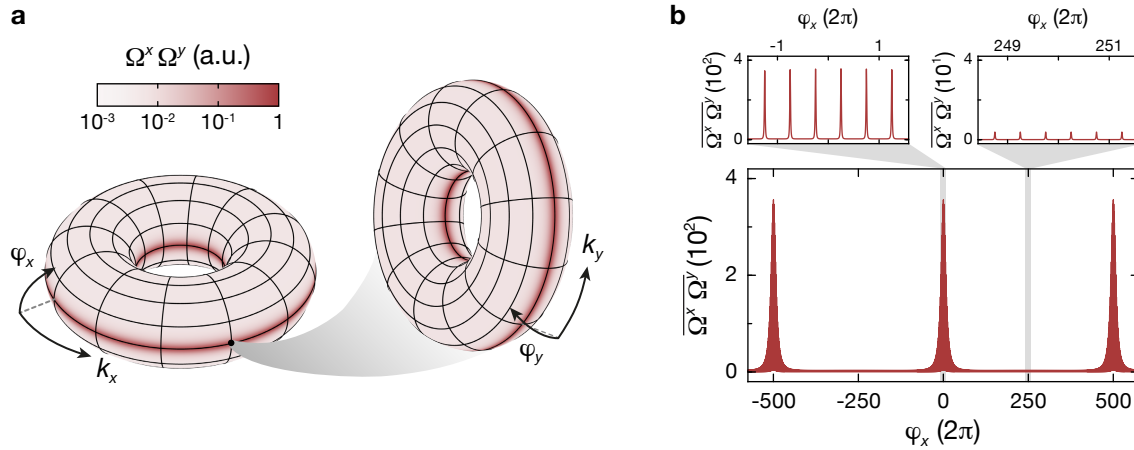


Figure 6.6 – Product of Berry curvatures $\Omega^x \Omega^y$ in the 4D generalized Brillouin zone. (a) 2D cuts through the generalized Brillouin zone showing $\Omega^x \Omega^y$ in the lowest subband for $V_{s,x} = V_{s,y} = 7E_{r,s}$, $V_{l,x} = V_{l,y} = 20E_{r,l}$ and $d_l = 2d_s$. The torus on the left is a cut along k_x and φ_x at $k_y = 0$ and $\varphi_y = \pi/2$, whereas the right one is a cut along k_y and φ_y for $k_x = \pi/(2d_l)$ and $\varphi_x = \pi/2$. Figure adapted from [150]. (b) Integrated Berry curvature $\overline{\Omega^x \Omega^y}(\varphi_x, \varphi_y) = \int \Omega^x \Omega^y d^2k$ versus φ_x as seen by a particle that is localized in a single unit cell for $\theta = 1$ mrad and $\varphi_y^{(0)} = \pi/2$. As φ_x is varied, the linear pumping response leads to a motion of the particle along x , starting from its initial position at $x = 0$. Thereby the particle sequentially samples different local lattice configurations $\varphi_y(x)$, which induces the non-linear response along y with an anomalous velocity determined by $\overline{\Omega^x \Omega^y}$. Since $\overline{\Omega^x \Omega^y}$ is strongly peaked as a function of both φ_x and φ_y in the tight-binding limit, the non-linear motion occurs in steps, corresponding to the pronounced peaks in the main plot. These in turn consist of many sharp peaks resulting from the step-like tunnelling of the particle between neighbouring sites along x in response to the pumping (zoom in insets).

6.2 Resolving the Non-Linear Response In-Situ

In the experiment, the pumping response of the lowest subband with $\nu_2 = +1$ is studied using a small Mott-insulating atom cloud. To directly observe the non-linear bulk response in the transverse direction, which is orders of magnitudes smaller than the linear response, the centre-of-mass displacement is measured in-situ using a novel double-differential imaging technique. Signatures of this new physical phenomenon and its non-linear 4D-like character are revealed by local probing of the transverse response. In Section 6.2.1, we discuss the preparation and characterization of the initial fractional Mott insulator, which creates a uniform distribution of atoms in the lowest subband. Subsequently, the double-differential imaging technique is introduced (Section 6.2.2) and the measurements of the in-situ centre-of-mass response are presented (Section 6.2.3).

6.2.1 Initial State Preparation

To experimentally probe the non-linear pumping response of the lowest subband, a Mott insulator with quarter filling and about 5000 atoms is prepared as an initial state, in which one atom is localized in the ground state of each 2×2 plaquette and thus samples all single-

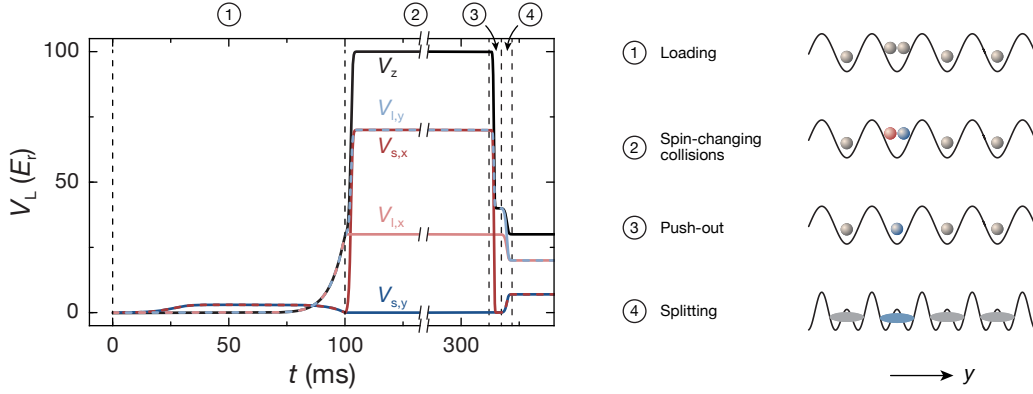


Figure 6.7 – Preparation of the initial state. The sequence for preparing the initial state consists of four parts. The corresponding ramps of the lattice depths are shown in the plot on the left (in units of the respective recoil energy). In the beginning (1), a Mott insulator with unit filling and a small residual doublon fraction is prepared in the long lattices along x and y as well as the vertical z -lattice. After that, atoms on doubly-occupied sites are transferred to different spin states ($F = 1$, $m_F = \pm 1$) via microwave-dressed spin-changing collisions (2). For this, the lattice depths are increased to maximize the on-site interaction energy. Subsequently, the lattices are lowered again to remove atoms in the $m_F = -1$ state by a resonant optical push-out, thereby converting doublons to singly-occupied sites (3). Finally, to obtain the Mott-insulating state with quarter filling in the desired superlattice configuration, each site in the long lattices is split to a 2×2 plaquette by ramping up the short lattices to their final depths and simultaneously changing the depths of long lattices to the respective final values.

particle eigenstates of the lowest subband. An overview of the entire loading sequence is given in Fig. 6.7. It consists of four parts: (1) loading of an $n = 1$ Mott insulator in the long lattices, (2) transfer of atoms on doubly-occupied sites to different hyperfine states by spin-changing collisions, (3) conversion to singly-occupied sites by an optical push-out pulse and (4) preparation of the final state in the 2D superlattice.

Starting from a Bose-Einstein condensate in the crossed dipole trap, a Mott-insulating state with unit filling is initially prepared in the two long lattices along x and y as well as the vertical z -lattice. For this, the blue-detuned short lattices are first increased to $V_{s,x} = V_{s,y} = 3.0(1)E_{r,s}$ within 50 ms to reduce the density of the atom cloud. Subsequently, the long lattices and the z -lattice are ramped up to $V_{l,x} = V_{l,y} = 30(1)E_{r,l}$ and $V_z = 30(1)E_{r,z}$ during 50 ms, while simultaneously switching off the short lattices. The superlattice phase along x is in the staggered configuration, $\varphi_x = \varphi_x^{(0)} = 0.000(5)\pi$, while the one along y is set to its final value $\varphi_y^{(0)}$. The latter is referenced to the initial position of the atom cloud along x , which is defined as $x_i = 0$ such that $\varphi_y = \varphi_y^{(0)}$ initially.

Removal of Doubly-Occupied Sites

Due to the low density of the unit-filled Mott insulator in the long lattices and the much smaller on-site interaction compared to the short lattices, doubly-occupied sites are easily created during this loading procedure. Typically, a doublon fraction, i.e. fraction of atoms in doubly-occupied unit cells, of about 25% is observed despite the reduction of the

initial density by the blue-detuned lattices. Therefore, the initial loading is followed by a cleaning sequence to convert doubly-occupied sites to singly-occupied ones via microwave-mediated spin-changing collisions (SCC) and a resonant optical push-out pulse [277].

Spin-changing collisions arise from the spin dependence of the interaction potential between two atoms [278–281]. Due to the exchange interaction, it has a different strength depending on the total angular momentum of the two-particle state. This leads to transitions between different atomic hyperfine states during a scattering process, which preserve the total angular momentum as well as its component along the quantization axis. For s -wave scattering, the transitions are driven by the difference between the scattering lengths for different total angular momenta. The coupling strength also depends on the overlap of the spatial wave functions of both particles and is about two orders of magnitude smaller than the on-site interaction energy for ^{87}Rb . The transitions are thus usually strongly suppressed due to the detuning induced by the quadratic Zeeman effect and the spin dependence of the on-site interaction energy, which have the same sign for ^{87}Rb . This can be compensated e.g. by a microwave dressing field that induces an additional AC Stark shift by a weak coupling to a different hyperfine manifold [277].

In the experiment, the lattices are raised to $V_{s,x} = 70(2)E_{r,s}$, $V_{1,x} = 30(1)E_{r,s}$, $V_{1,y} = 70(2)E_{r,s}$ and $V_z = 100(3)E_{r,z}$ after the initial loading to increase the on-site interaction energy, which in turn increases the coupling for the spin-changing collisions. At this point, all atoms are in the $(F = 1, m_F = -1)$ hyperfine state. To allow for the spin-changing collisions to take place, the atoms are brought to the $m_F = 0$ state by an adiabatic Landau-Zener transfer with a radio-frequency wave (see Fig. 6.8a for details). To turn the atoms on doubly-occupied sites into pairs of $m_F = \pm 1$ atoms, a weak microwave dressing field is switched on. It is slightly red-detuned from the $(F = 1, m_F = -1) \rightarrow (F = 2, m_F = -2)$ transition to compensate the quadratic Zeeman shift and the difference in the on-site interaction energy. The microwave frequency and power are chosen such that the two spin configurations become degenerate at a magnetic bias field of 1.59 G, where the detuning of the microwave is -0.2 MHz. The magnetic field is slowly ramped across the SCC resonance to adiabatically transfer the doublons from $|m_F = 0, m_F = 0\rangle$ and $|m_F = \pm 1, m_F = \mp 1\rangle$ (Fig. 6.8a). The conversion efficiency can be determined by measuring the doublon fraction that remains in $m_F = 0$ (see Section 6.3.2) and amounts to 98.2(1.0)%.

To remove one atom from each doubly-occupied site, the atoms in $(F = 1, m_F = -1)$ are transferred to $(F = 2, m_F = -2)$ by ramping the magnetic field over the corresponding resonance within 5 ms while the dressing microwave field is still on (Fig. 6.8a). The ramp time is chosen to be fast compared to the coupling of the spin-changing collisions, but slow with respect to the much larger microwave Rabi frequency. Afterwards, the microwave is switched off and the magnetic field is lowered to a small offset value to maintain the quantization axis. The lattices are ramped down to $V_{s,x} = 0E_{r,s}$, $V_{1,x} = 30(1)E_{r,1}$, $V_{1,y} = 40(1)E_{r,1}$ and $V_z = 40(1)E_{r,z}$ to allow for an efficient removal of the $F = 2$ atoms by a subsequent resonant optical push-out pulse, driving the $F = 2 \rightarrow F = 3$ D_2 transition, with a length of 2 ms (Fig. 6.8b). This push-out sequence is used for all measurements of the non-linear response with the exception of the in-situ data in Section 6.2.3, for

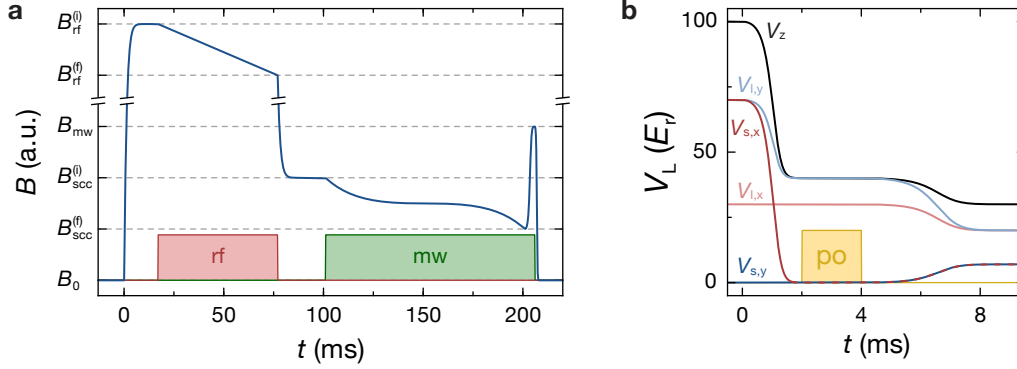


Figure 6.8 – Removal of doubly-occupied sites. (a) Sequence for microwave-dressed spin-changing collisions. In the first part, the atoms are transferred from the ($F = 1, m_F = -1$) hyperfine state, which they are initially prepared in, to the ($F = 1, m_F = 0$) state by an adiabatic Landau-Zener transfer. To this end, the magnetic field (blue solid line, not to scale) is first increased to $B_{\text{rf}}^{(f)} = 21.8(3)$ G and then slowly lowered to $B_{\text{rf}}^{(f)} = 21.0(3)$ G in the presence of a radio-frequency field (rf) at 15.0 MHz. Subsequently, pairs of $m_F = 0$ atoms are converted to an $m_F = +1$ and $m_F = -1$ atom each by microwave-mediated spin-changing collisions. For this, the magnetic field is decreased to $B_{\text{scc}}^{(i)} = 1.64(3)$ G and – after switching on the microwave dressing field (mw) at 6831.14 MHz – adiabatically ramped over the spin-changing collision resonance to $B_{\text{scc}}^{(f)} = 1.54(3)$ G within 100 ms. Finally, the $m_F = -1$ atoms are transferred to ($F = 2, m_F = -2$) by quickly increasing B to $B_{\text{mw}} = 1.78(3)$ G while the microwave is still on, thereby crossing the resonance at 1.69 G. (b) Standard sequence for the push-out of $F = 2$ atoms used for all band mapping measurements. After the spin-changing collisions, the lattice depths are lowered to facilitate the push-out by a 2 ms optical pulse (po) resonant on the $F = 2 \rightarrow F = 3$ D_2 transition. This converts doubly-occupied sites to singly-occupied ones by removing all $F = 2$ atoms from the lattice. Afterwards, the lattices are ramped to their final depths within 5 ms, splitting each long lattice site into a 2x2 superlattice plaquette.

which the initial centre-of-mass position is determined in addition (see Section 6.2.2 and Fig. 6.10b for details). It was confirmed experimentally that the push-out pulse does not lead to a significant loss of the ($F = 1, m_F = +1$) atoms located on the same sites due to light-assisted collisions [282–284].

As the last step of the initial state preparation, the lattices depths are changed to their final values for the respective sequence within 5 ms. In particular, the short lattices are ramped up, which splits each site of the long lattices to a four-site plaquette forming the unit cell of the 2D superlattice. This creates a Mott-insulating state with quarter filling, where each plaquette is occupied by a single atom in the ground state. The doublon fraction in this state is negligible and the fraction of atoms in the first excited band along both x and y is about 2% each, which is mostly due to excitations created during the push-out.

Determination of the System Size

To locally probe the transport properties of the tilted superlattice, the atom cloud has to be sufficiently small such that the position-dependent transverse superlattice phase $\varphi_y(x)$ is approximately constant throughout the cloud (see Section 6.1.4). While the size of

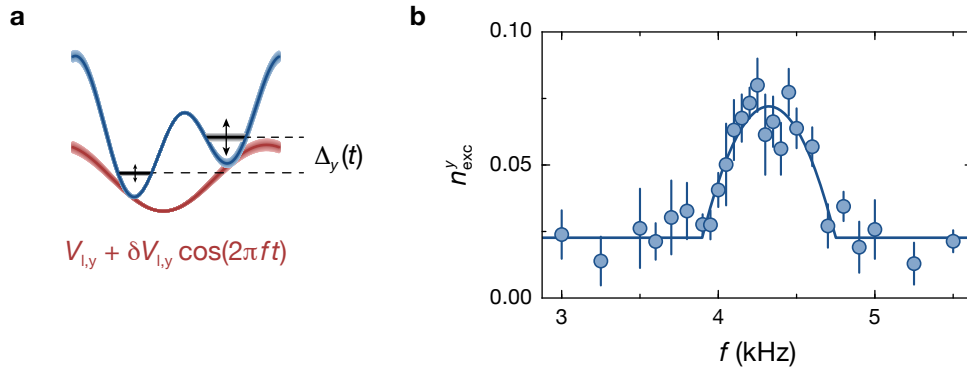


Figure 6.9 – Determination of the system size along x by lattice modulation spectroscopy. (a) Schematic illustration of the lattice modulation. The depth of the long y -lattice is modulated periodically with a frequency f and amplitude $\delta V_{1,y}$ in a tilted double-well configuration at a fixed phase $\varphi_y^{(0)}$. This leads to a modulation of the double-well tilt Δ_y , which can induce transitions between the ground and first excited state in the double well along y . (b) Measurement of the energy gap distribution within the atom cloud for $V_{s,y} = 7.0(2)E_{r,s}$, $V_{1,y} = 20.0(6)E_{r,l}$, $\varphi_y^{(0)} = 0.421(5)\pi$ and $\theta = 0.56(4)$ mrad. The fraction of atoms in the first excited band along y , n_{exc}^y , is depicted as a function of the modulation frequency for a modulation time of 100 ms and amplitude $\delta V_{1,y} = 0.64(2)E_{r,l}$. The solid line is a fit to the data assuming an ellipsoidal cloud shape as detailed in the main text, yielding an average length of $L_x = 21(2)d_s$. The data points are the average of 3-13 measurements with a mean atom number of 4000(900) and the error bars illustrate the error of the mean.

the system in the pumping direction after the initial loading procedure could in principle be inferred directly from the in-situ images, the optical resolution of the imaging system is not sufficient to do this accurately. An estimate for the system size can instead be obtained from the distribution of energy gaps in the double wells along y , which results from the position dependence of $\varphi_y(x)$ itself. This can be done using lattice modulation spectroscopy, where transitions between the two lowest subbands along y are induced by modulating the depth of the long y -lattice with a frequency f (Fig. 6.9a). To this end, localized atoms are prepared in the lowest subband as discussed above with final lattice depths of $V_{s,x} = V_{s,y} = 7.0(2)E_{r,s}$ and $V_{s,x} = V_{s,y} = 20.0(6)E_{r,l}$ at $\varphi_x = 0.000(5)\pi$ and $\varphi_y = 0.421(5)\pi$. In this lattice configuration, the ground-state atoms are fully localized on the lower-lying even sites along both x and y . By measuring the fraction of atoms on odd sites along y , which is equivalent to the fraction in the excited band, as a function of the modulation frequency after a fixed modulation time, one can determine the distribution of double-well energy gaps in the system (Fig. 6.9b).

Assuming that the initial Mott insulator has an ellipsoidal shape with a homogeneous density and neglecting effects of the discrete lattice structure and any surrounding superfluid atoms, the density of atoms at a given position x integrated along y and z is given by

$$n_x(x) = \frac{6N}{L_x^3} \left(\frac{L_x}{2} - x \right) \left(\frac{L_x}{2} + x \right) \quad (6.7)$$

for $|x| \leq L_x/2$ and a total atom number N . As φ_y depends linearly on x , the same holds for the distribution of the energy difference between the ground and first excited state of the

double wells along y if the system is sufficiently small such that the variation of φ_y is very small, $\varphi_y(L_x/2) - \varphi_y(-L_x/2) \ll 1$. The measured fraction of excited atoms can thus be fitted by a function of the form of Eq. (6.7) to determine the range of frequencies. Knowing the tilt angle and the dependence of the double-well gap on the superlattice phase, one can obtain an estimate for the extent of the system along x . For the measurement in Fig. 6.9, this gives an average length of $L_x/d_s = 21(2)$ lattice sites. This corresponds to a difference of φ_y of about 0.01π between the left and right edge of the system, which is comparable to the experimental uncertainty of the superlattice phase of $\pm 0.005\pi$. A cloud of this size is therefore very well suited to locally probe the pumping response of the system.

6.2.2 Double-Differential In-Situ Imaging

As the non-linear response is induced by two weak perturbations – the pumping and the tilt angle – it is orders of magnitude smaller than the linear response. For typical lattice parameters, the displacement along y is only a fraction of a lattice constant per cycle. This makes it very challenging to resolve the centre-of-mass motion via in-situ measurements, in particular since the number of pump cycles in the experiment is limited by heating (see Section 6.3.2). The limiting factor for resolving changes in the centre-of-mass position are shot-to-shot fluctuations and long-term drifts of the initial position of the atom cloud, which are on the order of $\pm 2d_s$ in the experiment (Fig. 6.10c). To minimize their effect on the measurement, a double-differential imaging technique is employed: the centre-of-mass position is determined for the initial state (y_i) and the final one after the pumping (y_f) and compared to a reference system that does not exhibit a non-linear response ($y_i^{(0)}$ and $y_f^{(0)}$). For the latter, an identical sequence with the same number of pump cycles is used, but instead of the superlattice along y only the short y -lattice with $V_{s,y} = 40(1)E_{r,s}$ is on during the pumping.

To obtain the initial and final position in a single sequence, a part of the atom cloud is imaged during the push-out sequence, whereas the remaining atoms are imaged after performing the pumping (Fig. 6.10a). For this, the push-out sequence is modified compared to the one for the band mapping measurements as shown in Fig. 6.10b. In addition to the atoms from doubly-occupied sites that are transferred to the $F = 2$ hyperfine manifold after the spin-changing collisions, a microwave π -pulse resonant on the $(F = 1, m_F = 0) \rightarrow (F = 2, m_F = 0)$ is applied for the atoms on singly-occupied sites. The density distribution imaged by the following imaging pulse, which together with the subsequent push-out pulse removes all $F = 2$ atoms from the lattice, is thus identical to the one of the atoms that remain in the lattice.

As the removal of $F = 2$ atoms creates holes on half of the singly-occupied sites, the initial atom number is doubled to about 10000 atoms compared to the band mapping measurements. This leads to an increase of the initial doublon fraction to about 50% such that roughly one third of the lattice sites contain holes in the initial state for the pumping. However, since the other atoms remain localized during the imaging and push-out, their distribution in momentum space is still homogeneous and the pumping response

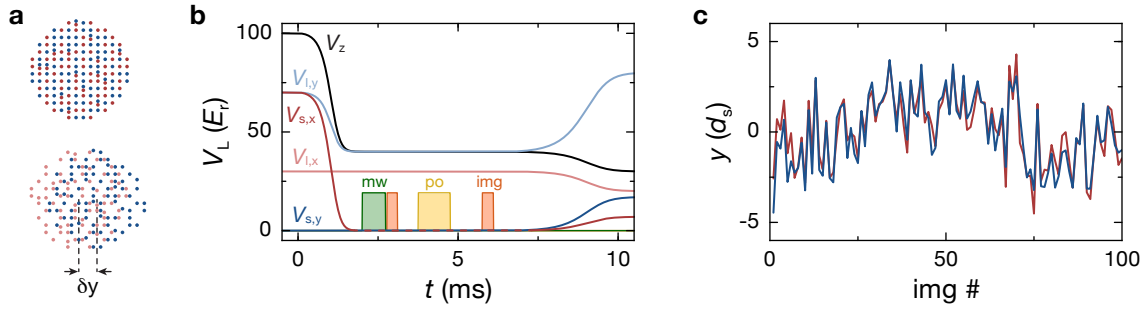


Figure 6.10 – Differential in-situ imaging with reference position. (a) Schematic illustration of the differential measurement of the non-linear centre-of-mass drift. Prior to the pumping, half of the atoms (red) are imaged during the push-out to obtain an initial reference position y_i . The centre-of-mass position of the remaining atoms is measured after the pumping (y_f) to determine the differential shift $\delta y = y_f - y_i$. (b) Push-out sequence for the differential in-situ measurements. After the spin-changing collisions, the lattice depths are reduced and atoms on singly-occupied sites, which remained in ($F = 1, m_F = 0$), are partially transferred to ($F = 2, m_F = 0$) by a microwave π -pulse (mw). All $F = 2$ atoms, including the ones originating from doubly-occupied sites, are then imaged by an imaging pulse (img), which is resonant on the $F = 2 \rightarrow F = 3$ D_2 transition. Subsequently, a 1 ms push-out pulse (po) is applied to completely remove all remaining $F = 2$ atoms, before taking the dark image with a second imaging pulse. At the end, the initial state for the pumping sequence is prepared by ramping up the lattices to their final values in 5 ms and splitting the long lattice sites into 2×2 plaquettes. (c) Comparison of the initial (red) and final (blue) centre-of-mass position for a sequence without pumping ($\varphi_x = 0$). The standard deviation over the entire set of points is $2.0d_s$ ($1.9d_s$) for the final (initial) position, whereas the one of the differential position δy is only $0.7d_s$.

should not be affected. This was confirmed by an independent measurement of the non-linear response using site-resolved band mapping as in Section 6.3.1. Furthermore, it was verified experimentally that the modified push-out sequence does not create more band excitations than the standard one without the reference image.

6.2.3 In-Situ Measurement of the Non-Linear Response

In an infinite system, the quantized centre-of-mass drift along y is a factor of $\theta\nu_2/\nu_1^x$ smaller than the linear response. Given the experimental heating rates and an angle θ on the order of 1 mrad, it would thus require the ability to resolve a displacement of less than 1% of a lattice constant. This is significantly smaller than the precision achieved by the double-differential imaging technique introduced in Section 6.2.2. However, as explained in Section 6.1.4, using a small atom cloud allows one to locally probe the transport at different points in the 4D generalized Brillouin zone. Locally, the response can be substantially larger than the quantized average due to the peaked structure of the Berry curvatures $\Omega^x\Omega^y$ (Fig. 6.6). In particular – unlike the integrated response – the local transport properties depend on the specific choice of lattice depths.

For suitable parameters, signatures of the non-linear centre-of-mass displacement can be observed at $\varphi_y^{(0)} = 0.500(5)\pi$ with the double-differential in-situ measurement as shown in Fig. 6.11a. When the pump parameter φ_x is varied starting from $\varphi_x^{(0)} = 0.000(5)\pi$,

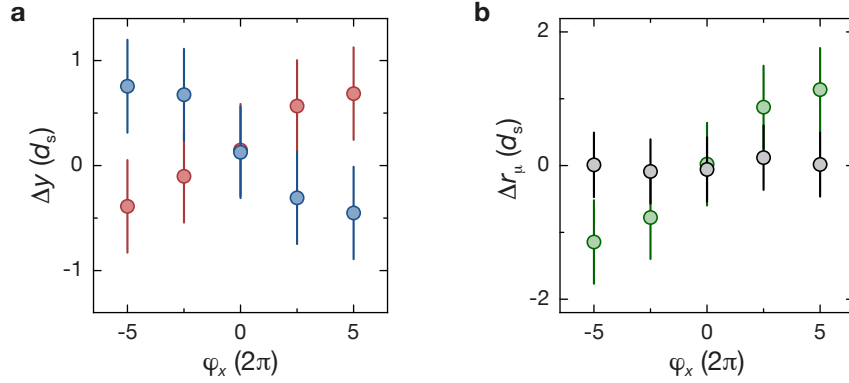


Figure 6.11 – Non-linear centre-of-mass response. (a) Double-differential centre-of-mass displacement along y , $\Delta y = (y_f - y_i) - (y_f^{(0)} - y_i^{(0)})$, as a function of the pump parameter φ_x for $\theta_1 = 0.78(2)$ mrad (red) and $\theta_2 = -0.85(2)$ mrad (blue) at $\varphi_y^{(0)} = 0.500(5)\pi$. The non-linear response is measured for $V_{s,x} = 7.0(2)E_{r,s}$, $V_{s,y} = 17.0(5)E_{r,s}$, $V_{l,x} = 20.0(6)E_{r,l}$ and $V_{l,y} = 80(3)E_{r,l}$ and compared to a reference configuration with $V_{s,y} = 40(1)E_{r,s}$ and $V_{l,y} = 0E_{r,l}$. The data points are the average of 100 measurements with the error bars indicating the total uncertainty resulting from the error of the mean and a systematic error of $\pm 0.3d_s$. (b) Difference of the centre-of-mass displacement for θ_1 and θ_2 in the x - (grey) and y -direction (green), $\Delta r_\mu = \Delta\mu(\theta_1) - \Delta\mu(\theta_2)$ with $\mu \in \{x, y\}$. The data points are calculated from the measurements shown in (a) using the double-differential displacement for the transverse response. For the linear response, Δr_x is determined directly without comparison to the reference sequence using $\Delta x = (x_i - x_f) - \delta\bar{x}$ with $\delta\bar{x}$ being the mean displacement of all points for the respective angle. This accounts for a residual constant offset between the measured initial and final position, which is possibly due to the different lattice configurations in which the two images are taken. Figure adapted from [150].

a drift in the y -direction can be seen in addition to the linear response along x . The sign of this transverse response depends on the pumping direction as expected, going to positive y for $\varphi_x > 0$ and to negative ones when $\varphi_x < 0$ at $\theta > 0$. Moreover, the sign of $\Delta y = (y_f - y_i) - (y_f^{(0)} - y_i^{(0)})$ reverses when the angle θ is inverted. The linear response along x , on the other hand, does not depend on θ (Fig. 6.11b). This constitutes the first observation of such a dynamical transverse bulk phenomenon and demonstrates the intrinsically 4D, non-linear nature of the transverse response as it originates from two independent perturbations in orthogonal subspaces.

6.3 Local Probing of the Non-Linear Response by Site-Resolved Band Mapping

To systematically study the local geometric properties of the non-linear response, the evolution of the transverse double-well imbalance is examined using site-resolved band mapping and compared to theoretical predictions. In Section 6.3.1, this method is presented and the relation between the measured imbalance and the centre-of-mass response is discussed. The response of the lowest subband can be isolated by carefully characterizing the

main contributions that cause a reduction of the response compared to an ideal system. In Section 6.3.2, a model is developed that accounts for these experimental imperfections, allowing for a precise quantitative study of the local ground-state transport properties. This is demonstrated in Section 6.3.3 by determining the non-linear response for different lattice configurations ranging from the Landau limit to the Hofstadter regime.

6.3.1 Measurement of the Double-Well Imbalance

While the non-linear response can be observed in-situ, it is too small to be quantified reliably, in particular when trying to locally probe it at different points in the 4D generalized Brillouin zone, where its magnitude can be substantially smaller. To this end, the site-resolved band mapping technique introduced in Section 3.2.1 is employed instead, which allows for a very precise determination of the total number of atoms on even (N_e^y) and odd lattice sites (N_o^y) along y . From this, one can obtain the average population imbalance of the double wells in the y -direction, $\mathcal{I}_y = (N_o^y - N_e^y) / (N_o^y + N_e^y)$.

For a small atom cloud, the transverse centre-of-mass drift manifests in a change of the double-well imbalance \mathcal{I}_y and the two quantities can be directly related as long as there are no transitions between neighbouring unit cells in the y -direction as shown below. Since the imbalance only distinguishes between even and odd sites, the directional centre-of-mass displacement otherwise leads to a periodic evolution of \mathcal{I}_y (Fig. 6.12a, see also Section 4.2.2). In the experiment, this evolution is probed for a small number of pump cycles, for which the aforementioned condition holds such that the bulk centre-of-mass response can be determined from the change in \mathcal{I}_y .

An example for such a measurement is depicted in Fig. 6.12b for $\varphi_y^{(0)} = 0.500(5)\pi$ together with the calculated imbalance assuming ideal transport. This demonstrates that the response can be resolved very well with this technique. The lattice depths during the pumping for this data set – as well as for all other measurements of the non-linear response using site-resolved band mapping unless stated otherwise – are $V_{s,x} = V_{s,y} = 7.0(2)E_{r,s}$ and $V_{l,x} = V_{l,y} = 20.0(6)E_{r,l}$. When comparing it with the ideal case, the measured imbalance agrees with the expected behaviour for small values of the pump parameter φ_x . After a few pump cycles, however, it begins to deviate with the measured response being smaller than the theoretically calculated one. This deviation is caused by experimental imperfections, namely a finite pumping efficiency in the x -direction, leading to a smaller linear response, as well as the creation of band excitations along y and doubly-occupied plaquettes.

Relation Between Double-Well Imbalance and Centre-of-Mass Position

The cloud's centre-of-mass position along y is defined as a sum over all unit cells

$$y_{\text{COM}} = \frac{d_l}{N} \sum_{ij} \left[(j - 1/4) N_{e,ij}^y + (j + 1/4) N_{o,ij}^y \right] \quad (6.8)$$

where the indices i and j denote the position of the unit cell along x and y , respectively, and $N_{e,ij}^y$ ($N_{o,ij}^y$) the expectation value for the atom number on the even (odd) sites along

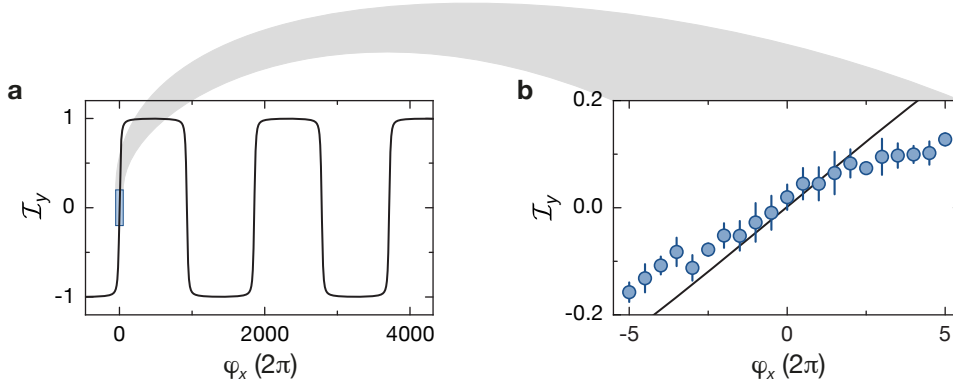


Figure 6.12 – Local probing of the non-linear response by site-resolved band mapping. (a) Evolution of the double-well imbalance along y as a function of φ_x calculated for the parameters of the measurement in (b). The monotonic centre-of-mass drift translates into alternating steps as the particles sequentially reside on either even or odd sites. Assuming ideal transport, the atoms move by one unit cell along y after about 1850 pump cycles in the x -direction. (b) To locally probe the response of the system, the double-well imbalance is measured versus φ_x for a small number of cycles in positive and negative pumping direction, shown here for $V_{s,x} = V_{s,y} = 7.0(2)E_{r,s}$, $V_{l,x} = V_{l,y} = 20.0(6)E_{r,l}$, $\varphi_y^{(0)} = 0.500(5)\pi$ and $\theta = 0.54(3)$ mrad. All data points are the average of seven measurements with the exception of the point at $\varphi_x = 0$, which was averaged 14 times. The error bars indicate the error of the mean. The black solid line corresponds to the ideal response curve from (a). Note that the theory curve does not take into account the variation of the Berry curvature Ω^x during the pumping, but assumes a homogeneous $\Omega^x = a_x \nu_1^x / (2\pi)$ for simplicity. Figure (b) adapted from [150].

y in the (i, j) -th unit cell. This can be expressed in terms of the double-well imbalance with $N_e^y = \sum_{ij} N_{e,ij}^y$ and $N_o^y = \sum_{ij} N_{o,ij}^y$ yielding

$$y_{\text{COM}} = \frac{d_1}{N} \sum_{ij} j \left(N_{e,ij}^y + N_{o,ij}^y \right) + \frac{d_1}{4} \mathcal{I}_y \quad (6.9)$$

If no transitions between unit cells along y occur, the first term does not change during the pumping as $\sum_i \left(N_{e,ij}^y + N_{o,ij}^y \right)$ remains constant for all j . The centre-of-mass displacement is thus given by

$$\delta y_{\text{COM}} = y_{\text{COM}}(\varphi_x) - y_{\text{COM}}(\varphi_x = 0) = \frac{d_1}{4} \delta \mathcal{I}_y \quad (6.10)$$

For ideal transport of localized atoms, the above condition holds if φ_y is limited to an interval $[l\pi, (l+1)\pi]$ with $l \in \mathbb{Z}$ during the pumping.

Eq. (6.8) is valid only in the deep tight-binding regime, where the distance between neighbouring lattice sites along y is always $d_s = d_1/2$, i.e. the centre-of-mass of the maximally localized Wannier functions on the individual lattice sites does not depend on φ_y . If this is not the case, the distances between the Wannier functions' centre-of-mass should be used instead of the lattice spacing d_s to define y_{COM} . Note, however, that regardless of this the reconstruction of the quantized centre-of-mass response for an infinite system from the change in the double-well imbalance as in Section 6.4 does not require any knowledge of

the Wannier functions. The reason for this is that the Wannier functions exhibit the same 2π periodicity with respect to φ_y as the underlying lattice potential. Therefore the contribution to the centre-of-mass motion from the variation of the lattice spacing vanishes when integrating over the entire 4D pump cycle and for the averaged response a similar relation as in Eq. (6.10) can be derived.

6.3.2 Model for Double-Well Imbalance with Experimental Imperfections

The reduction of the measured non-linear response compared to the one expected for an ideal system can be attributed to three main types of experimental imperfections: (i) a reduced linear response along x due to the finite pumping efficiency, which modifies the effective threading of $d\varphi_y/dt$, (ii) the excitation of atoms into the first excited subband along y , for which $\nu_2 = -1$ giving rise to a reversed non-linear response and (iii) the appearance of doubly-occupied plaquettes, which exhibit different local transport properties due to the repulsive on-site interaction. All of these imperfections can be quantified independently at each point during the pumping as detailed below and the response of the lowest subband can be isolated by taking these effects into account.

Measurement of Experimental Imperfections

Pumping Efficiency. The linear response along x can be probed by measuring the centre-of-mass position of the atom cloud as a function of the pump parameter φ_x . This data is then fitted using the model introduced in Section 4.2.2,

$$x_{\text{COM}}(\varphi_x) = \text{sgn}(\varphi_x) \sum_{i=1}^{|\varphi_x|/\pi} (2\beta_0\beta^i - \beta) d_s \quad \text{for } \varphi_x/\pi \in \mathbb{Z} \quad (6.11)$$

to determine the pumping efficiency β , i.e. the fraction of atoms that is transported by one lattice site during each half of a pump cycle¹. This yields $\beta = 0.986(2)$, which is independent of the tilt angle θ as shown by the measurement in Fig. 6.11b. The initial fraction of atoms in the lowest band along x , β_0 , is determined independently using the same technique as described below for the band excitations along y and amount to $\beta_0 = 0.980(4)$. Similar to the experiments in Section 4.2, the pumping efficiency is mainly limited by the creation of band excitations along x , which result from both non-adiabatic transitions induced by the pumping as well as technical heating in the superlattice. Additionally, as detailed in Section 4.2.2, the external confining potential can induce transitions between neighbouring double wells, which further reduce the pumping efficiency.

Band Excitations. The fraction of atoms in the first excited subband in the y -direction, n_{exc}^y , can be determined by taking advantage of the fact that the linear pumping response points in opposite directions for the lowest and first excited subband as $\nu_1^{y,\text{exc}} = -\nu_1^{y,\text{gs}}$

¹The slightly different form of Eq. (6.11) as compared to Eq. (4.7) arises from the fact that here the pump cycle starts from the staggered configuration at $\varphi_x = 0$, whereas for the measurements presented in Section 4 it starts in the symmetric double-well configuration at $\varphi_x = \pi/2$.

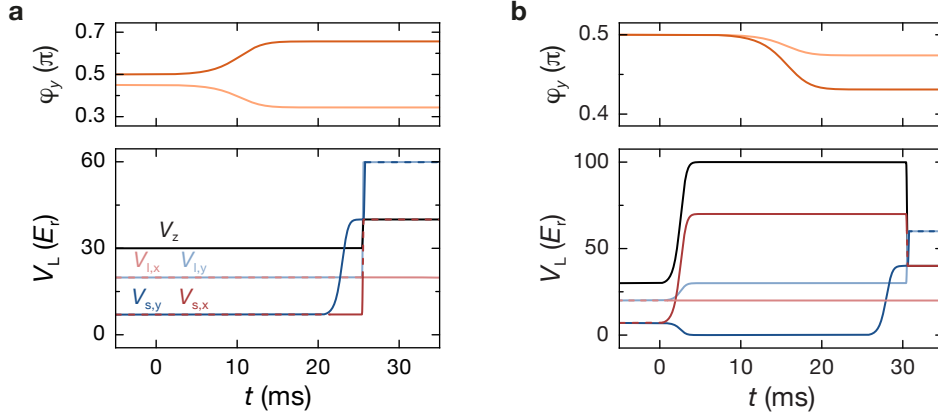


Figure 6.13 – Sequences for measuring band excitations along y and the doublon fraction. (a) Measurement of band excitations. After performing the pumping, $\varphi_y^{(0)}$ is ramped within 20 ms from its initial value to $\pi/2 \pm 0.156(5)\pi$ for $\varphi_y^{(0)} \geq \pi/2$ (dark orange) and $\varphi_y^{(0)} < \pi/2$ (light orange), respectively, to avoid crossing the symmetric double-well configuration at $\varphi_y^{(0)} = \pi/2$. The short lattice along y is then increased to $40(1)E_{r,s}$ to fully localize ground (excited) state particles on the lower (upper) site of each double well before freezing the atom distribution for the site-resolved band mapping. (b) Doublon detection. After the pumping, the double wells along y are merged into single sites of the long lattice by switching off the short y -lattice within 5 ms. Simultaneously, the other lattices are increased to $V_{s,x} = 70(2)E_{r,s}$, $V_{l,y} = 30(1)E_{r,s}$ and $V_z = 100(3)E_{r,z}$ to enhance the interaction energy. $\varphi_y^{(0)}$ is then changed to either $0.474(5)\pi$ (light orange) or $0.431(5)\pi$ (dark orange) before adiabatically splitting each long lattice site to a double well by increasing $V_{s,y}$ to $40(1)E_{r,s}$. For $\varphi_y^{(0)} = 0.474(5)\pi$, only single atoms are localized on one site while two atoms sit on different sites, whereas for $\varphi_y^{(0)} = 0.431(5)\pi$ all ground-state particles are fully localized on the lower-lying site.

(see Section 4.3). Ground-state and excited-state atoms can thus be separated spatially by adiabatically shifting $\varphi_y^{(0)}$ from its initial value to $\pi/2 \pm 0.156(5)\pi$ and subsequently suppressing the tunnelling by slowly ramping up the short y -lattice to $40(1)E_{r,s}$ (Fig. 6.13a). At this point, atoms in the excited state are perfectly localized on the higher-lying site, whereas ground-state atoms localize on the lower-lying site. The latter also holds for atoms on doubly-occupied plaquettes in the two-particle ground state since Δ_y is much larger than the on-site interaction. From the resulting double-well imbalance, one can thus directly infer n_{exc}^y .

Doubly-occupied Plaquettes. In a similar way, one can obtain the fraction of atoms on doubly-occupied plaquettes, n_2 , which are assumed to be in the respective two-particle ground state. Due to the repulsive interaction, two particles in the same double well² localize much later on the lower-lying site than single atoms when increasing the double-well tilt Δ_y . This allows for a determination of the doublon fraction by comparing the double-well imbalance between two different lattice configurations: one where Δ_y is sufficiently large such that atoms in both singly- and doubly-occupied double wells are fully localized on a single site ($\varphi_y^{(0)} = 0.431(5)\pi$) and a second one with a smaller double-well tilt ($\varphi_y^{(0)} = 0.474(5)\pi$), for which only single atoms are localized while two atoms are

²As detailed below, the 2×2 unit cell effectively reduces to a double well along y for $\varphi_x = l\pi$, $l \in \mathbb{Z}$, where all measurements are taken

distributed onto different sites to minimize the interaction energy. The doublon fraction can thus be determined from the difference between the two imbalances. The comparison between the two configurations is necessary to separate the contribution from single atoms in the excited state, which in both cases are localized on the opposite site as compared to single ground-state atoms. The experimental sequences used for this are shown in Fig. 6.13.

Model for Double-Well Imbalance with Experimental Imperfections

To account for the experimental imperfections mentioned above, a simple model is used for calculating the expected double-well imbalance. For a given φ_x , the average double-well imbalance along y can be expressed as

$$\mathcal{I}_y(\varphi_x) = n_{\text{gs}}^y(\varphi_x) \mathcal{I}_y^{\text{gs}}(\varphi_y) + n_{\text{exc}}^y(\varphi_x) \mathcal{I}_y^{\text{exc}}(\varphi_y) + n_2(\varphi_x) \mathcal{I}_y^{2,\text{gs}}(\varphi_y) \quad (6.12)$$

for a state with a fraction n_{gs}^y (n_{exc}^y) of atoms in the ground (first excited) state along y on singly-occupied plaquettes and a doublon fraction n_2 . All of these fractions in general depend on the pump parameter.

The double-well imbalances of the corresponding states are denoted by $\mathcal{I}_y^{\text{gs}}$, $\mathcal{I}_y^{\text{exc}}$ and $\mathcal{I}_y^{2,\text{gs}}$. These imbalances depend on the local phase of the superlattice along y , which in turn is determined by the centre-of-mass position of the cloud in the x -direction, x_{COM} . They can be obtained theoretically by calculating the eigenstates of the corresponding plaquette Hamiltonian. In the experiment, the double-well imbalance is measured only after an integer or half-integer number of pump cycles, $\varphi_x = l\pi$ with $l \in \mathbb{Z}$, where the x -superlattice is in the staggered configuration. For the experimental parameters, atoms on singly- as well as doubly-occupied plaquettes are very well localized on either even or odd sites along x since the energy offset $|\Delta_x|$ is much larger than both the intra-double-well tunnelling and the on-site energy. It is therefore sufficient to only consider the respective double-well Hamiltonian for the y -superlattice (see Section 3.2.2). Experimentally, $\mathcal{I}_y^{\text{gs}}$, $\mathcal{I}_y^{\text{exc}}$ and $\mathcal{I}_y^{2,\text{gs}}$ can be determined by studying the linear response that occurs when shifting $\varphi_y^{(0)}$. It was confirmed that the measured $\mathcal{I}_y^{\text{gs}}$ exhibits the theoretically expected behaviour.

The finite pumping efficiency manifests in a slower centre-of-mass motion in the x -direction such that the change of $\varphi_y(x_{\text{COM}})$ induced by the perturbing angle is smaller than expected. Correspondingly, this also reduces the non-linear response along y as the anomalous velocity $v_y \sim \dot{\varphi}_y$ [Eq. (5.37)]. For the pumping efficiency and initial ground-state fraction achieved in the experiment (see above), the displacement after one pump cycle is about 93% of the ideal value, which decreases to about 83% after five cycles.

Doubly-occupied plaquettes exhibit a different linear and non-linear pumping response than singly-occupied ones due to the interaction between the particles (Fig. 6.14a). In particular, the anomalous velocity in the vicinity of the symmetric double-well configurations is strongly reduced as the atoms preferably sit on different lattice sites. Note, however, that for the parameters used in the experiment the double-well tilts along both x and y in the staggered configurations are substantially larger than the on-site interaction. Therefore, as

long as the two atoms remain localized to the same plaquette, they are transported by the same quantized distance as a single atom when integrating over the entire 4D pump cycle. In the experiment, the doublon fraction initially increases linearly and then saturates to a constant value of about $n_2^f = 0.24(3)$ (Fig. 6.14b). While the final doublon fraction appears to be independent of $\varphi_y^{(0)}$, the growth rate becomes slower the farther away $\varphi_y^{(0)}$ is from the symmetric double-well configuration. This indicates that the creation of doubly-occupied sites is suppressed by a smaller coupling between the double-well ground states along y as well as by an increase of the effective interaction energy that is required to add a second atom to a singly-occupied plaquette. To model this behaviour, an exponentially decaying growth rate is assumed and the measured doublon fraction is fitted by the following function

$$n_2(\varphi_x) = n_2^f - (n_2^f - n_2^i) e^{-\varphi_x/\tau_\varphi} \quad (6.13)$$

Here, n_2^i is the initial doublon fraction, which is typically negligible, and τ_φ is the growth constant of the saturating increase.

Band excitations in the y -direction have the most pronounced effect on the transverse response as the non-linear response of the corresponding subband is inverted compared to the lowest band, i.e. $\nu_2^{\text{exc}} = -1$ (Fig. 6.14a). This is particularly relevant for lattice configurations in which single atoms are localized to a large extent because even a small number of band excitations already causes a noticeable change of \mathcal{I}_y . During the pumping, the fraction of atoms in the excited band n_{exc}^y grows linearly with the pump parameter within the range probed in the experiments. To determine the initial fraction and the slope, n_{exc}^y is determined prior to the pumping as well as after five pump cycles (Fig. 6.14c). The increase in n_{exc}^y per cycle depends strongly on the lattice configuration. It is largest in the symmetric double-well configuration, for which the band gap is minimal, and decreases when the gap becomes bigger (see also Fig. 6.15b below).

Non-Linear Response Including Experimental Imperfections

The expected evolution of the imbalance including the corrections for the experimental imperfections can be calculated using Eq. (6.12) by inserting n_{exc}^y , n_2 and φ_y . To this end, the models described above are used, which are fitted to the respective data to obtain $n_{\text{exc}}^y(\varphi_x)$, $n_2(\varphi_x)$ and $\varphi_y(\varphi_x)$. The resulting curve shows excellent agreement with the experimentally measured non-linear response as shown in Fig. 6.14d for the data from Fig. 6.12b. This demonstrates that the non-linear response can be quantified very well using the site-resolved band mapping.

Knowing the dominant experimental imperfections, the contribution of the lowest subband to the non-linear response can be extracted from the imbalance measurement. In Eq. (6.12), the only unknown is the local transverse superlattice phase φ_y , which changes as a function of the cloud's position x_{COM} . Following Eq. (6.1), this dependence is expected to be linear. Based on this, the following function is fitted to the imbalance data:

$$\mathcal{I}_y^{\text{fit}}(\varphi_x) = \mathcal{I}_y(\varphi_x) + \mathcal{I}_0 \quad \text{with } \varphi_y \rightarrow \varphi_y^{\text{fit}} = \varphi_y^{(0)} + \alpha (\varphi_y - \varphi_y^{(0)}) \quad (6.14)$$

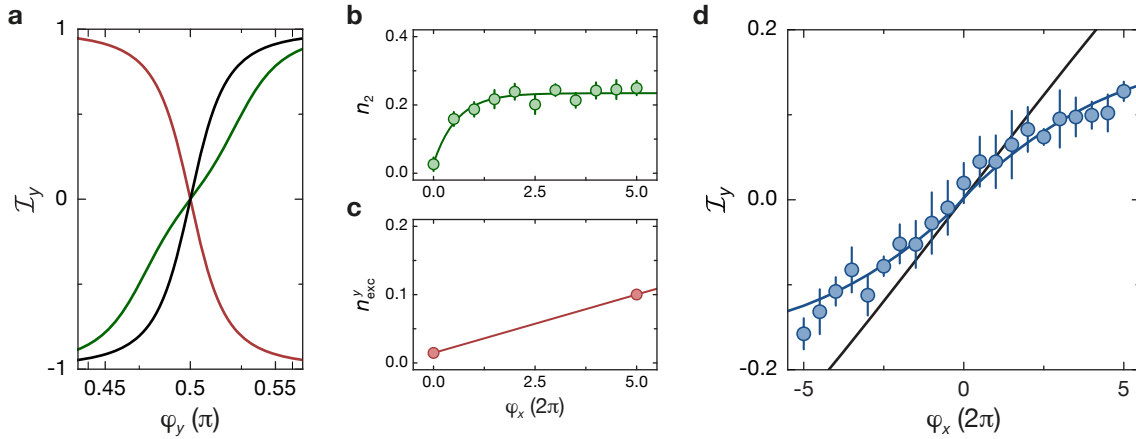


Figure 6.14 – Evolution of the double-well imbalance including experimental imperfections for $V_{s,y} = 7.0(2)E_{r,s}$, $V_{l,y} = 20.0(6)E_{r,l}$, $\varphi_y^{(0)} = 0.500(5)\pi$ and $\theta = 0.54(3)$ mrad. **(a)** Double-well imbalance \mathcal{I}_y along y versus superlattice phase φ_y for single atoms in the ground (black line) and first excited state (red) on a double well. Additionally, the imbalance is shown for two atoms in the two-particle ground state (green). All curves are calculated using the respective tight-binding double-well Hamiltonian. **(b)** Measured doublon fraction n_2 as a function of the pump parameter φ_x . Each data point is the average of seven measurements and the error bar indicates the error of the mean. The green solid line is a fit of Eq. (6.13) to the data yielding $n_2^i = 0.029(16)$, $n_2^f = 0.234(7)$ and $\tau_\varphi = 1.2(3)\pi$. **(c)** Fraction of atoms in the first excited subband along y measured in the initial state and after five pump cycles, averaged over 15 measurements each. The error of the mean is smaller than the size of the data points. The red line indicates the observed linear increase of band excitations during the pumping with a slope of 0.0171(11) per cycle obtained from the data. **(d)** Double-well imbalance \mathcal{I}_y versus φ_x . The data points show the measured imbalance as in Fig. 6.12b. The black line illustrates the response of an ideal system with only singly-occupied plaquettes in the ground state. Following Eq. (6.12), the blue line takes into account the finite pumping efficiency along x as well as the band excitations and doublons created during the pumping (from b and c). Note that this curve does not contain any additional free parameter, but only independently measured experimental quantities in the form of the fitting curves for the experimental imperfections. For simplicity, all theory curves assume a uniform evolution during each half of a pump cycle, i.e. they do not account for variations of Ω^x and the heating rates. Figure adapted from [150].

where α and \mathcal{I}_0 are the fit parameters. The prefactor α quantifies the change of φ_y with x as compared to the ideal case $\varphi_y^{\text{fit}} = \varphi_y$. The global offset \mathcal{I}_0 accounts for the experimental uncertainty of $\varphi_y^{(0)}$ and small overall shifts that might be caused by an improper calibration of the site-resolved band mapping measurement.

The response of the lowest subband can be obtained from the slope of the ground-state imbalance $\mathcal{I}_y^{\text{gs}}$ at $\varphi_x = 0$, which can be calculated from the ideally expected slope when α is known:

$$\left. \frac{\partial \mathcal{I}_y^{\text{gs}}(\varphi_y^{\text{fit}})}{\partial \varphi_x} \right|_{\varphi_x=0} = \left. \frac{\partial \mathcal{I}_y^{\text{gs}}(\varphi_y^{\text{fit}})}{\partial \varphi_y^{\text{fit}}} \frac{\partial \varphi_y^{\text{fit}}}{\partial \varphi_x} \right|_{\varphi_x=0} = \alpha \left. \frac{\partial \mathcal{I}_y^{\text{gs}}(\varphi_y)}{\partial \varphi_x} \right|_{\varphi_x=0} \quad (6.15)$$

For ground-state atoms, the change of the double-well imbalance per pump cycle is then given by

$$\delta \mathcal{I}_y^{\text{gs}} = \alpha \left[\mathcal{I}_y^{\text{gs}}(\varphi_y) \Big|_{\varphi_x=2\pi} - \mathcal{I}_y^{\text{gs}}(\varphi_y) \Big|_{\varphi_x=0} \right] \quad (6.16)$$

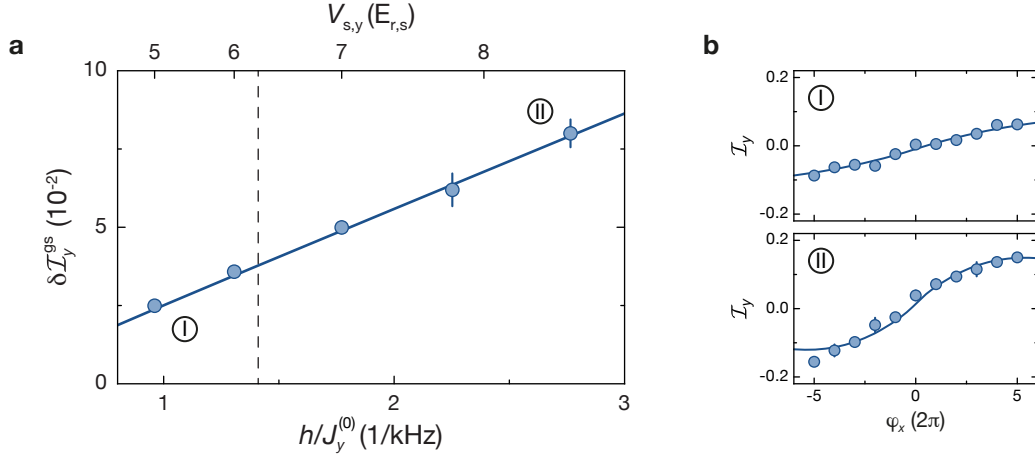


Figure 6.15 – Non-linear response of the lowest subband versus depth of the short lattice along y for $\varphi_y^{(0)} = 0.500(5)\pi$ and $\theta = 0.54(3)$ mrad. (a) Change of the double-well imbalance per cycle for the lowest subband, $\delta \mathcal{I}_y^{\text{gs}}$, as a function of $V_{s,y}$ with all other parameters as for the measurement in Fig. 6.12. $J_y^{(0)} = J_y(\varphi_y^{(0)}) + \delta J_y(\varphi_y^{(0)})/2$ with $\varphi_y^{(0)} = \pi/2$ denotes the maximum intra-double-well tunnelling rate in the y -direction and is calculated for the respective lattice parameters. $\delta \mathcal{I}_y^{\text{gs}}$ is determined by fitting the measured imbalance $\mathcal{I}_y(\varphi_x)$ as detailed in Section 6.3.2. The solid line shows the slope expected for an ideal system ($\alpha = 1$) and the error bars depict the uncertainty of $\delta \mathcal{I}_y^{\text{gs}}$ resulting from the fit error for α . The dashed line indicates the point where the first excited subband along y exhibits a topological transition between the Landau regime for $V_{s,y} < 6.25E_{r,s}$ and the Hofstadter regime for $V_{s,y} > 6.25E_{r,s}$. Figure adapted from [150]. (b) Two examples for the measurement of double-well imbalance \mathcal{I}_y versus φ_x as in Fig. 6.12b with $V_{s,y} = 5.0(2)E_{r,s}$ (I) and $V_{s,y} = 8.5(2)E_{r,s}$ (II), respectively. The solid line illustrates the expected evolution including corrections for experimental imperfections as in Fig. 6.14d, shifted by the fitted global offset \mathcal{I}_0 . For larger $V_{s,y}$, the energy gap to the first excited subband along y decreases, leading to a faster generation of band excitations. This manifests in a reduction of the non-linear response after multiple pump cycles.

In this way, the local transport properties of the lowest subband at a given $\varphi_y^{(0)}$ can be extracted from the measurement of the non-linear pumping response by site-resolved band mapping.

6.3.3 Non-Linear Response for Different Lattice Configurations

Using the technique for extracting the non-linear response for the lowest subband from the imbalance measurements described in Section 6.3.2, one can study how the local slope depends on the lattice configuration. In Fig. 6.15, the change of the imbalance per cycle, $\delta \mathcal{I}_y^{\text{gs}}$, is shown as a function of the depth of the short y -lattice $V_{s,y}$ with otherwise identical parameters as for the measurements in Fig. 6.12.

The measured slope $\delta \mathcal{I}_y^{\text{gs}}$ agrees very well with the theoretically expected one. With increasing $V_{s,y}$, the intra-double-well tunnelling rate decreases and the Berry curvature Ω^y becomes more and more localized around the symmetric double-well configurations, where the energy gap to the first excited subband is minimal. Since the 2D superlattice is a product of two orthogonal Rice-Mele models, the second Chern number of the lowest

subband and thus the averaged non-linear response of an infinite system are independent of $V_{s,y}$ (see also Section 4.2.1). This implies that the local slope in the vicinity of $\varphi_y = \pi/2$ has to increase accordingly. In the tight-binding limit, the slope at $\varphi_y = \pi/2$ scales like $1/J_y^{(0)}$ with $J_y^{(0)} = J_y(\varphi_y) + \delta J_y(\varphi_y)/2$ denoting the intra-double-well tunnelling rate in the symmetric double-well configuration. This behaviour is confirmed by the data, demonstrating the robustness of the non-linear response against perturbations of the system, which results from the topological protection.

As a function of the respective lattice depths, the two orthogonal 1D charge pumps forming the 2D charge pump both exhibit a Landau regime and a Hofstadter regime, in which the corresponding 2D quantum Hall system is the Landau Hamiltonian and the Harper-Hofstadter-Hatsugai model, respectively (see Section 2.3 and Section 4.3.2). For the superlattice along y , the two limits can be probed experimentally by tuning $V_{s,y}$ as in Fig. 6.15. In the first excited subband along y , a topological transition occurs between the two regimes with $\nu_1^{y,\text{exc}} = +1$ in the Landau limit for small $V_{s,y}$ and $\nu_1^{y,\text{exc}} = -1$ in the Hofstadter regime for large $V_{s,y}$. This transition also leads to a change of the corresponding second Chern number ν_2^{exc} from $+1$ to -1 such that atoms in the first excited subband move in opposite directions along y in the two limits. For the parameters of Fig. 6.15, the transition point is located at $V_{s,y} = 6.25E_{T,s}$. For the lowest subband, on the other hand, the two regimes are topologically equivalent as indicated by the fact that the direction of the non-linear response is the same for all values of $V_{s,y}$. The good agreement between the slope of an ideal system and the experimentally determined one in both regimes shows that the non-linear response for the lowest subband can be extracted reliably over a wide range of lattice configurations, even in the presence of atoms in the first excited subband.

6.4 Measurement of the Second Chern Number

From the local probing of the geometric properties of the non-linear response, its global topological properties can be obtained by integrating over the entire 4D generalized Brillouin zone. For a small cloud with uniform occupation of a given band as in the experiment, this requires measuring the response at different positions in the pumping directions (Section 6.4.1). By reconstructing the global response of an infinite system, the quantization of the non-linear transport can be verified through a determination of the corresponding topological invariant, the second Chern number ν_2 . This is demonstrated here for the lowest subband, for which $\nu_2 = +1$ is expected. Using the raw imbalance data without accounting for any experimental imperfections, this yields about 80% of the predicted quantized value (Section 6.4.2). In Section 6.4.3, a more sophisticated analysis including corrections for the experimental imperfections is performed to obtain a more precise value for ν_2 , which is found to be in agreement with the expected quantization of the transport. Finally, the characteristic feature of the non-linear response is revealed, namely its dependence on the magnetic field-like perturbation, which provides an additional way to determine the second Chern number (Section 6.4.4).

6.4.1 Reconstructing the Quantized Response of an Infinite System

For a given $\varphi_y^{(0)}$, a small atom cloud that homogeneously populates the lowest subband locally probes the pumping response of the system, which is determined by its 4D geometric properties. The average anomalous velocity of the cloud is proportional to $\overline{\Omega^x \Omega^y}(\varphi_x, \varphi_y^{(0)}) = \int \Omega^x \Omega^y d^2k$ as the uniform band occupation corresponds to a 2D integration along k_x and k_y within the 4D generalized Brillouin zone (see Sections 5.2.3 and 6.1.4). During one pump cycle, the entire range of $\varphi_x \in [0, 2\pi[$ is scanned and the resulting change of the double-well imbalance along y , which is obtained from the site-resolved band mapping measurement, is thus given by

$$\delta \mathcal{I}_y = \mathcal{I}_y(\varphi_x = 2\pi) - \mathcal{I}_y(\varphi_x = 0) = 4 \underbrace{\frac{1}{2\pi} \oint \Omega^x \Omega^y dk_x dk_y}_{\overline{\Omega}(\varphi_y^{(0)})} d\varphi_x \theta \quad (6.17)$$

A single measurement like this thereby integrates over three directions of the 4D Brillouin zone (Fig. 6.16). From this, the quantized response of an infinite system can be reconstructed by repeating the measurement at different positions along x , all of which are sampled simultaneously in an infinite system. As the system is translationally invariant along x in absence of a superlattice tilt ($\theta = 0$), the only position-dependent quantity is the transverse superlattice phase φ_y , which increases linearly with x for $\theta \neq 0$ [Eq. (6.1)]. Going to a different position at a constant phase offset $\varphi_y^{(0)}$ is hence equivalent to a shift of $\varphi_y^{(0)}$ for a cloud at a fixed initial position $x_i = 0$ (Fig. 6.16). By locally probing the non-linear response for all possible values of $\varphi_y^{(0)} \in [0, 2\pi[$, the integration along the remaining φ_y -direction can therefore be performed manually, which yields the quantized response characterized by the second Chern number.

The range of $\varphi_y^{(0)}$ over which the response has to be probed to allow for the reconstruction of the response of an infinite system can be restricted further by exploiting symmetries of the eigenstates in the generalized 4D Brillouin zone [222]. In a commensurate 1D superlattice with $d_{s,\mu}/d_{l,\mu} = p/q$ where p and $q > p$ are coprime integers, the system's Hamiltonian is invariant up to a global translation by an integer number of lattice sites under a shift of the superlattice phase by $2\pi l/q$ for integer l and $0 \leq l < q$ [285, 286]. The eigenstates $|u(k_\mu, \varphi_\mu)\rangle$ in these lattice configurations therefore differ only by a momentum-dependent phase factor, which can be interpreted as a gauge transformation. This immediately implies that the corresponding gauge-invariant Berry curvatures are identical. For mapping out the entire Brillouin zone, it is thus sufficient to only sample the interval $\varphi_y^{(0)} \in [0, 2\pi/q[$, i.e. $\varphi_y^{(0)} \in [0, \pi[$ in the case of $d_l = 2d_s$.

6.4.2 Direct Determination of the Second Chern Number

To reconstruct the transport properties of an infinite system, the local measurement of the non-linear response via the double-well imbalance \mathcal{I}_y as shown in Fig. 6.12 is repeated at different values of $\varphi_y^{(0)}$ (Fig. 6.17a). For each $\varphi_y^{(0)}$, the change of the imbalance per cycle,

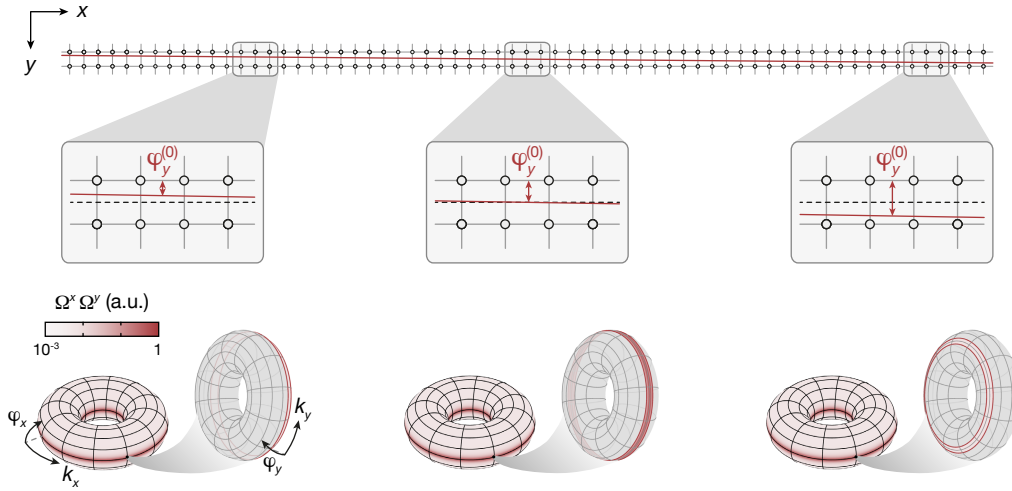


Figure 6.16 – Reconstructing the quantized response of an infinite system by local probing. The small atom cloud serves as a local probe of the system’s transport properties at the position of the cloud, indicated by the grey frames in the upper panel. For a uniformly populated band, the non-linear response during a full pump cycle at a given position along x is proportional to the integral of the product of Berry curvatures $\Omega^x \Omega^y$ over k_x, k_y and φ_x in the 4D generalized Brillouin zone (lower panel). The value of φ_y is determined by the position of the cloud as illustrated in the zoomed insets. By repeating the measurement of the non-linear response at different positions along x or correspondingly different values of $\varphi_y^{(0)}$, the quantized response of an infinite system can be reconstructed by manually performing the integration over the remaining fourth direction φ_y to sample the entire 4D Brillouin zone. Figure adapted from [150].

$\delta \mathcal{I}_y$, can be determined directly from these measurements by a linear fit to the differential imbalance between positive and negative pumping direction, $\Delta \mathcal{I}_y = \mathcal{I}_y(\varphi_x) - \mathcal{I}_y(-\varphi_x)$. To minimize the effect of the experimental imperfections, which reduce the non-linear response in particular for larger values of the pump parameter, the data taken into account for the fit can be limited to small numbers of pump cycles. For the analysis presented below and in Fig. 6.17, a cut-off of $\varphi_x/(2\pi) \leq 3$ is used.

By combining these results, the non-linear response can be mapped out as a function of $\varphi_y^{(0)}$. The measured response exhibits the pronounced peak around the symmetric double-well configuration $\varphi_y = \pi/2$ as expected from the distribution of the Berry curvatures within the Brillouin zone (Fig. 6.17b). From this, the response of an infinite system and thereby the second Chern number of the lowest subband can be obtained by averaging $\delta \mathcal{I}_y$ over $\varphi_y^{(0)}$, without requiring any a priori knowledge about the system. As detailed in Section 6.4.1, the averaging can be limited to the interval $\varphi_y^{(0)} \in [0, \pi[$ for $d_1 = 2d_s$. In this range, the only relevant contributions to the non-linear response originate in the vicinity of $\varphi_y^{(0)} = \pi/2$. Using linear interpolation between the data points shown in Fig. 6.17b results in a value of

$$\nu_2^{\text{exp}} = 0.84(17) \quad (6.18)$$

for the second Chern number, compared to an ideal value of $\nu_2 = +1$ for $d_1 = 2d_s$. The error of ν_2^{exp} takes into account the fit error of $\delta \mathcal{I}_y$ as well as the uncertainty of the tilt angle θ . Note that due to the discrete sampling of $\varphi_y^{(0)}$ the interpolation causes a systematic

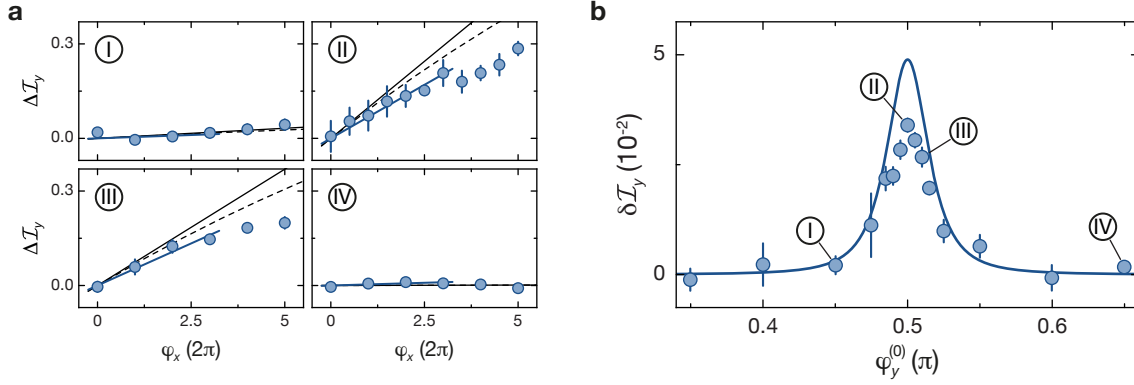


Figure 6.17 – Local probing of the non-linear bulk response for $V_{s,y} = 7.0(2)E_{r,s}$, $V_{l,y} = 20.0(6)E_{r,l}$ and $\theta = 0.54(3)$ mrad. (a) Differential double-well imbalance $\Delta \mathcal{I}_y = \mathcal{I}_y(\varphi_x) - \mathcal{I}_y(-\varphi_x)$ as a function of φ_x for $\varphi_y^{(0)} = 0.450(5)\pi$ (I), $0.500(5)\pi$ (II), $0.510(5)\pi$ (III) and $0.650(5)\pi$ (IV). $\Delta \mathcal{I}_y$ is calculated from the measured imbalances \mathcal{I}_y , averaged over seven measurements each, and the error bar indicates the error of the mean. The blue solid line is a linear fit to the data points with $\varphi_x/(2\pi) \leq 3$ to obtain the change of the imbalance per cycle, $\delta \mathcal{I}_y$. The black solid line illustrates the response of an ideal system and the dashed line includes corrections for the finite pumping efficiency based on Eq. (6.19). (b) Local non-linear response versus $\varphi_y^{(0)}$. The slope $\delta \mathcal{I}_y$ is determined as described in (a) and the error bars show the fit error. The blue line depicts the non-linear response expected for a system without any imperfections.

shift of ν_2^{exp} by about $+0.05$ when assuming the ideally expected shape of $\delta \mathcal{I}_y(\varphi_y^{(0)})$ for the experimental lattice parameters. The deviation of ν_2^{exp} compared to the ideal case is predominantly caused by the finite pumping efficiency along x (see below) and the band excitations in the y -direction, both of which give rise to a reduction of ν_2^{exp} by about -0.1 each. The contribution of doublons, on the other hand, is negligible for the lattice configuration in the experiment because they exhibit the same quantized transport as single localized atoms when averaging over the entire 4D Brillouin zone (see Section 6.3.2). Their local transport properties, however, are different and the appearance of doublons leads to a smaller non-linear response close to the peak of $\delta \mathcal{I}_y(\varphi_y^{(0)})$ at $\varphi_y^{(0)} = \pi/2$, but a larger response in the wings of the curve (Fig. 6.14a).

The pumping efficiency along x can be obtained independently by observing the centre-of-mass motion in the x -direction (see Section 6.3.2). This effect can be taken into account when determining $\delta \mathcal{I}_y$ by using the following fit function instead of the linear one as above:

$$\Delta \mathcal{I}_y(\varphi_x) = 2 \delta \mathcal{I}_y \frac{x_{\text{COM}}(\varphi_x)}{d_1} \quad (6.19)$$

with x_{COM} given by Eq. (6.11) and $\delta \mathcal{I}_y$ the only fit parameter. This allows for a determination of ν_2 corrected for the deviation caused by the finite pumping efficiency without relying on any additional assumptions about the system. For the data in Fig. 6.17, this analysis gives

$$\nu_2^{\text{exp}} = 0.94(19) \quad (6.20)$$

with the error determined as described above.

The measurement in Fig. 6.17 demonstrates that even without accounting for any experimental imperfections the raw bulk response for the infinite system is already close to the expected quantized value. In this sense, the experimental realization of this dynamical 4D quantum Hall system is indeed in the *quantum* Hall regime rather than in the classical one, where the response is dominated by contributions from many different excited states.

6.4.3 Determination of the Second Chern Number with Corrections

The ability to quantify the dominant experimental imperfections allows for isolating the contribution of the lowest subband to the non-linear response as detailed in Section 6.3.2. In this way, the second Chern number of this band can be determined with a much higher precision. To this end, in addition to the double-well imbalance \mathcal{I}_y , the fractions of atoms on doubly-occupied plaquettes as well as in the first excited subband along y are measured as a function of the pump parameter φ_x for each $\varphi_y^{(0)}$ as shown in Fig. 6.13. The non-linear response of the lowest subband is then quantified by determining the change of the imbalance per cycle for the ground-state band, $\delta\mathcal{I}_y^{\text{gs}}$. The latter is extracted from a fit of Eq. (6.14) to the experimentally measured double-well imbalance $\mathcal{I}_y(\varphi_x)$ accounting for the band excitations, doublons and the finite pumping efficiency along x .

In Fig. 6.18, the result of this procedure is presented for the imbalance measurements shown in Fig. 6.17. The experimentally determined $\delta\mathcal{I}_y^{\text{gs}}$ as well as the individual evolutions of $\mathcal{I}_y(\varphi_x)$ agree very well with the theoretical predictions. The second Chern number of the lowest subband can be determined from this data with a fit of the theoretically expected curve for $\delta\mathcal{I}_y^{\text{gs}}(\varphi_y^{(0)})$ to the measured one by scaling the former with a global factor. This factor directly quantifies the experimentally determined response of an infinite system as compared to the ideal case and thus corresponds to the ratio of the measured and theoretically expected second Chern numbers, $(\nu_2^{\text{exp}}/\nu_2)$. For the data in Fig. 6.18a, this yields

$$\nu_2^{\text{exp}} = 1.07(8) \quad (6.21)$$

The error of ν_2^{exp} includes the fit error of the scaling factor as well as the uncertainties of the tilt angle θ and of the lattice depths.

The experimental value ν_2^{exp} is consistent with the expected quantization of the non-linear response for $\nu_2 = +1$, thereby revealing the quantum nature of the 4D quantum Hall effect. Note that while the analysis presented above requires prior knowledge about the system, in particular about the scaling of the double-well imbalances with the transverse superlattice phase φ_y for localized ground-state and excited-state atoms as well as for doublons, these quantities can in principle be determined independently by studying the linear pumping response along y that occurs upon threading of $d\varphi_y^{(0)}/dt$.

6.4.4 Scaling of the Non-Linear Response with the Perturbing Angle

The essential feature of the non-linear response in a 4D quantum Hall system is its linear scaling with the magnetic perturbation as it arises from two independent perturbations in

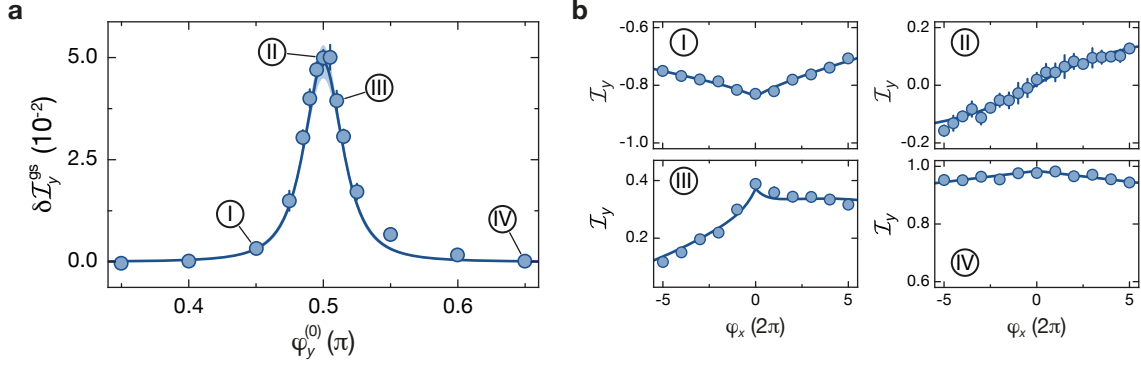


Figure 6.18 – Local probing of the non-linear bulk response accounting for experimental imperfections with $V_{s,y} = 7.0(2)E_{r,s}$, $V_{l,y} = 20.0(6)E_{r,l}$ and $\theta = 0.54(3)$ mrad. (a) Non-linear response of the lowest subband versus $\varphi_y^{(0)}$. The change of the imbalance per cycle for localized ground-state atoms, $\delta\mathcal{I}_y^{\text{gs}}$, is extracted from the measurements of $\mathcal{I}_y(\varphi_x)$ by fitting Eq. (6.14) to the data taking into account the independently obtained experimental imperfections (see Section 6.3.2). The errors bars give the uncertainty resulting from the fit error. The solid line illustrates the ideally expected response and the blue-shaded area indicates the uncertainty for the theory curve arising from the errors of the lattice depths and the tilt angle θ . (b) Examples for the measured imbalance curves $\mathcal{I}_y(\varphi_x)$ at $\varphi_y^{(0)} = 0.450(5)\pi$ (I), $0.500(5)\pi$ (II), $0.510(5)\pi$ (III) and $0.650(5)\pi$ (IV) as in Fig. 6.17a. Each data point represents the average of seven measurements with the error bar showing the error of the mean. The points at $\varphi_x = 0$ are additionally averaged over the two sets for positive and negative pumping direction. The blue lines are the expected responses of an ideal system when including the finite pumping efficiency, band excitations and doublons, shifted by the global offset \mathcal{I}_0 from the fit. Figure adapted from [150].

orthogonal subspaces, namely the applied electric and magnetic fields. Correspondingly, the non-linear pumping response of a 2D topological charge pump should exhibit the same dependence with respect to the perturbing tilt angle θ . This feature distinguishes the non-linear response from the linear one that would occur along the y -direction in response to a variation of $\varphi_y^{(0)}$. The latter is an intrinsically 2D effect induced by a single transverse perturbation, $d\varphi_y^{(0)}/dt$, and therefore characterized by a 2D topological invariant, which is associated to a single lattice direction. The non-linear response, on the other hand, results from the 4D non-commutative geometry underlying the 2D charge pump and is always determined by the same 4D topological invariant, irrespective of the orientation of the two perturbations that generate it, $d\varphi_\mu/dt$ and θ_ν with $\mu, \nu \in \{x, y\}$ and $\mu \neq \nu$ (see Section 5.2.5).

This dependence of the non-linear response on θ is already indicated by the measurement of the centre-of-mass drift, which reverses when changing the sign of θ (Fig. 6.11). To study this in more detail, the slope of the non-linear response is probed as a function of θ for $\varphi_y^{(0)} = 0.500(5)\pi$ by measuring the evolution of the double-well imbalance $\mathcal{I}_y(\varphi_x)$. The result using the same lattice configuration as for the imbalance measurements presented above can be found in Fig. 6.19. The observed behaviour of $\delta\mathcal{I}_y^{\text{gs}}(\theta)$ shows excellent agreement with the expected linear scaling, thereby revealing the intrinsic 4D character of the non-linear response.

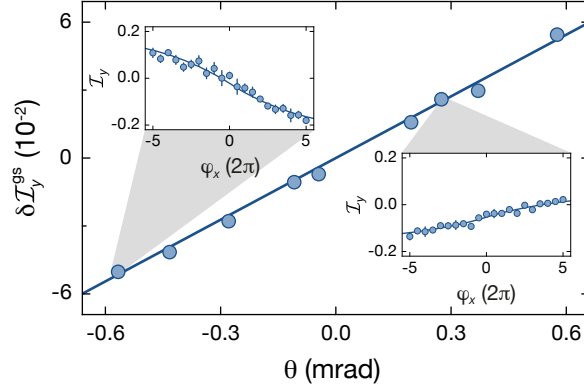


Figure 6.19 – Scaling of the non-linear response with the perturbing tilt angle θ . Change of the double-well imbalance per cycle for the lowest subband, $\delta\mathcal{I}_y^{\text{gs}}$, as a function of θ for $V_{s,y} = 7.0(2)E_{r,s}$, $V_{l,y} = 20.0(6)E_{r,l}$ and $\varphi_y^{(0)} = 0.500(5)\pi$. $\delta\mathcal{I}_y^{\text{gs}}$ is determined from a fit of the measured double-well imbalance $\mathcal{I}_y(\varphi_x)$ as described in Section 6.3.2. The uncertainties of $\delta\mathcal{I}_y^{\text{gs}}$ resulting from the fit error are smaller than the size of the data points. The solid line illustrates the expected linear scaling of the slope with θ in an ideal system. The insets contain two examples for measurements of $\mathcal{I}_y(\varphi_x)$ as in Fig. 6.18b including the expected responses when accounting for the measured experimental imperfections. Figure taken from [150].

The second Chern number of the lowest subband can also be extracted from these measurements by determining the slope of $\delta\mathcal{I}_y^{\text{gs}}(\theta)$, which for an infinite system is proportional to ν_2 :

$$\delta\mathcal{I}_y^{\text{gs}} = 4\nu_2 \theta \quad (6.22)$$

For finite systems Eq. (6.22) only holds if the system size $L_x/d_{l,y} \gg \theta$. Nonetheless, it is possible to obtain ν_2 by local probing of $\delta\mathcal{I}_y^{\text{gs}}(\theta)$ at a fixed value of $\varphi_y^{(0)}$ if the shape of $\delta\mathcal{I}_y^{\text{gs}}$ as a function of $\varphi_y^{(0)}$ is known. The measurements from Fig. 6.18 confirm that the experimentally determined curve for $\delta\mathcal{I}_y^{\text{gs}}(\varphi_y^{(0)})$ agrees with the one expected in an ideal system for the lattice configuration used in the experiment. Moreover, the shape of $\delta\mathcal{I}_y^{\text{gs}}$ depends only on intrinsic geometric properties of the system, namely the Berry curvatures $\Omega^x\Omega^y$, but it is independent of θ . In this case, the response of an infinite system can be extrapolated from a single measurement at a given $\varphi_y^{(0)}$ for each value of θ by scaling $\delta\mathcal{I}_y^{\text{gs}}(\varphi_y^{(0)})$ accordingly, similar to the fitting procedure used in Section 6.4.3.

The second Chern number can therefore be determined from a linear fit of $\delta\mathcal{I}_y^{\text{gs}}(\theta)$. For the data shown in Fig. 6.19, one obtains

$$\nu_2^{\text{exp}} = 1.01(8) \quad (6.23)$$

in agreement with the expected quantized transport for $\nu_2 = +1$. As in Eq. (6.21), the error state here includes contributions from the uncertainties of the angle and the lattice depths as well as the error of the fit. This constitutes an additional method to confirm the quantization of the non-linear bulk response.

Conclusion and Outlook

In this thesis, the implementation of 1D and 2D topological charge pumps for ultracold bosonic atoms in dynamically controlled optical superlattice potentials is reported. By periodically modulating a 1D superlattice in the adiabatic limit, a unidirectional quantized motion was induced in a fractional Mott insulator – constituting the first observation of quantized bulk transport with a topological charge pump. Extending the concept of topological charge pumping to 2D systems provides a powerful method to experimentally probe higher-dimensional quantum Hall physics. This allowed for the realization of a dynamical 4D integer quantum Hall effect, which manifests in an additional quantized non-linear response. Its experimental detection paves the way for the study of quantum Hall systems in four spatial dimensions.

Inspired by the theoretical explanation of the quantized Hall response [13], David Thouless proposed the 1D topological charge pump [10]. Such a pump can generate quantized currents in insulating states through an adiabatic periodic modulation and shares the same topological origin as the 2D integer quantum Hall effect (Section 2). Its experimental realization has been a long-standing goal in condensed matter physics, which is motivated by the fundamental physical importance as well as potential applications in precise current sources. Due to the high level of controllability and accessibility, ultracold atoms in optical superlattices are an ideal model system for the implementation of Thouless' proposal (Section 3.2 and Section 4.1). In a 1D superlattice potential, which is formed by the superposition of a short and long lattice with different periodicities, the required cyclic modulation can be realized by slowly shifting the relative position between the two lattices. It periodically changes the (tight-binding) parameters of the corresponding single-particle Hamiltonian. This pump path encloses a singularity, at which a gap in the energy spectrum closes. The degeneracy is responsible for the topologically non-trivial evolution of the eigenstates during the pumping. For a uniformly populated band, this results in a quantized displacement per cycle, which is quantified by the pump's first Chern number in analogy to the integer quantum Hall effect.

In the experiment, this quantized motion was observed in-situ for a fractional Mott-insulating state of atoms that are localized in the ground states of individual unit cells (Section 4.2). Per pump cycle, the centre-of-mass of the atom cloud shifted by one unit cell, consistent with the expected value of the first Chern number of the lowest band

$\nu_1^{\text{gs}} = +1$ in the experimental lattice configuration. The topological protection of the quantized transport was confirmed by measuring the displacement for a wide range of lattice depths, showing the transport's robustness with respect to perturbations. Furthermore, the efficiency of the pumping protocol was quantified and potential mechanisms limiting the efficiency were discussed. These include non-adiabatic transitions to higher bands, which could be quantified experimentally with a site-resolved band mapping technique. To unequivocally reveal the quantum nature of the transport, pumping of particles in the first excited band was investigated. In this case, a counter-intuitive reverse motion in the opposite direction of the sliding of the long lattice was observed as expected for $\nu_1^{\text{exc}} = -1$ (Section 4.3). Moreover, the topology of the pump cycle in the second band depends on the lattice depths. The associated topological transition, which is caused by the closing of the energy gap to the third band, was demonstrated experimentally.

Building on the analogy between a 1D topological charge pump and the 2D quantum Hall effect, it was proposed that topological charge pumping in 2D systems could be used to experimentally study signatures of 4D quantum Hall physics [71]. The characteristic feature of the quantum Hall effect in 4D [47, 48] is the appearance of a novel, non-linear Hall response that arises when the system is simultaneously perturbed by an electric and a magnetic field (Section 5.1). A non-linear pumping response is thus predicted to occur in a corresponding 2D topological charge pump (Section 5.2). Such a pump was realized experimentally in a 2D superlattice, in which the time-dependent phase of the superlattice along one axis acts as the pump parameter mimicking the electric field, while a small angle between the two lattices in the perpendicular direction serves as the equivalent of the magnetic field perturbation (Section 6.1).

Despite its small magnitude as a second-order effect, the non-linear bulk response transverse to the pumping direction could be resolved directly using a novel double-differential in-situ imaging technique (Section 6.2). The geometric properties of the non-linear response were probed locally with a small atom cloud and quantified using site-resolved band mapping (Section 6.3). From this, the response expected for an infinite system could be reconstructed by studying the transverse drift at different positions in the lattice (Section 6.4). By independently characterizing experimental imperfections limiting the pumping efficiency, the quantized nature of the non-linear response was demonstrated through the determination of the associated 4D topological invariant, the second Chern number. Additionally, the response's non-linear character as the result of two independent perturbations was revealed by probing its dependence on the perturbing tilt angle.

Future Directions

As an extension of the work presented here, there are a number of straightforward follow-up experiments that could be conducted. By choosing a different ratio of lattice constants, equivalent to a different flux in the corresponding 2D quantum Hall model, negative first Chern numbers could be realized even in the lowest band. This would lead to an anomalous transport of ground-state atoms in the reversed direction as compared to the motion

of the long lattice [218]. Furthermore, for a suitable choice of lattice constants, ν_1^{gs} can in principle take arbitrary integer values, in particular $|\nu_1^{\text{gs}}| > 1$, which induces a motion that can be much faster than the sliding lattice¹. This occurs for example for $d_s/d_l = 2/7$, in which case $\nu_1^{\text{gs}} = -3$ [218].

Another interesting prospect is to combine the dynamical superlattice used here with single-site-resolved imaging and manipulation techniques [287, 288]. The ability to control the lattice potential on the scale of a lattice constant would allow for the realization of hard-wall boundaries, for which topological edge states are predicted to appear in the Rice-Mele model [130, 289] (Section 2.2.1). With this, one could observe the quantized pumping of edge states going beyond previous results obtained in photonic systems [34] and directly confirm the bulk-edge correspondence [122]. Furthermore, it would enable the study of domain walls in the SSH model, at which solitons with fractional quantum numbers are expected [128, 129].

Instead of particles, topological pumps could also be used to transport other physical quantities. For example, a quantized motion of spins can be induced by a spin-dependent periodic modulation in analogy to the quantum spin Hall effect, leading to a counterpropagating motion of opposite spins [290, 291]. In the limit of isolated double wells, such a spin pump has already been implemented experimentally in the course of this thesis, demonstrating the generation of pure spin currents in absence of charge transport in antiferromagnetically ordered spin chains [178]. Besides a potential application as a source of spin currents, a spin pump could also be extended to an adiabatic quantum motor, in which only one species is pumped, while particles in another internal state are coupled by an on-site interaction [177].

Recently, a proposal for a topological energy pump in a 1D Floquet-driven system has been put forward [292], which would constitute a dynamical version of a 2D anomalous Floquet insulator [293]. To this end, the adiabatic pumping modulation is combined with a fast modulation of the tight-binding parameters. The latter include a complex phase in the tunnelling matrix elements, which serves as the pump parameter. Contrary to static systems, periodically driven systems can exhibit chiral boundary modes even if the bulk bands are topologically trivial [293]. Therefore, a situation can be realized where there is no particle transport in the bulk ($\nu_1 = 0$), but the edge states wind through the quasi-energy spectrum in a non-trivial manner during a pump cycle. Thereby, the system absorbs/loses an integer multiple of the energy corresponding to the driving frequency at the edges, leading to a quantized transport of energy through the system.

Furthermore, owing to their simplicity, topological charge pumps might serve as model systems to test new methods for probing non-trivial geometric and topological properties. One example for this is a recent proposal to determine the first Chern number by measuring heating rates in response to a chiral modulation [294]. When a system with topologically non-trivial Bloch bands is perturbed by moving it along a circular trajectory, the transition rate between different bands depends on the chirality of the perturbation.

¹Note that the displacement per cycle can already be larger than the long lattice constant d_l for $|\nu_1^{\text{gs}}| = 1$ if the unit cell of the superlattice is greater than d_l , e.g. $d_s/d_l = 2/3$.

In particular, the difference in the depletion rate of a uniformly populated band between left- and right-circular shaking, integrated over all driving frequencies, can be shown to be proportional to the band's Chern number. An equivalent scheme can be implemented with a topological charge pump by applying an oscillating external gradient (linear shaking) together with a small out-of-phase modulation of the pump parameter [295]. Using site-resolved band mapping, the heating rate could easily be measured for each value of the pump parameter and the behaviour of the associated 2D quantum Hall model could be reconstructed from this. Compared to direct measurements in 2D systems, this offers the advantage that no additional periodic driving is needed to engineer the topologically non-trivial band structure in the first place and other heating rates are thus expected to be substantially smaller.

As for topological charge pumps in 2D, there are two important properties of the 4D quantum Hall effect that have not been studied in the present experiments: the density-type pumping response [71, 101] and the time-reversal-symmetric non-linear Hall response [38, 71]. In a minimal 4D quantum Hall system, a density-type non-linear Hall response occurs when the magnetic perturbation is applied in the same plane as one of the intrinsic magnetic fields (Section 5.1.3). For a 2D charge pump, this maps onto a small modification of the lattice constant of the transverse long lattice as detailed in Section 5.2.1. The difficulty of observing this response in a cold-atom experiment arises from the fact that such a perturbation only affects the current density, whereas the centre-of-mass displacement remains invariant. An alternative way of probing this effect could be to prepare an initial state with a fixed density corresponding to a uniformly populated band in the absence of the magnetic perturbation and then switching on the perturbing field. This would transform the density mismatch into band excitations, which could either be determined directly or via their signature in the pumping response. In this way, the intrinsic 4D symmetry of the non-linear pumping response could be revealed since the two types of responses appear to be completely independent from a 2D perspective, but are nonetheless characterized by the same 4D topological invariant [71]. Note that the implementation of a perturbation in the lattice constant would also allow for the observation of a 2D non-linear Hall response in the centre-of-mass displacement as proposed in [82].

A time-reversal-symmetric 2D charge pump, on the other hand, would require the equivalent of an $SU(2)$ Yang-Mills gauge field, with the sign of the intrinsic magnetic fluxes depending on the orientation of the spin. This could be realized experimentally by making both the pump parameter (similar to [178]) and the magnetic perturbation spin-dependent [71]. The resulting charge pump would then exhibit a surprising behaviour, namely a quantized non-linear response, whereas all linear pumping responses would vanish owing to the system's time-reversal symmetry. With this, one could demonstrate the existence of a 4D quantum Hall effect in time-reversal-invariant systems.

Regarding 4D quantum Hall systems, a fascinating perspective is the potential implementation of such a model with four extended spatial dimensions utilizing the newly-developed technique to implement discrete synthetic dimensions with internal degrees of freedom [99–101]. This would open a wide range of possibilities to further explore 4D

quantum Hall physics. In finite systems, it would allow for the study of the edge phenomena associated with the topologically non-trivial nature of a 4D quantum Hall state, including the spatially isolated Weyl points that are predicted to occur on the opposing edges of a 4D quantum Hall system [225]. Furthermore, when adding interactions, higher-dimensional fractional quantum Hall phases with exotic topological excitations might be observed [48].

Interacting Topological Charge Pumps

Another interesting direction for future work are topological charge pumps with interactions. In this respect, two main topics stand out: (i) charge pumping away from the limiting case of hard-core bosons and free fermions studied so far and (ii) the question to which extent fractional quantum Hall states can potentially be probed using lower-dimensional topological charge pumps.

For fermionic systems, the effect of interactions was already studied by Niu and Thouless [11], who showed that the transport remains quantized in the presence of interactions as long as the many-body ground state is gapped and does not exhibit any long-range correlations (Section 2.2.3). Thus, a quantized motion is expected for both band-insulating and Mott-insulating states. Bosonic particles, on the other hand, form a Mott insulator for strong repulsive interactions [214] with a gap that is determined by the effective interaction energy within a unit cell and thus remains finite even in the hard-core limit (Section 3.2.2). As the on-site interaction is lowered, the gap decreases and increasing short-range correlations develop up to the transition into the superfluid phase. For a finite gap, the value of the Chern number cannot change as confirmed by numerical simulations [296]. The displacement should therefore be quantized, even though the momentum distribution becomes inhomogeneous and a breakdown of quantization would be expected in a single-particle picture. The observation of quantized bulk transport for finite interactions would constitute the first demonstration of a topologically non-trivial effect in an interacting cold-atom system. Interestingly, the properties of the edge states are profoundly altered by the interactions even though the bulk transport remains invariant. The bosonic SSH model, for example, possesses chiral symmetry, which protects the localized edge states, only in the limit of $U \rightarrow \infty$. For finite U , however, the edge states become increasingly delocalized and disappear into the bulk at a critical interaction strength, at which the system is still well within the Mott-insulating regime, seemingly violating the bulk-edge correspondence [289].

Interacting topological charge pumps have furthermore been discussed in the context of Floquet engineering, in which periodic driving of a system is used to realize Hamiltonians with very different properties than the underlying static model, e.g. topologically non-trivial band structures [297]. The success of this powerful method has been hindered by the strong heating induced by the driving, in particular in interacting systems [298]. Such processes and fundamental questions regarding the thermalization behaviour of periodically modulated interacting systems could also be studied in charge pumps. For ex-

ample, an intermediate pre-thermal state exhibiting quantized transport is predicted to appear in interacting charge pumps with partially occupied bands [141]. In this case, the periodic modulation of the pump leads to heating of the gapless initial state, for which the displacement can take arbitrary values, to an infinite-temperature state in the respective band. The displacement thus becomes quantized. Moreover, this state is robust for long times due to the exponentially suppressed non-adiabatic transitions to other bands (Section 2.2.3).

Given the close connection between non-interacting charge pumps and the integer quantum Hall effect, one may wonder whether generic fractional quantum Hall states also possess lower-dimensional dynamical analogues. Up to now, however, this remains an open question, which – following the experimental implementation of topological charge pumps – is being actively debated. A direct mapping in analogy to the one for non-interacting systems presented in Section 2.3 does not exist in the presence of interactions as the quasi-momentum states are no longer eigenstates of the many-body Hamiltonian. Furthermore, the interactions in a lower-dimensional system like the charge pump are fundamentally different from those in the higher-dimensional quantum Hall system.

One approach is based on the thin-torus limit of the 2D fractional quantum Hall effect [299], in which the homogeneous degenerate ground states of an extended system reduce to charge-density waves that are related by a global translation – the Tao-Thouless states [300]. In this limit, the uniform 2D system can be mapped onto a 1D lattice model similar to the non-interacting Laughlin charge pump [301] (Section 2.3.1). The interaction enters into the 1D model in the form of a long-range interaction, which favours a charge-density wave. Inspired by this, numerical simulations for fermions with dipolar interactions in a 1D dynamical superlattice were performed, which suggested the existence of degenerate ground states at fractional fillings with non-integer Chern numbers [302]. Similarly, a charge pump for bosonic particles in a superlattice potential with nearest- and next-nearest-neighbour interaction has been proposed, yielding a fractional displacement per cycle [303, 304]. While the ground states in the thin-torus limit are smoothly connected to the homogeneous fractional quantum Hall states in a large 2D system, the relation between the 1D case and the 2D fractional quantum Hall effect is being disputed [305]. Simultaneously, proposals were put forward for a fractional topological charge pump that directly realizes a thin-torus model in quasi-1D ladder systems [306] and using synthetic dimensions [307]. Another possible approach to relate fractional quantum Hall states to lower-dimensional charge pumps could be provided by recent work in [308]. This work demonstrates that integer topological invariants in interacting systems can be defined in an analogous way to the non-interacting case, if the Bloch waves are replaced by the eigenvectors of the inverse Green's function. This might allow for the realization of a corresponding topological charge pump, for which the inverse Green's function serves as an effective Hamiltonian. However, it is neither clear whether this relation can even be extended to fractional topological states nor if the implementation of the resulting effective Hamiltonian would be experimentally feasible.

References

- [1] G. S. Ohm. *Die galvanische Kette, mathematisch bearbeitet*. Reimann, Berlin, Germany (1827). See page: 1
- [2] P. Drude. *Zur Elektronentheorie der Metalle*. *Ann. Phys.* **306**, 566–613 (1900). See page: 1
- [3] A. Sommerfeld and H. Bethe. *Elektronentheorie der Metalle*. In *Aufbau der zusammenhängenden Materie. Handbuch der Physik, Vol. 24/2* (Ed. A. Smekal), pp. 333–622. Springer, Berlin, Germany (1933). See page: 1
- [4] F. Bloch. *Über die Quantenmechanik der Elektronen in Kristallgittern*. *Z. Physik* **52**, 555–600 (1929). See page: 1
- [5] A. Kundt. *Das Hall'sche Phänomen in Eisen, Kobalt und Nickel*. *Ann. Phys.* **285**, 257–271 (1893). See page: 1
- [6] R. Karplus and J. M. Luttinger. *Hall Effect in Ferromagnetics*. *Phys. Rev.* **95**, 1154–1160 (1954). See page: 1
- [7] D. Xiao, M.-C. Chang, and Q. Niu. *Berry phase effects on electronic properties*. *Rev. Mod. Phys.* **82**, 1959–2007 (2010). See pages: 1, 9, 11, 13, 14, 20, 21, 71
- [8] S. Pancharatnam. *Generalized theory of interference, and its applications*. *Proc. Indian Acad. Sci.* **44**, 247–262 (1956). See pages: 1, 9, 10
- [9] M. V. Berry. *Quantal phase factors accompanying adiabatic changes*. *Proc. R. Soc. Lond. A* **392**, 45–57 (1984). See pages: 1, 9, 10, 16
- [10] D. J. Thouless. *Quantization of particle transport*. *Phys. Rev. B* **27**, 6083–6087 (1983). See pages: 2, 9, 11, 14, 16, 24, 45, 125
- [11] Q. Niu and D. J. Thouless. *Quantised adiabatic charge transport in the presence of substrate disorder and many-body interaction*. *J. Phys. A: Math. Gen.* **17**, 2453–2462 (1984). See pages: 2, 9, 17, 21, 129
- [12] B. L. Altshuler and L. I. Glazman. *Pumping Electrons*. *Science* **283**, 1864–1865 (1999). See page: 2
- [13] D. J. Thouless, M. Kohmoto, M. P. Nightingale, and M. den Nijs. *Quantized Hall Conductance in a Two-Dimensional Periodic Potential*. *Phys. Rev. Lett.* **49**, 405–408 (1982). See pages: 2, 3, 9, 14, 24, 25, 66, 125

- [14] B. Simon. *Holonomy, the Quantum Adiabatic Theorem, and Berry's Phase*. Phys. Rev. Lett. **51**, 2167–2170 (1983). See pages: 2, 3, 14, 16
- [15] S.-S. Chern. *Characteristic Classes of Hermitian Manifolds*. Ann. Math. **47**, 85–121 (1946). See pages: 2, 14, 67
- [16] Q. Niu. *Towards a quantum pump of electric charges*. Phys. Rev. Lett. **64**, 1812–1815 (1990). See pages: 2, 9, 17, 31, 33, 41, 48
- [17] J. P. Pekola et al. *Single-electron current sources: Toward a refined definition of the ampere*. Rev. Mod. Phys. **85**, 1421–1472 (2013). See pages: 2, 31, 33
- [18] K. K. Likharev and A. B. Zorin. *Theory of the Bloch-wave oscillations in small Josephson junctions*. J. Low. Temp. Phys. **59**, 347–382 (1985). See pages: 2, 32
- [19] H. Scherer and B. Camarota. *Quantum metrology triangle experiments: a status review*. Meas. Sci. Technol. **23**, 124010 (2012). See pages: 2, 32
- [20] J. Zak. *Berry's phase for energy bands in solids*. Phys. Rev. Lett. **62**, 2747–2750 (1989). See pages: 2, 19, 20
- [21] R. D. King-Smith and D. Vanderbilt. *Theory of polarization of crystalline solids*. Phys. Rev. B **47**, 1651–1654 (1993). See pages: 2, 20, 47
- [22] R. Resta. *Macroscopic polarization in crystalline dielectrics: the geometric phase approach*. Rev. Mod. Phys. **66**, 899–915 (1994). See pages: 2, 20
- [23] L. J. Geerligs et al. *Frequency-locked turnstile device for single electrons*. Phys. Rev. Lett. **64**, 2691–2694 (1990). See pages: 2, 33
- [24] L. P. Kouwenhoven, A. T. Johnson, N. C. van der Vaart, C. J. P. M. Harmans, and C. T. Foxon. *Quantized current in a quantum-dot turnstile using oscillating tunnel barriers*. Phys. Rev. Lett. **67**, 1626–1629 (1991). See pages: 2, 33
- [25] H. Pothier et al. *Single electron pump fabricated with ultrasmall normal tunnel junctions*. Physica B **169**, 573–574 (1991). See pages: 2, 33
- [26] H. Pothier, P. Lafarge, C. Urbina, D. Esteve, and M. H. Devoret. *Single-Electron Pump Based on Charging Effects*. EPL **17**, 249–254 (1992). See pages: 2, 33
- [27] B. Spivak, F. Zhou, and M. T. Beal Monod. *Mesoscopic mechanisms of the photovoltaic effect and microwave absorption in granular metals*. Phys. Rev. B **51**, 13226–13230 (1995). See page: 2
- [28] P. W. Brouwer. *Scattering approach to parametric pumping*. Phys. Rev. B **58**, R10135–R10138 (1998). See pages: 2, 33
- [29] F. Zhou, B. Spivak, and B. Altshuler. *Mesoscopic Mechanism of Adiabatic Charge Transport*. Phys. Rev. Lett. **82**, 608–611 (1999). See pages: 2, 33

- [30] M. Switkes, C. M. Marcus, K. Campman, and A. C. Gossard. *An Adiabatic Quantum Electron Pump*. *Science* **283**, 1905–1908 (1999). See pages: 2, 33
- [31] P. W. Brouwer. *Rectification of displacement currents in an adiabatic electron pump*. *Phys. Rev. B* **63**, 121303 (2001). See pages: 2, 34
- [32] L. DiCarlo, C. M. Marcus, and J. S. Harris. *Photocurrent, Rectification, and Magnetic Field Symmetry of Induced Current through Quantum Dots*. *Phys. Rev. Lett.* **91**, 246804 (2003). See pages: 2, 34
- [33] M. Möttönen, J. J. Vartiainen, and J. P. Pekola. *Experimental Determination of the Berry Phase in a Superconducting Charge Pump*. *Phys. Rev. Lett.* **100**, 177201 (2008). See pages: 2, 34
- [34] Y. E. Kraus, Y. Lahini, Z. Ringel, M. Verbin, and O. Zilberberg. *Topological States and Adiabatic Pumping in Quasicrystals*. *Phys. Rev. Lett.* **109**, 106402 (2012). See pages: 3, 4, 9, 17, 34, 45, 127
- [35] M. Verbin, O. Zilberberg, Y. Lahini, Y. E. Kraus, and Y. Silberberg. *Topological pumping over a photonic Fibonacci quasicrystal*. *Phys. Rev. B* **91**, 064201 (2015). See pages: 3, 4, 34
- [36] K. v. Klitzing, G. Dorda, and M. Pepper. *New Method for High-Accuracy Determination of the Fine-Structure Constant Based on Quantized Hall Resistance*. *Phys. Rev. Lett.* **45**, 494–497 (1980). See pages: 3, 66, 73
- [37] R. B. Laughlin. *Quantized Hall conductivity in two dimensions*. *Phys. Rev. B* **23**, 5632–5633 (1981). See pages: 3, 24, 25, 26, 66, 75
- [38] X.-L. Qi, T. L. Hughes, and S.-C. Zhang. *Topological field theory of time-reversal invariant insulators*. *Phys. Rev. B* **78**, 195424 (2008). See pages: 3, 4, 27, 65, 66, 67, 68, 70, 77, 128
- [39] P. W. Anderson. *Basic Notions of Condensed Matter Physics*. Westview Press, Boulder, USA (1997). See page: 3
- [40] D. C. Tsui, H. L. Stormer, and A. C. Gossard. *Two-Dimensional Magnetotransport in the Extreme Quantum Limit*. *Phys. Rev. Lett.* **48**, 1559–1562 (1982). See pages: 3, 66
- [41] R. B. Laughlin. *Anomalous Quantum Hall Effect: An Incompressible Quantum Fluid with Fractionally Charged Excitations*. *Phys. Rev. Lett.* **50**, 1395–1398 (1983). See page: 3
- [42] F. D. M. Haldane. *Nonlinear Field Theory of Large-Spin Heisenberg Antiferromagnets: Semiclassically Quantized Solitons of the One-Dimensional Easy-Axis Néel State*. *Phys. Rev. Lett.* **50**, 1153–1156 (1983). See page: 3

- [43] F. D. M. Haldane. *Continuum dynamics of the 1-D Heisenberg antiferromagnet: Identification with the $O(3)$ nonlinear sigma model*. Phys. Lett. A **93**, 464–468 (1983). See page: 3
- [44] W. J. L. Buyers et al. *Experimental evidence for the Haldane gap in a spin-1 nearly isotropic, antiferromagnetic chain*. Phys. Rev. Lett. **56**, 371–374 (1986). See page: 3
- [45] C.-Z. Chang et al. *Experimental Observation of the Quantum Anomalous Hall Effect in a Magnetic Topological Insulator*. Science **340**, 167–170 (2013). See page: 3
- [46] M. Nakahara. *Geometry, Topology and Physics*. CRC Press, Boca Raton, USA, 2nd edition (2003). See pages: 3, 66
- [47] J. Fröhlich and B. Pedrini. *New applications of the chiral anomaly*. In *Mathematical Physics 2000* (Eds. A. Fokas, A. Grigoryan, T. Kibble, and B. Zegarlinski), pp. 9–47. Imperial College Press, London, United Kingdom (2000). See pages: 3, 65, 66, 67, 68, 70, 126
- [48] S.-C. Zhang and J. Hu. *A Four-Dimensional Generalization of the Quantum Hall Effect*. Science **294**, 823–828 (2001). See pages: 3, 65, 66, 67, 69, 70, 126, 129
- [49] C. L. Kane and E. J. Mele. *Quantum Spin Hall Effect in Graphene*. Phys. Rev. Lett. **95**, 226801 (2005). See pages: 4, 68
- [50] C. L. Kane and E. J. Mele. *Z_2 Topological Order and the Quantum Spin Hall Effect*. Phys. Rev. Lett. **95**, 146802 (2005). See pages: 4, 68
- [51] B. A. Bernevig and S.-C. Zhang. *Quantum Spin Hall Effect*. Phys. Rev. Lett. **96**, 106802 (2006). See pages: 4, 68
- [52] B. A. Bernevig, T. L. Hughes, and S.-C. Zhang. *Quantum Spin Hall Effect and Topological Phase Transition in HgTe Quantum Wells*. Science **314**, 1757–1761 (2006). See pages: 4, 68
- [53] X.-L. Qi and S.-C. Zhang. *Topological insulators and superconductors*. Rev. Mod. Phys. **83**, 1057–1110 (2011). See pages: 4, 65, 67, 68
- [54] M. König et al. *Quantum Spin Hall Insulator State in HgTe Quantum Wells*. Science **318**, 766–770 (2007). See pages: 4, 68
- [55] M. König et al. *The Quantum Spin Hall Effect: Theory and Experiment*. J. Phys. Soc. Jpn. **77**, 031007 (2008). See pages: 4, 68
- [56] A. Roth et al. *Nonlocal Transport in the Quantum Spin Hall State*. Science **325**, 294–297 (2009). See page: 4
- [57] L. Fu, C. L. Kane, and E. J. Mele. *Topological Insulators in Three Dimensions*. Phys. Rev. Lett. **98**, 106803 (2007). See pages: 4, 66, 68

- [58] J. E. Moore and L. Balents. *Topological invariants of time-reversal-invariant band structures*. Phys. Rev. B **75**, 121306 (2007). See pages: 4, 68
- [59] R. Roy. *Topological phases and the quantum spin Hall effect in three dimensions*. Phys. Rev. B **79**, 195322 (2009). See pages: 4, 68
- [60] L. Fu and C. L. Kane. *Topological insulators with inversion symmetry*. Phys. Rev. B **76**, 045302 (2007). See pages: 4, 68
- [61] D. Hsieh et al. *A topological Dirac insulator in a quantum spin Hall phase*. Nature **452**, 970–974 (2008). See pages: 4, 65, 68
- [62] A. Kitaev. *Periodic table for topological insulators and superconductors*. AIP Conf. Proc. **1134**, 22–30 (2009). See pages: 4, 65, 66, 68
- [63] S. Ryu, A. P. Schnyder, A. Furusaki, and A. W. W. Ludwig. *Topological insulators and superconductors: tenfold way and dimensional hierarchy*. New J. Phys. **12**, 065010 (2010). See pages: 4, 65, 66, 68
- [64] C.-K. Chiu, J. C. Y. Teo, A. P. Schnyder, and S. Ryu. *Classification of topological quantum matter with symmetries*. Rev. Mod. Phys. **88**, 035005 (2016). See pages: 4, 65, 66, 68
- [65] M. Sato and Y. Ando. *Topological superconductors: a review*. Rep. Prog. Phys. **80**, 076501 (2017). See page: 4
- [66] L. Fu. *Topological Crystalline Insulators*. Phys. Rev. Lett. **106**, 106802 (2011). See page: 4
- [67] T. H. Hsieh et al. *Topological crystalline insulators in the SnTe material class*. Nat. Commun. **3**, 982 (2012). See page: 4
- [68] Z. K. Liu et al. *Discovery of a Three-Dimensional Topological Dirac Semimetal, Na₃Bi*. Science **343**, 864–867 (2014). See page: 4
- [69] L. Lu et al. *Experimental observation of Weyl points*. Science **349**, 622–624 (2015). See pages: 4, 65, 69
- [70] S.-Y. Xu et al. *Discovery of a Weyl fermion semimetal and topological Fermi arcs*. Science **349**, 613–617 (2015). See pages: 4, 65, 69
- [71] Y. E. Kraus, Z. Ringel, and O. Zilberberg. *Four-Dimensional Quantum Hall Effect in a Two-Dimensional Quasicrystal*. Phys. Rev. Lett. **111**, 226401 (2013). See pages: 4, 6, 65, 74, 77, 78, 79, 83, 91, 126, 128
- [72] R. P. Feynman. *Simulating physics with computers*. Int. J. Theor. Phys. **21**, 467–488 (1982). See page: 4

- [73] I. M. Georgescu, S. Ashhab, and F. Nori. *Quantum simulation*. Rev. Mod. Phys. **86**, 153–185 (2014). See page: 4
- [74] I. Bloch, J. Dalibard, and S. Nascimbène. *Quantum simulations with ultracold quantum gases*. Nat. Phys. **8**, 267–276 (2012). See pages: 4, 36
- [75] C. Gross and I. Bloch. *Quantum simulations with ultracold atoms in optical lattices*. Science **357**, 995–1001 (2017). See pages: 4, 36
- [76] M. Ben Dahan, E. Peik, J. Reichel, Y. Castin, and C. Salomon. *Bloch Oscillations of Atoms in an Optical Potential*. Phys. Rev. Lett. **76**, 4508–4511 (1996). See page: 4
- [77] C. Raman et al. *Evidence for a Critical Velocity in a Bose-Einstein Condensed Gas*. Phys. Rev. Lett. **83**, 2502–2505 (1999). See page: 4
- [78] G. Roati et al. *Anderson localization of a non-interacting Bose-Einstein condensate*. Nature **453**, 895–898 (2008). See page: 4
- [79] J. Billy et al. *Direct observation of Anderson localization of matter waves in a controlled disorder*. Nature **453**, 891–894 (2008). See page: 4
- [80] M. Schreiber et al. *Observation of many-body localization of interacting fermions in a quasirandom optical lattice*. Science **349**, 842–845 (2015). See page: 4
- [81] C.-C. Chien, S. Peotta, and M. Di Ventra. *Quantum transport in ultracold atoms*. Nat. Phys. **11**, 998–1004 (2015). See pages: 5, 45, 73
- [82] H. M. Price, O. Zilberberg, T. Ozawa, I. Carusotto, and N. Goldman. *Measurement of Chern numbers through center-of-mass responses*. Phys. Rev. B **93**, 245113 (2016). See pages: 5, 71, 74, 128
- [83] J.-P. Brantut, J. Meineke, D. Stadler, S. Krinner, and T. Esslinger. *Conduction of Ultracold Fermions Through a Mesoscopic Channel*. Science **337**, 1069–1071 (2012). See pages: 5, 45
- [84] S. Krinner, D. Stadler, D. Husmann, J.-P. Brantut, and T. Esslinger. *Observation of quantized conductance in neutral matter*. Nature **517**, 64–67 (2014). See pages: 5, 45
- [85] N. Cooper. *Rapidly rotating atomic gases*. Adv. Phys. **57**, 539–616 (2008). See page: 5
- [86] Y. J. Lin, R. L. Compton, K. Jiménez-García, J. V. Porto, and I. B. Spielman. *Synthetic magnetic fields for ultracold neutral atoms*. Nature **462**, 628–632 (2009). See page: 5
- [87] M. Aidelsburger et al. *Experimental Realization of Strong Effective Magnetic Fields in an Optical Lattice*. Phys. Rev. Lett. **107**, 255301 (2011). See page: 5

- [88] J. Struck et al. *Engineering Ising-XY spin-models in a triangular lattice using tunable artificial gauge fields*. Nat. Phys. **9**, 738–743 (2013). See page: 5
- [89] M. Aidelsburger et al. *Realization of the Hofstadter Hamiltonian with Ultracold Atoms in Optical Lattices*. Phys. Rev. Lett. **111**, 185301 (2013). See pages: 5, 30
- [90] H. Miyake, G. A. Siviloglou, C. J. Kennedy, W. C. Burton, and W. Ketterle. *Realizing the Harper Hamiltonian with Laser-Assisted Tunneling in Optical Lattices*. Phys. Rev. Lett. **111**, 185302 (2013). See pages: 5, 30
- [91] M. Aidelsburger et al. *Measuring the Chern number of Hofstadter bands with ultracold bosonic atoms*. Nat. Phys. **11**, 162–166 (2015). See pages: 5, 30, 45, 73
- [92] G. Jotzu et al. *Experimental realization of the topological Haldane model with ultracold fermions*. Nature **515**, 237–240 (2014). See pages: 5, 45, 73
- [93] M. Atala et al. *Direct measurement of the Zak phase in topological Bloch bands*. Nat. Phys. **9**, 795–800 (2013). See pages: 5, 20, 47, 58, 65
- [94] L. Duca et al. *An Aharonov-Bohm interferometer for determining Bloch band topology*. Science **347**, 288–292 (2015). See page: 5
- [95] T. Li et al. *Bloch state tomography using Wilson lines*. Science **352**, 1094–1097 (2016). See page: 5
- [96] N. Fläschner et al. *Experimental reconstruction of the Berry curvature in a Floquet Bloch band*. Science **352**, 1091–1094 (2016). See page: 5
- [97] O. Boada, A. Celi, J. I. Latorre, and M. Lewenstein. *Quantum Simulation of an Extra Dimension*. Phys. Rev. Lett. **108**, 133001 (2012). See pages: 5, 78
- [98] A. Celi et al. *Synthetic Gauge Fields in Synthetic Dimensions*. Phys. Rev. Lett. **112**, 043001 (2014). See pages: 5, 78
- [99] M. Mancini et al. *Observation of chiral edge states with neutral fermions in synthetic Hall ribbons*. Science **349**, 1510–1513 (2015). See pages: 5, 78, 128
- [100] B. K. Stuhl, H.-I. Lu, L. M. Aycock, D. Genkina, and I. B. Spielman. *Visualizing edge states with an atomic Bose gas in the quantum Hall regime*. Science **349**, 1514–1518 (2015). See pages: 5, 78, 128
- [101] H. M. Price, O. Zilberberg, T. Ozawa, I. Carusotto, and N. Goldman. *Four-Dimensional Quantum Hall Effect with Ultracold Atoms*. Phys. Rev. Lett. **115**, 195303 (2015). See pages: 5, 71, 72, 74, 77, 78, 128
- [102] S. Sugawa, F. Salces-Carcoba, A. R. Perry, Y. Yue, and I. B. Spielman. *Observation of a non-abelian Yang monopole: from new Chern numbers to a topological transition*. arXiv:1610.06228 [cond-mat.quant-gas] (2016). See pages: 5, 67

- [103] M. Kolodrubetz. *Measuring the Second Chern Number from Nonadiabatic Effects*. Phys. Rev. Lett. **117**, 015301 (2016). See page: 5
- [104] M. Greiner. *Magnetischer Transfer von Atomen – ein Weg zur einfachen Bose-Einstein-Kondensation*. Diploma thesis, Ludwig-Maximilians-Universität München (2000). See pages: 6, 35, 36
- [105] M. Greiner. *Ultracold quantum gases in three-dimensional optical lattice potentials*. PhD thesis, Ludwig-Maximilians-Universität München (2003). See pages: 6, 35
- [106] M. Aidelsburger. *Ultracold atoms in periodically driven optical lattices*. Master's thesis, Ludwig-Maximilians-Universität München (2011). See pages: 6, 35, 39
- [107] M. Born and V. Fock. *Beweis des Adiabatenatzes*. Z. Physik **51**, 165–180 (1928). See pages: 9, 10
- [108] H. C. Longuet-Higgins, U. Öpik, M. H. L. Pryce, and R. A. Sack. *Studies of the Jahn-Teller effect – II. The dynamical problem*. Proc. R. Soc. Lond. A **244**, 1–16 (1958). See page: 9
- [109] B. I. Halperin. *Quantized Hall conductance, current-carrying edge states, and the existence of extended states in a two-dimensional disordered potential*. Phys. Rev. B **25**, 2185–2190 (1982). See pages: 9, 26
- [110] Y. Hatsugai. *Chern number and edge states in the integer quantum Hall effect*. Phys. Rev. Lett. **71**, 3697–3700 (1993). See pages: 9, 17
- [111] R. Bustos-Marún, G. Refael, and F. von Oppen. *Adiabatic Quantum Motors*. Phys. Rev. Lett. **111**, 060802 (2013). See pages: 9, 32
- [112] O. Romero-Isart and J. J. García-Ripoll. *Quantum ratchets for quantum communication with optical superlattices*. Phys. Rev. A **76**, 052304 (2007). See pages: 9, 32, 45
- [113] T. Kato. *On the Adiabatic Theorem of Quantum Mechanics*. J. Phys. Soc. Jpn. **5**, 435–439 (1950). See page: 10
- [114] Y. Aharonov and D. Bohm. *Significance of Electromagnetic Potentials in the Quantum Theory*. Phys. Rev. **115**, 485–491 (1959). See page: 11
- [115] J. H. Hannay. *Angle variable holonomy in adiabatic excursion of an integrable Hamiltonian*. J. Phys. A **18**, 221–230 (1985). See page: 11
- [116] T. T. Wu and C. N. Yang. *Concept of nonintegrable phase factors and global formulation of gauge fields*. Phys. Rev. D **12**, 3845–3857 (1975). See pages: 14, 16
- [117] M. Kohmoto. *Topological invariant and the quantization of the Hall conductance*. Ann. Phys. **160**, 343–354 (1985). See pages: 14, 16

- [118] P. A. M. Dirac. *Quantised singularities in the electromagnetic field*. Proc. Royal Soc. A **133**, 60–72 (1931). See page: 16
- [119] J. von Neumann and E. Wigner. *Über merkwürdige diskrete Eigenwerte. Über das Verhalten von Eigenwerten bei adiabatischen Prozessen*. Phys. Z. **30**, 467–470 (1929). See pages: 16, 67
- [120] J. E. Avron, R. Seiler, and B. Simon. *Homotopy and Quantization in Condensed Matter Physics*. Phys. Rev. Lett. **51**, 51–53 (1983). See page: 17
- [121] Y. Hatsugai. *Edge states in the integer quantum Hall effect and the Riemann surface of the Bloch function*. Phys. Rev. B **48**, 11851–11862 (1993). See pages: 17, 18
- [122] Y. Hatsugai and T. Fukui. *Bulk-edge correspondence in topological pumping*. Phys. Rev. B **94**, 041102 (2016). See pages: 17, 18, 58, 95, 127
- [123] K.-I. Imura, Y. Yoshimura, T. Fukui, and Y. Hatsugai. *Bulk-edge correspondence in topological transport and pumping*. arXiv:1706.04493 [cond-mat.mes-hall] (2017). See page: 17
- [124] R. Resta. *Manifestations of Berry’s phase in molecules and condensed matter*. J. Phys. Condens. Matter **12**, R107–R143 (2000). See pages: 19, 20
- [125] R. M. Martin. *Comment on calculations of electric polarization in crystals*. Phys. Rev. B **9**, 1998–1999 (1974). See page: 20
- [126] J. Zak. *Stark Ladder in Solids?* Phys. Rev. Lett. **20**, 1477–1481 (1968). See page: 20
- [127] P. Delplace, D. Ullmo, and G. Montambaux. *Zak phase and the existence of edge states in graphene*. Phys. Rev. B **84**, 195452 (2011). See page: 20
- [128] R. Jackiw and C. Rebbi. *Solitons with fermion number $\frac{1}{2}$* . Phys. Rev. D **13**, 3398–3409 (1976). See pages: 20, 42, 127
- [129] W. P. Su, J. R. Schrieffer, and A. J. Heeger. *Solitons in Polyacetylene*. Phys. Rev. Lett. **42**, 1698–1701 (1979). See pages: 20, 42, 127
- [130] M. J. Rice and E. J. Mele. *Elementary Excitations of a Linearly Conjugated Diatomic Polymer*. Phys. Rev. Lett. **49**, 1455–1459 (1982). See pages: 20, 42, 92, 94, 127
- [131] Q. Niu, D. J. Thouless, and Y.-S. Wu. *Quantized Hall conductance as a topological invariant*. Phys. Rev. B **31**, 3372–3377 (1985). See page: 21
- [132] L. Landau. *Zur Theorie der Energieübertragung. II*. Phys. Z. Sowjetunion **2**, 46–51 (1932). See pages: 21, 23
- [133] C. Zener. *Non-Adiabatic Crossing of Energy Levels*. Proc. Royal Soc. A **137**, 696–702 (1932). See pages: 21, 23

- [134] W.-K. Shih and Q. Niu. *Nonadiabatic particle transport in a one-dimensional electron system*. Phys. Rev. B **50**, 11902–11910 (1994). See pages: 21, 22, 23, 32
- [135] S. Choi et al. *Observation of discrete time-crystalline order in a disordered dipolar many-body system*. Nature **543**, 221–225 (2017). See page: 22
- [136] J. Zhang et al. *Observation of a discrete time crystal*. Nature **543**, 217–220 (2017). See page: 22
- [137] J. H. Shirley. *Solution of the Schrödinger Equation with a Hamiltonian Periodic in Time*. Phys. Rev. **138**, B979–B987 (1965). See page: 22
- [138] T. Kitagawa, E. Berg, M. Rudner, and E. Demler. *Topological characterization of periodically driven quantum systems*. Phys. Rev. B **82**, 235114 (2010). See page: 22
- [139] H. P. Breuer, K. Dietz, and M. Holthaus. *The role of avoided crossings in the dynamics of strong laser field – matter interactions*. Z. Phys. D **8**, 349–357 (1988). See page: 22
- [140] L. Privitera, A. Russomanno, R. Citro, and G. E. Santoro. *Non-adiabatic breaking of topological pumping*. arXiv:1709.08457 [cond-mat.quant-gas] (2017). See page: 23
- [141] N. H. Lindner, E. Berg, and M. S. Rudner. *Universal Chiral Quasisteady States in Periodically Driven Many-Body Systems*. Phys. Rev. X **7**, 011018 (2017). See pages: 23, 130
- [142] J. E. Avron, R. Seiler, and L. G. Yaffe. *Adiabatic theorems and applications to the quantum Hall effect*. Commun. Math. Phys. **110**, 33–49 (1987). See page: 23
- [143] M. Klein and R. Seiler. *Power-law corrections to the Kubo formula vanish in quantum Hall systems*. Commun. Math. Phys. **128**, 141–160 (1990). See pages: 23, 32
- [144] L. Landau. *Diamagnetismus der Metalle*. Z. Physik **64**, 629–637 (1930). See pages: 24, 25
- [145] P. G. Harper. *The general motion of conduction electrons in a uniform magnetic field, with application to the diamagnetism of metals*. Proc. Phys. Soc. A **68**, 879–892 (1955). See pages: 24, 28, 30, 77
- [146] M. Y. Azbel. *Energy spectrum of a conduction electron in a magnetic field*. Zh. Eksp. Teor. Fiz. **46**, 929–946 (1964). [Sov. Phys. JETP **19**, 634–645 (1964)]. See pages: 24, 28, 30, 77
- [147] D. R. Hofstadter. *Energy levels and wave functions of Bloch electrons in rational and irrational magnetic fields*. Phys. Rev. B **14**, 2239–2249 (1976). See pages: 24, 28, 30, 31, 77, 79

- [148] R. B. Laughlin. *Fractional Quantization*. In *Nobel Lectures, Physics 1996–2000* (Ed. G. Ekspong), pp. 264–286. World Scientific Publishing Co., Singapore, Singapore (2002). See pages: 24, 26
- [149] L. D. Landau and E. M. Lifshitz. *Quantum Mechanics (Non-Relativistic Theory)*. Butterworth-Heinemann, Oxford, United Kingdom (1977). See pages: 25, 42
- [150] M. Lohse, C. Schweizer, H. M. Price, O. Zilberberg, and I. Bloch. *Exploring 4D quantum Hall physics with a 2D topological charge pump*. *Nature* **553**, 55–58 (2018). See pages: 26, 75, 93, 98, 101, 108, 110, 115, 116, 119, 122, 123
- [151] L. Wang, M. Troyer, and X. Dai. *Topological Charge Pumping in a One-Dimensional Optical Lattice*. *Phys. Rev. Lett.* **111**, 026802 (2013). See pages: 27, 45, 59
- [152] Y. E. Kraus and O. Zilberberg. *Topological Equivalence between the Fibonacci Quasicrystal and the Harper Model*. *Phys. Rev. Lett.* **109**, 116404 (2012). See page: 27
- [153] D. Jaksch, C. Bruder, J. I. Cirac, C. W. Gardiner, and P. Zoller. *Cold Bosonic Atoms in Optical Lattices*. *Phys. Rev. Lett.* **81**, 3108–3111 (1998). See pages: 27, 41, 42
- [154] T. Roscilde. *Bosons in one-dimensional incommensurate superlattices*. *Phys. Rev. A* **77**, 063605 (2008). See pages: 27, 28, 42, 43
- [155] S. Kivelson. *Wannier functions in one-dimensional disordered systems: Application to fractionally charged solitons*. *Phys. Rev. B* **26**, 4269–4277 (1982). See pages: 27, 41
- [156] N. Marzari and D. Vanderbilt. *Maximally localized generalized Wannier functions for composite energy bands*. *Phys. Rev. B* **56**, 12847–12865 (1997). See pages: 27, 41
- [157] U. Bissbort. *Dynamical effects and disorder in ultracold bosonic matter*. PhD thesis, Johann-Wolfgang-Goethe-Universität Frankfurt (2013). See pages: 27, 41, 59
- [158] B. Damski, J. Zakrzewski, L. Santos, P. Zoller, and M. Lewenstein. *Atomic Bose and Anderson Glasses in Optical Lattices*. *Phys. Rev. Lett.* **91**, 080403 (2003). See page: 28
- [159] V. Guarrera, L. Fallani, J. E. Lye, C. Fort, and M. Inguscio. *Inhomogeneous broadening of a Mott insulator spectrum*. *New J. Phys.* **9**, 107 (2007). See page: 28
- [160] G. Roux et al. *Quasiperiodic Bose-Hubbard model and localization in one-dimensional cold atomic gases*. *Phys. Rev. A* **78**, 023628 (2008). See pages: 28, 43, 80
- [161] S. Aubry and G. André. *Analyticity breaking and Anderson localization in incommensurate lattices*. *Ann. Israel Phys. Soc.* **3**, 133–140 (1980). See page: 28
- [162] Y. Hatsugai and M. Kohmoto. *Energy spectrum and the quantum Hall effect on the square lattice with next-nearest-neighbor hopping*. *Phys. Rev. B* **42**, 8282–8294 (1990). See pages: 28, 30, 31, 83

- [163] M. Lohse, C. Schweizer, O. Zilberberg, M. Aidelsburger, and I. Bloch. *A Thouless quantum pump with ultracold bosonic atoms in an optical superlattice*. Nat. Phys. **12**, 350–354 (2016). See pages: 29, 46, 47, 49, 51, 52, 54, 58, 61, 62
- [164] C. R. Dean et al. *Hofstadter’s butterfly and the fractal quantum Hall effect in moire superlattices*. Nature **497**, 598–602 (2013). See page: 30
- [165] L. A. Ponomarenko et al. *Cloning of Dirac fermions in graphene superlattices*. Nature **497**, 594–597 (2013). See page: 30
- [166] M. C. Rechtsman et al. *Photonic Floquet topological insulators*. Nature **496**, 196–200 (2013). See page: 30
- [167] M. Hafezi, S. Mittal, J. Fan, A. Migdall, and J. M. Taylor. *Imaging topological edge states in silicon photonics*. Nat. Photonics **7**, 1001–1005 (2013). See page: 30
- [168] X. G. Wen, F. Wilczek, and A. Zee. *Chiral spin states and superconductivity*. Phys. Rev. B **39**, 11413–11423 (1989). See page: 31
- [169] Q. Niu and K. Ensslin. *Quantum wire CCD charge pump*. US patent No. 5,144,580 (1992). See pages: 31, 33
- [170] F. Piquemal and G. Genevès. *Argument for a direct realization of the quantum metrological triangle*. Metrologia **37**, 207–211 (2000). See page: 32
- [171] T. J. Quinn. *News from the BIPM*. Metrologia **26**, 69–74 (1989). See page: 32
- [172] B. Josephson. *Possible new effects in superconductive tunnelling*. Phys. Lett. **1**, 251–253 (1962). See page: 32
- [173] S. Shapiro. *Josephson Currents in Superconducting Tunneling: The Effect of Microwaves and Other Observations*. Phys. Rev. Lett. **11**, 80–82 (1963). See page: 32
- [174] P. J. Mohr, D. B. Newell, and B. N. Taylor. *CODATA recommended values of the fundamental physical constants: 2014*. Rev. Mod. Phys. **88**, 035009 (2016). See page: 32
- [175] M. W. Keller, A. L. Eichenberger, J. M. Martinis, and N. M. Zimmerman. *A Capacitance Standard Based on Counting Electrons*. Science **285**, 1706–1709 (1999). See page: 32
- [176] X.-L. Qi and S.-C. Zhang. *Field-induced gap and quantized charge pumping in a nanoscale helical wire*. Phys. Rev. B **79**, 235442 (2009). See page: 32
- [177] A. V. Ponomarev, S. Denisov, and P. Hänggi. *ac-Driven Atomic Quantum Motor*. Phys. Rev. Lett. **102**, 230601 (2009). See pages: 32, 127

- [178] C. Schweizer, M. Lohse, R. Citro, and I. Bloch. *Spin Pumping and Measurement of Spin Currents in Optical Superlattices*. Phys. Rev. Lett. **117**, 170405 (2016). See pages: 32, 40, 127, 128
- [179] P. Barmettler et al. *Quantum many-body dynamics of coupled double-well superlattices*. Phys. Rev. A **78**, 012330 (2008). See pages: 32, 45
- [180] D. V. Averin and K. K. Likharev. *Coulomb blockade of single-electron tunneling, and coherent oscillations in small tunnel junctions*. J. Low Temp. Phys. **62**, 345–373 (1986). See page: 33
- [181] L. J. Geerligs, D. V. Averin, and J. E. Mooij. *Observation of macroscopic quantum tunneling through the Coulomb energy barrier*. Phys. Rev. Lett. **65**, 3037–3040 (1990). See page: 33
- [182] M. W. Keller, J. M. Martinis, N. M. Zimmerman, and A. H. Steinbach. *Accuracy of electron counting using a 7-junction electron pump*. Appl. Phys. Lett. **69**, 1804–1806 (1996). See page: 33
- [183] M. D. Blumenthal et al. *Gigahertz quantized charge pumping*. Nat. Phys. **3**, 343–347 (2007). See page: 33
- [184] J. M. Shilton et al. *On the acoustoelectric current in a one-dimensional channel*. J. Phys. Condens. Matter **8**, L337–L343 (1996). See page: 33
- [185] M. Switkes. *Decoherence and adiabatic transport in semiconductor quantum dots*. PhD thesis, Stanford University (1999). See page: 34
- [186] A. O. Niskanen, J. P. Pekola, and H. Seppä. *Fast and Accurate Single-Island Charge Pump: Implementation of a Cooper Pair Pump*. Phys. Rev. Lett. **91**, 177003 (2003). See page: 34
- [187] M. Aunola and J. J. Toppari. *Connecting Berry’s phase and the pumped charge in a Cooper pair pump*. Phys. Rev. B **68**, 020502 (2003). See page: 34
- [188] M. Möttönen, J. P. Pekola, J. J. Vartiainen, V. Brosco, and F. W. J. Hekking. *Measurement scheme of the Berry phase in superconducting circuits*. Phys. Rev. B **73**, 214523 (2006). See page: 34
- [189] D. N. Christodoulides, F. Lederer, and Y. Silberberg. *Discretizing light behaviour in linear and nonlinear waveguide lattices*. Nature **424**, 817–823 (2003). See page: 34
- [190] J.-T. A. Chiang and Q. Niu. *Quantum adiabatic particle transport in optical lattices*. Phys. Rev. A **57**, R2278–R2280 (1998). See pages: 34, 45
- [191] P. H. Jones, M. Goonasekera, and F. Renzoni. *Rectifying Fluctuations in an Optical Lattice*. Phys. Rev. Lett. **93**, 073904 (2004). See pages: 34, 45, 60

- [192] T. Salger et al. *Directed Transport of Atoms in a Hamiltonian Quantum Ratchet*. *Science* **326**, 1241–1243 (2009). See pages: 34, 45
- [193] H. J. Metcalf and P. van der Straten. *Laser Cooling and Trapping*. Springer, New York, USA (1999). See page: 35
- [194] W. Ketterle, D. S. Durfee, and D. M. Stamper-Kurn. *Making, probing and understanding Bose-Einstein condensates*. In *Bose-Einstein Condensation in Atomic Gases* (Eds. M. Inguscio, S. Stringari and C. E. Wieman), pp. 67–176. IOS Press, Amsterdam, Netherlands (1999). See pages: 36, 37
- [195] L. P. Pitaevskii and S. Stringari. *Bose-Einstein Condensation*. Oxford University Press, Oxford, United Kingdom (2003). See page: 36
- [196] R. Grimm, M. Weidemüller, and Y. B. Ovchinnikov. *Optical Dipole Traps for Neutral Atoms*. In *Advances In Atomic, Molecular, and Optical Physics, Vol. 42* (Eds. B. Bederson and H. Walther), pp. 95–170. Academic Press, Cambridge, United States (2000). See page: 36
- [197] T. Rom. *Bosonische und fermionische Quantengase in dreidimensionalen optischen Gittern – Präparation, Manipulation und Analyse –*. PhD thesis, Ludwig-Maximilians-Universität München (2009). See page: 36
- [198] M. Lewenstein et al. *Ultracold atomic gases in optical lattices: mimicking condensed matter physics and beyond*. *Adv. Phys.* **56**, 243–379 (2007). See page: 36
- [199] A. L. Schawlow. *Spectroscopy in a new light*. *Rev. Mod. Phys.* **54**, 697–707 (1982). See page: 37
- [200] G. C. Bjorklund, M. D. Levenson, W. Lenth, and C. Ortiz. *Frequency modulation (FM) spectroscopy*. *Appl. Phys. B* **32**, 145–152 (1983). See page: 37
- [201] S. Fölling. *Probing strongly correlated states of ultracold atoms in optical lattices*. PhD thesis, Johannes-Gutenberg-Universität Mainz (2008). See page: 37
- [202] U. Schünemann, H. Engler, R. Grimm, M. Weidemüller, and M. Zielonkowski. *Simple scheme for tunable frequency offset locking of two lasers*. *Rev. Sci. Instrum.* **70**, 242–243 (1999). See page: 39
- [203] S. Trotzky. *Experiments with ultracold atoms in a bichromatic optical superlattice*. PhD thesis, Ludwig-Maximilians-Universität München (to be published). See pages: 39, 43
- [204] S. Peil et al. *Patterned loading of a Bose-Einstein condensate into an optical lattice*. *Phys. Rev. A* **67**, 051603 (2003). See page: 40
- [205] S. Fölling et al. *Direct observation of second-order atom tunnelling*. *Nature* **448**, 1029–1032 (2007). See pages: 40, 45

- [206] M. Atala et al. *Observation of chiral currents with ultracold atoms in bosonic ladders*. Nat. Phys. **10**, 588–593 (2014). See pages: 40, 47
- [207] J. Sebby-Strabley, M. Anderlini, P. S. Jessen, and J. V. Porto. *Lattice of double wells for manipulating pairs of cold atoms*. Phys. Rev. A **73**, 033605 (2006). See pages: 40, 45
- [208] M. Feld. *Ultracold bosonic atoms in bichromatic optical superlattices*. Diploma thesis, Technische Universität Kaiserslautern/Johannes-Gutenberg-Universität Mainz (2007). See page: 40
- [209] W. Kohn. *Analytic Properties of Bloch Waves and Wannier Functions*. Phys. Rev. **115**, 809–821 (1959). See pages: 41, 59
- [210] F. Görg. *Ultracold Fermionic Atoms in Optical Superlattices*. Master’s thesis, Technische Universität München/Ludwig-Maximilians-Universität München (2014). See page: 41
- [211] H. A. Gersch and G. C. Knollman. *Quantum Cell Model for Bosons*. Phys. Rev. **129**, 959–967 (1963). See page: 42
- [212] M. P. A. Fisher, P. B. Weichman, G. Grinstein, and D. S. Fisher. *Boson localization and the superfluid-insulator transition*. Phys. Rev. B **40**, 546–570 (1989). See pages: 42, 43
- [213] S. Onoda, S. Murakami, and N. Nagaosa. *Topological Nature of Polarization and Charge Pumping in Ferroelectrics*. Phys. Rev. Lett. **93**, 167602 (2004). See page: 42
- [214] P. Buonsante and A. Vezzani. *Phase diagram for ultracold bosons in optical lattices and superlattices*. Phys. Rev. A **70**, 033608 (2004). See pages: 43, 129
- [215] V. G. Rousseau et al. *Exact study of the one-dimensional boson Hubbard model with a superlattice potential*. Phys. Rev. B **73**, 174516 (2006). See page: 43
- [216] I. Danshita, J. E. Williams, C. A. R. Sá de Melo, and C. W. Clark. *Quantum phases of bosons in double-well optical lattices*. Phys. Rev. A **76**, 043606 (2007). See page: 43
- [217] Y. Qian, M. Gong, and C. Zhang. *Quantum transport of bosonic cold atoms in double-well optical lattices*. Phys. Rev. A **84**, 013608 (2011). See page: 45
- [218] R. Wei and E. J. Mueller. *Anomalous charge pumping in a one-dimensional optical superlattice*. Phys. Rev. A **92**, 013609 (2015). See pages: 45, 127
- [219] S. Nakajima et al. *Topological Thouless pumping of ultracold fermions*. Nat. Phys. **12**, 296–300 (2016). See page: 46
- [220] H.-I. Lu et al. *Geometrical Pumping with a Bose-Einstein Condensate*. Phys. Rev. Lett. **116**, 200402 (2016). See page: 46

- [221] T. Fukui, Y. Hatsugai, and H. Suzuki. *Chern Numbers in Discretized Brillouin Zone: Efficient Method of Computing (Spin) Hall Conductances*. J. Phys. Soc. Jpn. **74**, 1674–1677 (2005). See page: 46
- [222] P. Marra, R. Citro, and C. Ortix. *Fractional quantization of the topological charge pumping in a one-dimensional superlattice*. Phys. Rev. B **91**, 125411 (2015). See pages: 47, 118
- [223] Z. Ringel and Y. E. Kraus. *Determining topological order from a local ground-state correlation function*. Phys. Rev. B **83**, 245115 (2011). See page: 58
- [224] V. Mourik et al. *Signatures of Majorana Fermions in Hybrid Superconductor-Semiconductor Nanowire Devices*. Science **336**, 1003–1007 (2012). See page: 65
- [225] P. Hosur and X. Qi. *Recent developments in transport phenomena in Weyl semimetals*. C. R. Phys. **14**, 857–870 (2013). See pages: 65, 69, 129
- [226] J. Fröhlich and B. Pedrini. *Axions, quantum mechanical pumping, and primeval magnetic fields*. In *Statistical Field Theories* (Eds. A. Cappelli and G. Mussardo), pp. 289–303. Springer Netherlands, Dordrecht, Netherlands (2002). See pages: 65, 68
- [227] J. Hu and S.-C. Zhang. *Collective excitations at the boundary of a four-dimensional quantum Hall droplet*. Phys. Rev. B **66**, 125301 (2002). See pages: 65, 69, 70
- [228] H. Elvang and J. Polchinski. *The quantum Hall effect on R^4* . C. R. Phys. **4**, 405–417 (2003). See pages: 65, 69, 70
- [229] F. D. M. Haldane. *Model for a Quantum Hall Effect without Landau Levels: Condensed-Matter Realization of the "Parity Anomaly"*. Phys. Rev. Lett. **61**, 2015–2018 (1988). See page: 66
- [230] H. L. Störmer, J. P. Eisenstein, A. C. Gossard, W. Wiegmann, and K. Baldwin. *Quantization of the Hall effect in an anisotropic three-dimensional electronic system*. Phys. Rev. Lett. **56**, 85–88 (1986). See page: 66
- [231] B. I. Halperin. *Possible States for a Three-Dimensional Electron Gas in a Strong Magnetic Field*. Jpn. J. Appl. Phys. **26**, 1913–1919 (1987). See page: 66
- [232] M. Kohmoto, B. I. Halperin, and Y.-S. Wu. *Diophantine equation for the three-dimensional quantum Hall effect*. Phys. Rev. B **45**, 13488–13493 (1992). See page: 66
- [233] S. C. Zhang, T. H. Hansson, and S. Kivelson. *Effective-Field-Theory Model for the Fractional Quantum Hall Effect*. Phys. Rev. Lett. **62**, 82–85 (1989). See page: 66
- [234] S. C. Zhang. *The Chern–Simons–Landau–Ginzburg Theory of the Fractional Quantum Hall Effect*. Int. J. Mod. Phys. B **06**, 25–58 (1992). See page: 66

- [235] M. Koshino, H. Aoki, K. Kuroki, S. Kagoshima, and T. Osada. *Hofstadter Butterfly and Integer Quantum Hall Effect in Three Dimensions*. Phys. Rev. Lett. **86**, 1062–1065 (2001). See page: 66
- [236] M. Koshino and H. Aoki. *Integer quantum Hall effect in isotropic three-dimensional crystals*. Phys. Rev. B **67**, 195336 (2003). See page: 66
- [237] S.-C. Zhang. *To see a world in a grain of sand*. In *Science and Ultimate Reality: Quantum Theory, Cosmology, and Complexity* (Eds. J. D. Barrow, P. C. W. Davies, and C. L. Harper), pp. 667–690. Cambridge University Press, Cambridge, United Kingdom (2004). See pages: 66, 68, 69
- [238] P. Werner. *(4+1)-Dimensional Quantum Hall Effect & Applications to Cosmology*. Diploma thesis, École Polytechnique Fédérale de Lausanne/Eidgenössische Technische Hochschule Zürich (2000). See pages: 66, 67, 68, 70
- [239] B. A. Bernevig, C.-H. Chern, J.-P. Hu, N. Toumbas, and S.-C. Zhang. *Effective Field Theory Description of the Higher Dimensional Quantum Hall Liquid*. Ann. Phys. **300**, 185–207 (2002). See pages: 67, 68
- [240] J. E. Avron, L. Sadun, J. Segert, and B. Simon. *Topological Invariants in Fermi Systems with Time-Reversal Invariance*. Phys. Rev. Lett. **61**, 1329–1332 (1988). See page: 67
- [241] J. E. Avron, L. Sadun, J. Segert, and B. Simon. *Chern numbers, quaternions, and Berry's phases in Fermi systems*. Commun. Math. Phys. **124**, 595–627 (1989). See page: 67
- [242] D. Xiao, J. Shi, D. P. Clougherty, and Q. Niu. *Polarization and Adiabatic Pumping in Inhomogeneous Crystals*. Phys. Rev. Lett. **102**, 087602 (2009). See page: 67
- [243] C. N. Yang. *Generalization of Dirac's monopole to SU2 gauge fields*. J. Math. Phys. **19**, 320–328 (1978). See page: 67
- [244] A. M. Essin, J. E. Moore, and D. Vanderbilt. *Magnetoelectric Polarizability and Axion Electrodynamics in Crystalline Insulators*. Phys. Rev. Lett. **102**, 146805 (2009). See page: 67
- [245] V. Dziom et al. *Observation of the universal magnetoelectric effect in a 3D topological insulator*. Nat. Commun. **8**, 15197 (2017). See page: 67
- [246] F. D. M. Haldane. *Fractional Quantization of the Hall Effect: A Hierarchy of Incompressible Quantum Fluid States*. Phys. Rev. Lett. **51**, 605–608 (1983). See page: 67
- [247] M. Fabinger. *Higher-Dimensional Quantum Hall Effect in String Theory*. J. High Energy Phys. **2002**, 037 (2002). See page: 68

- [248] T. Kaluza. *Zum Unitätsproblem in der Physik*. Sitzungsber. Preuss. Akad. Wiss. pp. 966–972 (1921). See page: 68
- [249] O. Klein. *Quantentheorie und fünfdimensionale Relativitätstheorie*. Z. Physik **37**, 895–906 (1926). See page: 68
- [250] M. Joyce and M. Shaposhnikov. *Primordial Magnetic Fields, Right Electrons, and the Abelian Anomaly*. Phys. Rev. Lett. **79**, 1193–1196 (1997). See page: 68
- [251] N. P. Armitage, E. J. Mele, and A. Vishwanath. *Weyl and Dirac Semimetals in Three Dimensional Solids*. arXiv:1705.01111 [cond-mat.str-el] (2017). See page: 69
- [252] N. Maeda. *Chiral anomaly and effective field theory for the quantum Hall liquid with edges*. Phys. Lett. B **376**, 142–147 (1996). See page: 69
- [253] A. D. Sakharov. *Vacuum quantum fluctuations in curved space and the theory of gravitation*. Dokl. Akad. Nauk SSSR pp. 70–71 (1967). [Soviet Physics Uspekhi **34**, 394 (1991)]. See page: 69
- [254] G. E. Volovik. *Superfluid analogies of cosmological phenomena*. Phys. Rep. **351**, 195–348 (2001). See page: 69
- [255] P. W. Anderson. *More Is Different*. Science **177**, 393–396 (1972). See page: 69
- [256] C. Kallin and B. I. Halperin. *Excitations from a filled Landau level in the two-dimensional electron gas*. Phys. Rev. B **30**, 5655–5668 (1984). See page: 69
- [257] M. Stone. *Schur functions, chiral bosons, and the quantum-Hall-effect edge states*. Phys. Rev. B **42**, 8399–8404 (1990). See page: 69
- [258] Y. Chong and R. Laughlin. *Metallic nature of the four-dimensional quantum Hall edge*. Ann. Phys. **308**, 237–243 (2003). See page: 70
- [259] S. Weinberg and E. Witten. *Limits on massless particles*. Phys. Lett. B **96**, 59–62 (1980). See page: 70
- [260] M.-C. Chang and Q. Niu. *Berry Phase, Hyperorbits, and the Hofstadter Spectrum*. Phys. Rev. Lett. **75**, 1348–1351 (1995). See page: 71
- [261] M.-C. Chang and Q. Niu. *Berry phase, hyperorbits, and the Hofstadter spectrum: Semiclassical dynamics in magnetic Bloch bands*. Phys. Rev. B **53**, 7010–7023 (1996). See page: 71
- [262] Y. Gao, S. A. Yang, and Q. Niu. *Field Induced Positional Shift of Bloch Electrons and Its Dynamical Implications*. Phys. Rev. Lett. **112**, 166601 (2014). See page: 71
- [263] D. Xiao, J. Shi, and Q. Niu. *Berry Phase Correction to Electron Density of States in Solids*. Phys. Rev. Lett. **95**, 137204 (2005). See page: 72

- [264] K. Bliokh. *On the Hamiltonian nature of semiclassical equations of motion in the presence of an electromagnetic field and Berry curvature*. Phys. Lett. A **351**, 123–124 (2006). See page: 72
- [265] C. Duval, Z. Horváth, P. A. Horváthy, L. Martina, and P. C. Stichel. *Berry Phase Correction to Electron Density in Solids and "Exotic" Dynamics*. Mod. Phys. Lett. B **20**, 373–378 (2006). See page: 72
- [266] P. Gosselin, F. Ménas, A. Bérard, and H. Mohrbach. *Semiclassical dynamics of electrons in magnetic Bloch bands: A Hamiltonian approach*. EPL **76**, 651–656 (2006). See page: 72
- [267] H. M. Price and N. R. Cooper. *Mapping the Berry curvature from semiclassical dynamics in optical lattices*. Phys. Rev. A **85**, 033620 (2012). See page: 73
- [268] A. Dauphin and N. Goldman. *Extracting the Chern Number from the Dynamics of a Fermi Gas: Implementing a Quantum Hall Bar for Cold Atoms*. Phys. Rev. Lett. **111**, 135302 (2013). See page: 73
- [269] N. Goldman, G. Juzeliūnas, P. Öhberg, and I. B. Spielman. *Light-induced gauge fields for ultracold atoms*. Rep. Prog. Phys. **77**, 126401 (2014). See page: 73
- [270] X.-W. Luo et al. *Quantum simulation of 2D topological physics in a 1D array of optical cavities*. Nat. Commun. **6**, 7704 (2015). See page: 78
- [271] T. Ozawa, H. M. Price, N. Goldman, O. Zilberberg, and I. Carusotto. *Synthetic dimensions in integrated photonics: From optical isolation to four-dimensional quantum Hall physics*. Phys. Rev. A **93**, 043827 (2016). See page: 78
- [272] H. Kunz. *Quantized Currents and Topological Invariants for Electrons in Incommensurate Potentials*. Phys. Rev. Lett. **57**, 1095–1097 (1986). See page: 79
- [273] J. C. Y. Teo and T. L. Hughes. *Existence of Majorana-Fermion Bound States on Disclinations and the Classification of Topological Crystalline Superconductors in Two Dimensions*. Phys. Rev. Lett. **111**, 047006 (2013). See page: 94
- [274] W. A. Benalcazar, B. A. Bernevig, and T. L. Hughes. *Quantized electric multipole insulators*. Science **357**, 61–66 (2017). See page: 94
- [275] J. Noh et al. *Topological protection of photonic mid-gap cavity modes*. arXiv:1611.02373 [cond-mat.mes-hall] (2016). See page: 94
- [276] O. Zilberberg et al. *Photonic topological boundary pumping as a probe of 4D quantum Hall physics*. Nature **553**, 59–62 (2018). See page: 95
- [277] F. Gerbier, A. Widera, S. Fölling, O. Mandel, and I. Bloch. *Resonant control of spin dynamics in ultracold quantum gases by microwave dressing*. Phys. Rev. A **73**, 041602 (2006). See page: 103

- [278] C. K. Law, H. Pu, and N. P. Bigelow. *Quantum Spins Mixing in Spinor Bose-Einstein Condensates*. Phys. Rev. Lett. **81**, 5257–5261 (1998). See page: 103
- [279] H. Schmaljohann et al. *Dynamics of $F = 2$ Spinor Bose-Einstein Condensates*. Phys. Rev. Lett. **92**, 040402 (2004). See page: 103
- [280] A. Widera et al. *Coherent Collisional Spin Dynamics in Optical Lattices*. Phys. Rev. Lett. **95**, 190405 (2005). See page: 103
- [281] A. Widera. *Constructing Correlated Spin States with Neutral Atoms in Optical Lattices*. PhD thesis, Johannes-Gutenberg-Universität Mainz (2007). See page: 103
- [282] D. Sesko, T. Walker, C. Monroe, A. Gallagher, and C. Wieman. *Collisional losses from a light-force atom trap*. Phys. Rev. Lett. **63**, 961–964 (1989). See page: 104
- [283] M. T. DePue, C. McCormick, S. L. Winoto, S. Oliver, and D. S. Weiss. *Unity Occupation of Sites in a 3D Optical Lattice*. Phys. Rev. Lett. **82**, 2262–2265 (1999). See page: 104
- [284] J. Weiner, V. S. Bagnato, S. Zilio, and P. S. Julienne. *Experiments and theory in cold and ultracold collisions*. Rev. Mod. Phys. **71**, 1–85 (1999). See page: 104
- [285] E. Brown. *Bloch Electrons in a Uniform Magnetic Field*. Phys. Rev. **133**, A1038–A1044 (1964). See page: 118
- [286] J. Zak. *Magnetic Translation Group*. Phys. Rev. **134**, A1602–A1606 (1964). See page: 118
- [287] W. S. Bakr, J. I. Gillen, A. Peng, S. Fölling, and M. Greiner. *A quantum gas microscope for detecting single atoms in a Hubbard-regime optical lattice*. Nature **462**, 74–77 (2009). See page: 127
- [288] J. F. Sherson et al. *Single-atom-resolved fluorescence imaging of an atomic Mott insulator*. Nature **467**, 68–72 (2010). See page: 127
- [289] F. Grusdt, M. Hönig, and M. Fleischhauer. *Topological Edge States in the One-Dimensional Superlattice Bose-Hubbard Model*. Phys. Rev. Lett. **110**, 260405 (2013). See pages: 127, 129
- [290] R. Shindou. *Quantum Spin Pump in $S=1/2$ Antiferromagnetic Chains –Holonomy of Phase Operators in sine-Gordon Theory–*. J. Phys. Soc. Jpn. **74**, 1214–1223 (2005). See page: 127
- [291] L. Fu and C. L. Kane. *Time reversal polarization and a Z_2 adiabatic spin pump*. Phys. Rev. B **74**, 195312 (2006). See page: 127
- [292] M. H. Kolodrubetz, F. Nathan, S. Gazit, T. Morimoto, and J. E. Moore. *Topological Floquet-Thouless energy pump*. arXiv:1711.00014 [cond-mat.quant-gas] (2017). See page: 127

- [293] M. S. Rudner, N. H. Lindner, E. Berg, and M. Levin. *Anomalous Edge States and the Bulk-Edge Correspondence for Periodically Driven Two-Dimensional Systems*. Phys. Rev. X **3**, 031005 (2013). See page: 127
- [294] D. T. Tran, A. Dauphin, A. G. Grushin, P. Zoller, and N. Goldman. *Probing topology by “heating”: Quantized circular dichroism in ultracold atoms*. Sci. Adv. **3** (2017). See page: 127
- [295] N. Goldman. Private communications (2017). See page: 128
- [296] S.-L. Zhu, Z.-D. Wang, Y.-H. Chan, and L.-M. Duan. *Topological Bose-Mott Insulators in a One-Dimensional Optical Superlattice*. Phys. Rev. Lett. **110**, 075303 (2013). See page: 129
- [297] A. Eckardt. *Colloquium: Atomic quantum gases in periodically driven optical lattices*. Rev. Mod. Phys. **89**, 011004 (2017). See page: 129
- [298] M. Reitter et al. *Interaction Dependent Heating and Atom Loss in a Periodically Driven Optical Lattice*. Phys. Rev. Lett. **119**, 200402 (2017). See page: 129
- [299] E. J. Bergholtz and A. Karlhede. *Half-Filled Lowest Landau Level on a Thin Torus*. Phys. Rev. Lett. **94**, 026802 (2005). See page: 130
- [300] R. Tao and D. J. Thouless. *Fractional quantization of Hall conductance*. Phys. Rev. B **28**, 1142–1144 (1983). See page: 130
- [301] E. J. Bergholtz and A. Karlhede. *Quantum Hall system in Tao-Thouless limit*. Phys. Rev. B **77**, 155308 (2008). See page: 130
- [302] Z. Xu, L. Li, and S. Chen. *Fractional Topological States of Dipolar Fermions in One-Dimensional Optical Superlattices*. Phys. Rev. Lett. **110**, 215301 (2013). See page: 130
- [303] T.-S. Zeng, W. Zhu, and D. N. Sheng. *Fractional charge pumping of interacting bosons in one-dimensional superlattice*. Phys. Rev. B **94**, 235139 (2016). See page: 130
- [304] R. Li and M. Fleischhauer. *Finite-size corrections to quantized particle transport in topological charge pumps*. Phys. Rev. B **96**, 085444 (2017). See page: 130
- [305] J. C. Budich and E. Ardonne. *Fractional topological phase in one-dimensional flat bands with nontrivial topology*. Phys. Rev. B **88**, 035139 (2013). See page: 130
- [306] F. Grusdt and M. Hönig. *Realization of fractional Chern insulators in the thin-torus limit with ultracold bosons*. Phys. Rev. A **90**, 053623 (2014). See page: 130
- [307] L. Taddia et al. *Topological Fractional Pumping with Alkaline-Earth-Like Atoms in Synthetic Lattices*. Phys. Rev. Lett. **118**, 230402 (2017). See page: 130
- [308] Z. Wang and S.-C. Zhang. *Simplified Topological Invariants for Interacting Insulators*. Phys. Rev. X **2**, 031008 (2012). See page: 130

Acknowledgements

I would like to thank all the people that I had the pleasure to work with during the past years and which contributed to this thesis in one way or the other:

- My supervisor Immanuel Bloch for giving me the opportunity to do my PhD in his research group. In particular, I am thankful for the excellent environment for performing experiments which he created at LMU/MPQ, the freedom and independence that he trusted us with and the many conferences and workshops which I could attend.
- My colleagues at the Boson experiment, Christian Schweizer, Monika Aidelsburger, Marcos Atala, Julio Barreiro und Moritz Berngruber, for the great and productive time in the lab. I am deeply grateful to Marcos and Monika for patiently teaching me all the little secrets of the experiment, the inspiring discussions about physics and all the memorable moments, from testing the limits of geometric optics to baby-sitting unstable lasers. I really enjoyed working in the lab with Christian, benefiting from his incredible knowledge of electronics and mechanics and sharing the good times ("the experiment needs to rest a bit") and the bad ones ("schlimmer geht immer").
- Our theory collaborators Roberta Citro, Nathan Goldman, Hannah Price and Oded Zilberberg for all the invaluable support, the many things in physics which I learned from them and the patience with our slow progress in the lab. I am especially grateful to Hannah and Oded for proposing and encouraging us to perform the 2D pumping experiments and not letting go until we did so as well as all the hard work for and diligent proof-reading of the manuscript.
- The current and former members of the Bloch group at both LMU and MPQ for making my PhD such an enjoyable time, for help and advice on countless occasions and the many stimulating discussions. A special thank you to the Ytterbium team, who shared the floor with us, helped to ensure a culinary minimum standard and were always in for a little "Betriebsausflug" to Ballabeni & friends. I would also like to thank Ildiko Kecskesi for her kind and patient help with administrative matters and Bodo Hecker for electronics support. And the Munich mountaineering team for all the wonderful hikes and ski trips in the Alps and the great times that we spent together.
- My fellow PhD students of the ExQM graduate school and Thomas Schulte-Herbrüggen for the interesting and very diverse seminars and the wonderful workshop at Chiemsee

- Frank Pollmann for acting as the second referee for my thesis and Ralf Jungmann and Thomas Weitz for being part of my defense committee
- Everyone who corrected and proof-read this thesis for all the valuable comments
- My family and friends for all the support throughout the years, for offering distraction in stressful times and for always being there for me. And my girlfriend Diana for going to LMU with me in the middle of a freezing night to re-lock the superlattice laser :)